Hot Subdwarf Stars in Close-up View: Orbits, Rotation, Abundances and Masses of their Unseen Companions

Den Naturwissenschaftlichen Fakultäten
der Friedrich-Alexander-Universität Erlangen-Nürnberg
zur
Erlangung des Doktorgrades

vorgelegt von

Stephan Geier
aus Stadtsteinach

Als Dissertation genehmigt von den Naturwissenschaftlichen Fakultäten
der Universität Erlangen-Nürnberg

Contents

List of Figures

List of Tables

Zusammenfassung

Heiße unterleuchtkräftige Sterne oder hot subdwarfs (in diesem Kapitel kurz sdBs genannt) wurden im Jahr 1954 entdeckt. Obwohl ihre Spektren denen von heißen Hauptreihensternen sehr ähnlich sind, erwiesen sich diese Sterne als wesentlich kleiner und damit deutlich leuchtschwächer. Man fand heraus, dass es sich dabei um alte Sterne handeln musste, die sich bereits zum Roten Riesen entwickelt und danach einen Großteil ihrer Hülle verloren hatten. Ein Zusammenhang zwischen diesen Objekten und dem Horizontalast, der aus Sternen besteht, die in ihren Kernen Helium verbrennen, konnte nachgewiesen werden. Die hot subdwarfs begrenzen den Horizontalast im Blauen. Dieser Bereich wird daher auch als extremer Horizontalast (Extreme Horizontal Branch, EHB) bezeichnet.

Die wichtigste offene Frage im Zusammenhang mit sdBs betrifft ihre Entstehung. Es herrscht allgemeine Übereinstimmung darin, dass diese Sterne sehr dünne Wasserstoffhüllen besitzen, in ihren Kernen aber Helium verbrennen und etwa die halbe Masse der Sonne haben müssen. Die zu dünnen Wasserstoffhüllen sind der Grund, warum sie nicht mehr in der Lage sind, Wasserstoffschalenbrennen zu zünden und den asymptotischen Riesenast emporzusteigen, wie dies die meisten anderen Sterne tun. Stattdessen entwickeln sie sich nach der Phase des Heliumbrennens direkt zu Weißen Zwergen und kühlen ab. Um den EHB zu erreichen, müssen ihre Vorläufer im Roten–Riesen–Stadium fast ihre gesamte Hülle verloren haben. Verschiedene Szenarien für diesen hohen Massenverlust wurden vorgeschlagen, aber bislang konnte noch keine dieser Theorien alle beobachteten Eigenschaften von sdBs erklären. Mit der Verfügbarkeit großer Teleskope und empfindlicherer Instrumente wurden detaillierte spektroskopische Analysen von großen sdB Samplen möglich. Diese zeigten, dass die Sterne, die man als hot subdwarfs bezeichnete, in Unterklassen aufgeteilt werden müssen und dass Objekte aus verschiedenen Unterklassen wahrscheinlich auch unterschiedliche Entwicklungswege durchlaufen haben. Der EHB bleibt daher einer der weißen Flecken in der stellaren Astrophysik. Dies hat auch wichtige Konsequenzen für andere Teilgebiete der Astronomie wie etwa die Sternentwicklung in alten Populationen, aus denen Kugelsternhaufen und elliptische Galaxien bestehen.

Doch der Grund für die intensive Forschung auf diesem Gebiet liegt nicht nur darin begründet, dass sdBs mehr oder weniger überall in der Galaxie und darüber hinaus zu finden sind. Die Eigenschaften dieser Sterne selbst erwiesen sich in mehrfacher Hinsicht als bemerkenswert. Die Entdeckung von fünf unterschiedlichen Klassen pulsierender sdB Sterntypen führte zu intensiven Studien dieser Objekte, und sie erwiesen sich als perfekte Laboratorien für asteroseismische Analysen. Außerdem sind die Atmosphären der sdB Sterne chemisch pekuliär und durch detaillierte Messungen der Elementhäufigkeiten kann man viel über Diffusionsprozesse in Sternatmosphären lernen. Eine Reihe von Konferenzen, die sich den sdB Sternen widmen, wurde 2003 ins Leben gerufen und zieht seitdem Wissenschaftler aus aller Welt an, die sich für ganz unterschiedliche Aspekte der sdB Forschung interessieren. Die letzte Konferenz wurde im Jahr 2007 von unserer

Arbeitsgruppe in Bamberg ausgerichtet.

Eng verbunden mit der offenen Frage der Entstehung von sdBs ist eine weitere wichtige Eigenschaft dieser Sterne. Etwa die Hälfte der sdBs befinden sich in engen Doppelsternsystemen mit kleinen Begleitern wie Weißen Zwergen oder späten Hauptreihensternen (Main Sequence, MS), die sie mit Perioden von weniger als zwei Stunden und Abständen kleiner als der Radius unserer Sonne umkreisen können. Solche Systeme sind von außerordentlicher Bedeutung für unser Verständnis der Sternentwicklung. Doppelsternszenarien, die einen mehr oder weniger stabilen Massentransfer zwischen den Vorläufersternen beinhalten, wurden als alternativer Entstehungsweg für sdBs vorgeschlagen. Populationssynthese–Modelle auf der einen und die Analyse von großen sdB Samplen auf der anderen Seite erlaubten es, diese Szenarien mit den beobachteten Eigenschaften von sdBs zu vergleichen. Unter den bekannten sdB Doppelsternen gibt es viele sehr spezielle und damit interessante Objekte. Bedeckende Doppelsterne ermöglichen es uns zum Beispiel, alle Parameter des Systems zu bestimmen, auch die Sternmassen. Andere Doppelsterne zeigen Variationen in ihren Lichtkurven, verursacht entweder durch eine Deformierung des sdBs aufgrund der Gezeitenkräfte eines kompakten Begleiters oder durch reflektiertes Licht von der aufgeheizten Oberfläche eines ansonsten kühlen Hauptreihenbegleiters, der von dem heißen sdB beschienen wird. Pulsierende sdBs in engen Doppelsternsystemen sind auch bekannt und bieten die einmalige Gelegenheit, von asteroseismischen Analysen abgeleitete Sternparameter zu verifizieren.

Der beste bekannte Kandidat für einen doppelt entarteten Vorläufer einer Supernova des Typs Ia (SN Ia) ist ein Doppelstern bestehend aus einem sdB und einem massereichen Weißen Zwerg. SN Ia sind die wichtigsten Standardkerzen zur Messung der größten Distanzen im Universum. Die bedeutendste Entdeckung der beobachtenden Kosmologie, die beschleunigte Expansion des Universums, basiert auf solchen Messungen. Ein sehr gutes Verständnis der SN Ia Vorläuferpopulation ist notwendig, um systematische Fehler dieser Methode abschätzen zu können. Leider ist diese Vorläuferpopulation noch weitgehend unverstanden.

Die kürzliche Entdeckung eines planetaren Begleiters um einen pulsierenden sdB Stern ist von besonderer Bedeutung, da dieses Objekt die Rote Riesen Phase des Vorläufersterns überlebt haben muss. Außerdem könnten Planeten um sdBs recht häufig sein und bei der Entstehung dieser Sterne eine Rolle spielen.

Bisher wurden 81 sdB Doppelsterne genauer untersucht und die Parameter ihrer Umlaufbahnen bestimmt. Obwohl die Verteilung ihrer Umlaufperioden abgeleitet werden konnte, blieben Masse und Art ihrer unsichtbaren Begleiter in den meisten Fällen unklar. Das primäre Ziel dieser Studie ist es, die Massen dieser Begleiter zu bestimmen und sie eindeutig zu identifizieren. Hochaufgelöste Spektren und eine neue Analysemethode wurden genutzt, um dieses Ziel zu erreichen.

Nachdem ein Überblick über den gegenwärtigen Stand der sdB Forschung gegeben wurde (Kap. 1), werden die bisherigen Resultate zu sdBs in Doppelsternen näher betrachtet, Orbitparameter für einige neu entdeckte Doppelsterne bestimmt und einige Doppelstern-Kandidaten mit variabler Radialgeschwindigkeit (RV) präsentiert (Kap. 2). Wir konnten Orbitparameter von sieben Systemen bestimmen. Vorläufige Lösungen wurden für weitere vier Systeme berechnet. Neun enge Doppelsterne wurden entdeckt durch Messung von variablen Radialgeschwindigkeiten. Alle analysierten Doppelsterne haben kurze Perioden zwischen $0.14\,\mathrm{d}$ und $0.98\,\mathrm{d}$. Mittels der stellaren Massenfunktion und unter der Annahme der wahrscheinlichsten Masse für die sdBs konnten untere Grenzen für die Massen der Begleiter gesetzt werden. In einigen Fällen half die Entdeckung von Reflektionseffekten oder Flussexzessen im roten Spektralbereich beziehungsweise

das Fehlen derselben, die Beschaffenheit des Begleiters weiter einzugrenzen.

Drei Systeme bestehen aus sdBs und kompakten Objekten – sehr wahrscheinlich Weiße Zwerge. In einem Fall erlaubt der Nachweis einer Bedeckung sogar, den Begleiter eindeutig als Weißen Zwerg zu identifizieren. Die Begleiter von zwei sdBs sind späte Hauptreihensterne, die sich durch einen Reflektionseffekt in ihren Lichtkurven verraten. Ein Doppelstern mit vorläufiger Orbitlösung beherbergt höchstwahrscheinlich ein kompaktes Objekt. Ein doppelliniges sdB+G System befindet sich in einem Orbit mit kurzer Umlaufperiode. In allen anderen Systemen konnte die Art des Begleiters nicht geklärt werden.

In Kap. 3 wird eine neue Analysemethode eingeführt, die es erlaubt, die bislang unbekannten Inklinationswinkel und damit auch die Massen der unsichtbaren Begleiter zu bestimmen. Diese neuartige Technik erfordert hochaufgelöste Spektren. Mit verschiedenen Teleskopen und Instrumenten weltweit, darunter auch dem 10 m Keck Teleskop auf Hawaii und dem 8 m ESO-VLT in Chile, gelang es uns, Spektren einer großen Anzahl von Einzel-sdBs sowie sdBs in engen Doppelsternsystemen aufzunehmen – mit Abstand das größte Sample hochaufgelöster sdB Spektren, das bisher analysiert wurde.

Die Resultate werden vorgestellt und systematische Fehlerquellen im Detail diskutiert. Die Begleiter der meisten sdBs sind späte Hauptreihensterne oder Weiße Zwerge. Ein kurzperiodisches System beherbergt einen massereichen Weißen Zwerg und erfüllt die Kriterien für einen SN Ia Kandidaten. Überraschenderweise entdeckten wir einige sdBs mit massereichen, aber unsichtbaren und damit kompakten Begleitern, die daher Neutronensterne (NS) oder stellare schwarze Löcher (Black Holes, BH) sein müssen. Die potentielle Entdeckung einer noch unbekannten Population dieser exotischen Objekte erforderte eine kritische Auseinandersetzung mit unserer Analysemethode.

Die wichtigste Voraussetzung für unsere Analysemethode besteht in der üblichen Annahme, dass die Rotation des sdBs in einem engen Doppelsternsystem mit seiner Umlaufperiode synchronisiert ist. Kap. 4 beschäftigt sich daher mit der Frage der Synchronisation in sdB Doppelsternen. Sowohl theoretische Zeitskalen, als auch empirische Belege für Synchronisation werden diskutiert. Die Messung der schwächsten bekannten ellipsoidalen Verformung eines Sterns mittels einer hoch präzisen Lichtkurve aufgenommen mit dem MOST Satelliten, erlaubte es uns, Synchronisation in einem sdB+WD Doppelsternsystem mit einer Periode von über einem halben Tag nachzuweisen.

Drei post-RGB Sterne wurden ebenfalls analysiert und es zeigte sich, dass diese Objekte generell nicht synchronisiert sind. Die Gründe dafür sind wahrscheinlich die kürzeren Entwicklungszeiten und die unterschiedliche innere Struktur dieser Objekte. Zwei super-synchron rotierende sdBs in engen Doppelsternsystemen, die bisher für post-EHB Sterne gehalten wurden, gehören sehr wahrscheinlich ebenfalls zur Klasse der post-RGB Objekte.

In Kap. 5 wird ein mögliches Entstehungsszenario für sdB+NS/BH Systeme vorgestellt, das zwei Common Envelope-Phasen und eine Supernova-Explosion umfasst, und Vorhersagen über die Häufigkeit dieser Systeme werden abgeleitet. Der beobachtete Anteil der sdB+NS/BH Systeme war deutlich höher als der theoretisch vorhergesagte. In Kap. 6 werden Auswahleffekte und deren Einfluss auf den Anteil der sdB+NS/BH Systeme sowie die Inklinationswinkelverteilung des Doppelstern-Samples qualitativ diskutiert. Um Konsistenz zwischen Theorie und Beobachtung herzustellen, müssen einige der sdBs niedrigere Massen haben, als gemeinhin angenommen. Diese Massen sind aber nach wie vor konsistent mit Doppelstern Entwicklungsrechnungen. Selbst unter den konservativsten Annahmen bleiben einige sdB+NS/BH Systemen übrig, was einen starken Anhaltspunkt für die Existenz dieser Systeme darstellt.

Dieser neu entdeckte Zusammenhang zwischen sdBs, die überall in der Galaxis zahlreich vorkommen, und massereichen kompakten Objekten könnte zu einem gewaltigen Anstieg der Anzahl bekannter Neutronensterne oder Schwarzer Löcher führen und etwas Licht in diese dunkle Population und deren Verbindung mit den Röntgen-Doppelsternen bringen.

Wir führten die erste systematische Untersuchung der Rotationseigenschaften von sdB Sternen durch. Ausgehend von hochaufgelösten Spektren bestimmten wir die projizierten Rotationsgeschwindigkeiten von 49 Einzel-sdBs (Kap. 7) und 51 sdBs in engen Doppelsternsystemen. Im Falle von langsam rotierenden Sternen benutzten wir alle geeigneten Metallinien. Bei schnell rotierenden Sternen wurden Balmer- und Heliumlinien verwendet, um Modellspektren mit passender Rotationsverbreiterung zu fitten. SdB Einzelsterne sind langsame Rotatoren, die sich mit einer beinahe gleichartigen Geschwindigkeit von etwa $8\,\mathrm{km s^{-1}}$ drehen, während die Rotation von sdBs in engen Doppelsternsystemen eindeutig von den Gezeitenkräften der unsichtbaren Begleiter beeinflusst wird.

Das wichtigste Nebenprodukt dieser Studie ist die Bestimmung der Metallhäufigkeiten eines großen Samples von sdB Sternen. In Kap. 8 werden die Analyse der Daten erläutert, die Resultate vorgestellt und diskutiert. Die Trends der Häufigkeiten mit der Temperatur und ein Vergleich mit früheren Resultaten von blauen Horizontalaststernen (Blue Horizontal Branch, BHB) zeigen deutlich, dass Diffusionsprozesse tatsächlich für die beobachteten Häufigkeitsmuster verantwortlich sind. Die Entdeckung einer neuen Unterklasse von mit Kohlenstoff angereicherten sdBs wird vorgestellt und im Zusammenhang mit der Entstehung von sdBs diskutiert. Mit Kohlenstoff angereicherte sdBs könnten das fehlende Verbindungsglied zwischen helium- und wasserstoffreichen Subdwarfs darstellen, dass von den neuesten theoretischen Modellen vorhergesagt wird.

Die Entdeckung von sdB+NS/BH Kandidaten im Zuge dieser Arbeit führte zu einem großen Survey, der von einer internationalen Gruppe von Astronomen durchgeführt und vom Autor dieser Dissertation koordiniert wird. Kap. 9 bietet einen kurzen Ausblick und führt den (HYPER-)MUCHFUSS Survey ein, dessen Ziel es ist, sdB+NS/BH Systeme im Halo unserer Galaxis zu finden und der im Jahr 2007 gestartet wurde.

Abstract

Hot subluminous stars or hot subdwarfs (in this Chapter just called sdBs) have been discovered back in 1954. Showing similar spectral appearance as hot main sequence stars, they turned out to be much smaller and hence much less luminous. It became clear that these objects are old stars, which already passed through the Red Giant stage and lost most of their mass during their evolution. Their relation to the Horizontal Branch, which is populated by helium core burning stars, became clear. In fact the hot subdwarf stars form the bluest part of the Horizontal Branch, which was called Extreme Horizontal Branch (EHB).

The most important open question about sdB stars concerns their formation. It is general consensus, that these objects have very thin hydrogen envelopes around a helium burning core of about half a solar mass. The thin hydrogen envelopes are the reason why they are not able to ignite hydrogen shell burning and to ascend the Asymptotic Giant Branch as more normal stars do. Instead they evolve directly towards the white dwarf cooling tracks after the helium core burning phase. In order to reach the EHB their Red Giant progenitors must have lost most of their envelope. Different scenarios have been proposed to explain this huge mass loss, but up to now no formation theory could explain all the observed features of sdBs. With the advent of large telescopes and better instrumentation more detailed spectroscopic studies of large sdB samples became possible. They revealed that the stars termed hot subdwarfs have to be further divided into subclasses and that some of the members of these subclasses most likely evolve in very different ways. The EHB therefore remains one of the white spots in stellar astrophysics. This has severe consequences for other fields of astronomy like stellar evolution in old populations, which are the constituents of globular clusters and old elliptic galaxies.

But the reason for extensive research in this area is not only the fact that sdBs showed up more or less everywhere in our Galaxy and beyond. The stars themselves turned out to be peculiar in more than one respect. The discovery of five different types of pulsators among the sdBs led to extensive studies of these objects and they became perfect laboratories for asteroseismic analyses. Furthermore the atmospheres of sdBs are chemically peculiar and a lot can be learned about diffusion processes in stellar atmospheres by studying their elemental abundances in detail. A series of workshops dedicated to sdB stars has been started in 2003 and attracts scientists from all around the world interested in different aspects of sdB research. The last meeting has been hosted by our group in Bamberg in 2007.

Closely related to the open question of sdB formation is another important property of these objects. About half of the sdBs reside in close binary systems with small stellar companions like white dwarfs or late main sequence stars (MS) orbiting around each other at periods as short as two hours and with minimum separations smaller than the radius of the Sun. Such systems are of utmost importance for our understanding of stellar evolution. Binary formation channels involving more or less stable mass transfer between the progenitor stars or mergers of compact

objects have been proposed to provide an alternative scenario of sdB formation. Population synthesis studies on one hand and observations of large sdB samples on the other hand allowed for the first time a comparison of these formation scenarios with the observed general properties of sdBs. Among the known sdB binaries are also a lot of very special objects. Eclipsing systems for example allow us to determine all parameters of the binaries simultaneously, including their masses. Other binaries show variations in their lightcurves due to tidal distorsion caused by a compact companion or reflected light from the heated surface of a cool main sequence secondary. Pulsating sdBs in close binaries are also known and offer the unique opportunity to verify stellar parameters derived by asteroseismic analyses. The best known candidate for a double degenerate progenitor of supernovae type Ia (SN Ia) is a binary consisting of an sdB and a massive white dwarf. SN Ia are the most important standard candles to measure the largest distances in the Universe. The most momentous discovery in observational cosmology, the accelerated expansion of the Universe, was based on such measurements. A very good understanding of the SN Ia progenitor population is necessary to quantify systematic errors of this method. The progenitor population still remains poorly understood.

The recent discovery of a planetary companion of a pulsating sdB star is of particular interest, since this object must have survived the red giant phase of the subdwarf progenitor star. Furthermore planetary companions to sdBs may be quite common and closely related to their formation.

Up to now about 80 sdB binaries have been studied in detail and their orbital parameters have been determined. Although the distribution of their orbital periods could be derived, the masses and nature of their unseen companions remain unclear in most cases. The primary aim of this study is to determine the masses of these companions and clarify their nature. In order to achieve this, high resolution spectra and a new analysis method are used.

After giving an overview over the current state of hot subdwarf research (Chap. 1), the previous results on subdwarf binaries in general are reviewed, orbital solutions of newly discovered subdwarf binaries are presented and new candidates with detected radial velocity (RV) variability are introduced (Chap. 2). We have determined orbital solutions of seven subdwarf binaries. Preliminary orbital parameters have been derived for another four systems. Nine close binary systems have been discovered by the detection of radial velocity shifts. All analysed binaries have short orbital periods from $0.14\,\mathrm{d}$ to $0.98\,\mathrm{d}$. Using the most likely mass for the subdwarf primaries and the mass function, the minimum masses of the companions could be constrained. In some cases the detection (or non-detection) of reflection effects in the lightcurves or flux excesses in the red helped to further constrain the nature of the companions.

Three systems consist of subdwarfs and compact objects – most likely white dwarfs. In one of these cases the detection of eclipses allows us to clearly identify the companion as white dwarf. The companions of two sdBs are late main sequence stars, which are revealed by reflection effects in their lightcurves. One binary with preliminary orbital solution has most likely a compact secondary. A double-lined sdB+G system resides in a short period orbit. For all other systems the information is insufficient to clarify the nature of the companions.

In Chap. 3 a new analysis method is introduced, which allows to determine the previously unknown inclinations as well as companion masses of sdB binaries. This novel technique requires high resolution spectroscopy. Using different telescopes and instruments spread all over the world including the 10m Keck telescope at Hawaii and the 8m ESO-VLT in Chile, we were able to obtain spectra of a large sample of single as well as close binary sdBs – in fact by far the largest high resolution sample of these objects ever analysed. The results are presented and systematic

error sources are discussed in detail.

The companions of most sdBs are late main sequence stars or white dwarfs. One short period system harbours a massive white dwarf and therefore qualifies as another candidate for SN Ia progenitor. Most surprisingly we found several subdwarfs with massive, but invisible and hence compact companions, which must therefore be neutron stars (NS) or stellar mass black holes (BH). The possible discovery of a yet unknown population of these exotic objects required a critical reevaluation of our analysis method.

The most important prerequisite for our analysis method consists of the common assumption that the rotation of the sdB primary in a close binary system is tidally locked to its orbital motion. Chap. 4 therefore deals with the question of orbital synchronisation in sdB binaries. Both theoretical timescales and empirical evidence for synchronisation are discussed. The detection of the shallowest ellipsoidal deformation of a star with a high precision light curve obtained with the MOST satellite allowed us to prove synchronisation in an sdB+WD binary with a period longer than half a day.

Three post-RGB stars have been analysed in the same way and it turned out that these objects are in general not synchronised. The reasons for this are most likely the shorter evolutionary timescales and the different internal structure of these objects. Two super-synchronously spinning sdBs in close binaries previously understood as post-EHB stars most likely belong to the class of post-RGB objects, too.

In Chap. 5 a possible formation channel for sdB+NS/BH systems, which requires two common envelope phases and one supernova explosion, is introduced and predictions about the number fraction of these binaries are made. The observed fraction of sdB+NS/BH systems turned out to be much higher than the one predicted by theory. In Chap. 6 a qualitative discussion of selection effects is undertaken to investigate their influence on the derived number fraction of sdB+NS/BH binaries and the derived distribution of inclinations. To reach consistency between theory and observations, some of the sdBs must have masses lower than the canonical one but still consistent with binary evolution calculations. Even under the most conservative assumptions a few sdB+NS/BH binaries are present in our sample, which provides strong indication that these systems really exist.

This new connection between hot subdwarfs, which are numerous in the Galaxy, and massive compact objects may lead to a tremendous increase in the number of known neutron stars and black holes and shed some light on this dark population and its evolutionary link to the X-ray binary population.

We conducted the first systematic investigation of the rotational properties of sdB stars. From high resolution spectra we measured the projected rotational velocity of 49 single (Chap. 7) and 51 close binary sdBs. In the case of slow rotators we made use of all suitable metal lines. For fast rotating stars Balmer and helium lines have been used to fit model spectra with appropriate rotational broadening. Single sdBs are slow rotators spinning with an almost uniform rotational velocity of about $8\,\mathrm{kms}^{-1}$, while the rotation of sdBs in close binary systems is clearly affected by the tidal influence of the invisible companion.

The most important spin-off result of our study is the determination of metal abundances of a large sample of sdB stars. In Chap. 8 the data analysis is explained, the results are presented and discussed. The trends of the abundances with temperature and a comparison with previous results on Blue Horizontal Branch (BHB) stars clearly illustrate that diffusion processes are indeed responsible for the observed abundance patterns. The discovery of the new subclass of carbon enriched sdBs is reported and discussed in terms of sdB formation. Carbon rich sdBs

could be the missing link between helium and hydrogen rich subdwarfs predicted by most recent theoretical models.

The discovery of candidate sdB+NS/BH systems in the course of this project motivated a new large survey performed by an international group of astronomers and led by the author. Chap. 9 contains a brief outlook and introduces the (HYPER-)MUCHFUSS survey dedicated to find sdB+NS/BH binaries in the halo of our Galaxy, which was initiated in 2007.

Chapter 1

Hot subdwarf stars: A review

1.1 General properties

The first survey for faint blue stars in the Northern hemisphere was conducted by Humason & Zwicky (1947). Spectroscopic follow-up observations with the most sophisticated instrument of these days, the 5m Palomar telescope were undertaken by Greenstein (1954) and led to the discovery of the first hot subluminous star (HZ 44). Subluminous stars are defined to be less luminous than main-sequence stars of similar spectral type and are situated below the main sequence in the Hertzsprung-Russell-Diagram (HRD, see Fig. 1.1). Since main sequence stars are also called dwarfs in contrast to the giant stars of the same spectral type, subluminous stars were therefore called subdwarfs. Similar surveys were undertaken by Feige (1958), Slettebak & Brundage (1971), Downes (1986) and especially Green, Schmidt & Liebert (1986). In the course of the Palomar Green (PG) survey of UV-excess objects in the Northern hemisphere several hundreds of hot subdwarfs were found. Larger and deeper surveys have increased the number of known hot subdwarfs to more than 2300 (Edinburgh-Cape survey EC, Kilkenny, O'Donoghue & Stobie 1990; Montreal-Cambridge-Tololo survey MCT, Demers et al. 1990; Hamburg quasar survey HQS, Hagen et al. 1995; Hamburg ESO survey HE, Wisotzki, Reimers & Wamsteker 1991; ESO supernovae Ia progenitor survey SPY, Napiwotzki et al. 2003). From the Sloan Digital Sky Survey (SDSS) and the Sloan Extension for Galactic Understanding and Exploration (SEGUE) another 1300 hot subdwarf stars could be identified so far (Hirsch priv. comm.).

Depending on their spectral appearance, hot subdwarf stars can be further divided into subclasses. The original definition of hot subdwarf B stars comes from Sargent & Searle (1968), who introduced it for stars with colours similar to main sequence B stars, but with much broader Balmer lines. From the different classification schemes available in literature (e.g. Green et al. 1986; Jeffery et al. 1997) the most common one by Moehler et al. (2000) is used here. Hot subdwarf B (sdB) stars show strong and broad Balmer and weak (or no) He I lines. sdOB stars show strong and broad Balmer lines as well as weak lines from He I and He II, while sdO stars only display weak He II lines besides their strong Balmer lines. He-sdBs are dominated by strong He I and sometimes weak He II lines. Hydrogen absorption lines are very weak or not present at all. He-sdOs show strong He II and sometimes weak He I lines. Balmer lines are not present or heavily blended by the strong He II lines of the Pickering series.
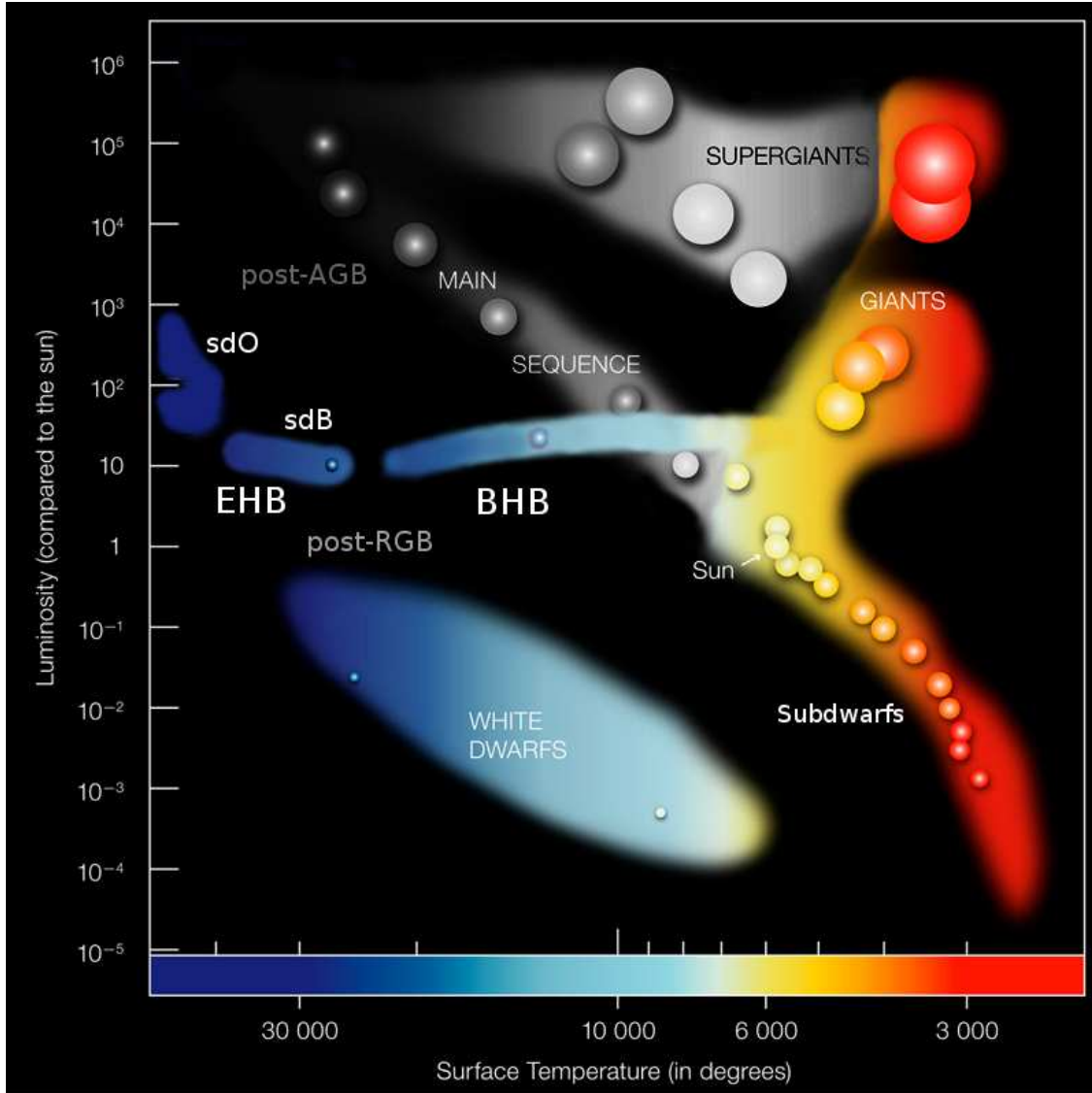
Figure 1.1: Schematic Hertzsprung-Russell diagram (ESO PR Photo 28c/07 with modifications by the author).

1.2 Single star formation and evolution scenarios

In the HRD the hot subdwarf stars are situated at the blueward extension of the Horizontal Branch (HB), the so called Extreme or Extended Horizontal Branch (EHB, Heber et al. 1984, Heber et al. 1986, Saffer et al. 1994). The most common class of hot subdwarfs, the sdB stars, are located directly on the EHB and are therefore considered to be helium core burning stars. They have very thin hydrogen dominated atmospheres ($n_{He}/n_{H} \leq 0.01$) and masses around $0.5 M_{\odot}$ (Heber et al. 1986). Their effective temperatures (T_{eff}) range from $20\,000\,\mathrm{K}$ to $40\,000\,\mathrm{K}$ and their logarithmic surface gravities ($\log g$) are one to two orders of magnitude higher than in main sequence stars of the same spectral type, usually between 5.0 and 6.0 (cgs). They consist

of a helium burning core surrounded by a thin hydrogen-rich envelope ($M_{\mathrm{env}} < 0.02\,M_{\odot}$).

The formation of these objects is still puzzling (see Fig. 5.1). SdB stars can only be formed, if the progenitor looses its envelope almost entirely after passing the Red Giant Branch (RGB) and the remaining hydrogen-rich envelope has not retained enough mass to sustain a hydrogen-burning shell, which is the case in cooler HB stars. Therefore the star can not evolve in the canonical way and ascend the Asymptotic Giant Branch (AGB). In contrast to this the star remains on the EHB until the helium core burning stops, and after a short time of helium shell burning eventually reaches the white dwarf (WD) cooling tracks. According to evolutionary calculations of EHB stars (e.g. Dorman et al. 1993) the average lifetime on the EHB is of the order of 10^8 yr. In this canonical post-EHB scenario the hotter ($T_{\mathrm{eff}} = 40\,000 - 80\,000\,\mathrm{K}$) and much less numerous hydrogen rich sdOs can be explained as rather short-lived helium shell burning stars evolving away from the EHB.

The reason for the very high mass loss at the tip of the RGB after the helium flash is still unclear. Several single star scenarios are currently under discussion: Stellar wind mass loss at the RGB (D'Cruz et al. 1996), helium mixing by internal rotation in the RGB phase (Sweigart 1997a) and envelope stripping processes in dense clusters (De Marchi & Paresce 1996) or through a supernova explosion of the companion in a binary system (Marietta, Burrows & Fryxell 2000). All these scenarios require either a fine-tuning of parameters or extreme environmental conditions which are unlikely to be met for the bulk of the observed subdwarfs in the field. A promising single star scenario has recently been proposed by Hu et al. (2008). If the progenitor star is heavy enough helium ignites under non-degenerate conditions. This channel requires less fine-tuning as the allowed mass range for the sdBs is broader.

The formation of He-sdO/Bs is even more enigmatic than in the case of hydrogen rich sdO/Bs. Most (but not all) He-sdOs are concentrated at a very small region in the HRD, slightly blueward of the EHB at $T_{\mathrm{eff}} = 40\,000 - 80\,000\,\mathrm{K}$ and $\log g = 5.60 - 6.10$ (Ströer et al. 2007). The He-sdBs are scattered above the EHB. The late hot flasher scenario provides a possible channel to form these objects (Lanz et al. 2004; Miller-Bertolami et al. 2008). After ejecting most of its envelope at the tip of the RGB, the stellar remnant evolves directly towards the WD cooling tracks and experiences a late core helium flash there. Helium is mixed into the atmosphere and the star ends up close to the helium main sequence. Depending on the depth of the mixing, stars with more or less helium in the atmospheres and different atmospheric parameters can be formed in this way. In a most recent paper Miller-Bertolami et al. (2008) argued that due to diffusion processes in their atmospheres He-sdOs will turn into hydrogen rich subdwarfs before they evolve towards the WD graveyard. According to new results by Unglaub (2008) the stellar wind in He-sdOs is not able to prevent gravitational settling of helium in the atmosphere and the timescale of this process is predicted to be shorter than the evolutionary timescale. Again a highly efficient envelope ejection at the tip of the RGB is required. Therefore also the helium rich subdwarf stars are not able to ascend the AGB and evolve directly to the WD cooling tracks.

Some hot subluminous stars may also be not connected to EHB-evolution at all. At least three objects are known with spectra and atmospheric parameters similar to normal sdBs, which are not lying on the EHB (HD 188112 Heber et al. 2003; NGC 6121$-$V46 O'Toole et al. 2006; SDSS J123410.37$-$022802.9 Liebert et al. 2004). These objects are considered to be direct progenitors of white dwarfs, which descend from the Red Giant Branch. For these post-RGB objects which cross the EHB, Driebe et al. (1998) calculated evolutionary tracks and masses of about $0.20 - 0.33\,M_{\odot}$. To form such objects the mass loss at the RGB has to be even more

extreme than in the case of EHB stars. The fact that two of these stars reside in close binary systems and SDSS J123410.37−022802.9 is suspected to be a binary may provide a possible formation channel.

From a purely observational point of view also post-AGB objects in a certain evolutionary stage, like the so called low gravity or luminous He-sdOs (Jeffery 2008) belong to the class of hot subdwarfs and are situated above the EHB in the HRD. In this study we use the terms (He-)sdO/B exclusively to name helium core burning stars connected to some kind of EHB evolution. Post-AGB stars of any kind shall not be discussed in this thesis.

1.3 Hot subdwarf binaries: Observations, formation and evolution

The first subdwarf binary with a main sequence F companion visible in the spectrum (HD 113001) was discovered by Wallerstein & Spinrad (1960). Ferguson, Green & Liebert (1984) derived a binary frequency of about 50 % from their analysis of hot subdwarfs from the PG survey. Allard et al. (1994) estimated a fraction of 54 − 66 % from photometry of a larger sample taken from the PG and KPD surveys. Thejll et al. (1995) and Ulla & Thejll (1998) confirmed these numbers by investigating infrared flux excesses caused by cool companions. Aznar Cuadrado & Jeffery (2001) obtained atmospheric parameters of sdB stars from their spectral energy distribution from UV to infrared and again found more than 50 % binaries with MS companions. Making use of infrared colours from the Two Micron All Sky Survey (2MASS) Stark & Wade (2003) tried to account for selection effects and found a binary fraction of about 30 % in an approximately volume-limited sample. Reed & Stiening (2004) performed a similar analysis and ended up with consistent results. The most recent effort was made by Lisker et al. (2005), who detected spectral signatures of cool companions in about 30 % of the sdB stars from the SPY survey. This number has to be considered as lower limit due to selection biases. In general selection effects make it difficult to compare the fractions of sdB+MS binaries from the different studies. About half of the hot subdwarf stars seem to have main sequence companions.

Thackeray (1970) reported the discovery of a single-lined short period binary sdO (HD 49798) and derived the orbital parameters. A determination of the atmospheric parameters by Kudritzki & Simon (1978) revealed that this star is more likely a post-AGB object and not connected to the EHB. The first close binary sdOB (most likely) associated with the EHB was the eclipsing system LB 3459 (AA Dor) discovered by Kilkenny et al. (1978). Menzies & Marang (1986) reported the discovery of the similar eclipsing sdB binary HW Vir (Wood, Zhang & Robinson 1993). In the following years the interest of the scientific community shifted to close binary WD systems, but starting with the work of Saffer, Livio & Yungelson (1998) a growing number of subdwarf binaries have been discovered and analysed using time resolved spectroscopy or light curve analyses (Jeffery & Pollacco 1998; Kilkenny et al. 1998; Koen, Orosz & Wade 1998; Moran et al. 1999; Orosz & Wade 1999; Maxted et al. 2000a; Maxted et al. 2000b; Rauch 2000; Drechsel et al. 2001; Napiwotzki et al. 2001; Maxted et al. 2002; Heber et al. 2003; Ahmad et al. 2004; Green et al. 2004; Heber et al. 2004; Maxted et al. 2004; Morales-Rueda et al. 2004; O'Toole, Heber & Benjamin 2004; O'Toole et al. 2006; Geier et al. 2007; Østensen et al. 2007; Połubek et al. 2007; Vučković et al. 2007; Wils et al. 2007; Edelmann 2008; For et al. 2008; Geier et al. 2008; Green et al. 2008; Napiwotzki 2008; Østensen et al. 2008; Vučković et al. 2008). Systematic surveys for radial velocity (RV) variable stars revealed that a large fraction of the sdB stars (40 − 70 %) are members of close binaries with orbital periods

A. Single hot subdwarfs

Envelope loss near the tip of FGB by stellar wind (rotation, Z ?)

$M_{sdB} = 0.45 - 0.49 M_\odot$

He WD merger (1 or 2 CE phases)

$M_{sdB} = 0.40 - 0.65 M_\odot$

B. Stable RLOF ($q < 1.2 - 1.5$)

Stable RLOF near the tip of FGB

Wide hot subdwarf binary with MS companion

$P_{orb} = 10 - 500$ days

$M_{sdB} = 0.30 - 0.49 M_\odot$

Common-Envelope Channels

C. Stable RLOF+CE ($q < 1.2 - 1.5$)

Stable RLOF

Wide WD binary with MS companion

Unstable RLOF leads to dynamical mass transfer

Common-envelope (CE) phase

Short-period hot subdwarf binary with WD companion

D. CE only ($q > 1.2 - 1.5$)

Unstable RLOF leads to dynamical mass transfer

Common-envelope (CE) phase

Short-period hot subdwarf binary with MS companion

$P_{orb} = 0.1 - 10$ days

$M_{sdB} = 0.40 - 0.49 M_\odot$

Figure 1.2: Single and binary channels to produce hot subdwarfs (Han et al. 2007).

13

ranging from 0.07 d to a few days (Maxted et. al 2001; Morales-Rueda et al. 2003; Napiwotzki et al. 2004a; Edelmann et al. 2005a). SdB stars therefore have one of the highest close binary fractions. All known companions of sdBs in radial velocity variable close binary systems are white dwarfs or late type main sequence stars. In some cases brown dwarf (BD) companions are under discussion.

With all these results at hand it is evident that binary interaction must play an important role in the process of formation and evolution of hot subdwarf stars. For the close binary systems common envelope (CE) ejection is the most probable formation channel (Paczyński 1976, see Fig. 1.5). In this scenario two main sequence stars of different masses evolve in a binary system. The more massive one will be the first to reach the red giant phase and fill its Roche lobe. If the mass transfer to the companion is dynamically unstable, a common envelope is formed. Due to friction the two stellar cores loose orbital energy, which is deposited within the envelope and leads to a shortage of the binary period. Eventually the common envelope is ejected and a close binary system is formed, which contains a helium core burning sdB and a main sequence companion. If this companion reaches the red giant branch, another common envelope phase is possible and can lead to a close binary with a white dwarf companion and an sdB. The CE ejection scenario is able to explain the formation of the observed close binary sdBs with WD or late MS companions.

If the mass transfer to the companion is dynamically stable, no common envelope is formed, the companion fills its Roche lobe and the primary slowly accretes matter from the secondary (see Fig. 1.4). The companion eventually looses most of its envelope and evolves to an sdB. This leads to sdB binaries with much larger separation and therefore much longer orbital periods. Although lots of sdBs have spectroscopically visible main sequence or giant companions, no system with a period ≈ 1000 d was detected up to now. Therefore the so called stable Roche Lobe overflow (RLOF) channel remains without proof. It has to be pointed out that stable RLOF channel and CE ejection may also be mixed. After a phase of stable RLOF producing a wide binary consisting of a WD and an MS star, a CE ejection phase can lead to the formation of close sdB+WD binary.

An alternative way of forming a single sdB is the merger of two helium white dwarfs (Webbink 1984; Iben & Tutukov 1984, see Fig. 1.3). Close He WD-binaries are formed as a result of two CE-phases. Loss of angular momentum through emission of gravitational radiation will cause the system to shrink. Given the initial separation is short enough the two white dwarfs eventually merge and if the mass of the merger is high enough, core helium burning is ignited and an sdB with very thin hydrogen envelope is formed. Mergers of sdBs and He-WDs may be an alternative way of forming single He-sdOs (Podsiadlowski 2008; Justham et al. in prep.). Most recently Politano et al. (2008) proposed a new evolutionary channel. The merger of a red giant and a low mass MS star during a common envelope phase may lead to the formation of a rapidly rotating hot subdwarf star. Soker (1998) proposed a similar scenario with a planetary companion.

These three binary channels for sdB formation were adressed in detail by Han et al. (2002, 2003), who carried out a binary population synthesis. The observed distribution of orbital parameters could be reproduced by these simulations. One important result of this study is, that although most sdBs are still expected to have masses around $0.47\,M_{\odot}$ as predicted by single star evolution, the possible mass range is broader. Subdwarfs formed after two CE phases may have masses as low as about $0.3\,M_{\odot}$ whereas subdwarfs formed through the WD merger channel may be as massive as $0.7\,M_{\odot}$. The derived theoretical distributions of atmospheric parameters were compared with observations by Lisker et al. (2005). According to this study, no simulation set

of Han et al. (2003) is fully consistent with the observed distribution of atmospheric parameters. A combination of single star and binary formation channels is therefore most likely necessary to fully understand the process of sdB formation.

Despite the fact that about half of the sdBs and also hydrogen rich sdOs (the observed sample is still low) are in close binary systems, the population of He-sdOs observed so far consists mostly of single stars. Napiwotzki (2008) found only one RV variable He-sdO in the SPY sample, which corresponds to a fraction of only 3 %. Combined with the results from Ströer et al. (2007), who found most He-sdOs to be concentrated at the hot end of the EHB, Napiwotzki (2008) concluded that sdBs and He-sdOs do not represent different evolutionary stages of one class of stars. While sdBs are supposed to evolve on the EHB in the canonical way, He-sdOs are most likely formed by the merger of two He-WDs (Iben 1990; Saio & Jeffery 2000), which would be consistent with the lack of close binaries detected. The only RV variable He-sdO discovered in the SPY sample turned out to be a double lined system and may be very similar to the known He-sdB+He-sdB binary PG 1544+488 (Ahmad & Jeffery 2003). This rare type of subdwarf binaries may have been formed via a special type of the CE-ejection channel (Podsiadlowski priv. comm.). In contrast to this result Green et al. (2008) reported a higher binary fraction of He-sdOs from the PG sample. The formation of He-sdOs therefore remains an open question.

In an ongoing project Moni Bidin et al. (2008 and references therein) are looking for close binary subdwarfs in Globular Clusters (GCs). The binary fraction in three GCs was found to be lower than 11 %, in the best studied cluster NGC 6752 the upper limit could even be constrained to 4 %. Although preliminary results suggest, that this fraction is higher in the peculiar GC NGC 2808, the numbers are not consistent with the large close binary fraction of field sdBs. The reason for this is not clear. Dynamical effects in the cluster environment may be responsible. Recently Han (2008) explained the lack of sdB binaries in GCs as age effect. According to his binary population synthesis models the relative contribution of the different formation channels proposed in Han et al. (2002, 2003) is dependent on the age of the stellar population. In old populations the CE ejection channels responsible for the formation of close binaries contribute much less. Hence the fraction of close binaries among the subdwarf stars goes down. The numbers derived by Han (2008) are in good agreement with the observations in the field as well as in GCs. To further investigate the age dependence of the sdB close binary fraction it would be necessary to disentangle the field population and clearly distinguish between subdwarfs formed in the thin disk, the thick disk or the halo. Pauli et al. (2003, 2006) have shown that this can be done by a kinematical analysis for white dwarfs. In consequence, the close binary fractions of hot subdwarfs have to be derived in all these populations.

1.4   Pulsating hot subdwarfs and asteroseismology

Some hot subdwarf stars show non-radial pulsations. The V 361 Hya (or EC 14026−2647) stars are characterized by rapid oscillations with periods between 80 s and 600 s (Kilkenny et al. 1997, see Fig. 1.6). These pulsations correspond to low-order, low-degree p-modes. They are driven by a κ-mechanism, which is powered by a local enrichment of iron due to radiative levitation in the stellar envelope (Charpinet et al. 1997). The V 1093 Her stars (also known as PG 1716+426 or Betsy-stars) show low-amplitude oscillations with longer periods from 2 000 s to 9 000 s (Green et al. 2003). These pulsations correspond to mid-order, low-degree g-modes driven by the same mechanism as their short period relatives (Fontaine et al. 2003). More than 65 sdB pulsators of both kinds are known up to now (34 V 361 Hya and 31 V 1093 Her, Fontaine et al. 2008). Three
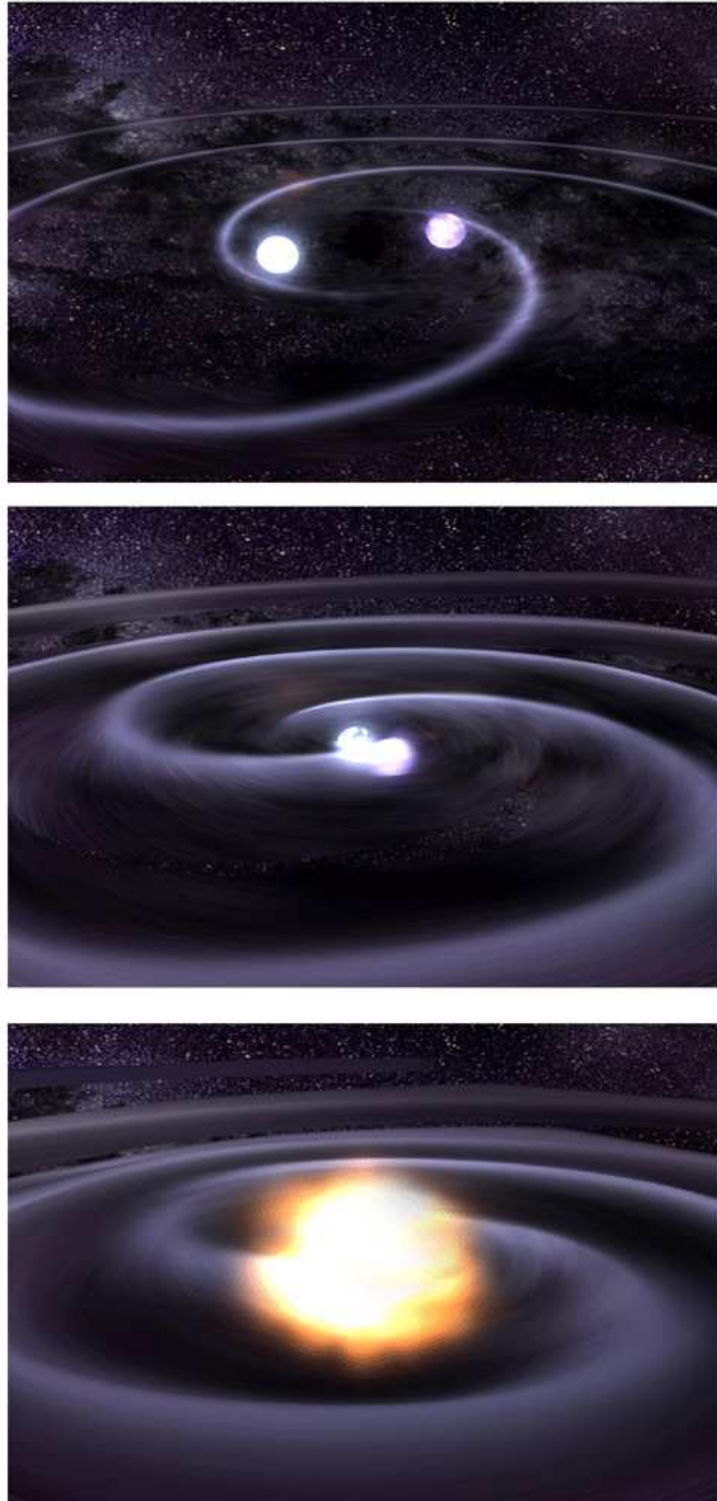
Figure 1.3: Artist's conception of a WD merger process (Credit: GSFC/D. Berry).
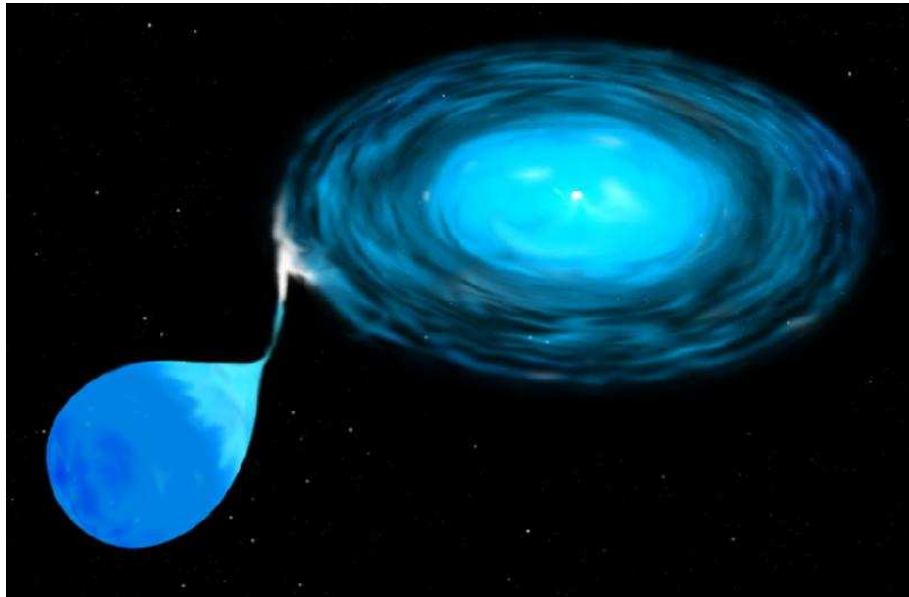
Figure 1.4: Artist's conception of stable mass transfer to a compact companion (Credit: NASA).
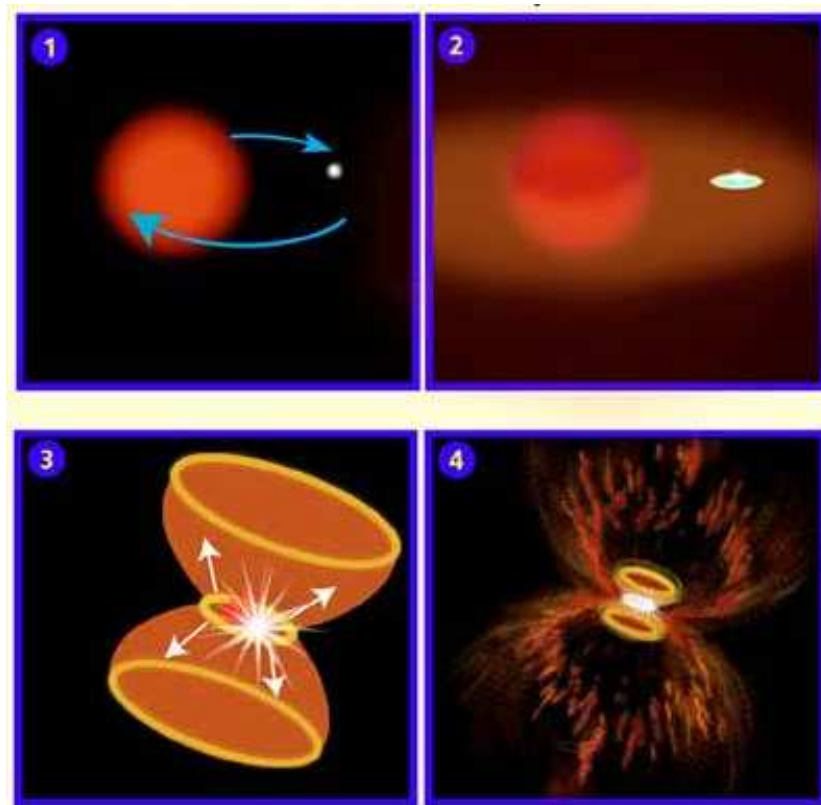
Figure 1.5: Artist's conception of common envelope ejection (Credit: NASA).
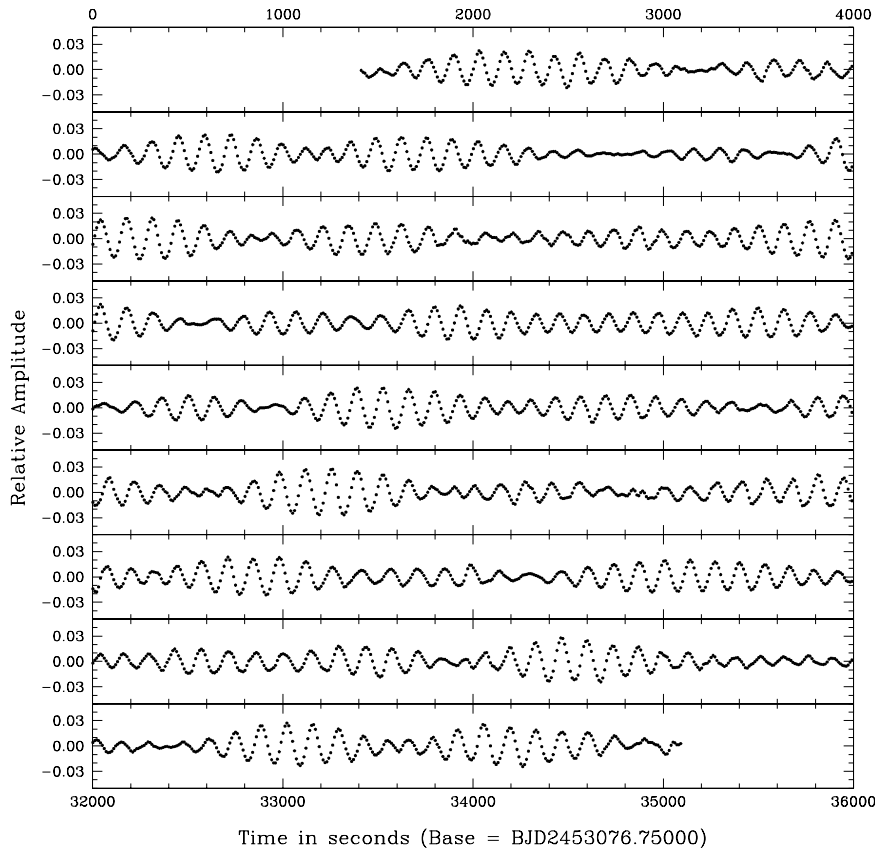
Figure 1.6: Example of a very high quality light curve for the short period sdB pulsator PG 1219+534 obtained with the LAPOUNE instrument at the CFHT. The plot is taken from Fontaine et al. (2008).

hybrid pulsators, which show both types of pulsations simultaneously, have been discovered as well (Baran et al. 2005; Oreiro et al. 2005; Schuh et al. 2006; Lutz et al. 2008).

Especially the V 361 Hya pulsators turned out to have a high potential for asteroseismic probes of the internal structure of sdBs. Given the observed pulsation modes can be clearly identified, which is not a trivial task at all and requires a combination of time resolved high-precision photometry and spectroscopy, the fundamental parameters of the pulsating subdwarf can be derived by matching observed with computed modes (see Brassard et al. 2001 for details). A lot of progress has been made in the last years on the observational as well as on the theoretical side. The most important fundamental parameter, the mass, could be determined for 12 short period pulsators so far. The preliminary mass distribution (Fontaine et al. 2008) is quite similar to the theoretical distribution of Han et al. (2003) for low masses up to $0.60\,M_\odot$ and shows a peak at $0.47\,M_\odot$ (see Fig. 1.7).

The modelling of V 1093 Her stars in the same way was not possible so far and requires high quality light curves as well as advanced models, which take the core structure of the stars into account (Fontaine et al. 2008). Although the progress in asteroseismic modelling is quite impressive, the so called forward modelling approach requires the fitting of a lot of indepedent

18
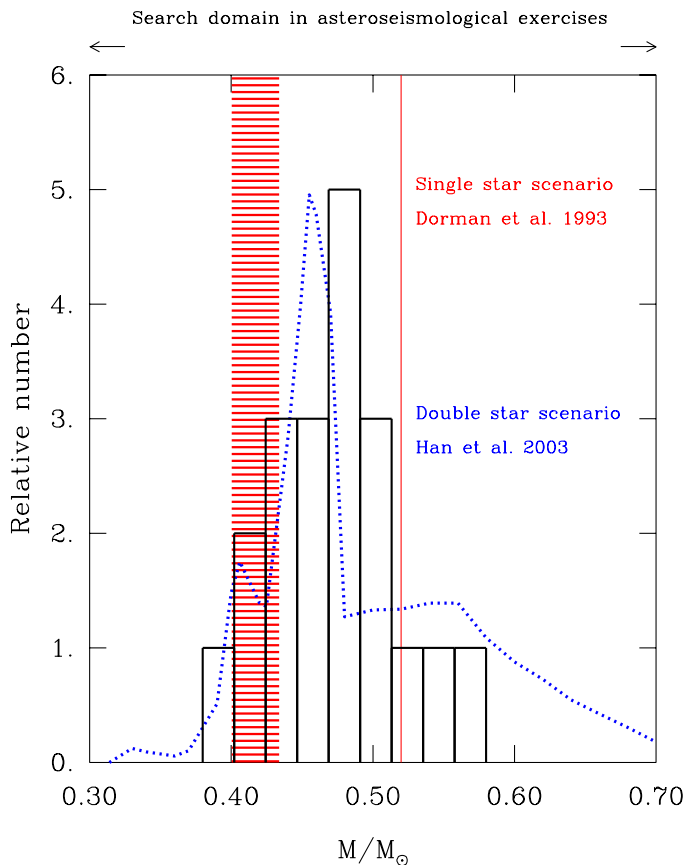
Figure 1.7: Mass distribution of 12 short period pulsating sdBs. The dotted line corresponds to the best simulation set of Han et al. (2003). The plot is taken from Fontaine et al. (2008).

parameters, from which only a few can be checked directly by observations. That is why the derived subdwarf masses have to be verified with independent methods to prove that the astero-seismic approach provides reliable results. Eclipsing or ellipsoidal variable close binary systems with pulsating subdwarf primaries are ideally suited for this purpose (e.g. KPD 1930+2752, Geier et al. 2007).

Ahmad & Jeffery (2005) detected pulsations with periods between 2 000 s to 3 000 s in a He-sdB. Woudt et al. (2006) found very short period oscillations ranging from 60 s and 120 s in a hot sdO star. A driving mechanism for this kind of pulsations requiring radiative levitation has recently been proposed by Fontaine et al. (2008). Koen (2007) reported a strange pulsation pattern in a close binary sdB+M system. In addition to a clear reflection effect, the subdwarf oscillates with periods between 2 200 s and 11 000 s and an enigmatic phase shift between the photometric bands. The confusing behaviour of this object lacks any explanation so far.
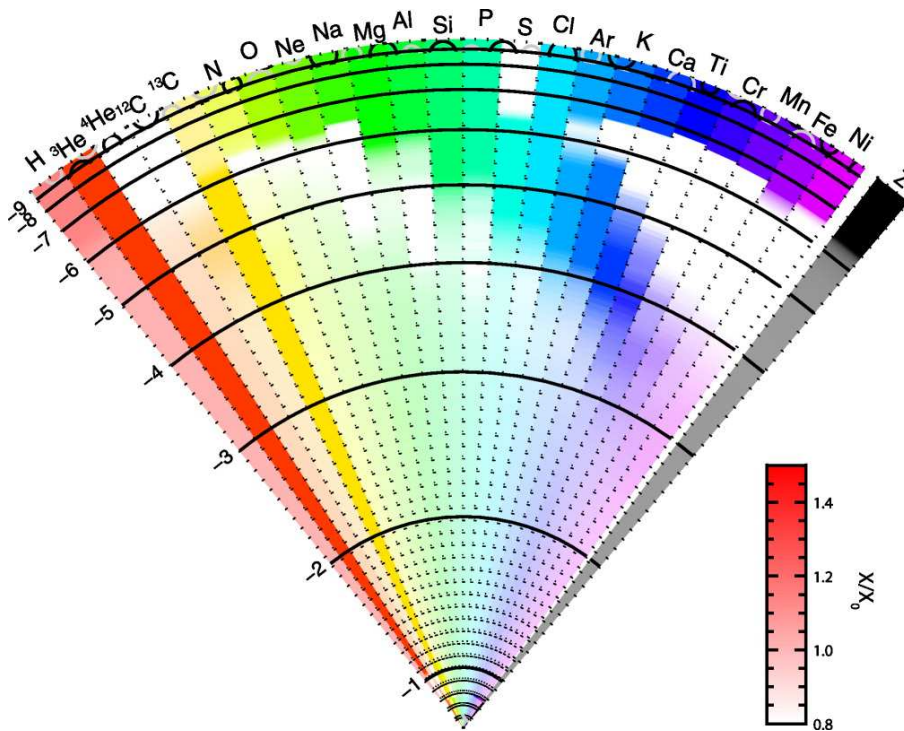
Figure 1.8: Colour-coded concentrations of elements in a $0.61\,M_\odot$ BHB star $30\,$Myr after leaving the Zero Age Horizontal Branch (ZAHB) taken from Michaud et al. (2008). The scale of the radius is linear. The logarithmic value of mass coordinate $\log\Delta M/M_*$ is shown on the left. The concentrations are given with respect to the abundances on the ZAHB. Unfortunately no such detailed calculations are available for EHB stars up to now.

1.5   Hot subdwarf atmospheres and diffusion processes

Hot subdwarf stars are very important to study the physical properties of hot stellar atmospheres. Sargent & Searle (1966) discovered the helium deficiency of sdB stars for the first time. This finding seemed to be at variance with the big-bang theory of nucleosynthesis. Greenstein, Truran & Cameron (1967) suggested that diffusion within the hot atmosphere of sdBs could cause the helium deficiency. Peculiar metal abundances were first reported by Baschek, Sargent & Searle (1972) for HD 4539. While some metals showed solar abundances, others were depleted or even enriched. Studies of optical spectra remained scarce. Heber et al. (1999, 2000) analysed high resolution spectra of four pulsating sdB stars taken with Keck/HIRES. Edelmann et al. (2006) reported preliminary results from the analysis of high-resolution optical spectra of 49 subluminous B stars.

Hot stars display a much larger number of spectral lines in the UV than in the optical. With the advent of the IUE satellite it became possible to determine abundances of C, N and Si from the strong UV resonance lines for nine sdB stars (Lamontagne et al. 1987 and references therein). For two sdB stars also lines of heavier metals have been analysed from IUE spectra (Baschek et al. 1982a, 1982b). The most detailed analysis of UV spectra has been carried out by O'Toole & Heber (2006) based on spectra obtained with STIS onboard HST. The FUSE

satellite opened the FUV-regime for abundance studies. Many sdBs have been observed, but most of the analyses are still under way (Fontaine et al. 2006; Chayer et al. 2006; Blanchette et al. 2008).

Atmospheric diffusion processes have been invoked to explain abundance pecularities in a wide range of stars including white dwarfs, luminous blue variables, low mass halo stars, Ap or Am stars, and HgMn stars (see Vauclair & Vauclair 1982 for a review).

Most recently Michaud et al. (2008) analysed the effects of atomic diffusion on horizontal branch models (See Fig. 1.8). For sdB stars the first theoretical diffusion models yielded only little success (e.g. Michaud, Vauclair & Vauclair 1983). Since then several attempts have been made to model the atmospheres of sdBs (Bergeron et al. 1988; Michaud et al. 1989; Fontaine & Chayer 1997; Ohl et al. 2000; Unglaub & Bues 2001). Radiative levitation and mass loss caused by stellar winds have been invoked to counteract the gravitational settling. Although some observed abundances could be reproduced, it was not possible to solve the entire puzzle so far.

Especially in the globular cluster environment, where very different helium abundances and metallicities are invoked to explain the formation of sdBs (see Sect. 1.8), but also in younger populations it is important to investigate how different chemical compositions of the progenitor stars would affect the spectral appearance of the sdB population. Unfortunately, the abundance patterns in sdB stars turned out to be peculiar. The abundance patterns of sdBs therefore seem to be built by atmospheric effects and no information about the formation process can be obtained. A detailed abundance analysis of a huge sample of hot subdwarfs is necessary to further investigate the influence of diffusion processes on the observed composition. The influence of gravitational settling and radiative levitation depends on the atmospheric parameters and is different for each element. If it would be possible to find elements less affected by diffusion, their abundances may tell us something about sdB formation. The results from Ströer et al. (2007) and Hirsch et al. (2008) provide evidence, that at least in the case of the He-sdOs diffusion alone cannot explain the observed abundance patterns. Improved models for diffusion in hot subdwarf atmospheres are required to quantify the effects of diffusion on the abundance pattern. Detailed abundance analyses of sdBs from different populations are necessary to guide the development of such models. Field sdO/B stars are the most promising objects to start with, because due to their relative brightness high quality spectra can be easily obtained.

1.6   Hot subdwarfs and extrasolar planets

Since the discovery of the first extrasolar planet much effort has been put into projects devoted to find more of these objects and study them in detail. The discovery of a planetary companion to the short period pulsating sdB V 391 Pegasi (or HS 2201+2610) is of particular importance for several reasons (see Fig. 1.10, Silvotti et al. 2007a). First of all, this is the only known planet orbiting an evolved star. This means that it must have survived the RGB phase. But more important in terms of sdB formation and evolution is the fact, that this planet was detected via a small, but periodically change in the period of the dominant pulsation mode (the so called O-C-method, see Fig. 1.9).

The high accuracy needed to measure this change required a huge observational effort. V 391 Pegasi was monitored by time series photometry with 17 different telescope over a timespan of seven years (151 single runs, Silvotti et al. 2007b) making this star one of the best studied sdB pulsators. That means that it was not possible so far to use the O-C-method with the required
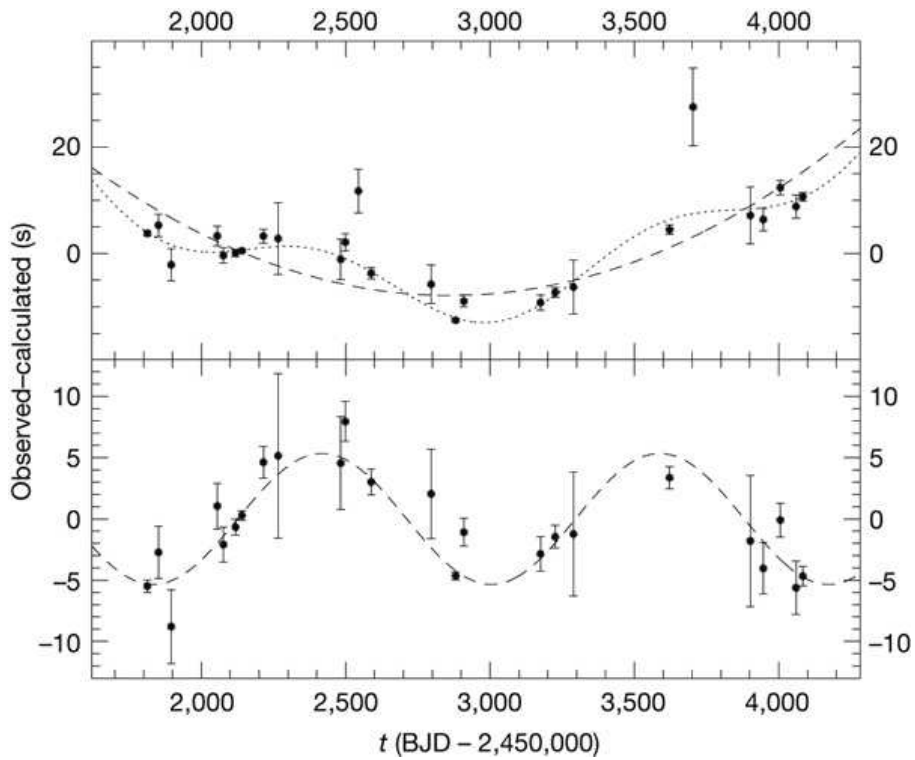
Figure 1.9: O-C-diagram of the pulsating sdB V 391 Pegasi. In the lower panel the sinusoidal modulation in the main pulsation mode is shown. This modulation is most likely caused by a giant planet (Silvotti et al. 2007a).
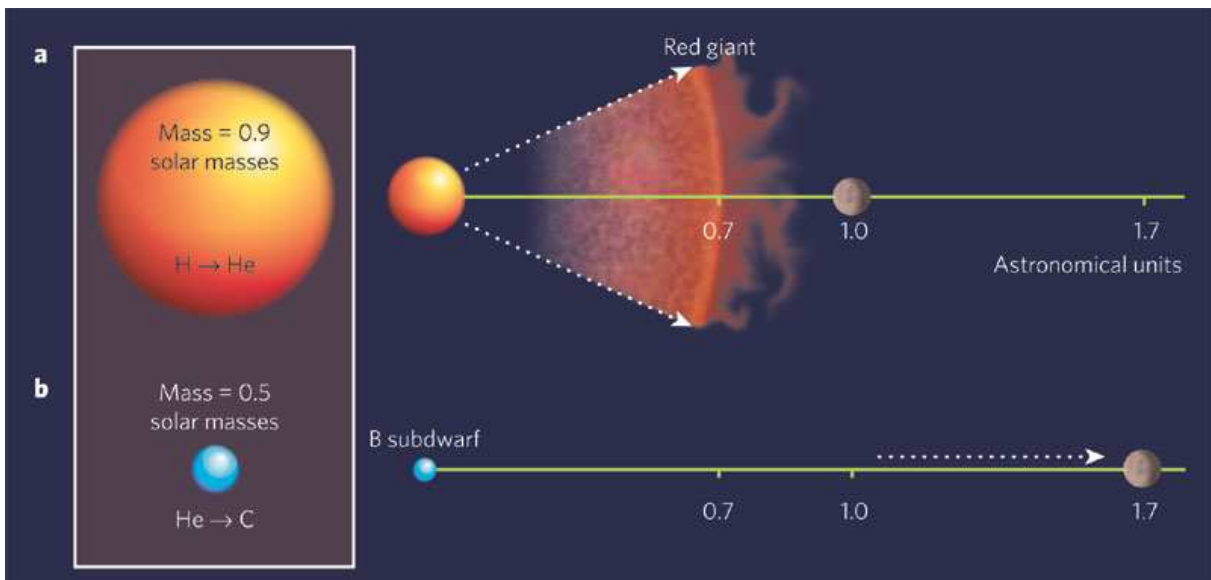
Figure 1.10: Schematic view of the evolution of V 391 Pegasi. The giant planet must have survived the Red Giant phase of the progenitor star (Silvotti et al. 2007a).
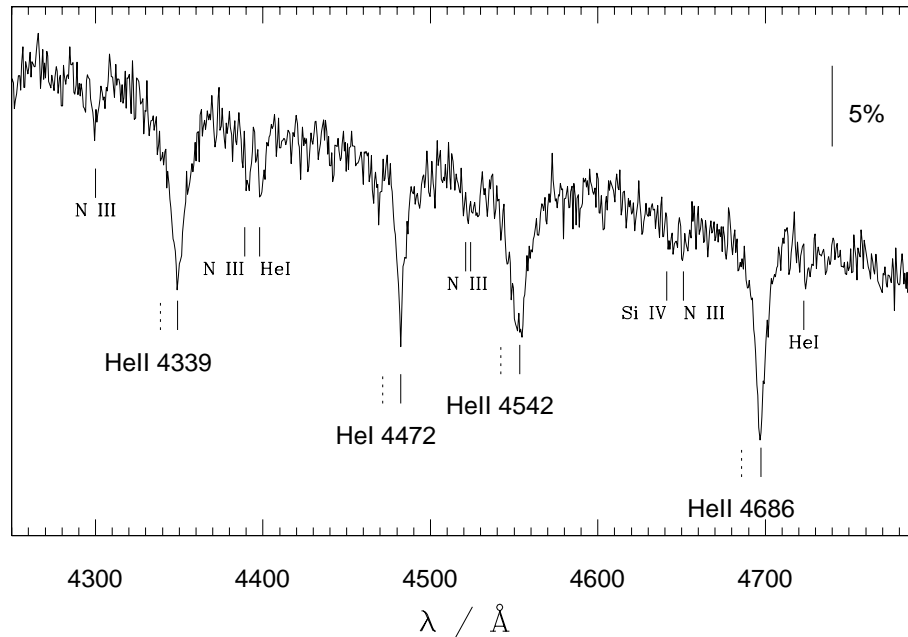
Figure 1.11: Spectrum of the HVS He-sdO US 708 obtained with the LRIS instrument at the Keck telescope. The dashed vertical lines mark the rest wavelengths of the helium lines. It can be clearly seen that the lines are extremely red-shifted (Hirsch et al. 2005).

accuracy in any other case. V 391 Pegasi is therefore not only the first sdB where a planetary companion was detected, but also the first where it was possible to detect one (or not). It is again very unlikely that this discovery was made by chance. Hundreds of solar type stars are currently monitored to detect planetary transits or small RV variations and only around a few of them planets have been detected. Looking for a planet orbiting one sdB and finding one is hard to explain by pure luck. The conclusion is obvious that planets may be quite common around sdBs and this in turn may have severe implications for the formation and evolution of hot subdwarf stars as already pointed out by Soker (1998). More observations of pulsating sdBs are needed to investigate this question.

1.7 Hot subdwarfs as hyper-velocity stars

Stars moving at velocities higher than the Galactic escape velocity were predicted by Hills (1988) and initially discovered by Brown et al. (2005), Hirsch et al. (2005) and Edelmann et al. (2005b). In the course of a survey dedicated to search for this so called hyper-velocity stars (HVS) and conducted by Brown et al. (2006a, 2006b, 2007a, 2007b, 2008) 13 more HVSs have been found. Hills (1988) predicted that the tidal disruption of a binary by the supermassive black hole in the Galactic centre could accelerate stars to velocities high enough to escape the gravitational force of the Galaxy. Yu & Tremaine (2003) estimated a HVS formation rate of $10^{-5}\,\mathrm{yr}^{-1}$. If the Galactic center should host a tight binary of an SMBH and an intermediate mass black hole (IMBH) the formation rate would be ten times larger. Gnedin et al. (2005) and Bromley et al. (2006) pointed out that the space distribution of HVSs puts constraints on the

shape of the Galactic dark matter halo.

One of the key issues to clarify the origin of these objects are their evolutionary states, which constrain their ages. Most of the known HVSs are classified as late B type main sequence stars. In this case the stars would be young and in some cases the travel time from the Galatic centre to their observed position would be longer than their lifetimes. Edelmann et al. (2005b) for example showed that the confirmed MS-B star HE 0437−5439 could not be ejected in the Galactic centre, but may instead come from the Large Magellanic Cloud (LMC). There are no other hints for an SMBH in the LMC so far. Other possible sources of HVS could be the IMBHs predicted to exist in some globular clusters. If some HVSs should turn out to be horizontal branch stars instead of main sequence stars, their lifetimes would in any case be long enough to be ejected from the Galactic centre. In the parameter range in question it is hard to distinguish the two possibilities. Detailed analyses of the atmosperic parameters as well as the abundances are necessary and require high quality spectra (a more detailed review is given in Heber et al. 2008).

It is interesting that one of only 16 known HVS turned out to be a He-sdO (US 708, Hirsch et al. 2005) and is therefore the first confirmed old and evolved EHB star in the sample (see Fig. 1.11). It is again justified to doubt that this is a mere conincidence. What makes hot subdwarfs and late B type stars so special? Is the discovery of these objects only caused by selection effects? Does the high binary fraction of hot subdwarfs play a role? Only a large sample of HVSs can provide answers to questions like this.

1.8 Hot subdwarfs and globular clusters

The term EHB star has its origins in the study of globular clusters. The horizontal branch is a feature that appeared in colour-magnitude diagrams of Galactic globular clusters. Its extreme extension could due to the faintness of the EHB stars only recently be observed with the HST. Greenstein (1971) and Caloi (1972) identified the hottest HB stars with the known field sdB stars. On of the big open questions in globular cluster research deals with the striking degree of variation in the HB morphology of different globular clusters, which is especially affecting the EHB (see Fig. 1.12). There is common consensus that this is caused by different stellar evolution due to different primordial metallicities of the clusters (Sandage & Wallerstein 1960). But it soon became clear that this effect cannot explain the entire phenomenon (Sandage & Wildey 1967; van den Bergh 1967). The search for the origin of this so called second parameter goes on for about four decades now (for a more detailed review see Moni Bidin et al. 2008).

The shape of the EHB in globular clusters is of course directly related to the formation of the EHB stars. In addition to the formation scenarios for field sdBs discussed above, other mechanisms may affect the formation of sdBs in the cluster environment. A super-solar He abundance in the stellar envelope can account for the enhanced mass loss at the tip of the RGB necessary to form a hot subdwarf. Helium could be mixed into the envelope through internal rotation (e.g. Sweigart 1997b) or dredged-up induced by H-shell instabilities (von Rudloff et al. 1988). The discovery of a helium enriched stellar sub-population in the globular clusters ω Cen (Bedin et al. 2004; Piotto et al. 2005) and maybe NGC 2808 (Piotto et al. 2007; D'Antona et al. 2005), which also have extended EHBs, could provide an explanation without the need for non-canonical effects in the stellar envelope. As described in Sect. 1.3. binary formation channels may also provide a possible explanation for the EHB population in GCs.

In the dense environment of globular clusters, especially towards their cores, dynamical
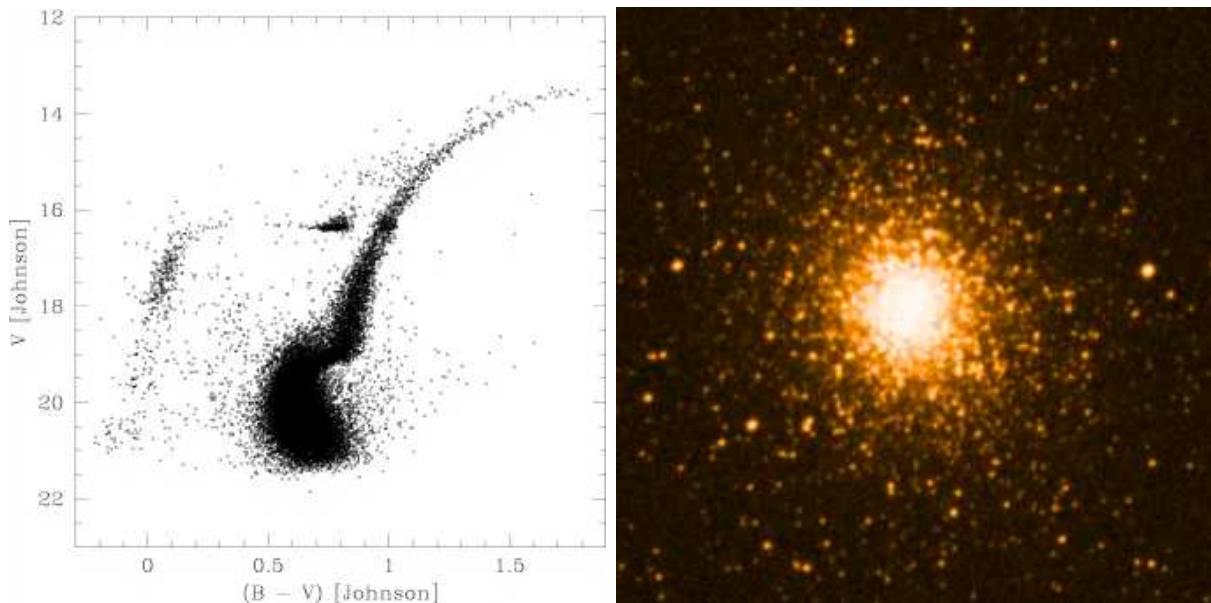
Figure 1.12: *Left panel* Color magnitude diagram of the peculiar globular cluster NGC 2808. The HB structure is complicated, the EHB densely populated (Sosin et al. 1997). *Right panel* Digitized Sky Survey (DSS) image of NGC 2808.

effects may play a role. Especially mergers caused by stellar collisions or close encouters could lead to the formation of sdBs (Heggie 1975; Bailyn et al. 1992). Fusi Pecci et al. (1993) and Buonanno et al. (1997) for example showed that globular clusters with denser cores tend to have more extended EHBs. If dynamical effects in globular clusters really play a significant role in sdB formation, the subdwarf population should be more concentrated towards the cluster centers. But no radial gradient could be found in globular clusters with the most strongly populated EHBs (Bedin et al. 2000; D'Cruz et al. 1996; Rich et al. 1997). The presence of clusters with similar dynamical history and different HB morphology also argue against dynamical interactions as an origin for sdB formation (Ferraro et al. 1997; Crocker et al. 1988).

1.9   Hot subdwarfs and the UV-upturn in early-type galaxies

Far-ultraviolet radiation was first detected from early type galaxies by the OAO-2 satellite in 1969 (Code 1969). Contrary to all expectations elliptical galaxies (as well as the bulges of spiral galaxies), known to harbour old stellar population, contained bright UV sources and the energy distribution of this radiation increased to shorter wavelengths between 2 000 Å and 1 200 Å (see Fig. 1.13), implying the presence of a hot thermal source with $T_{\mathrm{eff}} > 20\,000\,\mathrm{K}$. These early results were confirmed by subsequent space missions (ANS, de Boer 1982; IUE, Bertola et al. 1982; HUT, Brown et al. 1997). The mysterious effect was called UV-upturn (see the review by O'Connell 1999). Old stellar populations do not contain main sequence stars hot enough to account for the UV excess. Due to the severe implications of the UV-upturn for the formation and evolution of stars as well as the chemical properties, dynamics and ages of galaxies the origin of this effect was heavily discussed for almost 30 years.

Different scenarios including a hot point source at the galatic center or recent episodes of star formation were proposed. The spatial distribution of the UV-light within the galaxies revealed that it is emitted from stars with dynamics similar to the dominating old stellar population (see O'Connell 1999 and references therein). Young stars and active galactic nuclei (AGNs) could be excluded, because they would have been resolved as point sources. Hills (1971) was the first to argue that highly evolved, hot, low-mass stars could be responsible and suggested post-AGB stars as possible sources. Hot horizontal branch stars as well as Blue Stragglers could be excluded, because their temperatures were not high enough to account for the excess (e.g. Wu et al. 1980). Post-AGB stars or central stars of planetary nebulae turned out to be too hot. EHB and post-EHB stars on the other hand were fully consistent with the observed UV-flux distributions and it became well established that these objects are the dominant source of the UV-upturn in early-type galaxies (Ferguson et al. 1991; Dorman et al. 1995; Brown et al. 1995, 1997). For the first time Brown et al. (2000) directly detected EHB stars in the elliptical galaxy M 32.

Again the formation of sdBs is the crucial point in exploring the UV-upturn. Two models involving single-star evolution have been proposed as explanation. The so called metal-poor model claims the existence of a very old metal-poor stellar population as progenitors of the sdBs (Lee 1994; Park & Lee 1997). The metal-rich model on the other hand assumes enhanced mass-loss of metal-rich stars at the tip of the RGB (Bressan et al. 1994; Yi et al. 1997). Han et al. (2007) recently used their binary evolution code sucessfully to reproduce most of the properties of elliptical galaxies with UV-excess. Binary sdBs may therefore again be the key also for the understanding of the UV-upturn phenomenon. Since direct spectroscopy of sdBs in other galaxies is impossible, the study of subdwarfs in different populations of our own Galaxy is the way to go (see the most recent results from Busso & Moehler 2008 on subdwarfs in the Galactic bulge).

1.10 Hot subdwarf stars, supernovae and cosmology

Double degenerate systems in close orbits are viable candidates for progenitors of type Ia supernovae (see Fig. 1.14). Supernovae of type Ia (SN Ia) play an important role in the study of cosmic evolution. They are regarded as the best standard candles for determining the cosmological parameters H_0, Ω, and Λ (e.g. Riess et al. 1998; Leibundgut 2001; Perlmutter et al. 1999; Nobili et al. 2005, see Fig. 1.15). Although the most important discovery in modern cosmology, the accelerated expansion of the universe, was initially derived from distance measurements of SN Ia at high redshifts, the nature of their progenitors is still under debate (Livio 2000). The progenitor population provides crucial information for backing the assumption that distant SN Ia can be used as standard candles like the ones in the local universe.

There is general consensus that only the thermonuclear explosion of a white dwarf (WD) is compatible with the observed features of SN Ia. For this a white dwarf has to accrete mass from a close companion to reach the Chandrasekhar limit of $1.4\,M_\odot$ (Hamada & Salpeter 1961). Two main scenarios of mass transfer are currently under discussion. In the so-called single degenerate scenario (Whelan & Iben 1973), the mass-donating component is a red giant/subgiant, which fills its Roche lobe and is continually transferring mass to the white dwarf. According to the so-called double degenerate scenario (Iben & Tutukov 1984), the mass-donating companion is a white dwarf, which eventually merges with the primary due to orbital shrinkage caused by gravitational wave radiation (see Fig 1.3).
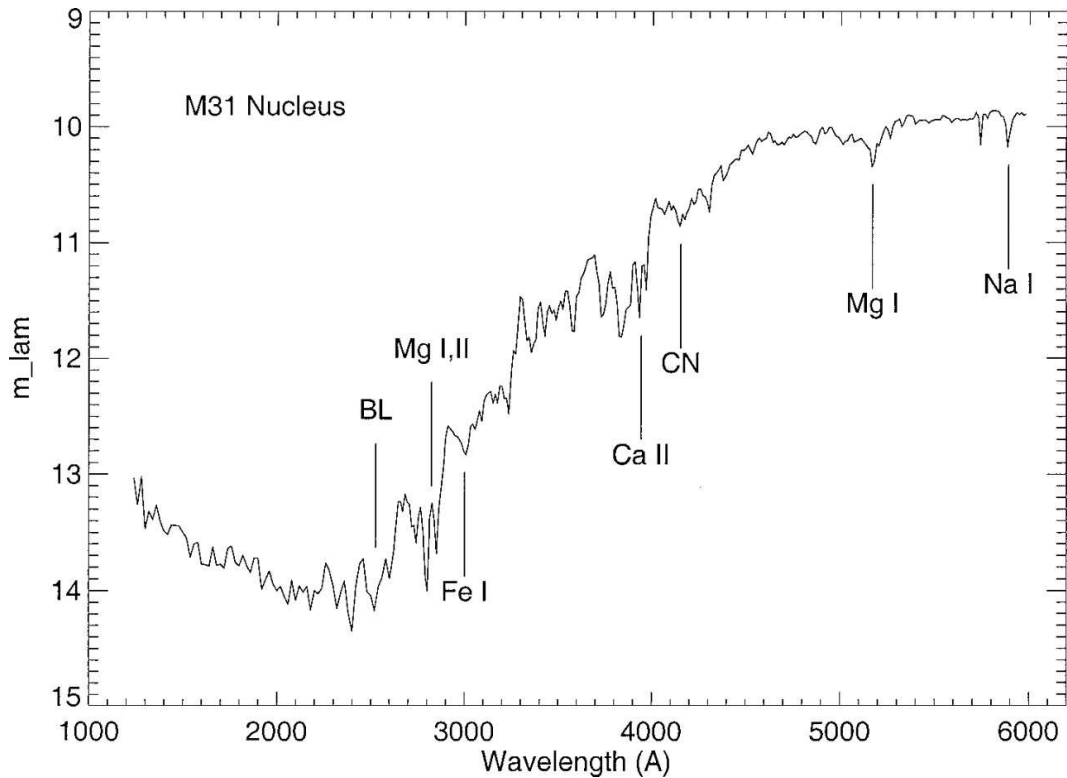
Figure 1.13: Composite UV-optical energy distribution for the center of the Sb galaxy M 31. The plot is taken from O'Connell (1999).

A progenitor candidate for the double degenerate scenario must have a total mass near or above the Chandrasekhar limit and has to merge in less than a Hubble time. Systematic radial velocity (RV) searches for double degenerates have been undertaken (e.g. Napiwotzki 2003 and references therein). The largest of these projects was the ESO SN Ia Progenitor Survey (SPY). More than 1 000 WDs were checked for RV-variations (e.g. Napiwotzki et al. 2003). SPY detected ~ 100 new double degenerates (only 18 were known before). One of them may fulfill the criteria for progenitor candidates (Napiwotzki et al. 2001).

The best known double degenerate SN Ia candidate system KPD 1930+2752 has an sdB primary, which will become a WD within about 10^8 yr before the merger occurs in about 2×10^8 yr (Maxted et al. 2000; Geier et al. 2007). It is very unlikely that this discovery was made by chance. From the observational point of view, sdBs are an especially well suited population to look for SN Ia progenitor candidates. Only about 10 % of the field DAs turned out to be double degenerates, whereas half of all known sdBs are close binaries and most of them have WD companions. The lifetimes of sdBs on the EHB are short compared to the merging times for typical orbital periods of sdB binaries. That is why all sdBs will eventually have evolved into white dwarfs before the merger occurs. Furthermore sdBs are much more luminous than WDs and the dominant population of faint blue stars at high galactic latitudes up to 16.5 mag. This means that much more bright sdBs can be observed than WDs, which makes surveys a lot easier and requires smaller telescopes.
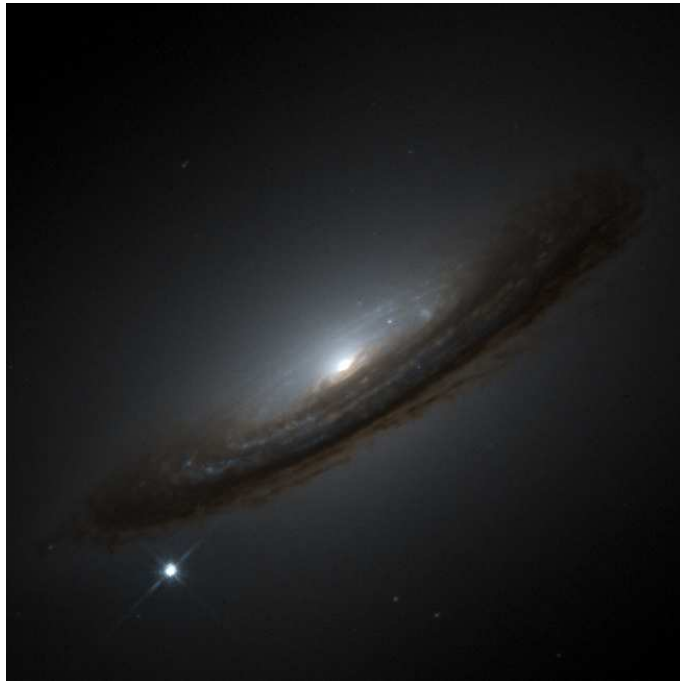
Figure 1.14: Supernova type Ia SN1994d in the galaxy NGC 4526 (Credit: NASA).
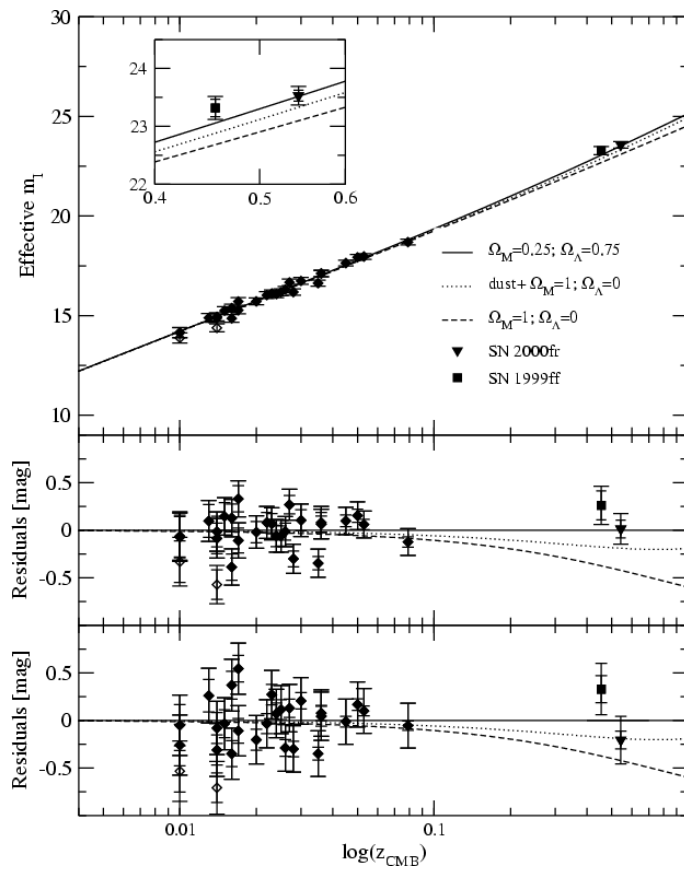
Figure 1.15: Hubble diagram from the Supernova Cosmology Project (Nobili et al. 2005).

Chapter 2

Hot subdwarf stars in close binary systems: Previous work and new discoveries

2.1 General statistics

After the discovery of close binary subdwarfs, several studies aimed at determining the fraction of hot subdwarfs residing in such systems. Samples of hot subdwarfs have been checked for RV variations with medium resolution spectroscopy at different epochs. Green et al. (1997) reported the close binary fraction of hot subdwarfs to be higher than 53%. Maxted et al. (2001) found $60 - 78\%$ of their subdwarf sample to be RV variable. Napiwotzki et al. (2004a) on the other hand reported only 39% close binaries. Preliminary results from Edelmann (priv. comm.) are closer to these lower numbers.

Several studies were undertaken to determine the orbital parameters of subdwarf binaries (the surveys of Edelmann et al. 2005a; Green et al. 2008; Morales-Rueda et al. 2003, 2004; Napiwotzki et al. in prep.; Copperwheat et al. in prep. and references given in Sect. 1.3 for single-lined binaries). The orbital periods range from $0.07 - 10\,\mathrm{d}$ with a peak at $0.5 - 1.0\,\mathrm{d}$ (see Fig. 2.2). The catalogue of Ritter & Kolb (1998) lists 80 close binary subdwarfs with published orbital parameters (until December 2007). One more was published since then (For et al. 2008).

Since almost all of these binaries are single-lined (see Fig. 2.1 upper panel), only lower limits could be derived from the stellar mass functions, which are in general compatible with late main sequence stars of spectral type M or compact objects like white dwarfs. For single-lined binaries with longer orbital periods the stellar mass function can help to further constrain the nature of the unseen companion. Assuming the canonical mass (normally about $0.47 - 0.50\,M_\odot$) for the subdwarf, the minimum mass of the companion can get high enough to exclude main sequence stars, because they would contribute significantly to the flux and therefore appear in the spectra. This mass limit lies around $0.45\,M_\odot$. With this rather crude method, the companions of about 13 binaries from the catalogue of Ritter & Kolb (1998) can be most likely constrained to be compact objects like white dwarfs.

If close binary stars are double–lined, the mass ratio of the system can be derived from the RV semiamplitudes of the two components. Until recently, only one double–lined He-sdB+He-sdB binary was known (PG 1544+488, Ahmad & Jeffery 2004, see Fig. 2.1 lower panel). Shallow
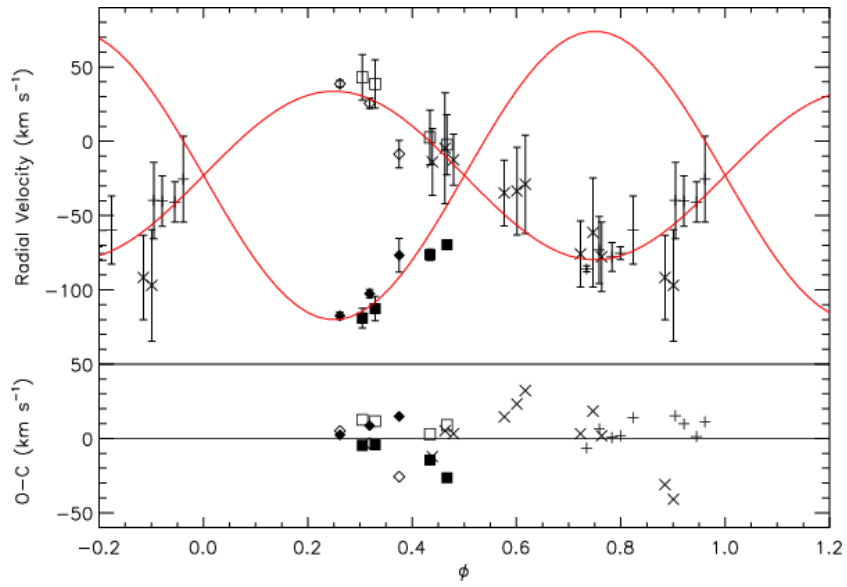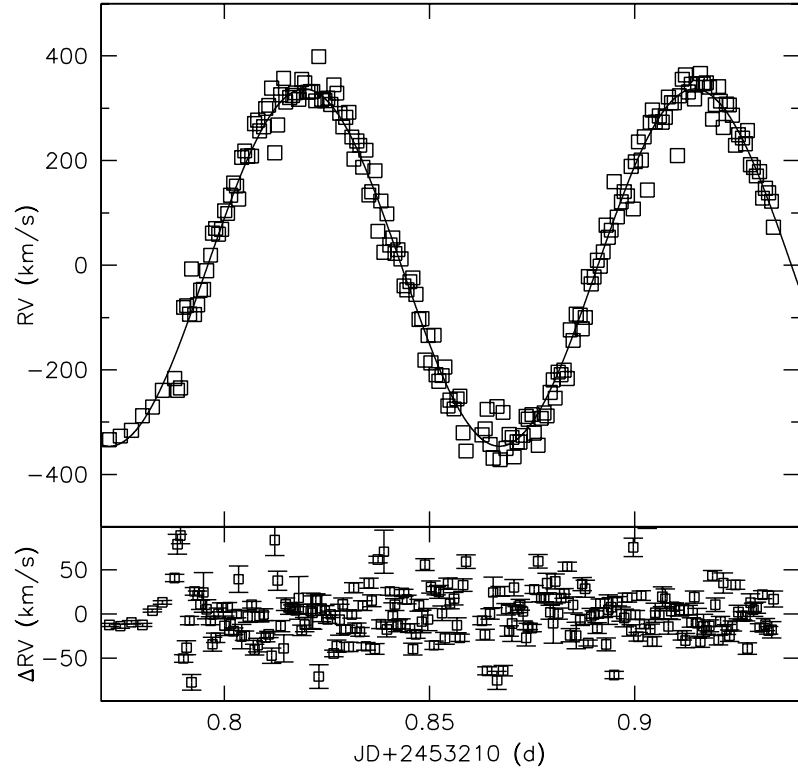
Figure 2.1: *Upper panel* Radial velocity curve of the single-lined close binary sdB+WD system KPD 1930+2752 (Geier et al. 2007). *Lower panel* Radial velocity curve of the double-lined close binary He-sdB+He-sdB system PG 1544+488 (Ahmad et al. 2004).
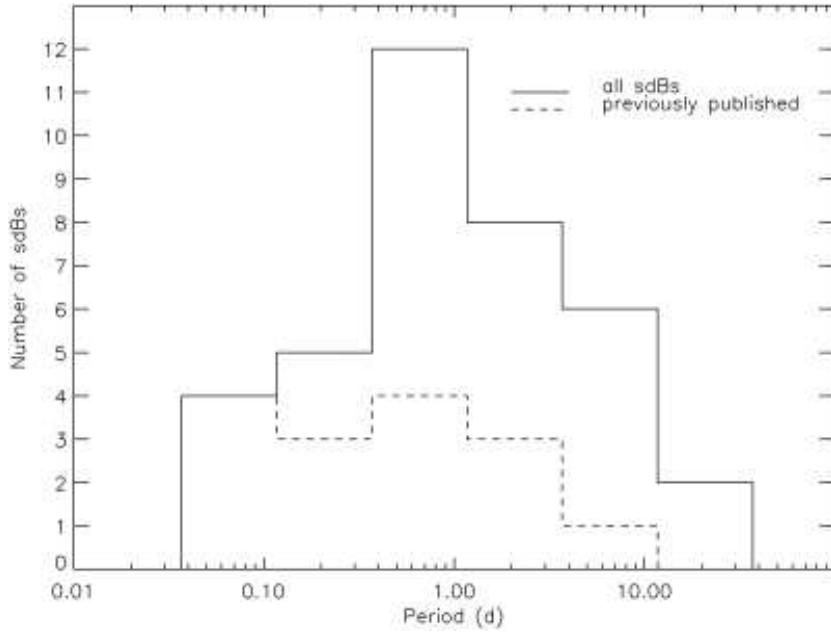
Figure 2.2: Orbital period distribution of close binary sdBs (Morales-Rueda et al. 2003).
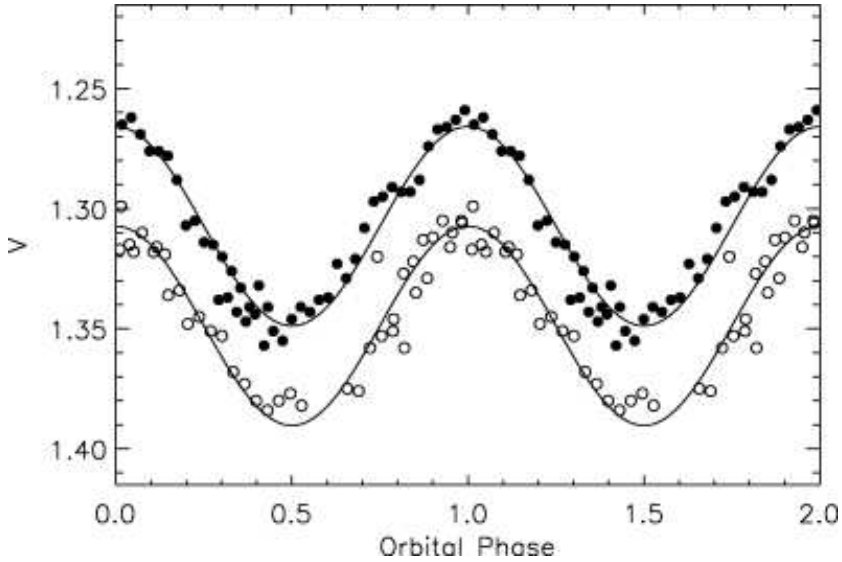
Figure 2.3: Light curve of the sdB+M binary PG 1017+086 showing a reflection effect (Maxted et al. 2002).

emission lines of M dwarf companions could be detected in high resolution spectra of two additional subdwarfs (HW Vir Edelmann 2006; AA Dor Vučković et al. 2008). Double–lined sdB binaries with main sequence companions of spectral type K, F or G are numerous (e.g. Stark & Wade 2003; Lisker et al. 2005), but no RV variability could be detected in these systems so far.

Several close binary sdBs were discovered because of variations detected in their light curves. In short period sdB binaries with orbital periods up to about half a day and high inclination the hemisphere of the cool companion directed towards the subdwarf is significantly heated up by the hot primary. This leads to a characteristic modulation of the light curve with the orbital period, which is a clear indication for a cool M-star or Brown Dwarf (BD) companion (see Fig. 2.3). Twelve sdB+M binaries with reflection effect are known so far (HW Vir Wood, Zhang, & Robinson 1993; AA Dor Rauch et al. 2000; HS 0705+6700 Drechsel et al. 2001; PG 1017+086 Maxted et al. 2002; HS 2333+3927 Heber et al. 2004; PG 1329+159 Maxted et al. 2004; BUL-SC 16 335 Polubek et al. 2007; HE 0230−4323 Koen 1999; PG 1336−018 Vučković et al. 2007; NSVS 14256825 Wils et al. 2007; HS 2231+2441 Østensen et al. 2007, 2008; KBS 13 For et al. 2008). Since detailed physical models of the reflection effect are not available yet, several free parameters have to be adjusted to fit the observed light curves. Only very limited constraints can therefore be put on the companion masses and radii from an observed reflection effect alone.

The absence of a reflection effect can also help to constrain the nature of the unseen companions. This method usually only works for binaries with periods of less than 0.5 d because otherwise the expected reflection effect from an M dwarf companion gets too shallow to be detectable (Drechsel priv. comm.). Maxted et al. (2004) used this method to exclude M dwarf companions in the case of 20 binaries. But since 15 of them have orbital periods exceeding half a day, we doubt that these results are really significant. In one case it is possible to conclude that the companion must be a compact object. Ten sdB binaries have been reported to show eclipses in their light curves (see Fig. 2.4). Seven of them (HW Vir, HS 0705+6700, AA Dor, PG 1336−018, BUL-SC 16 335, NSVS 14256825 and HS 2231+2441) have late M companions, while KPD 0422+5421 (Orosz & Wade 1999), PG 2345+318 and PG 0941+280 (Green et al. 2004) show shallow variations caused by the eclipse of a white dwarf.

A massive white dwarf companion was also identified as companion of KPD 1930+2752 (Geier et al. 2007), which shows an ellipsoidal variation in its light curve caused by the tidal distortion of the sdB. Similar signs of tidal deformation could be detected in KPD 0422+5421 (see Fig. 2.4 lower panel) and NGC 6121−V46 (O'Toole et al. 2006). These stars must have white dwarf companions, because the effect of tidal distortion in the light curve is much weaker than a reflection effect, if present.

From 81 close binary subdwarfs with known orbital parameters, 12 have bona fide M dwarf companions, while 6 companions have to be white dwarfs. In another 12 binaries compact companions are most likely. One of the binaries has a subdwarf companion. The nature of the unseen companions in the remaining 51 binaries could not be clarified with the methods described here.

2.2 Determination of hot subdwarf and companion masses in close binaries

In the rare cases where binaries are eclipsing and double-lined, all parameters including the masses of the components can be determined. If the spectra of the eclipsing binaries are single-lined, additional information is necessary to constrain the parameters. Although the inclination angle and the fraction of the radii of both components can be derived from the light curve, ambiguities remain. Families of equal solutions for different masses of the primary and the secondary exist. The critical point in most analyses of eclipsing subdwarf binaries is the precise determination of the subdwarfs surface gravity, which is necessary to derive the mass at given

radius. Theoretical mass-radius relations are used to derive masses of WDs and M stars of given radii.

The most reliable results can be expected in the case of the two eclipsing systems where lines of the companion could be detected. Although it is important to point out that these shallow emission lines are reflected light from the heated hemisphere of the cool companion. Not much is known about the properties and the size of this region. This possible source of uncertainties must be kept in mind. For the sdOB+M binary AA Dor Vučković et al. (2008) derive a minimum mass of $0.45\,M_\odot$ for the subdwarf primary and $0.09\,M_\odot$ for the M dwarf secondary. Edelmann (2008) gives an sdB mass of $0.53\,M_\odot$ and a companion mass of $0.15\,M_\odot$ in the case of the sdB+M binary HW Vir.

Drechsel et al. (2001) derived a mass of $0.48\,M_\odot$ for the subdwarf primary and a companion mass of $0.13\,M_\odot$ for the M dwarf in HS 0705+6700. Due to problems measuring the surface gravity of the sdB Vučković et al. (2007) were not able to determine a unique solution in the case of the sdB+M binary PG 1336−018. Three solutions with primary masses of about $0.39\,M_\odot$, $0.47\,M_\odot$ and $0.53\,M_\odot$ were derived. The corresponding secondary masses are $0.11\,M_\odot$, $0.12\,M_\odot$ and $0.13\,M_\odot$. Orosz & Wade (1999) determined an sdB mass of $0.53\,M_\odot$ and a nearly equal mass of $0.51\,M_\odot$ for the white dwarf secondary. Because of the low surface gravity of the subdwarf primary in HS 2231+2441 Østensen et al. (2008) argue that this object is most likely a post-RGB star with a low mass of about $0.27\,M_\odot$. In this case the companion would be a brown dwarf. The ellipsoidal variable sdB+WD binary KPD 1930+2752 has been analysed by Geier et al. (2007), who constrain the subdwarf mass to $0.45 - 0.52\,M_\odot$ and the companion mass to $0.91 - 0.96\,M_\odot$.

Asteroseismology provides an alternative way to constrain the parameters of subdwarfs in close binaries (see Sect. 1.4). In two cases the masses of subdwarfs with close companions could be determined (Feige 48: $0.52\,M_\odot$ van Grootel et al. 2008; PG 1336−018: $0.47\,M_\odot$ Charpinet et al. 2008). Pulsating subdwarfs in close binary systems are therefore important laboratories to check and improve asteroseismic analysis methods.

It can be seen that all derived subdwarf masses are not only consistent with the theoretical mass range for the CE-ejection channel in Han et al. (2002, 2003), but also very close to the canonical mass of $0.47\,M_\odot$ derived from models of single star evolution.

2.3 Orbital parameters of new close binary subdwarfs

The potential of close binary sdBs for determining fundamental parameters, performing astero-seimic analysis, clarifying the process of common envelope ejection and therefore the question of sdB formation has been demonstrated in the last sections. Especially peculiar systems like eclipsing or pulsating binaries turned out to be important laboratories. Discovering more of these interesting objects therefore makes much sense.

Here we give orbital solutions of seven subdwarf binaries and preliminary orbital parameters for another four systems. Nine new close binary systems have been discovered by the detection of radial velocity shifts. Since some of these binaries show features in their light curves like reflection effects and pulsations, they are promising targets for more detailed analyses.

2.3.1 Target selection, observations and data reduction

Most of our targets were discovered in the course of the ESO Supernovae Ia Progenitor Survey (SPY) dedicated to find double degenerate progenitor candidates of SN Ia (Napiwotzki et al. 2003, see Sect. 1.10). Several candidate close binary sdBs have been identified which show RV variability. The hot subdwarf binaries from SPY are followed-up to determine their orbital parameters in an ongoing campaign (Napiwotzki et al. 2001; Karl et al. 2006; Napiwotzki et al. in prep.). This campaign is continued here. Several targets were taken from other sources, especially the ones with detected variations in their light curves. The targets were chosen in close collaboration with R. Østensen, who supervises the online subdwarf database (Østensen 2006).

For the ESO Supernovae Ia Progenitor Survey (SPY), high resolution spectra were taken over the course of four years, using the Ultraviolet Visual Echelle Spectrograph (UVES) at the VLT. The setup used for our SPY project operated the instrument in dichroic mode, using Dichroic No. 1 at central wavelengths of $3900 \,\text{Å}$ in the blue and $5640 \,\text{Å}$ in the red. Nearly complete wavelength coverage from $3200 \,\text{Å}$ to $6650 \,\text{Å}$ with only two small $80 \,\text{Å}$ wide gaps at $4580 \,\text{Å}$ and $5640 \,\text{Å}$ is achieved. A 2x2 binning was used to reduce read out noise. A slit width of 2".1 was used to minimize slit losses, which means that the spectral resolution is seeing dependent ($R \approx 20\,000 - 40\,000$).

The spectra were reduced with a procedure developed by Karl using the ESO MIDAS package, partly based on the UVES online reduction pipeline. For details of the reduction process see Lisker et al. (2005) and Karl (2004). Different spectra from one star were shifted to rest wavelength and coadded to achieve better quality.

At this point it has to be noted, that S/N and resolution of these spectra are quite inhomogeneous. The main objective of the SPY survey was the search for RV variable white dwarfs. To achieve this, as many objects as possible have to be observed per unit time and with acceptable quality. A wide slit and short exposure times ($300 - 600 \,\text{s}$) are the consequences. Even with an 8 meter telescope the results are therefore not always perfect for a full quantitative spectral analysis.

The follow-up campaigns were performed at the European Southern Observatory (ESO) La Silla, Chile using the New Technology Telescope (NTT) equipped with the ESO Multi Mode Instrument (EMMI). Using grating number 3 and 1.0" slit the spectral resolution was about $1 \,\text{Å}$. The wavelength range was $3\,880 - 4\,380 \,\text{Å}$. Bias and dome flats were taken during daytime. Calibration lamp spectra were taken after every single exposure. Standard routines from the ESO MIDAS package were used for data reduction.

Additional observations were performed with the ISIS spectrograph mounted at the William Herschel Telescope (WHT), operated by the Isaac Newton Group of Telescopes (ING), Spain. We used the instrument with a $5\,700 \,\text{Å}$ dichroic and an average slit width of 1.5" dependent on the conditions. Using grating R600B in the blue arm and grating R600R in the red arm the spectral resolution was about $2 \,\text{Å}$ with a wavelength coverage in the blue from $3\,500 - 5\,100 \,\text{Å}$ and from $5\,600 - 6\,800 \,\text{Å}$ in the red. The process of data reduction is described in Maxted et al. (2000b). Table 2.1 gives an overview of all follow-up runs.

2.3.2 Radial velocity measurements, power spectra and RV curves

Radial velocities of the individual observations were determined by calculating the shifts of the measured wavelengths to laboratory measurements. Therefore, a simultaneous fit of a set of

Table 2.1: Follow-up observations. The first column lists the date of observation, while in the second the used telescope and instrumentation is shown.

Date		Telescope & Instrument	
2004	January 01 – 04	ESO NTT	EMMI
2007	May 30 – June 02	ESO NTT	EMMI
2008	January 10 – 14	ESO NTT	EMMI
2008	April 29 – May 01	ING WHT	ISIS

mathematical functions to the observed line profiles was performed using the FITSB2 routine (Napiwotzki et al. 2004b). A linear function was used to reproduce the overall spectral trend, a Lorentzian to model the line wings and a Gaussian for the innermost line core. The central wavelength of the Lorentzian was fixed to that of the Gaussian for physical reasons. All visible and suitable Balmer and helium lines were used. In preparation for further analysis, all measured radial velocities as well as the times of observation have been heliocentrically corrected. As reference, the mid exposure time was used.

The period search was carried out by means of a periodogram based on the Singular Value Decomposition (SVD) method. A sine-shaped RV curve was fitted to the observations for a multitude of phases, which were calculated as a function of period. The difference between the observed radial velocities and the best fitting theoretical RV curve for each phase set was evaluated in terms of the logarithm of the sum of the squared residuals (χ^2) as a function of period. This method finally results in the data-set's power spectrum which allows to determine the most probable period P of variability (see Lorenz et al. 1998). From the best fit RV curve corresponding to the most probable period, the ephemeris, the system's velocity γ and the radial velocity semi-amplitude K were derived.

The single radial velocity measurements are given in the Appendix. The radial velocity curves as well as the power spectra are plotted in Fig. 2.5 and Figs. B.1-B.10 in the Appendix. Derived orbital parameters are given in Tab. 2.2. The orbits of all binaries are circular.

2.3.3 Constraints on the nature of the unseen companions

Since the spectra of the programme stars are single-lined, they reveal no information about the orbital motion of the sdBs' companions, and thus only their mass functions can be calculated.

$$f_{\mathrm{m}} = \frac{M_{\mathrm{comp}}^3 \sin^3 i}{(M_{\mathrm{comp}} + M_{\mathrm{sdB}})^2} = \frac{PK^3}{2\pi G}. \tag{2.1}$$

Although the RV semi-amplitude K and the period P are determined by the RV curve, the mass of the sdB M_{sdB}, the companion mass M_{comp} and the inclination angle i remain free parameters (G is the gravitational constant). The right side of Eq. 3.1 gives the minimum mass of the unseen companion without any assumption made about the mass of the subdwarf primary.

The canonical mass of $0.47\,M_{\odot}$ was chosen to estimate the masses of the unseen companions (see Sects. 1.2, 1.3, 1.4). If no spectral signatures of cool companions were visible (e.g. Mg I lines), main sequence stars with masses higher than $0.45\,M_{\odot}$ could be excluded because of their high luminosities in comparison to the sdB stars. Stars only observed with EMMI could not been

Table 2.2: Derived orbital parameters of the programme stars.

Object	T_0 [$-2\,450\,000$]	P [d]	γ [kms^{-1}]	K [kms^{-1}]
ASAS 102322$-$3737.0	4 477.227861	0.14 ± 0.01	12.1 ± 1.1	77.8 ± 1.5
HE 1423$-$0119	4 253.714704	0.198 ± 0.001	-52.7 ± 6.7	44.5 ± 10.9
PG 0941$+$280	4 476.175827	0.3112 ± 0.0001	80.6 ± 0.8	144.6 ± 0.9
WD 0107$-$342	3 340.48039	0.37765 ± 0.00002	25.0 ± 1.6	129.5 ± 1.9
V 1405 Ori	4 477.336245	0.404 ± 0.04	-37.8 ± 3.8	95.9 ± 5.3
Albus 1	4 477.569870	0.76 ± 0.03	-6.6 ± 1.4	30.3 ± 1.6
HE 1130$-$0620	1 683.620834	0.9782 ± 0.0002	16.6 ± 3.6	53.5 ± 5.5
Preliminary parameters				
HE 1415$+$0309	4 252.987582	0.17(0.39)	128(95)	211(171)
HE 1140$-$0500	2 393.587789	0.27	-76.7 ± 3.1	45.7 ± 4.0
HS 2043$+$0615	3 340.564050	0.46 ± 0.01	-66.2 ± 2.5	98.0 ± 3.3
KPD 0629$-$0016	4 477.275561	0.9 ± 0.1	-17.8 ± 3.6	50.0 ± 4.0

Table 2.3: Derived minimum companion masses and types of the programme stars. *Subdwarfs with cool companions identified by Lisker et al. (2005).

Object	$f(M)$ [$M_\odot$]	$M_{2\mathrm{min}}$ [$M_\odot$]	Composition
ASAS 102322$-$3737.0	0.007	0.14	sdB+M
HE 1423$-$0119	0.0018	0.08	sdO+WD
PG 0941$+$280	0.097	0.43	sdB+WD
WD 0107$-$342	0.085	0.40	sdB+WD
V 1405 Ori	0.037	0.27	sdBV+M
Albus 1	0.002	0.09	He-sdB+WD/MS/BD
HE 1130$-$0620	0.016	0.19	sdO+MS/WD
Preliminary parameters			
HE 1415$+$0309	0.17(0.20)	0.56(0.62)	sdB+WD
HE 1140$-$0500	0.0027	0.09	sdB+G*
HS 2043$+$0615	0.0045	0.30	sdB+MS/WD
KPD 0629$-$0016	0.0012	0.17	sdBV+MS/WD

checked for spectral features of cool companions since the spectral range was too limited. Taking the most likely subdwarf mass into account, an assumption about the minimum companion mass is possible by solving the mass function for $i = 90°$. For minimum masses below $0.45\,M_\odot$ the companions can be late type main sequence stars as well as white dwarfs or other massive compact objects like neutron stars or black holes. If the minimum mass exceeds $0.45\,M_\odot$ the main sequence scenario can most likely be rejected and the companion must be a compact object.

Table 2.4: Radial velocity variable stars. †Stars with previously measured RVs by Beers et al. (1992). *Subdwarfs with cool companions identified by Lisker et al. (2005)

Object	ΔRV [kms^{-1}]	Type
BPS CS 22879$-$149†	192 ± 8	sdB
HE 1518$-$0948	184 ± 15	He-sdO/post-AGB
HE 2322$-$4559	171 ± 22	sdB+G*
HS 1536+0944	146 ± 21	sdB+K*
BPS CS 22947$-$99†	89 ± 8	sdB
HE 1033$-$2353	61 ± 8	sdB
BPS CS 22879$-$82†	49 ± 32	sdB
BPS CS 22947$-$299†	37 ± 9	sdB
BPS CS 22937$-$84†	16 ± 8	sdB

Due to projection effects high orbital inclinations are more probable than low ones (see e.g. Gray 1992). Companion masses near the lower limit are more likely than high companion masses.

2.3.4 Results

The derived orbital parameters of the programme stars, the mass functions and minimum companion masses are given in Tab. 2.2. The most likely types of the unseen companions are given as well. Only the radial velocity curve and published or yet unpublished informations about flux excesses and light curves are used here to constrain the nature of the companions.

ASAS 102322$-$3737.0 (Fig. 2.5) has recently been identified as bright subdwarf candidate by colour selection. The light curve of this star taken in the course of the All Sky Automated Survey (Pojmanski 2002) shows a variation with a period of $P = 0.139$ d most likely identified as reflection effect from a close M dwarf companion (Østensen priv. comm.). The orbital period derived from the radial velocity curve as well as the minimum mass of the companion are in perfect agreement with this scenario. A full analysis of this newly discovered reflection effect sdB+M binary will be published by Østensen et al. (in prep.).

HE 1423$-$0119 (Fig. B.1) is a hot sdO star, which was analysed in Ströer et al. (2007). Although the minimum mass of the unseen companion would be compatible with a very late M star or even a brown dwarf (for sdO masses lower than canonical), this scenario is unlikely. The star was recently checked for light curve variations due to a reflection effect and no such feature could be detected (Østensen priv. comm.). Since the orbital period of the system is short and the primary very hot, this non-detection leads to the conclusion, that the companion has to be a compact object, most likely a low mass He-WD.

PG 0941+280 (Fig. B.2) is an eclipsing binary with sdB primary and WD companion (Green et al. 2004). The orbital period derived here agrees with the result of Green et al. (2004). Due to the high inclination of the binary, the minimum companion mass given in Tab. 2.2 should be very close to the real mass of the WD. A detailed light curve analysis is required to constrain the parameters of this interesting binary.

The unseen companion of the sdB binary **WD 0107$-$342** (Fig. B.3) is a compact object,

most likely a white dwarf. In addition to the high minimum mass of the companion, this star has been checked for a flux excess in the infrared by Farihi et al. (2005). No excess and therefore no indication for a cool MS companion was found.

V 1405 Ori (Fig. B.4) is a short period pulsating sdBV of V 361 Hya type discovered by Koen et al. (1999). In addition to the pulsations the light curve shows a long period variation (0.4 d) identified as reflection effect coming from a cool M dwarf companion (Østensen priv. comm.). Due to the limited number of RV measurements no unique orbital solution could be derived from the RV curve. The power spectrum shows prominent peaks at about 0.1 d, 0.4 d and 0.6 d. Taking into account the additional information from the light curve the peak at 0.404 ± 0.04 d could be identified as the correct solution. The derived minimum mass of the companion is consistent with an M dwarf. A full analysis of this sdBV+M binary will be published by Terndrup et al. (in prep.).

The bright star **Albus 1** (Fig. B.5), previously misclassified as DA, has been identified to be a He-rich sdB by Vennes et al. (2007). The minimum mass of the companion is very low, which means that the most probable companion is a low mass M star or maybe a brown dwarf (in case of a subdwarf mass lower than $0.47\,M_\odot$). A low mass He-WD cannot be excluded as well. The phased radial velocity curve shows a large and yet unexplained scatter at minimum RV, which may be related to a similar phenomenon as in the case of KPD 0629−0016 discussed below.

HE 1130−0620 (Fig. B.6) is another hot sdO star, which was analysed in Ströer et al. (2007). The derived minimum mass for the companion is compatible with a low mass WD as well as an M star. Due to the rather long orbital period of this binary, it will be hard to distinguish between the two possibilities from the light curve since a reflection effect would be very shallow.

For some of our programme stars only preliminary parameters can be given so far. More observations are needed to clearly derive the correct orbital parameters and exclude prominent aliases. **HE 1415+0309** (Fig. B.7) is an sdB star from the SPY sample (Lisker et al. 2005). The power spectrum shows two almost equally prominent peaks at orbital periods of 0.17 d and 0.39 d. Although the period is not well determined, both derived orbital solutions give quite similar minimum masses for the unseen companion. A main sequence companion can be excluded since it would be visible in the spectra. Therefore the companion is most likely a white dwarf. Should the binary have low inclination, a neutron star or black hole binary would also be possible.

HE 1140−0500 (Fig. B.8) was also analysed by Lisker et al. (2005) and described as sdB+G binary with visible Mg I lines from the cool companion in the spectra. Unfortunately the EMMI spectra do not cover this spectral range and the UVES spectra are too noisy to measure RVs from these lines. With better spectra it should be possible to obtain the orbital parameters of both components. All known close binary sdB+MS systems have late M dwarf companions and are therefore single–lined. HE 1140−0500 is therefore the first double–lined and RV variable sdB+MS binary discovered so far. Considering the low minimum mass of the companion, the system is most likely seen at very low inclination.

HS 2043+0615 (Fig. B.9) is an sdB from the SPY sample with a minimum companion mass compatible with an M star or a low mass white dwarf. The light curve of this star shows a modulation of 8 % with a period of about 0.3 d (Østensen priv. comm.). Since the most likely orbital period derived from the radial velocity curve is 0.46 d, the light curve variation cannot clearly be identified as reflection effect. This modulation as well as the nature of the unseen companion remains unknown.

KPD 0629−0016 (Fig. B.10) was discovered to be a slowly pulsating sdB of V1093 Her type by Koen & Green (1999). From low resolution spectra they were not able to detect the RV variability of this star. According to the preliminary orbital solution the companion is most likely a late M star or a low mass white dwarf. The light curve taken by Koen & Green (1999) is not sufficient to distinguish between the two possibilities. Should the preliminary orbital period of 0.9 d turn out to be correct, a reflection effect would be to weak to be detectable with the instrument they used. Furthermore, the observed light curve only covers about 0.3 d and has been detrended before searching for pulsations. At an orbital phase of about 0.8 the RV curve seems to be superimposed by a short period variation (≈ 0.1 d) with an RV semiamplitude of about $20 \, \mathrm{km s^{-1}}$. Since the sampling at this phase is particularly high, this modulation may be present at all phases. The RV curve of the He-sdB Albus 1 shows a similar behaviour. A possible explanation could be RV variations due to pulsations. More observations are needed to reach a dense phase coverage of these binaries.

Nine new close binary subdwarfs have been discovered by detecting radial velocity variations (see Tab. 2.4) and have to be followed-up to derive orbital parameters. Five stars were taken from the catalogue of Beers et al. (1992), who also gave first epoch radial velocities for these objects. These RV measurements have been compared to our new results. **BPS CS 22879−149** shows the highest RV shift and is most likely a very short period binary.

Four stars were observed in the course of the SPY survey and identified as RV variables. While **HE 1033−2353** shows no spectral signs of a cool companion, **HE 2322−4559** and **HS 1536+1944** have main sequence companions and their spectra appear to be double-lined (Lisker et al. 2005). These systems are in this respect quite similar to HE 1140−0500 (see Fig. B.8) and constitute a new class of hot subdwarf binaries. Follow-up observations are needed to obtain the orbital parameters of both binary components. **HE 1518−0948** is a hot helium star, which was analysed by Ströer et al. (2007). Only upper limits could be given for the surface gravity of this objects. It is therefore unclear, if the star is a He-sdO or a post-AGB object. Only one close binary He-sdO is known so far (Ahmad & Jeffery 2004). Due to the high temperature of this star, a reflection effect should be detectable, if the companion is a main sequence star.

2.3.5   Discussion

The period distribution of all known subdwarf binaries is shown in Fig. 2.6. Compared to the larger samples of Morales-Rueda et al. (2003), Edelmann et al. (2005a) and Napiwotzki et al. (in prep.) the binaries analysed here have orbital periods scattered around the peak at $0.1 - 1.3$ d. Common envelope ejection is the most likely formation channel for all analysed binaries. The fraction of close binaries with helium rich sdO (He-sdO) primaries on the other hand turned out to be very low (Ströer et al. 2007). Only one close binary He-sdB+He-sdB and one candidate He-sdO+He-sdO have been discovered so far (Ahmad & Jeffery 2004; Lisker et al. 2005) indicating a different evolutionary scenario for these subdwarfs. The discovery of an RV shift in the single-lined candidate He-sdO HE 1518−0948 may again change this picture.

All known companions to hot subdwarfs in close binary systems are either white dwarfs or late M stars. Main sequence companions of K, F and G type with luminosities comparable to the smaller, but hotter subdwarfs are known as well (earlier MS stars would totally outshine the subdwarfs). These systems with composite spectra are usually wide binaries, where no RV variability can be detected. According to the scenarios of Han et al. (2002, 2003) a population of subdwarf binaries with main sequence companions should exist, which was formed by stable

Roche lobe overflow. These binaries should have orbital periods of hundreds of days. Although several surveys are underway aiming at finding such long period systems (e.g. Edelmann et al. in prep., Morales-Rueda et al. in prep.), none could be found up to now. Our discovery of strong RV variability in three double-lined sdB+MS binaries indicates that such systems may also be formed by Common Envelope ejection, because only this channel is able to produce binaries with short periods and high RV amplitudes. Another possible scenario would be a hierarchical triple system with a close binary sdB+WD/M and a remote F/G companion. In this case the spectral lines of the cool companion should show no variability. More observations are needed to derive the orbital parameters of these interesting systems and find out more about their composition.

Brown dwarf companions as well as giant exoplanets may play an important role in the formation of hot subdwarf stars (see Sect. 1.3, 1.6). Rauch et al. (2000, 2003) found indications for a brown dwarf companion in the eclipsing sdOB binary AA Dor. Recent results by Vučković et al. (2008) on the other hand suggest that the companion of this star is more likely a late M star. Three more candidate systems were published by Maxted et al. (2002) and Edelmann et al. (2005a). The eclipsing binary HS 2231+2441 may also be orbited by a substellar companion (Østensen et al. 2008). With the He-sdB binary Albus 1 another candidate for a brown dwarf companion has been discovered here.
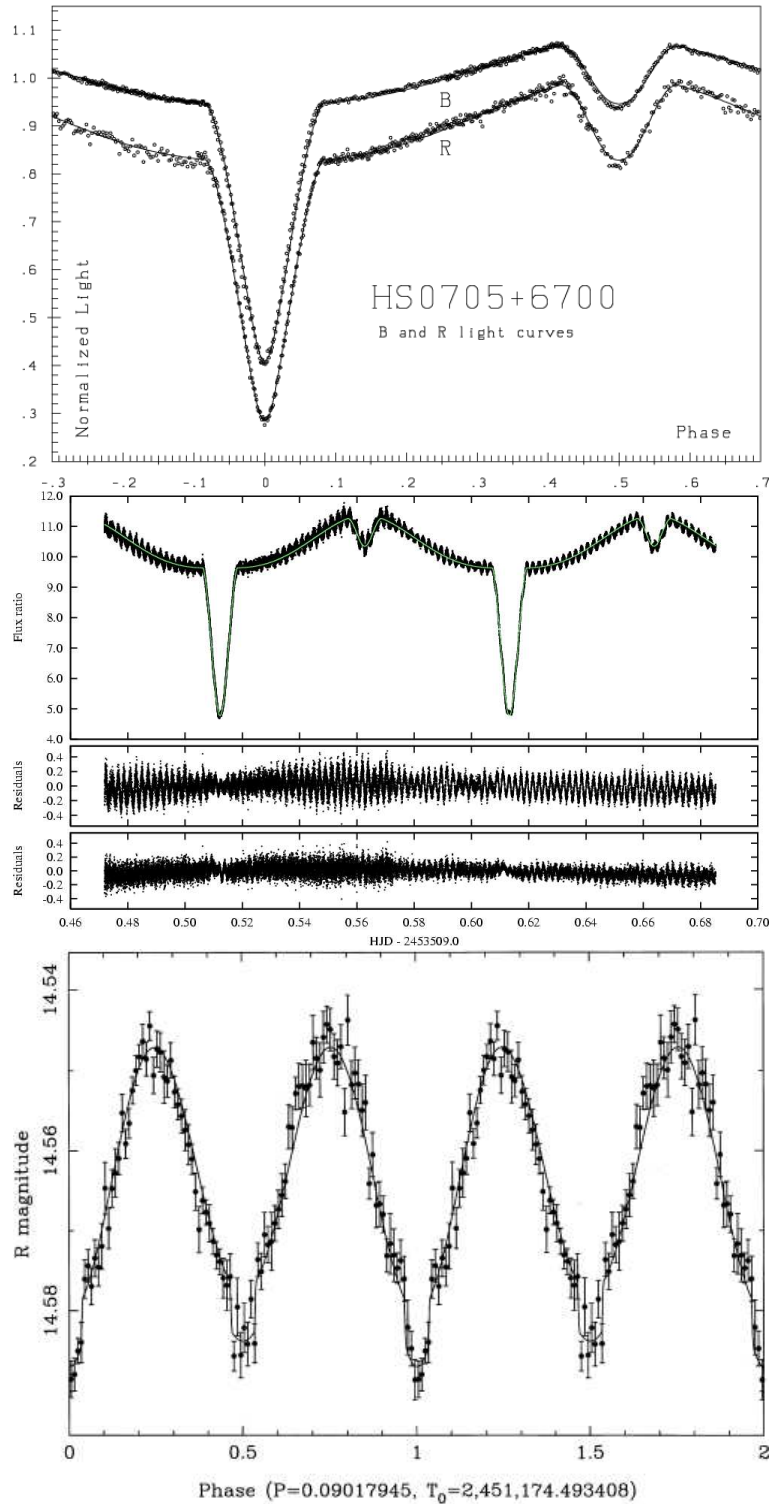
Figure 2.4: Light curves of eclipsing sdB binaries. *Upper panel* The sdB+M binary HS 0705+6700 shows reflection effect and eclipses (Drechsel et al. 2001). *Middle panel* In the case of the sdBV+M binary short period pulsating are present in addition to reflection effect and eclipses (Vučković et al. 2007). *Lower panel* The variations of the sdB+WD binary KPD 0422+5421 are caused by the ellipsoidal deformation of the subdwarf. Shallow eclipses of the WD secondary can be seen (Orosz & Wade 1999).

42
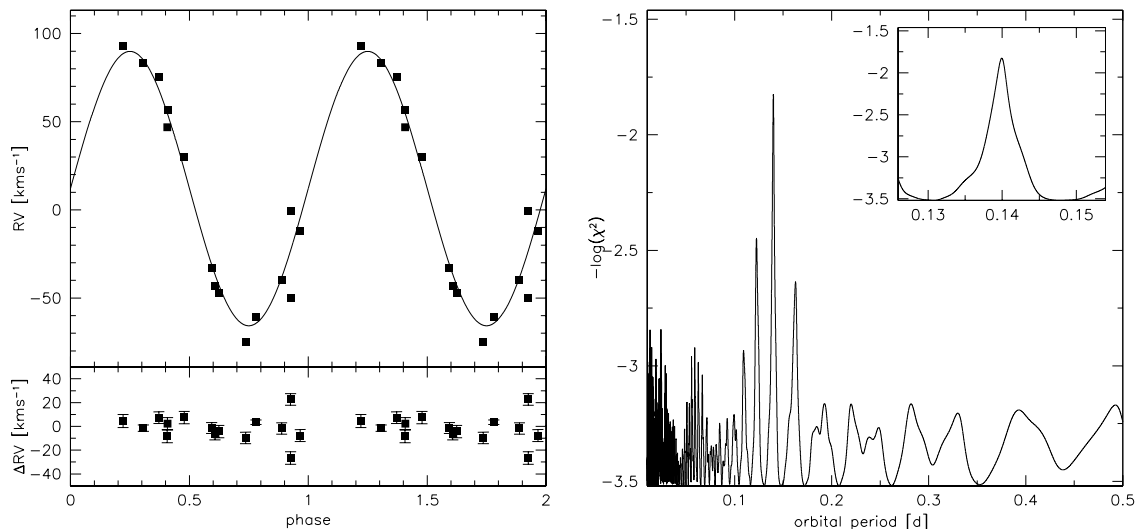
ASAS 102322

Figure 2.5: Radial velocity curve and power spectrum of ASAS 102322. The left panel shows the radial velocity plotted against orbital phase. The RV data was phase folded with the most likely orbital period. The right panel shows the power spectrum. $-log\chi^2$ is plotted against the orbital period in days. The region around the most prominent peak is plotted in the small window.
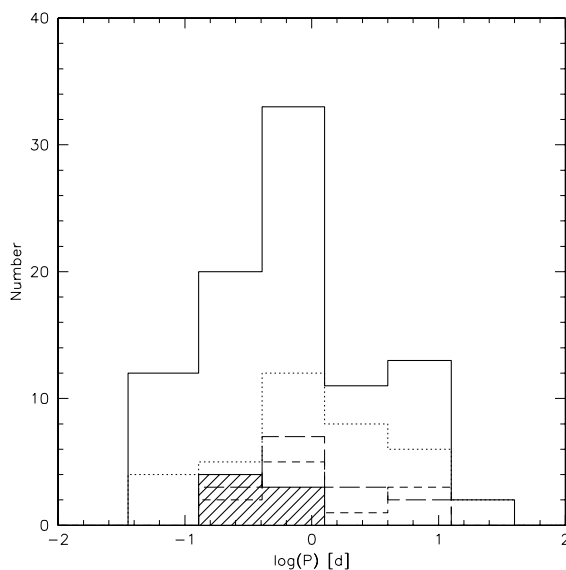
Figure 2.6: Histogram of orbital periods. The shaded histogram shows the results presented here. Periods distribution of other samples are given as well (short-dashed, Edelmann et al. 2005a; long-dashed, Napiwotzki et al. in prep.; dotted, Morales-Rueda et al. 2003). The solid histogram shows the period distribution of all known subdwarf binaries (Catalogue of Ritter & Kolb 1998 until December 2007; For et al. 2008; Napitwotzki et al. in prep. and our results).

Chapter 3

Constraining binary parameters

From Chap. 2 it became apparent that although the orbital parameters of many sdB binaries have been derived, the nature of their unseen companions remains unclear in most cases. Here we present an alternative method, which allows us to constrain the masses of the invisible companions much better. This method, which requires high resolution spectra, was applied to about 40 % of the known sdB binary systems. A similar method is also used to determine the masses of the unseen companions in X-ray binaries (see a review by Charles & Coe (2006).

3.1   Analysis method

Since the spectra of the programme stars are single-lined, they reveal no information about the orbital motion of the sdBs' companions, and thus only their mass functions can be calculated (see Fig. 3.1).

$$f_{\mathrm{m}} = \frac{M_{\mathrm{comp}}^3 \sin^3 i}{(M_{\mathrm{comp}} + M_{\mathrm{sdB}})^2} = \frac{PK^3}{2\pi G} \tag{3.1}$$

Although the RV semi-amplitude K and the period P are determined by the RV curve, M_{sdB}, M_{comp} and $\sin^3 i$ remain free parameters.

In the following analysis we adopted the mass range of Han et al. (2002, 2003) if no indepedent mass determinations are available. But it has to be stressed that from both observational and theoretical side the canonical value of $0.47 \, M_{\odot}$ is the most likely one.

In close binary systems, the rotation of the stars gets synchronised to their orbital motion. In this case their rotational periods equal the orbital period of the binary. If the sdB primary is synchronised in this way its rotational velocity v_{rot} can be calculated.

$$v_{\mathrm{rot}} = \frac{2\pi R_{\mathrm{sdB}}}{P} \tag{3.2}$$

The stellar radius R is given by the mass radius relation.

$$R = \sqrt{\frac{M_{\mathrm{sdB}} G}{g}} \tag{3.3}$$

The measurement of the projected rotational velocities $v_{\mathrm{rot}} \sin i$ therefore allows to constrain the systems' inclination angles i. With M_{sdB} as free parameter the mass function can be solved
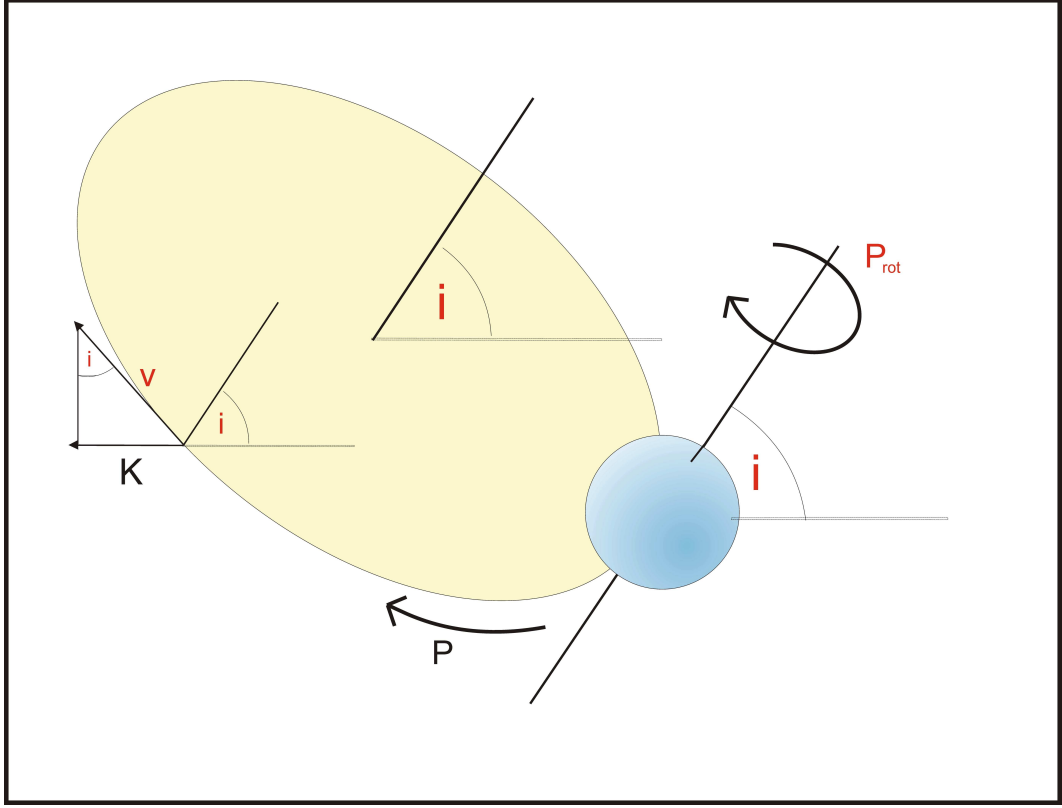
Figure 3.1: Schematic view of a single-lined binary system.

and the inclination angle as well as the companion mass can be derived (see Fig. 3.2). Because of $\sin i \leq 1$ a lower limit for the sdB mass is given by

$$M_{\mathrm{sdB}} \geq \frac{v_{\mathrm{rotsini}}^2 P^2 g}{4\pi^2 G} \tag{3.4}$$

This method was already sucessfully applied to the sdB+WD binary KPD 1930+2752 (Geier et al. 2007).

There are no spectral signatures of companions visible. Main sequence stars with masses higher than $0.45\,M_\odot$ could therefore be excluded because of their high luminosities in comparison to the sdB stars. In this case spectral features of the cool secondary (e.g. Mg I lines at $\approx 5\,170\,\text{Å}$) get visible in the spectra (Lisker et al. 2005).

Another possibility to detect M dwarf companions are reflection effects in the binary light curves. Some of our programme stars have already been checked for modulations in their light curves. Unfortunately, this method only works, if the binary inclination is high and the orbital period short enough. Synthetic light curve modelling of sdB+M systems shows that the expected amplitude of a reflection effect drops below 1 mmag for orbital periods longer than 0.5 d. This period therefore provides an upper limit for the detectability of reflection effects in sdB binaries from the ground.
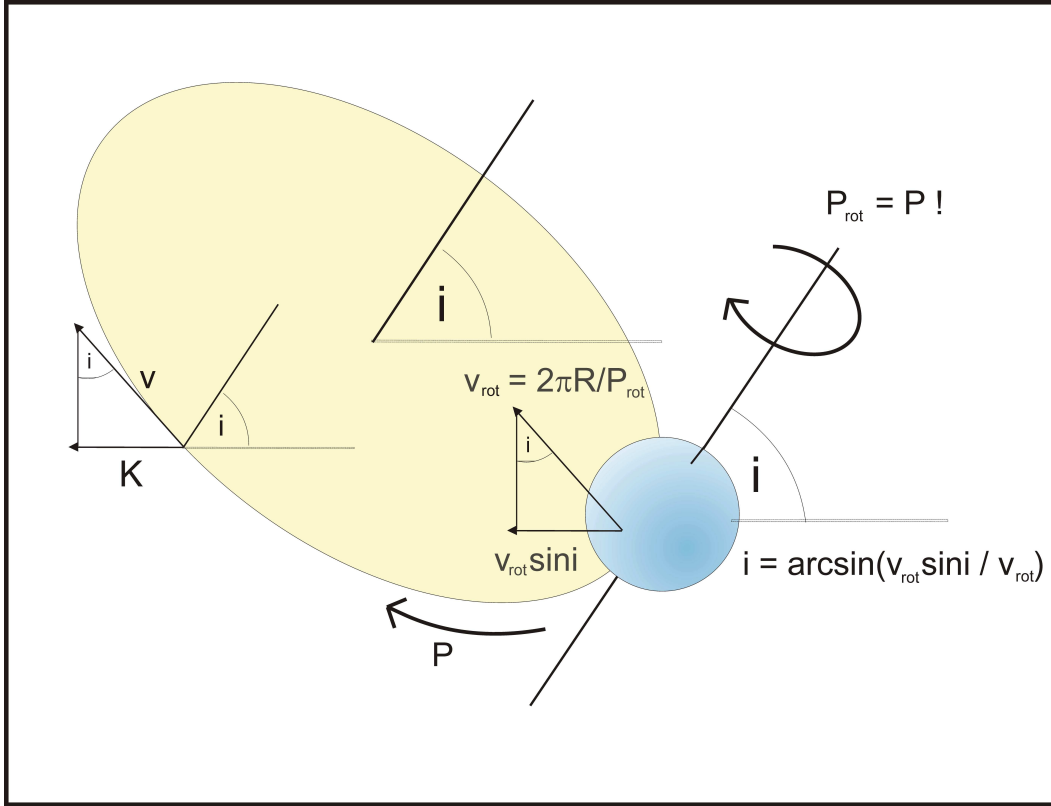
Figure 3.2: Schematic view of a single-lined binary system with synchronised rotation.

3.2 Observations and data reduction

68 stars (19 stars in close binaries, 49 single and wide binary stars) were observed at least twice in the course of the SPY project. For some of the radial velocity variable systems follow-up observations with UVES in the same setup were undertaken to derive the orbital parameters (see Sect. 2.3.1 and Napiwotzki et al. in prep.).

High resolution spectra ($R = 30\,000$) of 13 known close binary subdwarfs have been taken with the HRS fiber spectrograph at the Hobby Eberly Telescope (HET) in the second and third trimester 2007. The spectra were reduced by T. Kupfer using standard ESO MIDAS routines.

Another sample of 11 known bright subdwarf binaries was observed by H. Edelmann with the FEROS spectrograph ($R = 48\,000$) mounted at the ESO 2.2m telescope. The spectra were downloaded from the ESO science archive and reduced with the FEROS-DRS pipeline under the ESO MIDAS context in optimum extraction mode. One FEROS spectrum was provided by L. Morales-Rueda and reduced in the same way.

Three spectra of subdwarf binaries observed with the FOCES spectrograph ($R = 30\,000$) mounted at the CAHA 2.2m telescope as well as one spectrum taken with the HIRES instrument ($R = 45\,000$) at the Keck telescope were provided by H. Edelmann. Another HIRES spectrum and two spectra taken with the echelle spectrograph ($R = 20\,000$) at the 1.5m Palomar telescope back in 1989 were provided by U. Heber.

3.3 Measuring low projected rotational velocities from metal lines

From medium to low S/N spectra of sdBs it is not possible to measure projected rotational velocities below $25\,\mathrm{km s^{-1}}$ using Balmer or helium lines because of their high pressure broadening. Sharp metal lines are much more sensitive to rotational broadening. To measure low projected rotational velocities with high precision it is necessary to make use of a lot of weak metal lines.

In order to derive $v_{\mathrm{rot}}\sin i$, we compared the observed spectra with rotationally broadened, synthetic line profiles using a semi-automatic analysis pipeline. The profiles were computed for the stellar parameters given in Lisker et al. (2005) and Tab. 3.5 using the LINFOR program (developed by Holweger, Steffen and Steenbock at Kiel university, modified by Lemke 1997).

For a standard set of 68 metal lines from 24 different ions for the UVES spectra or 187 metal lines from 24 different ions in case of the brighter stars with higher S/N a model grid with appropriate atmospheric parameters and different elemental abundances was automatically generated with LINFOR. A simultaneous fit of elemental abundance, projected rotational velocity and radial velocity was then performed separately for every identified line using the FITSB2 routine (Napiwotzki et al. 2004b). For a more detailed description of the line selection and abundance determination see Sect. 8.1.

Bad lines were automatically rejected. This rejection procedure included several criteria. First the fitted radial velocity had to be low, because all spectra were corrected to zero RV before. High measured RVs were considered as misidentifications or noise features. Then the fit quality given by the χ^2 had to be comparable to the average. Bad fits were excluded. Extrapolations of elemental abundances were excluded as well. Finally equivalent width and depth of the fitted line was measured and compared to the noise to distinguish between lines and noise features. Mean value and error were calculated from all measurements (see Figs. 3.4, 3.5). Because not all lines were present or suitable for fits in all stars, the number of fitted lines differs. In some cases the line list has been modified and lines were included or excluded manually after visual inspection. All outputs of the pipeline have been checked by visual inspection.

3.4 Systematic errors in the determination of the projected rotational velocity from metal lines

Since the velocities measured from the metal lines were low, a correct treatment of the errors was crucial. For this, synthetic spectra with fixed rotational broadening were computed and convolved with the instrumental profile. A standard list of metal lines and average sdB parameters ($T_{\mathrm{eff}} = 30\,000\,\mathrm{K}$, $\log g = 5.50$) were adopted. Random noise was added to mimic the observed spectra. Now the rotational broadening was measured in the way described above using a grid of synthetic spectra with different rotational and instrumental broadenings as well as S/N levels.

Variations in the instrumental profile (up to $1.0\,\mathrm{km s^{-1}}$ for bad S/N and seeing, about $0.5\,\mathrm{km s^{-1}}$ in case of high S/N and good seeing) and the noise level ($2 - 6\,\mathrm{km s^{-1}}$ per line dependent of S/N which has to be divided by $\sqrt{N_{\mathrm{lines}}}$ to get the average error) were the dominant error sources.

Because a wide slit was used for the UVES spectra, the instrumental profile was seeing dependent. The seeing of all single exposures was measured with the DIMM seeing monitor at Paranal Observatory and taken from the ESO science archive (Sarazin & Roddier 1990).
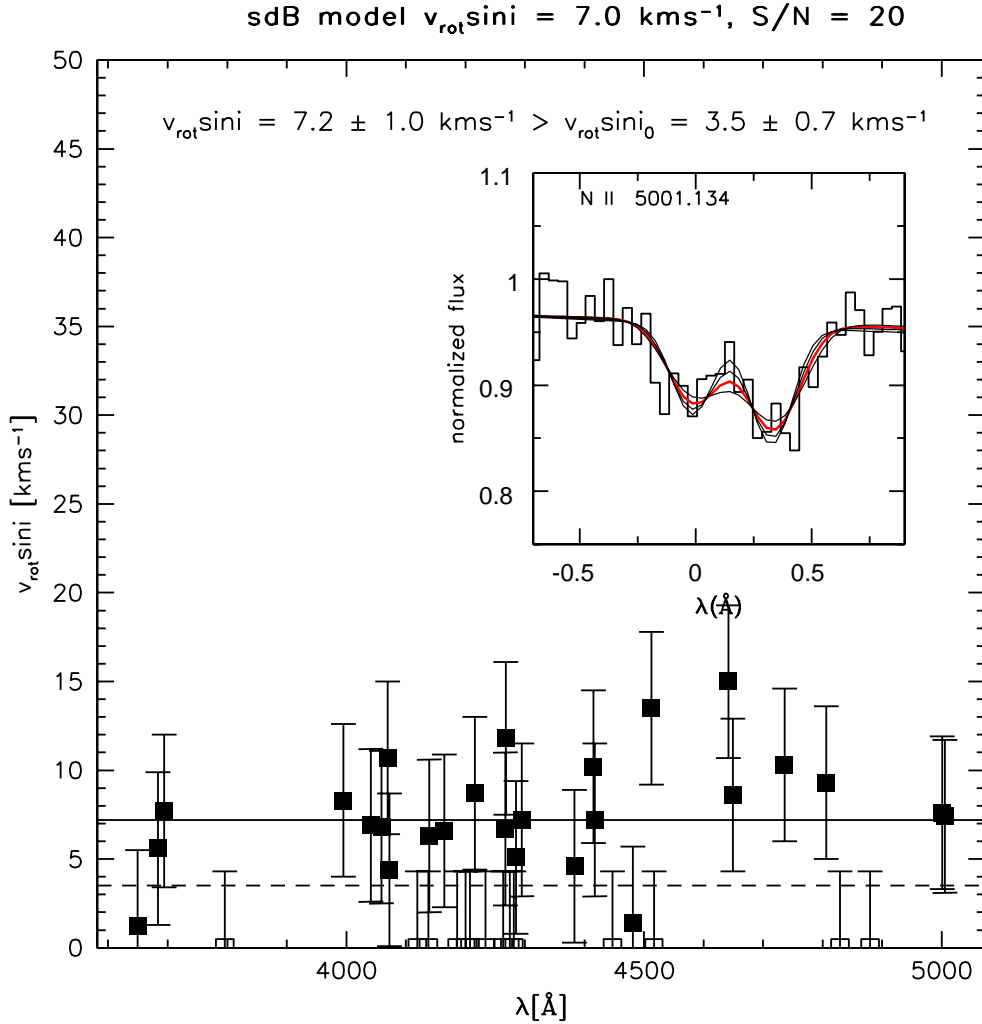
Figure 3.3: Fit result for a standard sdB model ($T_{\mathrm{eff}} = 30\,000\,\mathrm{K}$, $\log g = 5.50$) with a rotational broadening of $7.0\,\mathrm{kms}^{-1}$. Instrumental profile and noise ($S/N = 20$) were added. The wavelength of the analysed lines is plotted against the measured $v_{\mathrm{rot}}\sin i$. The dashed line corresponds to the average including the zero values (empty squares) of $3.5\,\mathrm{kms}^{-1}$, which is systematically lower than the true rotational broadening. Rejection of the zero values leads to a proper result (solid line) of $7.2\,\mathrm{kms}^{-1}$. The accuracy is remarkable given the poor S/N and the mediocre fit of the N II doublett shown in the upper right corner. The thick solid line is the best fit $v_{\mathrm{rot}}\sin i$. The three thin lines correspond to fixed rotational broadenings of $0, 5, 10\,\mathrm{kms}^{-1}$.

The DIMM seeing was consistent with the width of the echelle orders. The error in these measurements is considered to be lower than the change of seeing during the exposures (up to 0".2). For the HIRES and Palomar spectra a seeing of 1".0 was assumed, because no information about the actual conditions were available. The resolution of the spectra taken with the fiber spectrographs FEROS, FOCES and HET/HRS was assumed as constant.

Changes in the instrumental resolution because of temperature variations and for other
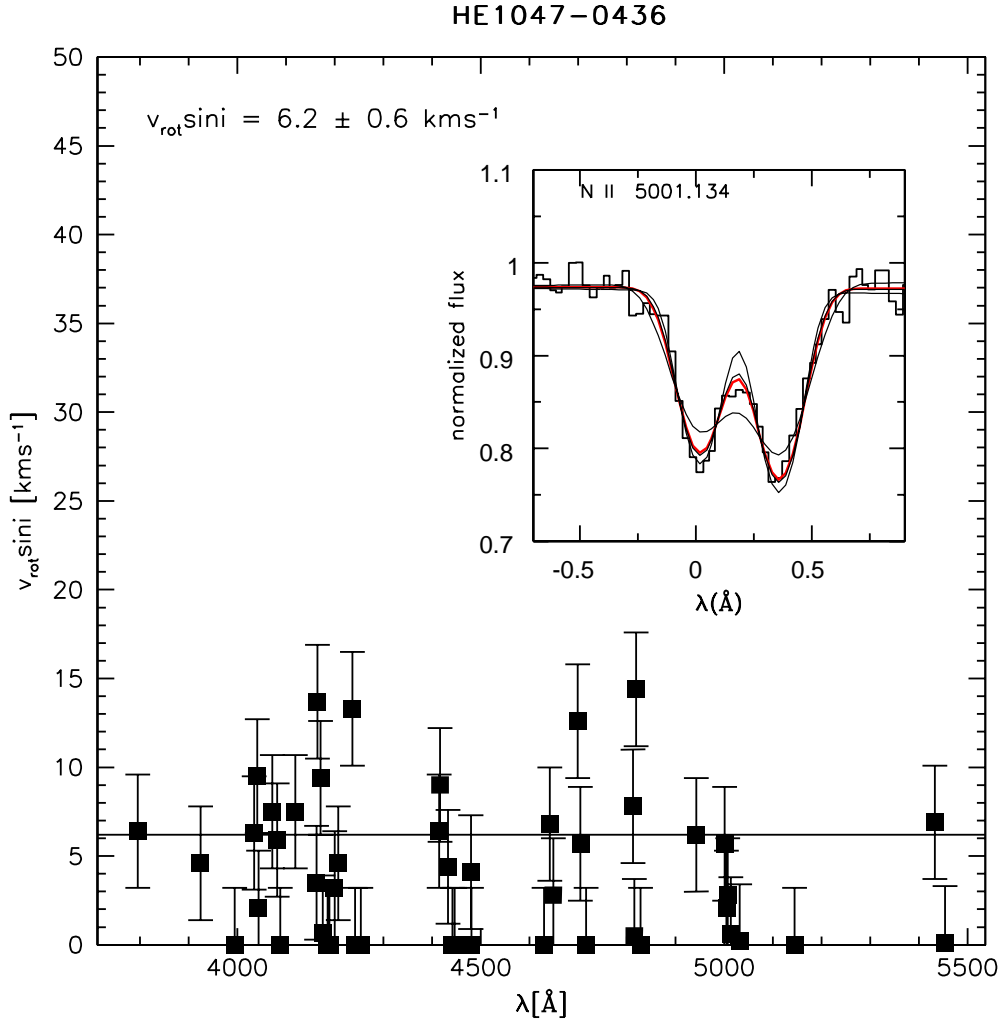
Figure 3.4: Fit result for HE 1047−0436 (see Fig. 3.3)

reasons were considered as negligible. A variation of the atmospheric parameters within the derived error limits gives an error of $0.2\,\mathrm{kms^{-1}}$ and is therefore negligible, too.

Due to noise effects some lines were measured to be not rotationally broadened at all. Because the metal lines are weak, single noise peaks can significantly disturb the spectra. If for example a noise peak sits on the right wing of the line while the left wing is undisturbed, the fit routine will find an optimum solution with respect to the whole line. This means the effect of the noise peak will be weakened. But if the peak sits near the line core, there is no symmetric and undisturbed counterpart. So the effect is more significant and in case of very low rotation leads to a zero measurement. Simulations with model spectra showed that negative peaks which fill the line core have much less effect. The measured $v_{\mathrm{rot}} \sin i$ is of course slightly higher, but in this case the wings get more important for fit quality and the influence of the noise peak is weakened. This explains the assymmetric distribution of measured $v_{\mathrm{rot}} \sin i$ with more zero outliers than ones with high $v_{\mathrm{rot}} \sin i$.
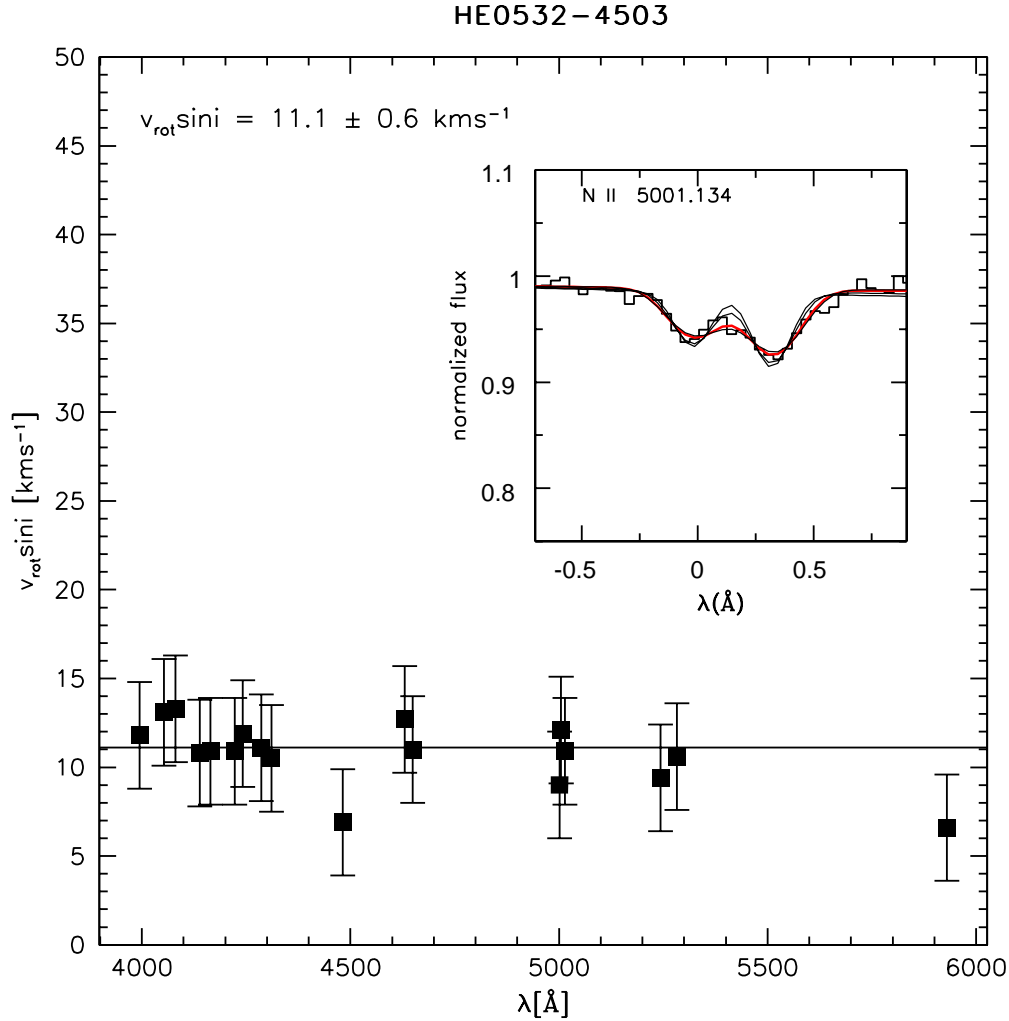
Figure 3.5: Fit result for HE 0532−4503 (see Fig. 3.3).

That is why including these zero values in the calculation of the mean led to a systematic shift of $v_{\mathrm{rot}}\sin i$ to lower values (see Fig. 3.3). For this reason all zero values were excluded and the artificial rotational broadening could be measured properly. As the lower limit for this method we derived $v_{\mathrm{rot}}\sin i > 4.5\,\mathrm{kms}^{-1}$. If more than two thirds of the lines were measured to zero, a projected rotational velocity lower than $4.5\,\mathrm{kms}^{-1}$ was adopted.

The FITSB2 routine allows us to fit a lot of lines simultaneously and to use different methods of calculating the fitting error (e.g. bootstrapping). In principle it is possible to measure the rotational broadening from all lines simultaneously and derive the error. But in practice this approach is problematic. The problem of fitting up to 25 parameters (24 abundances and $v_{\mathrm{rot}}\sin i$) can be circumvented when using a grid of model spectra with relative abundance scale (e.g. relative to solar) as long as no blends of lines from different elements are fitted. But it is still a very demanding task in terms of computer power to fit up to more than 50 lines simultaneously and derive the error using a bootstrapping algorithm. To compare this approach

with our method we fitted up to nine lines of a synthetic spectrum with noise, rotational and instrumental broadening added simultaneously. The bootstrap error was consistent with the error we derived with the method described above. Furthermore our error estimate turned out to be slightly higher, which makes our approach more conservative.

Recently Berger et al. (2005) estimated the influence of applying a wavelength dependent limb darkening law on the measurements of projected rotational velocities in DAZ white dwarf spectra from SPY. In case of the Ca II K lines they used, a small difference in the line cores was found. Nevertheless, the systematic deviation in $v_{\rm rot} \sin i$ was lower than $1\,{\rm km s}^{-1}$. Because systematic errors caused by this effect would lead to higher real projected rotational velocities than measured, the influence of a wavelength dependent limb darkening law on our results was tested as well. We found the effect to be even lower, because the analysed metal lines are much weaker than the Ca II K lines used by Berger et al. (2005) and the effect becomes more significant for stronger lines. A limb darkening law independent of wavelength is therefore appropriate for our analysis.

No significant microturbulence could be measured which is consistent with the analysis of Edelmann (2005a). Unconsidered effects would in any case cause an extra broadening of the lines and therefore a lower projected rotational velocity than measured. This fact is important for the interpretation of the results and will be discussed in detail in Sect. 3.9.

3.5 Measuring high projected rotational velocities from hydrogen and helium lines

In short period binaries the sdB is spun up by the tidal interaction with the companion. In this case the projected rotational velocity can get larger than $100\,{\rm km s}^{-1}$. This leads to a strong broadening of the metal lines, which eventually melt into the continuum. Our simulations revealed that in spectra with S/N values typical for our data the metal lines can be used to measure $v_{\rm rot} \sin i$-values up to about $25\,{\rm km s}^{-1}$. To measure higher projected rotational velocities from metal lines very high quality spectra are needed.

Due to stronger pressure broadening Balmer and helium lines are less sensitive to rotational broadening than metal lines. From our simulations we derive detection limits of $v_{\rm rot} \sin i \approx 15\,{\rm km s}^{-1}$ for helium lines and $v_{\rm rot} \sin i \approx 25\,{\rm km s}^{-1}$ for the Balmer line cores given an $S/N \approx 100$. For lower quality data these limits go up significantly. At typical S/N values of our data the Balmer and helium get sensitive at $v_{\rm rot} \sin i \approx 50\,{\rm km s}^{-1}$.

To measure the $v_{\rm rot} \sin i$ of such short period binaries we calculated LTE model spectra with the appropriate atmospheric parameters (see references in Tab. 3.5) and performed a simultaneous fit of rotational broadening and helium abundance to all usable Balmer line cores and helium lines using the FITSB2 routine (Napiwotzki et al. 2004b, see Sect. 3.7). All systematic effects discussed in the last section become negligible in this case. The quoted uncertainties are 1σ-χ^2-fit errors.

3.6 Rotation of sdBs in close binaries

Projected rotational velocities of 49 close binary subdwarfs have been measured (Tabs. 3.1, 3.2). Two measurements were taken from literature (Tab. 3.3). As can be seen in in Fig. 3.6 the $v_{\rm rot} \sin i$-distribution of the RV variable sdBs (Tabs. 3.1, 3.2, 3.3) differs from the uniform

Table 3.1: Projected rotational velocities of 19 close binary sdBs from SPY. [c] Companion visible in the spectrum †Preliminary result

	m_B [mag]	S/N	seeing [arcsec]	N_{lines}	$v_{\text{rot}} \sin i$ [kms^{-1}]
HE 0230−4323	13.8	59	0.9	40	12.7 ± 0.7†
HE 0532−4503	16.1	83	0.8	65	11.1 ± 0.6
HE 0929−0424	15.4	25	0.6	9	7.1 ± 1.0
HE 1033−2353	16.0	13	0.6	7	9.3 ± 2.3
HE 1047−0436	14.7	37	0.6	37	6.2 ± 0.6
HE 1140−0500^c	14.8	18	0.9	5	5.2 ± 2.7
HE 1309−1102^c	16.1	7	0.6	7	7.6 ± 2.3
HE 1421−1206	15.1	21	0.5	18	6.7 ± 1.1
HE 1448−0510	15.0	27	0.6	8	7.2 ± 1.7
HE 2135−3749	13.7	84	1.0	53	6.9 ± 0.5
HE 2150−0238	15.8	27	0.8	16	8.3 ± 1.5
HE 2208+0126	15.6	24	0.8	15	< 5.0
HE 2322−4559^c	15.5	23	0.7	16	10.9 ± 1.1
HS 1536+0944^c	15.6	19	1.1	15	12.2 ± 1.6
HS 2043+0615	16.0	22	1.3	26	12.3 ± 1.1
HS 2357+2201	13.3	29	0.7	26	6.1 ± 1.1
HS 2359+1942	14.4	14	0.6	26	< 5.0
WD 0048−202	15.1	24	0.6	16	7.2 ± 1.3
WD 0107−342	14.7	43	1.1	24	20.4 ± 0.9

distribution of the single stars (Fig. 7.1 further discussed in Chap. 7). A large fraction of binary sdBs exceeds the derived maximum $v_{\text{rot}} = 8.3\,\text{kms}^{-1}$ significantly. The most likely reason for this is tidal interaction with the companion. For close binary systems, the components' stellar rotational velocities are considered to become tidally locked to their orbital motions, which means that the orbital period of the system equals the rotational period of the companions. The $v_{\text{rot}} \sin i$-distribution shown here is a clear indication for tidal interaction within the binary system.

3.7 Determination of the surface gravity and systematic errors

Since the precise determination of the atmospheric parameters, especially the surface gravity, is of utmost importance for our analysis, this section is devoted to the systematic uncertainties dominating the determination of these parameters. Spectra of sdB stars in the literature were analysed either with metal line-blanketed LTE model atmospheres or with NLTE model atmospheres neglecting metal line blanketing altogether. As pointed out by Heber et al. (2000) and Heber & Edelmann (2004), systematic differences between these two approaches are present. Most importantly the gravity scale differs by about 0.06 dex.

Table 3.2: Projected rotational velocities of 30 radial velocity variable sdBs from the bright star sample. For binaries with high $v_{\mathrm{rot}} \sin i$ helium lines and Balmer lines cores (H/He) are used instead of metal lines.

	m_B [mag]	S/N	N_{lines}	$v_{\mathrm{rot}} \sin i$ [kms^{-1}]	Instrument
BPS CS 22169−0001	12.6	109	5	8.5 ± 1.5	FEROS
CD -24 731	11.6	42	8	12.1 ± 1.7	FEROS
CPD −64 481	11.0	152	38	4.1 ± 0.5	FEROS
Feige 48	13.1	37	36	8.5 ± 0.8	HIRES
HD 171858	9.6	90	55	6.7 ± 0.5	FEROS
HS 0705+6700	14.2	28	H/He	158 ± 12	HRS
HW Vir	10.3	130	H/He	78.3 ± 1.0	FEROS
JL 82	12.2	55	57	10.4 ± 0.6	FEROS
KPD 1946+4340	14.1	55	H/He	41.7 ± 1.2	HRS
PB 7352	12.0	61	39	7.4 ± 0.7	FEROS
PG 0001+275	12.8	129	24	12.6 ± 0.8	FOCES
PG 0101+039	11.8	99	17	10.9 ± 1.1	FOCES
PG 0133+114	10.7	194	17	5.9 ± 0.8	FOCES
PG 1032+406	10.8	20	H/He	24.0 ± 10.0	Palomar
PG 1043+760	13.4	15	H/He	73.5 ± 14.4	Palomar
PG 1101+249	12.5	66	24	8.1 ± 0.8	HIRES
PG 1116+301	14.3	42	8	9.0 ± 1.7	HRS
PG 1232−136	13.1	37	40	6.2 ± 0.8	FEROS
PG 1248+164	14.4	47	13	8.9 ± 1.3	HRS
PG 1336−018	14.0	40	H/He	74.6 ± 2.3	FEROS
PG 1329+159	13.3	52	26	10.7 ± 0.9	HRS
PG 1432+159	13.6	50	22	9.5 ± 1.0	HRS
PG 1512+244	13.0	87	17	6.3 ± 0.9	HRS
PG 1627+017	11.3	64	11	5.7 ± 1.3	HRS
PG 1716+426	13.7	61	24	10.9 ± 0.9	HRS
PG 1725+252	12.8	55	17	7.6 ± 1.1	HRS
PG 1743+477	13.6	57	27	<5.0	HRS
TON S 135	13.1	47	35	6.6 ± 0.8	FEROS
TON S 183	12.4	55	57	6.7 ± 0.7	FEROS
UVO 1735+22	11.5	230	H/He	45.0 ± 1.0	FOCES

Table 3.3: Projected rotational velocities of two radial velocity variable sdBs from literature.

	$v_{\rm rot} \sin i$ [kms^{-1}]	Reference
KPD 1930+2752	92.3 ± 1.5	Geier et al. 2007
PG 1017+086	118 ± 5	Maxted et al. 2002

Geier et al. (2007) investigated the influence of using different model grids to determine the atmospheric parameters of the sdOB+WD binary KPD 1930+2752. New grids of models and synthetic spectra were calculated to account for NLTE effects and metal line blanketing simultaneously. Since the temperature/density structure of an sdB atmosphere is only slightly affected by NLTE effects (if at all), the LTE approximation is valid to this end. NLTE effects may become more important for the line formation of Balmer and helium lines. Therefore, a "hybrid" approach was chosen by calculating the temperature/density stratification from metal line-blanketed LTE model atmospheres and then performing line formation calculations for hydrogen and helium, allowing for departures from LTE (Przybilla et al. 2006). Both of the Kurucz codes, ATLAS9 and ATLAS12, were used to calculate metal line-blanketed model atmospheres (Kurucz 1993, 1996). The coupled statistical equilibrium and radiative transfer equations were solved and spectrum synthesis with refined line-broadening theories was performed using DETAIL and SURFACE (Giddings 1981; Butler & Giddings 1985). Both codes have undergone major revisions and improvements over the past few years. State-of-the-art NLTE model atoms for hydrogen and helium were utilised (Przybilla & Butler 2004; Przybilla 2005).

The Stark broadening of hydrogen lines is important for determining temperature and gravity. Up to now all spectral analyses of sdB stars have used synthetic Balmer-line spectra based on the unified theory of Vidal, Cooper & Smith (1973, VCS) with the improvements of Lemke (1997). Since new broadening tables for Balmer lines have become available (Stehlé & Hutcheon 1999, SH), also synthetic spectra were calculated from these tables to investigate systematic effects on the synthetic spectra.

A medium resolution and high S/N spectrum was analysed with the FITPROF routine by means of an χ^2 fit (Napiwotzki 1999). Rotational broadening was accounted for by choosing an appropriate value for the projected rotational velocity. The formal statistical errors were small, i.e. $\Delta T_{\rm eff} \approx 100 \, {\rm K}, \Delta \log g \approx 0.005 \, {\rm dex}, \Delta \log \frac{n({\rm He})}{n({\rm H})} \approx 0.005 \, {\rm dex}$. However, systematic errors due to inaccuracies in the model atmospheres and synthetic spectra are much larger. To investigate this the different grids of models described above were used to determine the atmospheric parameters.

Simultaneous fits of the hydrogen and some helium lines (He I 4026 Å, He II 5412 Å and in particular He II 4686 Å) were performed with different model grids: The metal line-blanketed LTE model atmosphere grids of O'Toole & Heber (2006) (Fit A in Table 3.4), high-metallicity models (Fit B in Table 3.4, see Fig. 3.7), the new grid of hybrid models that account for both metal line blanketing and departures from LTE using ATLAS9 with supersolar metallicity (labelled C in Table 3.4).

Then the influence of Balmer line broadening was checked by using synthetic spectra calculated from ATLAS9 models, 10 times solar metallicity with the hybrid approach and SH
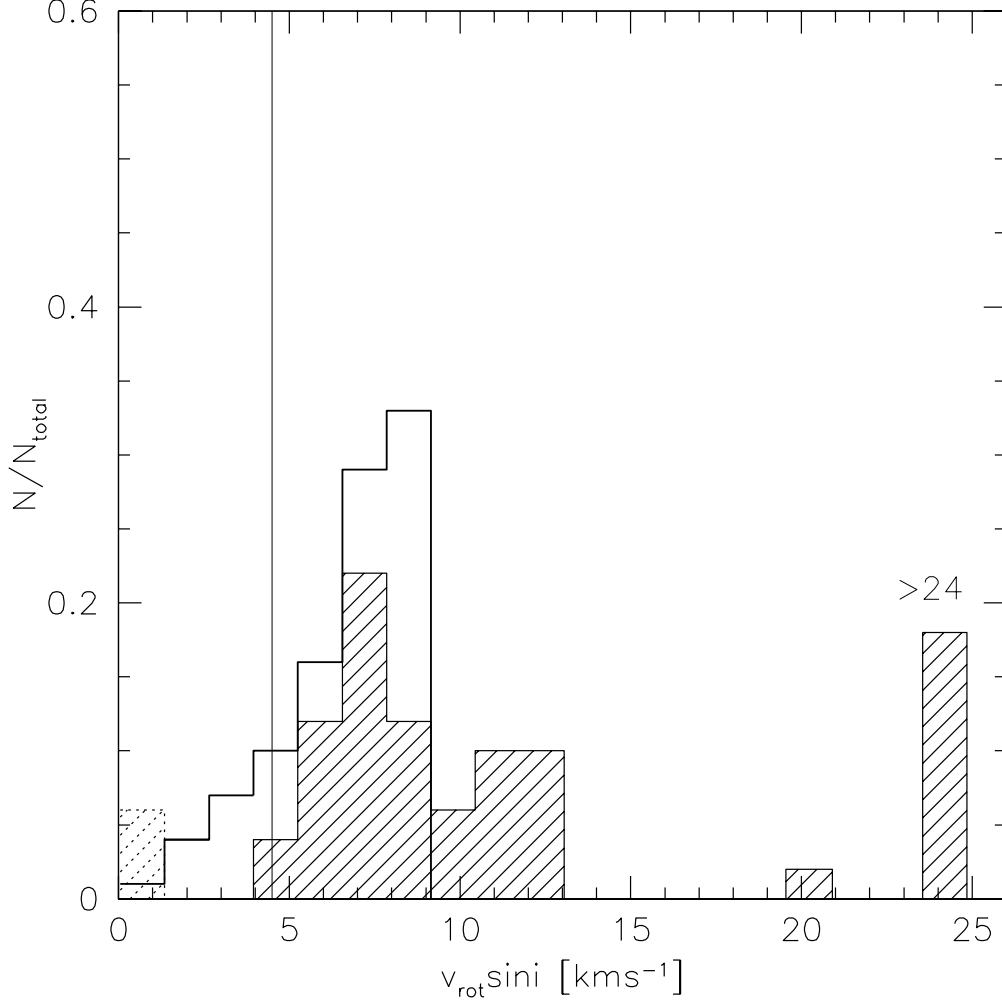
Figure 3.6: The measured $v_{\rm rot} \sin i$ of 51 RV variable sdBs is plotted against relative fraction of stars as shaded histogram. The size fo the bins is given by the average error of the measurements and is therefore slightly different than in Fig. 7.1. The blank histogram marks the expected uniform distribution of $v_{\rm rot} \sin i$ under the assumption of randomly oriented polar axes and the same rotational velocity $v_{\rm rot} = 8.3\,{\rm kms}^{-1}$ for all stars. The solid vertical line at $v_{\rm rot} \sin i \approx 4.5\,{\rm kms}^{-1}$ marks the detection limit. All sdBs with lower $v_{\rm rot} \sin i$ are stacked into the first bin (dotted histogram). All sdBs with $v_{\rm rot} \sin i$ higher than $24\,{\rm kms}^{-1}$ are summed up in the last bin.

broadening tables instead of VCS tables (Fit D in Table 3.4). Finally ATLAS9 was replaced by ATLAS12 and the analysis repeated (Fit E in Table 3.4) using the same approach as in the previous step.

The resulting parameters from the different grids are summarised in Table 3.4. As can be seen, systematic effects on the effective temperature are small, as models A to E differ by 530 K or less. The gravities, however, differ by as much as 0.12 dex. The "hybrid" models yield a gravity that is 0.06 dex higher than do the LTE models for supersolar metal content. The replacement of
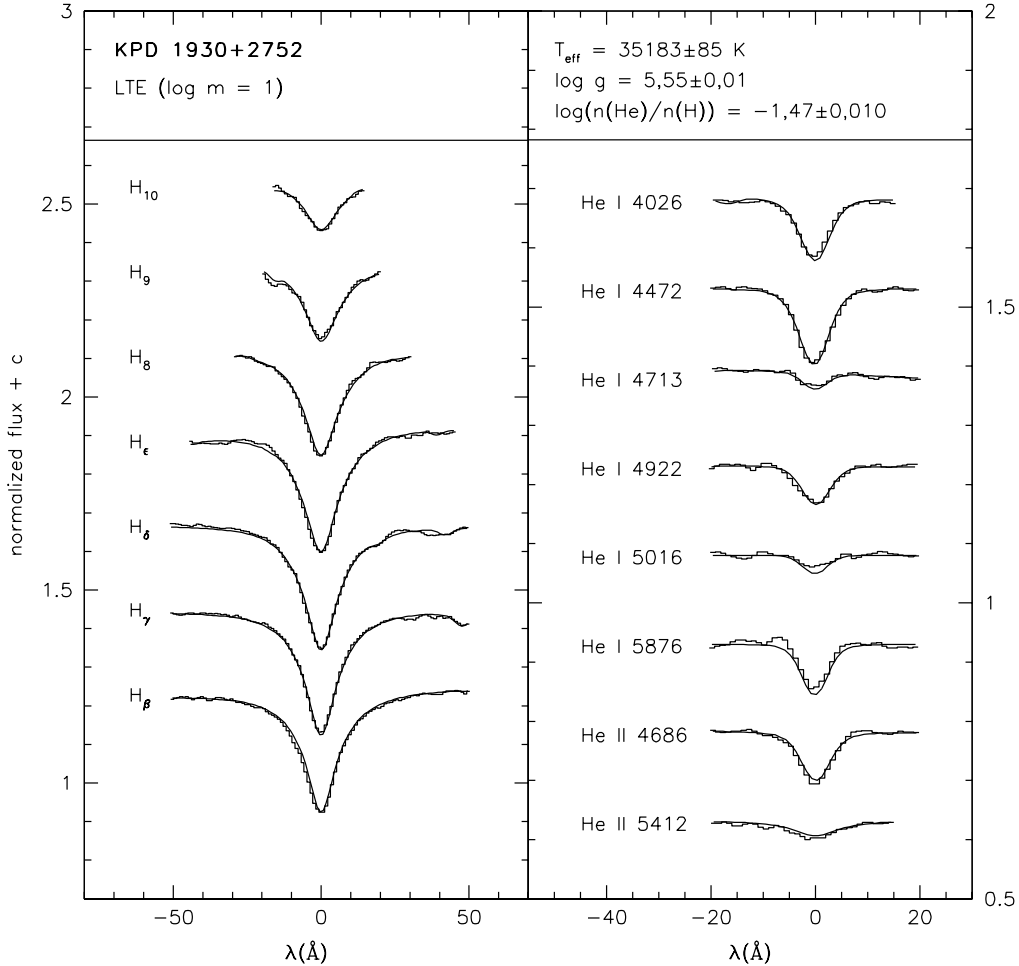
Figure 3.7: Example fit of LTE model spectra to Balmer and helium lines of KPD 1930+2752. Plot taken from Geier et al. (2007).

the VCS tables by SH tables systematically increases gravity by another 0.06 dex. It is possible that part of the shift is explained by differences in table organisation and interpolation (Lemke 1997). It is impossible to judge which of the models in Table 3.4 is preferable.

It has to be pointed out that since KPD 1930+2752 is a short period pulsating, fast rotating and relatively hot sdOB star, these systematic errors should be regarded as upper limits. The atmospheric parameters of our programme stars are taken from literature and were derived in most cases by fitting LTE models (Tab. 3.5). The adopted errors in $\log g$ are between $0.04 - 0.07$ dex. The error in surface gravity starts to dominate the error budget of the derived parameters as soon as the error in $v_{\mathrm{rot}} \sin i$ drops below about $1.0 \, \mathrm{kms}^{-1}$. Atmospheric parameters of PG 1232−136, TON S 183, PG 1336−018 and PG 1627+017 have been determined by fitting model spectra in the way described above. LTE models with solar metallicity have been used.

Table 3.4: Atmospheric parameters of KPD 1930+2752 derived from model atmosphere fits, where A12=Kurucz ATLAS12 code, VCS=Vidal, Cooper & Smith (1973), SH=Stehlé & Hutcheon (1999), lf=line formation. Taken from Geier et al. (2007)

	model	$[m/H]$	T_{eff}	$\log g$	$\log \frac{n(\mathrm{He})}{n(\mathrm{H})}$
A	LTE VCS	0	35 720 K	5.67	-1.56
B	LTE VCS	+1	35 183 K	5.55	-1.47
C	NLTE (lf) VCS	+1	35 353 K	5.61	-1.50
D	NLTE (lf) SH	+1	35 212 K	5.67	-1.51
E	NLTE (lf) SH A12	+1	35 712 K	5.67	-1.58
	adopted		35 200 K	5.61	-1.50
			± 500	± 0.06	± 0.02

3.8 Constraining masses and nature of the unseen companions

Derived inclinations, subdwarf and possible companion masses are given in Tab. 3.6. If the mass could not be constrained with alternative methods (see Tab. 3.6 references) the theoretically predicted mass range was taken from Han et al. (2002, 2003). From 41 sdB binaries, for which all necessary parameters have been determined, 32 could be solved consistently under the assumption of synchronisation. In nine cases the derived minimum sdB masses exceeded the reasonable mass range. This means that the sdB primaries spin faster than synchronised. It has to be pointed out that only subdwarfs rotating faster than synchronised can be found in this way. If an sdB should rotate slower than synchronised, one would always get a consistent solution with higher companion mass, which would of course be wrong.

3.8.1 Low mass companions - White dwarfs, M stars, brown dwarfs

Eleven of the analysed systems have companion masses, which are compatible with either white dwarfs (WD) or late M dwarfs (MS) (see e.g. Fig. 3.8). Adopting the canonical sdB mass, five of them must have WD companions because no lines from cool companions are visible. In six cases, the minimum mass derived under the assumption of synchronisation is higher than the lower limit of $0.3\,M_\odot$ for helium core burning. Should the subdwarfs in these binaries have masses that low, the binaries could be eclipsing. For **PG 1512+244** the derived minimum mass is $0.5\,M_\odot$, close to the canonical value. If the assumption of tidal synchronisation is correct, this system should be eclipsing. The same is true for **PG 1116+301** where an inclination of 90° is derived for all possible subdwarf masses. Follow-up photometry with long time base is needed to check these predictions, since the orbital periods of both binaries are rather long (1.27 d and 0.86 d see Tab. 3.5).

The companion mass ranges of **PG 1248+164, JL 82, PG 1116+301** and **HE 1421−1206** are very low ($0.15-0.3\,M_\odot$). If the companions should be WDs their masses could be low enough for them to belong to the recently discovered class of Extremely Low Mass (ELM) WDs (see Kilic et al. 2007 for a review). Binary interaction with neutron star companions is discussed as formation channel for these objects. The discovery of sdB+ELM-WD binaries would require a different explanation. Unfortunately it is not possible to distinguish between WD and late MS

Table 3.5: Stellar parameters: Effective temperatures, surface gravities, orbital periods, radial velocity semi-amplitudes, and system velocities of the visible components. The parameters are taken from [1]Drechsel et al. (2001), [2]Edelmann (2003), [3]Edelmann et al. (2005a), [4]Edelmann (2008), [5]Geier et al. (2007), [6]Geier et al. (2008), [7]Heber (1986), [8]Lisker et al. (2005), [9]Maxted et al. (2001), [10]Maxted et al. (2002), [11]Morales-Rueda et al. (2003), [12]Moran et al. (1999), [13]Napiwotzki et al. (2001), [14]Napiwotzki et al. (in prep.), [15]O'Toole et al. (2004), [16]O'Toole & Heber (2006), [17]Saffer et al. (1998), [18]Vučković et al. (2007) and this work[19]: The orbital parameters of WD 0107−342 are derived in Sect. 2.3.2, the parameters of PG 0101+039 in Sect. 4.4.1. Atmospheric parameters of PG 1232−136, TON S 183, PG 1336−018 and PG 1627+017 have been determined by fitting model spectra. The method is described in Sect. 3.7 and Geier et al. (2007).

System	T_{eff} [K]	$\log g$	P [d]	K [km s^{-1}]	γ [km s^{-1}]
PG 1017−086[10]	30300	5.61	0.0729938 ± 0.0000003	51.0 ± 1.7	-9.1 ± 1.3
KPD 1930+2752[5]	35200	5.61	0.0950933 ± 0.0000015	341.0 ± 1.0	5.0 ± 1.0
HS 0705+6700[1]	28800	5.40	0.09564665 ± 0.00000039	85.8 ± 3.7	-36.4 ± 2.9
PG 1336−018 [18,19]	31300	5.61	0.101015999 ± 0.00000001	78.7 ± 0.6	-25
HW Vir[2,4]	28500	5.63	0.115 ± 0.0008	84.6 ± 1.1	-13.0 ± 0.8
PG 1043+760[9,11]	27600	5.39	0.1201506 ± 0.00000003	63.6 ± 1.4	24.8 ± 1.4
BPS CS 22169−0001[2,3]	39100	5.43	0.1780 ± 0.00003	14.9 ± 0.4	2.8 ± 0.3
PG 1432+159[10,12]	26900	5.75	0.22489 ± 0.00032	120.0 ± 1.4	-16.0 ± 1.1
PG 1329+159[9,11]	29100	5.62	0.249699 ± 0.0000002	40.2 ± 1.1	-22.0 ± 1.2
HE 0532−4503[8,14]	25400	5.32	0.2656 ± 0.0001	101.5 ± 0.2	8.5 ± 0.1
CPD −64 481[3,16]	27500	5.60	0.2772 ± 0.0005	23.8 ± 0.4	94.1 ± 0.3
PG 1101+249[12,17]	29600	5.82	0.35386 ± 0.00006	134.6 ± 1.3	-0.8 ± 0.9
PG 1232−136[3,19]	27500	5.62	0.3630 ± 0.0003	129.6 ± 0.04	4.1 ± 0.3
Feige 48[15,16]	29500	5.54	0.376 ± 0.003	28.0 ± 0.2	-47.9 ± 0.1
WD 0107−342[8,19]	24300	5.32	0.37765 ± 0.00002	129.5 ± 1.9	25.0 ± 1.6
KPD 1946+4340[11]	34500	5.37	0.403739 ± 0.0000008	156.0 ± 2.0	-5.5 ± 1.0
HE 0929−0424[8,14]	29500	5.71	0.4400 ± 0.0002	114.3 ± 1.4	41.4 ± 1.0
HE 0230−4323[8,4]	31100	5.60	0.45152 ± 0.00002	62.4 ± 1.6	16.6 ± 1.0
PG 1743+477[9,11]	25500	5.41	0.515561 ± 0.0000001	121.4 ± 1.0	-65.8 ± 0.8
PG 0001+275[2,3]	25400	5.30	0.529842 ± 0.0000005	92.8 ± 0.7	-44.7 ± 0.5
PG 0101+039[6]	27500	5.54	0.569899 ± 0.000001	104.7 ± 0.4	7.3 ± 0.2
PG 1725+252[9,11]	28900	5.54	0.601507 ± 0.0000003	104.5 ± 0.7	-60.0 ± 0.6
PG 1248+164[9,11]	26600	5.68	0.73232 ± 0.000002	61.8 ± 1.1	16.2 ± 1.3
JL 82[2,3]	25000	5.02	0.73710 ± 0.00005	34.6 ± 1.0	-1.6 ± 0.8
TON S 183[3,19]	26100	5.20	0.8277 ± 0.0002	84.8 ± 1.0	50.5 ± 0.8
PG 1627+017[11,19]	23500	5.40	0.829226 ± 0.0000008	73.6 ± 0.9	-43.7 ± 0.5
PG 1116+301[9,11]	32500	5.85	0.85621 ± 0.000003	88.5 ± 2.1	-0.2 ± 1.1
HE 2135−3749[8,14]	30000	5.84	0.9240 ± 0.0003	90.5 ± 0.6	45.0 ± 0.5
HE 1421−1206[8,14]	29600	5.55	1.188 ± 0.001	55.5 ± 2.0	-86.2 ± 1.1
HE 1047−0436[8,13]	30200	5.66	1.21325 ± 0.00001	94.0 ± 3.0	25 ± 3.0

System	$T_{\rm eff}$ [K]	$\log g$	P [d]	K [km s^{-1}]	
PG 0133+114[11]	29600	5.66	1.23787 ± 0.000003	82.0 ± 0.3	-0.3 ± 0.2
PG 1512+244[9,11]	29900	5.74	1.26978 ± 0.000002	92.7 ± 1.5	-2.9 ± 1.0
UVO 1735+22[2,3]	40500	5.45	1.278 ± 0.001	103.0 ± 1.5	20.6 ± 0.4
HE 2150−0238[8,14]	30200	5.83	1.321 ± 0.005	96.3 ± 1.4	-32.5 ± 0.9
HD 171858[2,3]	27700	5.30	1.63280 ± 0.000005	87.8 ± 0.2	62.5 ± 0.1
PG 1716+426[9,11]	27400	5.47	1.77732 ± 0.00001	70.8 ± 1.5	-3.9 ± 0.8
PB 7352[2,3]	25000	5.35	3.62166 ± 0.000005	60.8 ± 0.3	-2.1 ± 0.3
TON S 135[3,7]	25000	5.60	4.122 ± 0.0008	41.4 ± 1.5	-3.7 ± 1.1
CD −24 731[3,16]	35400	5.90	5.85 ± 0.003	63 ± 3	20 ± 5
HE 1448−0510[8,14]	34700	5.59	7.159 ± 0.005	53.7 ± 1.1	-45.5 ± 0.8
WD 0048−202[8,14]	30000	5.50	7.44 ± 0.015	47.9 ± 0.4	-26.5 ± 0.4

companions in this mass and orbital period range. Since two of these stars have high derived inclinations, a photometric search for possible eclipses should be undertaken.

Another remarkable object with high inclination and even lower companion mass $(0.08 - 0.14\,M_\odot)$ is **PG 1043+760**. Due to its short period of 0.12 d a reflection effect should be easily detectable. But Morales-Rueda et al. (2003) report a non-detection of variations in the light curve making it the best candidate for sdB+ELM-WD. Adopting the canonical sdB mass this system could be eclipsing.

The companion of **PG 0101−039** is a white dwarf, because despite the long orbital period of 0.57 d an MS companion could be excluded. The light curve of this binary was taken with the MOST satellite. Instead of a reflection effect the shallowest ellipsoidal deformation ever detected could be verified (see Sect. 4.4.3). The mass of the white dwarf is quite typical.

PG 1017−086 is the sdB binary with the shortest orbital period known to date. Maxted et al. (2002) report the detection of significant reflection and exclude an eclipsing binary. Taking these informations into account, one can constrain the inclination angle to be lower than 74° (no eclipses!) and derive a minimum sdB mass of $0.49\,M_\odot$. The minimum mass of the companion is therefore constrained to $0.07\,M_\odot$. The companion is therefore most likely a brown dwarf (BD) or a very late M dwarf. PG 1017−086 remains the only candidate sdB+BD binary. The two other candidates (**BPS CS 22169−0001** and **CPD −64 481**) published by Edelmann et al. (2005a) have been analysed here and turned out to have very low inclinations and therefore companion masses too high for BDs (see Tab. 3.6).

HS 0705+6700 is an eclipsing sdB+M binary with reflection effect. Drechsel et al. (2001) performed a detailed photometric and spectroscopic analysis of this system and derived an inclination of 84°.4, an sdB mass of $0.483\,M_\odot$ and a companion mass of $0.134\,M_\odot$. Although most of the parameters derived here agree quite well with these results, the minimum sdB mass derived is to high to be consistent with Drechsel et al. (2001). From medium resolution, high S/N spectra Drechsel et al. (2001) derived $v_{\rm rot}\sin i = 110\pm14\,{\rm km s^{-1}}$, consistent with synchronisation and the absolute parameters derived, while our solution is $v_{\rm rot}\sin i = 158\pm12\,{\rm km s^{-1}}$. The most likely reason for this discrepancy is the very limited quality of the spectra taken with HET/HRS.

Much better agreement is reached for **HW Vir**, the prototype eclipsing sdB+M binary, where excellent high resolution spectra were available. Edelmann (2008) recently determined
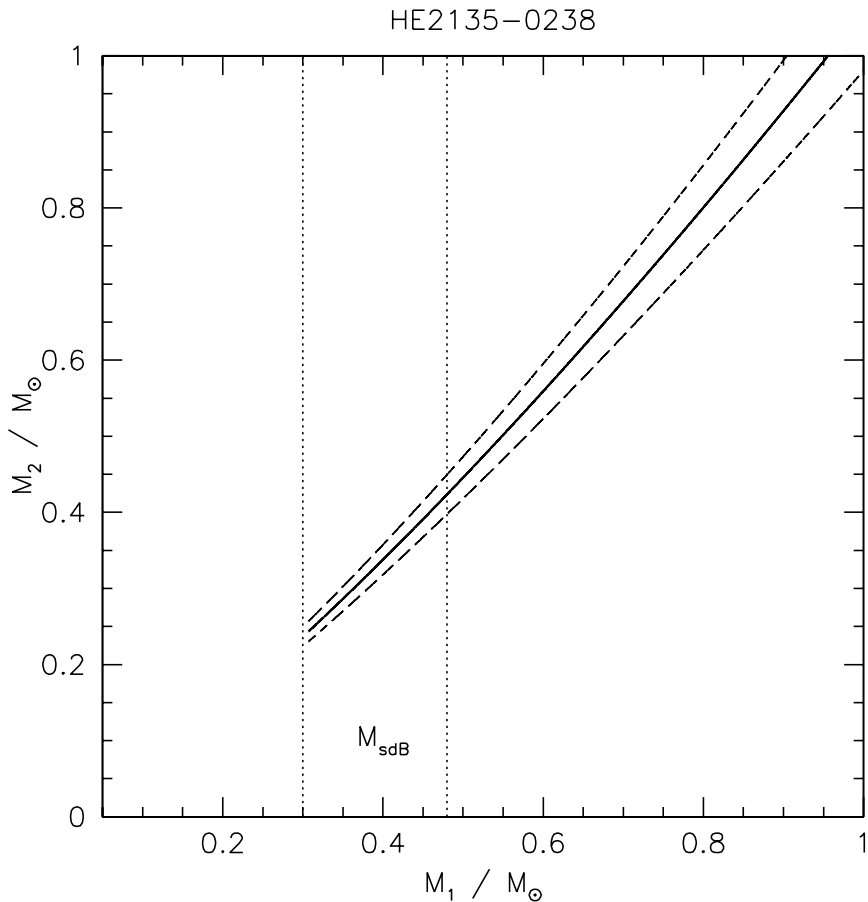
Figure 3.8: Mass of the sdB primary plotted against the mass of the unseen companion. The companion mass error is indicated by the dashed lines. The mass range of the CE ejection channel (Han et al. 2002) is marked with dotted vertical lines.

the absolute parameters of this system spectroscopically using shallow emission lines of the secondary to obtain its RV curve for the first time. Edelmann (2008) derives an sdB mass of $0.53\,M_\odot$ and a companion mass of $0.15\,M_\odot$. With this sdB mass our derivation of the companion mass is in almost perfect agreement $(0.16\,M_\odot)$. The derived inclination angle of $75 \pm 3°$ is close to the photometric solution $80°.6 \pm 0°.2$ given by Wood, Zang & Robinson (1993).

The eclipsing and pulsating sdBV+M binary **PG 1336−018** (NY Vir) has been analysed by Vučković et al. (2008). No unique solution could be found. Due to problems with normalisation and merging of their UVES spectra, they were not able to measure $\log g$ with sufficient accuracy. Therefore we used our new FEROS spectrum to determine the atmospheric parameters by fitting NLTE models: $T_{\text{eff}} = 33\,200\,\text{K}$, $\log g = 5.61 \pm 0.05$. The method is described in Sect. 3.7. While the $\log g$ agrees very well, the temperature derived was about $2\,000\,\text{K}$ hotter than given in Vučković et al. (2008). The derived parameters agree best with the low mass solution of Vučković et al. (2008): Mass of the sdB $0.398\,M_\odot$, companion mass $0.11\,M_\odot$ and inclination angle $80°.7$. With this sdB mass we derive a companion mass of $0.12\,M_\odot$ and an inclination angle of $67 \pm 6°$. For higher subdwarf masses, the inclination would get too low to be compatible
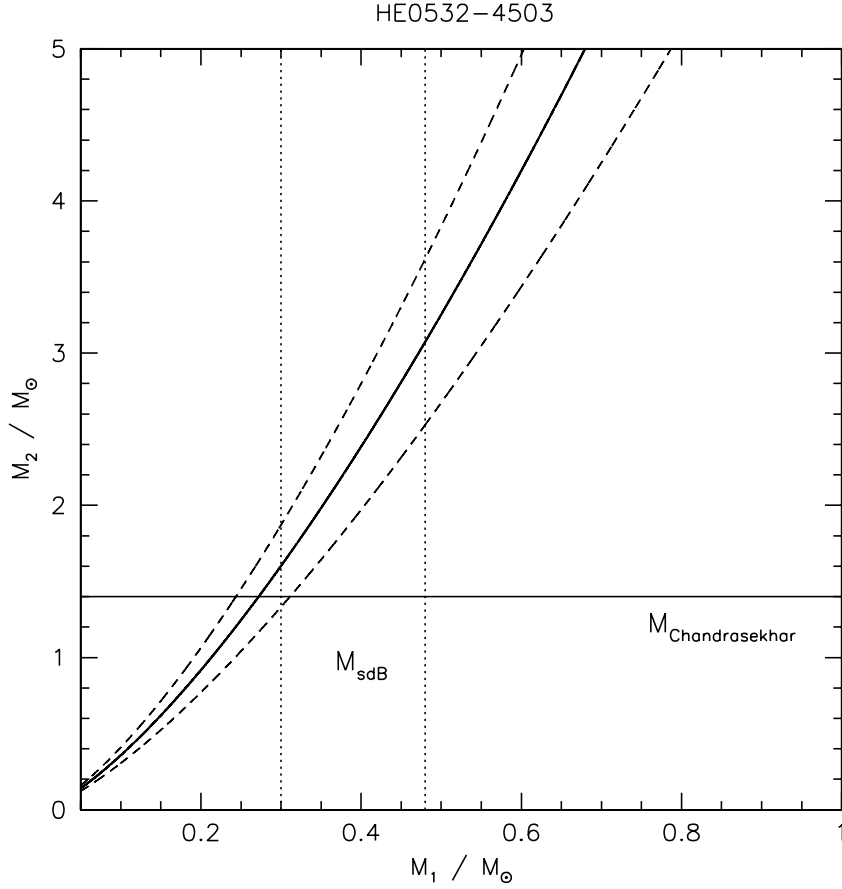
Figure 3.9: Mass of the sdB primary plotted against the mass of the unseen companion. The companion mass error is indicated by the dashed lines. The mass range of the CE ejection channel (Han et al. 2002) is marked with dotted vertical lines.

with an eclipsing binary.

In a most recent asteroseismic study, Charpinet et al. (2008) derived the fundamental parameters of this star by fitting simultaneously the observed pulsation modes. The $\log g = 5.74$ is $0.13\,$dex higher than the value Vučković et al. (2008) and we derive from high resolution spectroscopy. Vučković et al. (2008) reported problems in measuring the surface gravity and the quality of the FEROS spectrum we used to determine the atmospheric parameters was not very good. Furthermore, pulsations and reflection effect can severely influence the atmospheric parameters of a pulsating sdB. Charpinet et al. (2008) used low resolution, high S/N spectra and determined the atmospheric parameters with a NLTE model grid: $T_{\rm eff} = 32\,800\,$K, $\log g = 5.76$. Since low resolution spectra with high S/N are better suited to measure these parameters, these values should be more accurate than the ones derived from high resolution spectra.

Adopting the asteroseismic values for the surface gravity and the sdB mass of $0.459\,M_{\odot}$ for our analysis, the companion mass is $0.12\,M_{\odot}$ and the inclination angle $80 \pm 10°$. This result is in almost perfect agreement with the second solution from Vučković et al. (2008): $M_{\rm sdB} = 0.467\,M_{\odot}$, $M_{\rm comp} = 0.122\,M_{\odot}$, $i = 80°.7$. Charpinet et al. (2008) concluded that the
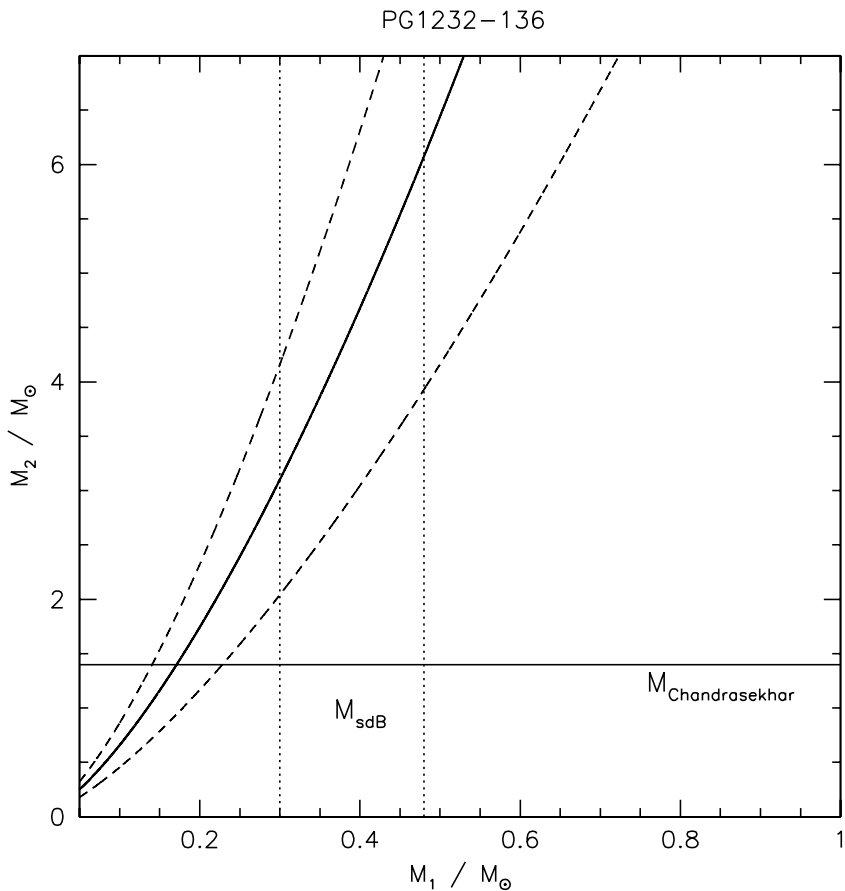
Figure 3.10: Mass of the sdB primary plotted against the mass of the unseen companion. The companion mass error is indicated by the dashed lines. The mass range of the CE ejection channel (Han et al. 2002) is marked with dotted vertical lines.

binary must be synchronised to account for the observed rotational splitting of the pulsation modes and predict a $v_{\rm rot} \sin i = 74.9 \pm 0.6 \, {\rm kms}^{-1}$. This predicted value is perfectly consistent with our measured value of $v_{\rm rot} \sin i = 74.6 \pm 2.3 \, {\rm kms}^{-1}$. However, our measurement was obtained from only one FEROS spectrum with a rather long exposure time of 20 min. Given the short orbital period of this binary, orbital smearing may affect the line broadening depending on the phase where the exposure was taken. Our result can therefore be seen as firm upper limit and the perfect match with theory makes it rather unlikely that orbital smearing is very strong in the spectrum we used.

In the light curves of the three binaries **BPS CS 22169−0001**, **HE 0230−4323** as well as **PG 1329+159** reflection effects have been detected, too (see references in Tab. 3.6). The derived companion mass ranges are consistent with the masses of late M dwarfs. HE 0230−4323 also shows a superimposed strange pattern of strong pulsations, which are currently not understood (Koen 1999). These pulsations may affect the metal line broadening. The measured projected rotational velocity (see Tab. 3.1) should therefore be regarded as preliminary result.

The mass of the pulsating subdwarf in the close binary **Feige 48** has been determined in an

asteroseismic analysis (van Grootel et al. 2008) to $0.52\,M_\odot$. The derived companion mass is $0.27\,M_\odot$. Due to the derived very low inclination a reflection effect is most likely not detectable. Therefore the nature of the unseen companion remains unclear. It may be a low mass WD as well as a late M dwarf.

3.8.2   High mass white dwarf companions - candidates for SN Ia progenitors

The nature of the unseen companion in the binary KPD 1930+2752 could be clarified by Geier et al. (2007). The short period system consists of a synchronously rotating, tidally distorted sdB and a massive WD. The combined mass of the systems reaches the Chandrasekhar limit and the stars will most probably merge in 200 Myr. KPD 1930+2752 is the best double degenerate candidate for SN Ia progenitor so far.

Here we discovered that the companion of **WD 0107−342** (GD 687) is most likely a massive white dwarf since the flux distribution of this star shows no excess in the infrared (Farihi et al. 2005) and the derived mass range is quite high. Compared to KPD 1930+2752, the orbital period of WD 0107−342 is rather long. This leads to a merging time of 9.9 Gyr, which is just a little shorter than the Hubble time. With a total mass of $1.29 \pm 0.11\,M_\odot$ for the most likely subdwarf mass it is consistent with the Chandrasekhar limit of $1.4\,M_\odot$, but placed at the edge of the progenitor parameter space (see Fig. 3.11).

In contrast to KPD 1930+2752, where the primary mass could be tightly constrained by an additional analysis of the subdwarfs ellipsoidal deformation visible as variation in its light curve, no such constraint can be put on the primary mass of WD 0107−342 yet. The subdwarf mass could therefore be lower and the total mass could fall well below the Chandrasekhar limit. Taking into account the evolved status of the sdB near the TAEHB it is also possible that it is not a helium core burning star, but a post-RGB object descending directly towards the WD cooling tracks and just crossing the EHB by chance. Driebe et al. (1998) calculated evolutionary tracks for these He-WD progenitor objects, which give a mass of about $0.25\,M_\odot$ for WD 0107−342 (see Sect. 4.6). Since most empirical mass determinations of sdBs converge at a value near $0.5\,M_\odot$, we nevertheless consider this mass the most likely one. The discovery of two progenitor candidates with subdwarf primaries proves that the sdB binaries are a very well suited population to look for these and similar interesting objects.

From the theoretical point of view, Ergma et al. (2001) questioned the double degenerate scenario in the case of KPD 1930+2752. Their simulations suggest that the merger will lead to a single massive ONeMg white dwarf rather than a supernova explosion. A similar scenario may be possible in the case of WD 0107−342. The merger of two white dwarfs is a rather complicated process compared to slow accretion of material onto a heavy white dwarf. Detailed merger simulations in 3D are urgently needed to learn more about this possible SN Ia progenitor channel. The analysis of double degenerate systems which could qualify as SN Ia candidates like KPD 1930+2752 and WD 0107−342 will help to put constraints on such simulations.

3.8.3   Massive compact companions - Neutron stars or black holes

The most surprising result of this study was that nine subdwarf binaries with heavy companions were discovered (see e.g. Figs. 3.9, 3.10). For all except one (PG 1627+017) of these binaries main sequence companions could be excluded, because they would significantly contribute to the flux or even outshine the subdwarf primary. The massive companions therefore have to be compact objects. In the case of **PG 1432+159, PG 1101+249, HE 0929−0424, PG 1725+252,**
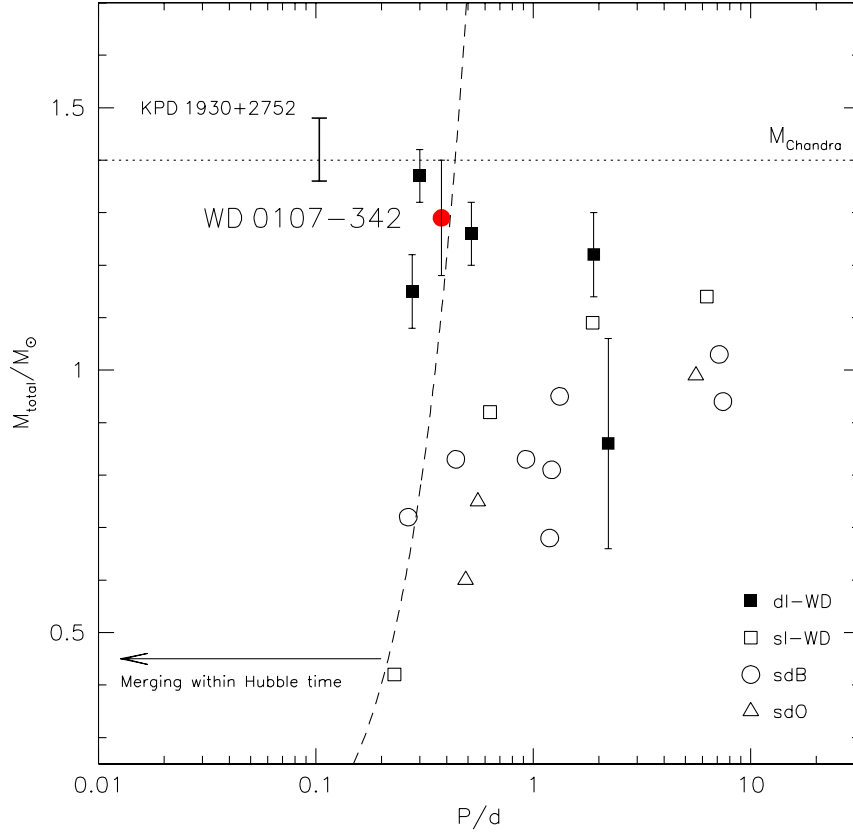
Figure 3.11: Total mass plotted against logarithmic period of double degenerate systems from the SPY survey. WD 0107−342 is marked with the red circle. For KPD 1930+2752 only a mass range is given. The filled rectangles mark double-lined WDs, for which the absolute mass can be derived. The open symbols mark single-lined WDs, sdBs, and sdOs. Only lower mass limits can be derived for these binaries by adopting $\sin i = 1$ (Napiwotzki et al. 2001; Karl 2004; Napiwotzki et al. 2002; Karl et al. 2003).

TON S 183 and **PG 1627+017** the companions could be massive WDs. Adopting the canonical sdB mass the companions exceed the Chandrasekhar mass limit and therefore have to be neutron stars (NS) or even black holes (BH). The unseen companion of **HE 0532−4503** almost reaches the Chandrasekhar limit for the lowest reasonable sdB mass. For higher subdwarf masses the companion has to be a NS or a BH. In the case of **PG 1232−136** and **PG 1743+477** there are no consistent solutions with WD companions at all. PG 1232−136 may have a massive NS or a BH companion. For PG 1743+477 only a lower limit can be given for the companion mass, which is higher than all theoretical NS masses. The companion of this sdB has to be a BH. Adopting the canonical sdB mass the lower limit rises to $> 7.5\,M_\odot$.

Table 3.6: Derived ranges of inclination angles, companion masses and possible nature of the companions. Additional constraints to clarify the nature of the unseen companion: [r]The detection of a reflection effect from a cool MS/BD or a [n]non-detection to exclude this option. The presence of eclipses[ec] or ellipsoidal deformations[el] in the light curves. No signatures of a MS companion within the given mass range are visible in the flux distribution or in the spectrum[f]. These informations are taken from [1]Charpinet et al. (submitted), [2]Drechsel et al. 2001, [3]Edelmann 2008, [4]Farihi et al. 2005, [5]Geier et al. 2007, [6]Geier et al. 2008, [7]Koen 1999, [8]Lisker et al. 2005, [9]Maxted et al. 2002, [10]Maxted et al. 2004, [11]Østensen priv. comm., [12]van Grootel et al. 2008 and [13]Vučković et al. 2007. If the mass couldn't be constrained with alternative methods (see references) the theoretically predicted mass range was taken from Han et al. (2002).†Preliminary result.

System	i [deg]	M_{sdB} [$M_\odot$]	M_{comp} [$M_\odot$]	Companion
PG 1017−086[9]	<74	>0.49	>0.073 ± 0.0003	MS/BD[r]
KPD 1930+2752[5]	73 − 81	0.45 − 0.52	0.91 − 0.96	WD[el]
HS 0705+6700[2]	>85	>0.62	>0.13	MS[r,ec]
PG 1336−018[1,13]	80 ± 10	0.459	0.121 ± 0.001	MS[r]
HW Vir[3]	75 ± 3	0.53	0.16 ± 0.001	MS[r,ec]
PG 1043+760[10]	41 − 83	0.30 − 0.47	0.08 − 0.14	WD[n]
BPS CS 22169−0001[11]	4 − 16	0.30 − 0.47	0.11 − 0.27	MS[r]
PG 1432+159	14 − 22	0.30 − 0.47	1.06 − 3.26	WD/NS/BH
PG 1329+159[9]	15 − 24	0.30 − 0.47	0.19 − 0.37	MS[r]
HE 0532−4503[8]	13 − 18	0.30 − 0.47	1.34 − 3.52	WD/NS/BH[f]
CPD −64 481	6 − 11	0.30 − 0.47	0.29 − 0.74	MS/WD
PG 1101+249	21 − 34	0.30 − 0.47	0.86 − 2.49	WD/NS/BH [f]
PG 1232−136	13 − 20	0.30 − 0.47	2.04 − 7.00	NS/BH[f]
Feige 48[12]	18 ± 2	0.52	0.27 ± 0.01	MS/WD
WD 0107−342[4]	34 − 59	0.30 − 0.47	0.40 − 0.95	WD[f]
KPD 1946+4340	−	−	−	not sychronised
HE 0929−0424[8]	20 − 31	0.30 − 0.47	0.73 − 2.35	WD/NS/BH[f]
HE 0230−4323[8]†	33 − 63	0.30 − 0.47	0.16 − 0.32	MS[r]
PG 1743+477	<18	0.30 − 0.47	>4.00	NS/BH[f]
PG 0001+275	28 − 44	0.30 − 0.47	0.41 − 0.87	MS/WD
PG 0101+039[6]	35 − 59	0.30 − 0.47	0.36 − 0.82	WD[el,n]
PG 1725+252	24 − 41	0.30 − 0.47	0.55 − 1.60	WD/NS[f]
PG 1248+164	45 − 88	0.30 − 0.47	0.15 − 0.29	MS/WD
JL 82	24 − 36	0.30 − 0.47	0.15 − 0.29	MS/WD
TON S 183	20 − 33	0.30 − 0.47	0.64 − 1.99	WD/NS/BH[f]
PG 1627+017	18 − 39	0.30 − 0.47	0.39 − 1.40	MS/WD/NS
PG 1116+301	90	0.35 − 0.47	0.18 − 0.32	MS/WD
HE 2135−3749	62 − 90	0.31 − 0.47	0.23 − 0.44	MS/WD
HE 1421−1206	48 − 90	0.33 − 0.47	0.17 − 0.29	MS/WD
HE 1047−0436	56 − 90	0.37 − 0.47	0.28 − 0.58	MS/WD
PG 0133+114	53 − 90	0.35 − 0.47	0.28 − 0.51	MS/WD
PG 1512+244	90	>0.50	>0.41	MS/WD

System	i [deg]	M_{sdB} $[M_\odot]$	M_{comp} $[M_\odot]$	Companion
UVO 1735+22	–	–	–	not synchronised
HE 2150−0238	–	–	–	not synchronised
HD 171858	$53 - 90$	$0.34 - 0.47$	$0.37 - 0.65$	MS/WD
PG 1716+426	–	–	–	not synchronised
PB 7352	–	–	–	not synchronised
TON S 135	–	–	–	not synchronised
CD −24 731	–	–	–	not synchronised
HE 1448−0510	–	–	–	not synchronised
WD 0048−202	–	–	–	not synchronised

3.9 Distribution of companion masses and systematic effects

Fig. 3.12 shows the mass distribution of the whole sample under the assumption of canonical sdB mass $0.47\,M_\odot$. Up to $20\,\%$ of the analysed subdwarfs may have massive compact companions. Given the low number of known neutron stars and stellar mass black holes this fraction seems unreasonably high and may cast doubts about the analysis method used here. Looking at the low mass end of the mass distribution (Fig. 3.13) one can see a peak at companion masses ranging from $0.2 - 0.4\,M_\odot$. Most of the low mass objects $< 0.4\,M_\odot$ have been clearly identified as M dwarfs (red histogram). The bona fide WD companions show a broad distribution around the average single WD mass of $0.6\,M_\odot$, which is expected from binary formation theory. Because mass transfer is involved, there should be deviations from the normal mass distribution of single WDs. We therefore conclude that the low mass distribution of our sample looks reasonable and no obvious systematics can be seen. Nevertheless, the high fraction of heavy compact companions remains suspicious. The following sections are therefore devoted to a detailed discussion of our results and the question of orbital sychronisation in hot subdwarf binaries.

In the light of this challenging discovery the reliability of our method has to be discussed again. Only the high precision of the $v_{\mathrm{rot}}\sin i$ measurements made it possible to constrain the parameters reasonably. The projected rotational velocities were low and very close to the detection limit. As described above we tried to quantify all possible systematic effects and the overall results were very consistent. Only slight changes in $v_{\mathrm{rot}}\sin i$ would lead to inconsistent solutions, because the method is very sensitive to this parameter. But even if there would be unaccounted systematic effects (e.g. unresolved short period pulsations), they would always cause an extra broadening of the lines. The measured broadening is then due to rotation plus unaccounted effects, which means the measured rotational broadening is higher than the real one. All systematic effects therefore lead to lower $v_{\mathrm{rot}}\sin i$ (see Sect. 3.4). But the unexpectedly high masses of the companions are derived because of the unexpectedly low measured projected rotational velocities as can be seen from the equations given in Sect. 3.1. Unaccounted systematic effects would therefore lead to even higher companion masses.
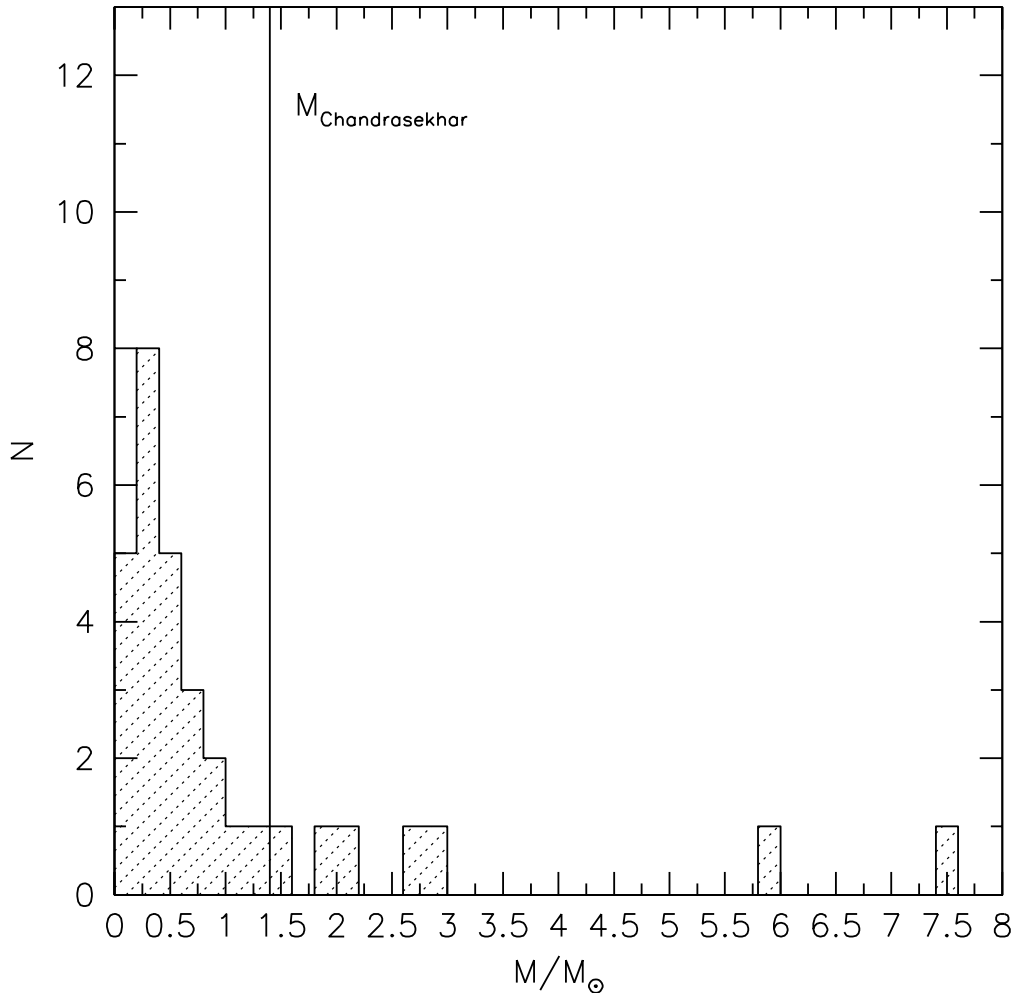
Figure 3.12: Mass distribution of the unseen companion stars. The companion mass is plotted against the total number of binaries under the assumption of canonical sdB mass $0.47 \, M_\odot$. The solid vertical line marks the Chandrasekhar limit. The last bin at $7.5 \, M_\odot$ is a lower limit.

3.10   sdB+NS/BH systems as X-ray sources?

The question arises whether the putative massive compact objects in the sdB+NS/BH binary candidates should be detectable in X-rays. None of the sdB primaries fills its Roche lobe and therefore no matter is transferred to and accreted by the companion via Roche lobe overflow as it is the case in Low Mass X-ray Binaries (LMXBs). On the other hand there are theoretical predictions of stellar wind mass loss in sdBs of the order of $10^{-12} \, M_\odot \mathrm{yr}^{-1}$ (e.g. Vink & Cassisi 2002; Unglaub 2008). Although the predicted mass loss rates are low, they may be sufficient to cause detectable X-ray flux powered by wind accretion of the NS or BH companions similar to High Mass X-ray Binaries (HMXBs, e. g. Frank et al. 2002). In fact the single-lined close binary post-AGB star HD 49798 turned out to be an X-ray source (Israel et al. 1997). Since
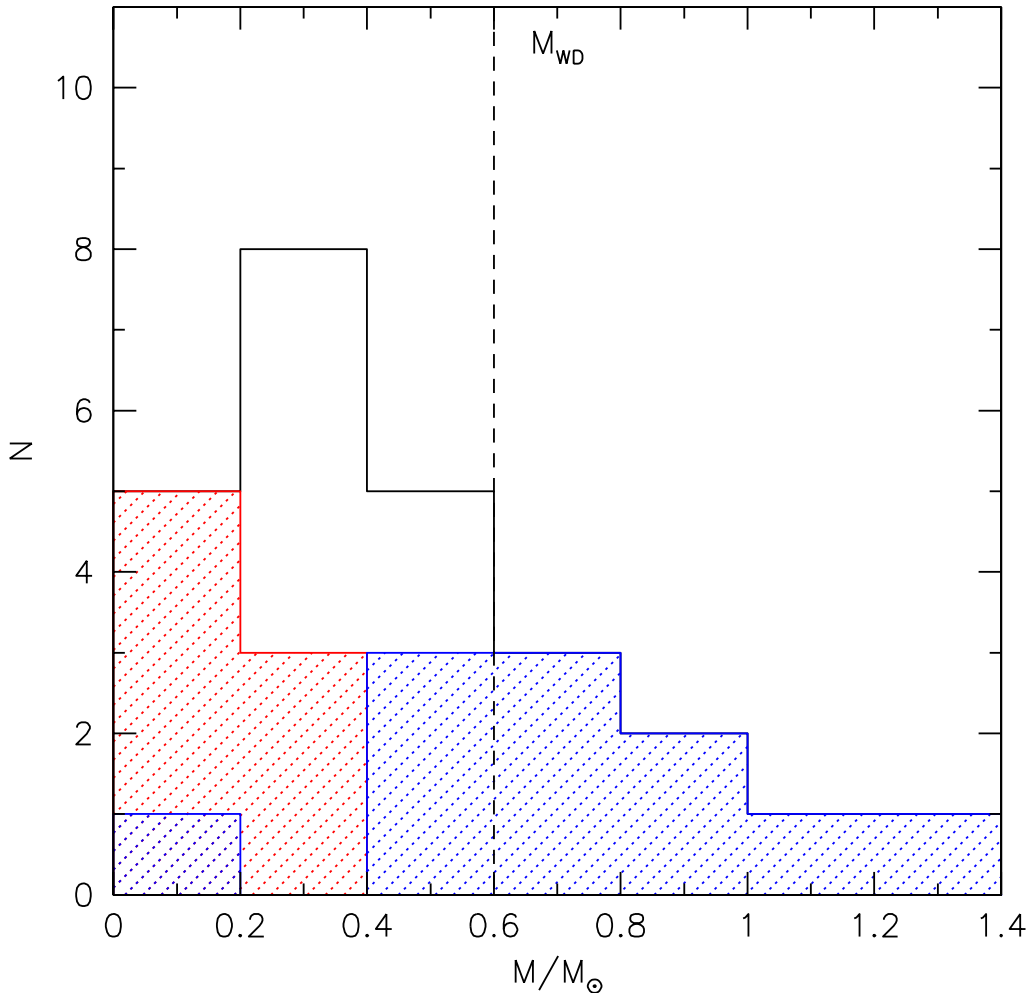
Figure 3.13: Detail of the mass distribution shown in Fig. 3.12. The companion mass is plotted against the total number of binaries under the assumption of canonical sdB mass $0.47\,M_\odot$. The blue histogram shows the fraction of subdwarfs with confirmed WD companions, the red histogram the detected M dwarf companions. The dashed vertical line marks the average WD mass.

that star is not filling its Roche lobe, wind accretion of a degenerate companion must be the reason. Although this binary is very similar to the objects discussed here, it has to be pointed out that the hot primary is much larger than an sdB star and the wind mass loss rate is much higher.

In order to estimate the X-ray luminosities of the candidate systems the parameters derived from our spectroscopic analysis are used (see Sect. 3.8.3) and Bondi$-$Hoyle accretion is assumed. The accreted mass rate $\dot{M}_\mathrm{acc}$ is derived to

$$\dot{M}_\mathrm{acc} = \dot{M}_\mathrm{W} \frac{\pi R_\mathrm{acc}^2}{4\pi a^2} \tag{3.5}$$

where $R_{\mathrm{acc}} = 2GM_{\mathrm{comp}}/v_{\mathrm{W}}^2$ and a is the binary separation derived from the orbital parameters using Keplers third law. For the stellar wind mass loss rate $\dot{M}_{\mathrm{W}}$ an upper limit of $10^{-12}\,M_{\odot}\mathrm{yr}^{-1}$ is adopted. It has to be pointed out that this quantity is purely based on theoretical predictions since no direct measurements of wind mass loss in sdBs have ever been performed. Although Vink & Cassisi (2002) and Unglaub (2008) predict mass loss rates of up to $10^{-11}\,M_{\odot}\mathrm{yr}^{-1}$ for hotter sdBs, this number is considered too high to be consistent with observation. Unglaub (2008) most recently pointed out that at such high mass loss rates the normally diffusion dominated atmospheres of sdB stars should become convective. All sdBs in our candidate systems show diffusion dominated abundance patterns, which are perfectly consistent with results obtained from the large sample analysed in Chap. 8 (an abundance analysis of HE 0532−4503 and HE 0929−0424 is given there). Hence we conclude that $10^{-12}\,M_{\odot}\mathrm{yr}^{-1}$ is a realistic upper limit for the wind mass loss rate in sdBs (see also Fontaine & Chayer 1997).

Another poorly constrained ingredient in our calculations is the wind velocity v_{W}. For the strong winds in HMXBs it is usually approximated as $v_{\mathrm{W}} \approx 3v_{\mathrm{esc}}$ (e.g. Lamers & Cassinelli 1999), where the escape velocity is $v_{\mathrm{esc}} = \sqrt{2GM_{\mathrm{sdB}}/R_{\mathrm{sdB}}}$. The mass of the sdB is assumed to be $0.47\,M_{\odot}$ and the radius R_{sdB} is calculated with Eq. 6.2. G is the gravitational constant. Whether this assumption holds for the weak and possibly fractionated winds of sdBs is not known so far. The escape velocity is usually taken as lower limit for the wind velocity. The X-ray luminosities are calculated (c is the speed of light) assuming an efficiency of $10\,\%$ for the energy production by accretion onto a BH:

$$L_{\mathrm{X}} \approx 0.1\dot{M}_{\mathrm{acc}}c^2 \qquad (3.6)$$

The detectable bolometric X-ray flux is then given by

$$f_{\mathrm{X}} = L_{\mathrm{X}}/4\pi d^2 \approx 2.4 \times 10^{-5}\frac{\dot{M}_{\mathrm{W}}c^2}{d^2}\frac{R_{\mathrm{sdB}}^2}{a^2}\frac{M_{\mathrm{comp}}^2}{M_{\mathrm{sdB}}^2} \qquad (3.7)$$

The distances d have been derived from the sdB luminosities $L = 4\pi\sigma R_{\mathrm{sdB}}^2 T_{\mathrm{eff}}^4$. The distance modulus as well as apparent visual magnitudes and appropriate bolometric corrections from literature were used. Tab. 3.7 gives the resulting distances, X-ray luminosities and fluxes of all candidate systems. The largest fluxes are expected for PG 1432+159, PG 1232−136 and PG 1743+477.

The ROSAT all-sky survey catalogue (RASS, Voges et al. 1999) has been checked and no sources have been detected at the positions of the candidate sdB+NS/BH systems. The detection limit of this survey reaches down to about $10^{-13}\,\mathrm{erg/cm^2s}$, which is most cases higher than the derived fluxes. In two cases the derived fluxes are near the detection limit of ROSAT. It has to be pointed out that these fluxes have not been corrected for interstellar neutral hydrogen absorption and should therefore be taken as upper limits. Cackett & Miller (2006) observed HE 0532−4503 with the XRT instrument on board of the Swift satellite and were not able to detect an X-ray source. They give an upper limit for the X-ray flux of $1 - 7 \times 10^{-14}\,\mathrm{erg/cm^2s}$, higher than the predicted flux (see Tab. 3.7).

The non-detection of these putative sources in the RASS survey and with Swift XRT is consistent with their predicted fluxes below or near the detection limits, given the uncertainties in the calculation of these fluxes. The only way of constructing a contradiction between these non-detections and the theoretical predictions lies in tuning the uncertain parameters $\dot{M}_{\mathrm{W}}$ and v_{W}. Should the wind mass loss be one order of magnitude higher than assumed here and the wind

Table 3.7: Derived X-ray properties of candidate sdB+NS/BH systems.

	d [kpc]	L_{X} [erg/s]	f_{X} [erg/cm^{2}s]
PG 1432+159	0.5	6×10^{29}	8×10^{-14}
HE 0532$-$4503	2.4	2×10^{30}	8×10^{-15}
PG 1101+249	0.5	2×10^{29}	3×10^{-14}
PG 1232$-$136	0.5	1×10^{30}	2×10^{-13}
HE 0929$-$0424	1.9	2×10^{29}	2×10^{-15}
PG 1743+477	0.7	2×10^{30}	2×10^{-13}
PG 1725+252	0.5	9×10^{28}	1×10^{-14}
TON S 183	0.6	2×10^{29}	2×10^{-14}
PG 1627+017	0.5	6×10^{28}	8×10^{-15}

speed significantly lower than three times the escape velocity, the derived X-ray luminosities can be pushed beyond the RASS detection limit (see Eq. 3.7). Due to the fact that these quantities are very weakly constrained by observations, we conclude that it is not possible to disprove the existence of NS or BH companions in this way. The sensitivity of XMM-Newton or Chandra on the other hand is high enough to detect all targets listed, if they host a BH and our estimates on $\dot{M}_{\mathrm{W}}$ and v_{W} are correct. The detection limit of the XMM-Newton Medium sensitivity Survey (XMS) reached down to 2×10^{-14} erg/cm^{2}s in the intermediate band between 0.5 and 4.5 keV (Barcons et al. 2003). The Chandra Deep Field North Survey even reached a detection limit of 2.5×10^{-17} erg/cm^{2}s between 0.5 and 2.0 keV within 2 Ms of exposure time (Alexander et al. 2003).

Chapter 4

Orbital synchronisation of sdB binaries

The results presented in the last chapter are based on the assumption of tidal synchronisation. Since especially the discovery of sdB+NS/BH systems challenges our understanding of stellar evolution it is necessary to investigate, whether this assumption is valid in the case of sdBs. A thorough discussion of tidal synchronisation in sdB binaries both from the theoretical and the observational point of view is therefore given.

4.1   Theoretical timescales for synchronisation

The question is not yet answered, which mechanism is responsible for orbital synchronisation in binaries. Theoretical timescales for synchronisation are given by Zahn (1977) and Tassoul & Tassoul (1992), but unfortunately they are not consistent for stars with radiative envelopes and convective cores like hot subdwarfs.

Zahn (1977) was the first to calculate synchronisation and circularisation timescales for main sequence stars in close binary systems. Observations of eclipsing binaries were in good agreement with his theoretical calculations for late type MS stars with radiative cores and convective envelopes. Tidal friction caused by the equilibrium tide, which forms under the tidal influence of the close companion, is very efficient in this case because convection connects the inner regions of the stellar envelope with its surface. For radiative envelopes another mechanism is needed to explain the observed degree of synchronism in early type MS binaries. Dynamical tides, which are excited at the boundary layer between convective core and radiative envelope are thought to be radiatively damped at the stellar surface and to transfer angular momentum outwards. This mechanism turns out to be much less efficient and the predicted synchronisation timescales were too long to explain the degree of synchronism in some early type MS stars (e.g. Giuricin et al. 1984). Tassoul & Tassoul (1992) introduced another hydrodynamical braking mechanism. Tidally induced meridional currents in the nonsynchronous binary components should lead to synchronisation and circularisation of the system. This mechanism is very efficient, but it was debated whether it is valid or not (Rieutord 1992; Tassoul & Tassoul 1997). Claret et al. (1995, 1997) studied both mechanisms, put in new evolutionary models and compared it to the available observations. Due to the necessary calibration of many uncertain parameters a definitive answer to the question could not been given, which mechanism is in better agreement with observation.

Applying the theory of tidal synchronisation to sdB binaries is not an easy task. One of the key results of both theories for comparison with observations is that tidal circularisation of the orbit is achieved after the companions are synchronised. This means that once an orbital solution is found and the orbit turns out to be circular, both companions can be considered as synchronised without knowing something about their rotation. This simple law cannot be used in case of sdBs. The reason is that close binary sdBs were most likely formed via the CE ejection channel (see Sect. 1.3). The common envelope phase is very effective in circularising the orbit and all known close binary sdBs have circular orbits or show only slight eccentricities (Edelmann et al. 2005a). On the other hand the binary period is quickly decreasing and it is not clear whether synchronisation can be achieved at these short timescales. While Hurley et al. (2002) assume the companions to be co-rotating after CE ejection and implement this in their binary evolution code, Terman et al. (1994) modelled the double core evolution in three dimensions and found the companions to be non-synchronously rotating.

Stellar structure plays an important role. The synchronisation timescale of Zahn (1977) scales with $(R_C/R)^8$, where R_C is the radius of the convective core and R the stellar radius. The larger the convective core of a star, the shorter the timespan until synchronisation is reached. For sdB stars this important quantity turned out to be strongly dependent on the mass of the hydrogen layer even though this layer is considered to be very thin (Han priv. comm.). The hydrogen layer mass is more or less a free parameter.

To get an idea about the synchronisation times of the analysed binaries we used the formulas of Zahn (1977) and Tassoul & Tassoul (1992).

$$t_{\text{sync}}(\text{Zahn}) = 52^{-5/3} \left(\frac{R^3}{GM} \right)^{1/2} \left(\frac{I}{MR^2} \right) \frac{(1+q)^{5/6}}{q^2} E_2^{-1} \left(\frac{a}{R} \right)^{17/2} \tag{4.1}$$

Here $M = M_{\text{sdB}}$, $R = R_{\text{sdB}}$, $q = M_{\text{comp}}/M_{\text{sdB}}$ and a is the separation of the companions, which can be calculated from the measured orbital parameters using Keplers third law. E_2 is a tidal coefficient which is very sensitive to the structure of the star, especially the size of the convective core. Here we use the first approximation of Zahn (1977) $E_n = (R_C/R)^{2n+4}$ and put in $R_C/R \approx 0.15$ derived from sdB models calculated by Han (priv. comm.). As hydrogen layer mass for these models $10^{-4} M_\odot$ was chosen based on results consistent with asteroseismology (e.g. Brassard et al. 2001). From the same models we get $\frac{I}{MR^2} \approx 0.04$.

$$t_{\text{sync}}(\text{Tassoul}) = 5.35 \times 10^{2+\gamma-N/4} \frac{1+q}{q} L^{-1/4} M^{5/4} R^{-3} P^{11/4} \tag{4.2}$$

In this equation M, R (solar units) and q are defined in the same way as above. P is the orbital period in days. The luminosity $L = 4\pi\sigma R^2 T_{\text{eff}}^4$ can be calculated using the T_{eff} measurements given in Tab. 3.5. The parameter N is connected with the different ways of energy transport within the outer layers of the stellar envelope. It is assumed to be 0 in stars with radiative envelopes. The parameter γ can be adjusted to account for large deviations from synchronism and contributions of both companions. Here the value $\gamma = 1.6$ used by Claret et al. (1995) was chosen.

It has to be noted, that this approach is only a crude approximation. As stated by Claret et al. (1997) the differential equations which govern the orbital parameters of a binary must be integrated. For this EHB evolution has to be taken into account. A detailed study of this problem goes beyond the scope of this thesis.
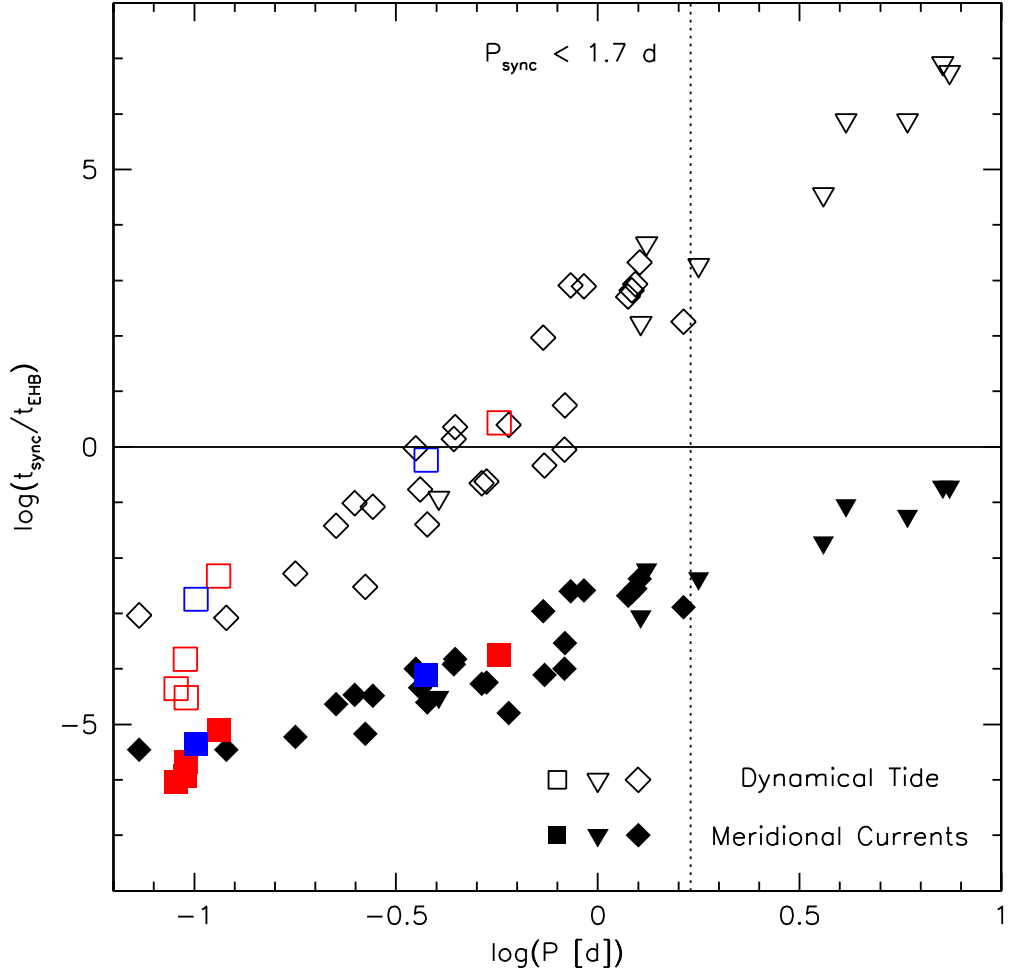
Figure 4.1: The logarithm of the orbital period is plotted against the synchronisation times of Zahn (1977, blank symbols) and Tassoul & Tassoul (1992, filled symbols) both divided by the average lifetime on the EHB (Dorman et al. 1993) and in logarithmic scale. The solid horizontal line marks the border between synchronisation within the EHB lifetime and synchronisation times longer than the EHB lifetime. The squares mark sdB binaries, where the primaries are proved to be synchronised (see next section). Red squares mark eclipsing or ellipsoidal variable binaries, blue squares binaries where synchronisation could be shown by asteroseismology. The systems marked with diamonds could be solved consistently under the assumption of synchronisation, while the systems marked with triangles rotate faster than synchronised.

Fig. 4.1 shows the results of our calculations and compares it with the observations. The logarithm of the orbital period of the analysed sdBs, which is the most important parameter in both theories, is plotted against the synchronisation times divided by the average lifetime on the EHB $t_{\mathrm{EHB}} \approx 10^8 \, \mathrm{yr}$ (Dorman et al. 1993) on logarithmic scale. A binary is thought to be synchronised, if the EHB lifetime is much longer than the synchronisation time. What can be

seen immediately is that the timescales of Zahn and Tassoul differ by $2-6$ orders of magnitude. This inconsistency casts the theoretical approach into doubt. Observational evidence is needed to constrain the timescales of tidal synchronisation in close binary sdBs.

For periods shorter than 0.4 d both theories predict synchronised rotation and are consistent with our observations. In the period range $0.4 - 1.3$ d only the synchronisation times of Tassoul are consistent with observation, while the timescales of Zahn quickly exceed Hubble time. For orbital periods longer than 1.3 d the assumption of synchronisation does not yield consistent results any more, although the timescales of Tassoul would still predict synchronised rotation. All sdB binaries but one, which cannot be solved consistently under the assumption of synchronisation have orbital periods longer than 1.3 d.

The binary $HE\,2150-0238$ cannot be solved consistently despite of the fact that its period of 1.3 d is very close to that of $HE\,1047-0436$, $PG\,0133+114$ and $PG\,1512+244$, which can be solved. This strange behaviour may be explained, if stellar evolution is taken into account. Actually t_{EHB} is just an approximation, because the age of an sdB depends on its position on the EHB. In Fig. 4.6 one can see that $HE\,2150-0238$ it situated very near the Zero Age Extreme Horizontal Branch (ZAEHB) while the other sdBs are more evolved (see Tab. 3.5) and therefore older. Should the timescales for synchronisation at orbital periods around 1.3 d be of the order of a few 10^7 yr $HE\,2150-0238$ may simply be too young to be synchronised. $HD\,171858$ on the other hand appears to be synchronised at a longer period of 1.6 d. This star is already evolving away from the EHB and is therefore even older than the subdwarfs populating the EHB. We conclude that at orbital periods of $1.3 - 1.6$ d the sychronisation timescales of sdB binaries are of the order of the lifetime on the EHB. All sdBs in binaries with longer orbital periods spin faster than sychronised.

Two sdBs which don't fit into this scheme are $KPD\,1946+4340$ and $UVO\,1735+22$. Both stars are situated well above the EHB suggesting a highly evolved status and therefore high age (see Fig. 4.6). Both stars rotate not only faster than synchronised, they also spin much faster than the rest of the non-synchronised binaries ($\approx 40\,\mathrm{km s^{-1}}$). $UVO\,1735+22$ has an orbital period of 1.3 d right at the edge of the binaries, which can be solved consistently. On the other hand, given that it is a post-EHB star it should nevertheless be old enough to be synchronised (like $HD\,171858$). $KPD\,1946+4340$ has an orbital period of 0.4 d and clearly lies in the region of synchronisation. This behaviour cannot be explained in the framework of EHB evolution and an alternative scenario is discussed in the Sect. 4.6.

In general the synchronisation mechanism of Zahn (1977) is not efficient enough to explain the observed level of synchronisation, while the mechanism of Tassoul & Tassoul (1992) on the other hand appears to be too efficient. Nevertheless, care has to be taken interpreting these results, because both theories give timescales for the sychronisation of whole stars from the core to the surface, while only the rotational broadening at the surface can be derived from line broadening. Goldreich & Nicolson (1989) showed that in stars with radiative envelopes and Zahn's braking mechanism at work, the synchronous rotation proceeds from the surface towards the core of the star. This means that the outer layers of a star are synchronised faster than the rest. This effect would explain at least to a certain extent the discrepancy between Zahn's theory and our results. Unfortunately it was not possible to quantify this effect so far (e.g. review by Zahn 2005).

Tidal synchronisation does not necessarily lead to an equality of orbital and rotational period. Higher spin resonances are possible and would change the derived parameters significantly (in case of the planet Mercury the ratio of orbital and rotational period is 3/2). To fall into a

higher resonance, the binary eccentricity has to be high at some point of its evolution. But close sdB binaries underwent at least one common envelope phase (maybe two in case of compact companions), which lead to a circularisation of the orbit. For these reasons, higher resonances are unlikely to occur in this evolutionary channel.

4.2   Empirical evidence: Eclipsing systems

The timescale of the synchronisation process is highly dependent on the tidal force exerted by the companion. If the companion is very close and the orbital period therefore very short, synchronisation is established much faster than in binaries with longer orbital periods. If an sdB binary with given orbital period is proven to be synchronised, all other sdB binaries with shorter orbital periods should be synchronised as well. Although the timescales also scale with sdB radius and companion mass, the orbital period is dominating at first order.

We have seen in Sect. 3.8.1 that the derived parameters of the elipsing binaries PG 1336−018, HS 0705+6700 and HW Vir are consistent with synchronised orbits. This essentially means that the calculated $v_{\rm rot} \sin i$ for synchronous rotation, which can be obtained as described in Sec. 4.1 given the orbital period, the radius of the sdB and the inclination angle are known, is consistent with the measured value. In eclipsing systems, all these parameters can be measured.

This provides clear empirical evidence that at least the upper layers of the stellar envelope are synchronised to the orbital motion of the eclipsing sdB binaries in our sample. We therefore conclude that all sdBs in close binaries with orbital periods up to 0.12 d should be synchronised as well.

4.3   Empirical evidence: Ellipsoidal deformation

Two known sdBs clearly show ellipsoidal variations in their light curves with periods exactly half the orbital periods (KPD 0422+5421 Orosz & Wade 1999; KPD 1930+2752 Geier et al. 2007). This alone is only an indication for tidal synchronisation, because the lightcurve variations have to be present at the proper orbital phases as well. To really prove synchronisation it is necessary that the stellar parameters determined independently from the light curve analysis are consistent with a synchronised orbit. This is the case for KPD 0422+5421 as well as KPD 1930+2752. Both ellipsoidal variable systems have very short periods of ≈ 0.1 d and high inclination. Otherwise ellipsoidal variations are very hard to detect.

4.4   Empirical evidence: PG 0101+039

PG 0101+039, an sdB+WD binary ($P = 0.567$ d, Maxted et al. 2001) shows very weak luminosity variations at half the orbital period detected in a 16.9 day long, almost uninterrupted light curve obtained with the MOST satellite (Randall et al. 2005). In order to verify that we indeed see ellipsoidal variations, we had to show that the observed light curve can be consistently modelled. Beforehand, we had to derive the complete set of system parameters using the analysis method described in Sect. 3.1.

4.4.1 Radial velocity curve

Based on spectra obtained in 1998, Moran et al. (1999) determined the orbital period $P = 0.569908 \pm 0.000007$ d. However, these ephemerides are not accurate enough to phase the MOST photometry, because the time span of six years between spectroscopic and photometric observations is too long. Therefore we combined the velocities of Moran (1999) with those from eight MMT-spectra taken in 1996, 1997 and 2002 (Randall et al. 2005) and five spectra obtained with the Steward 2.3m Bok telescope from 2000. The latter were determined using the double-precision version of the IRAF fxcor package, against the combined template for the star. In addition we obtained three high resolution spectra ($R = 30\,000$) in 2000 at the 2.2 m telescope at the German-Spanish Astronomical Center (DSAZ) equipped with the FOCES-spectrograph. RVs were determined by cross correlation with a model spectrum at rest wavelength.

This provided us with 57 velocities distributed between 1996 and 2000. A sine curve was fitted to the observed velocities using an χ^2 minimising method and the power spectrum was generated as described in Sect. 2.3.2. The orbital parameters were measured (see Fig. 4.2): $\gamma = 7.3 \pm 0.2\,\mathrm{km\,s^{-1}}$, $K = 104.5 \pm 0.3\,\mathrm{km\,s^{-1}}$, $P = 0.569899 \pm 0.000001$ d and $HJD(0) = 2452545.064275$. The period error was derived with a bootstrapping algorithm. The period is sufficiently accurate to allow the MOST photometry to be phased properly. However, it should be kept in mind that the error quoted is a purely statistical one. To investigate possible systematic errors, which can occur when radial velocities obtained with different instruments are combined, we also used another method to verify our results. In this case the fitting was performed with the system velocity γ as an additional free parameter for every individual dataset. The results using both methods were perfectly consistent within the quoted errors. However, additional systematic effects may still be present.

PG 0101+039
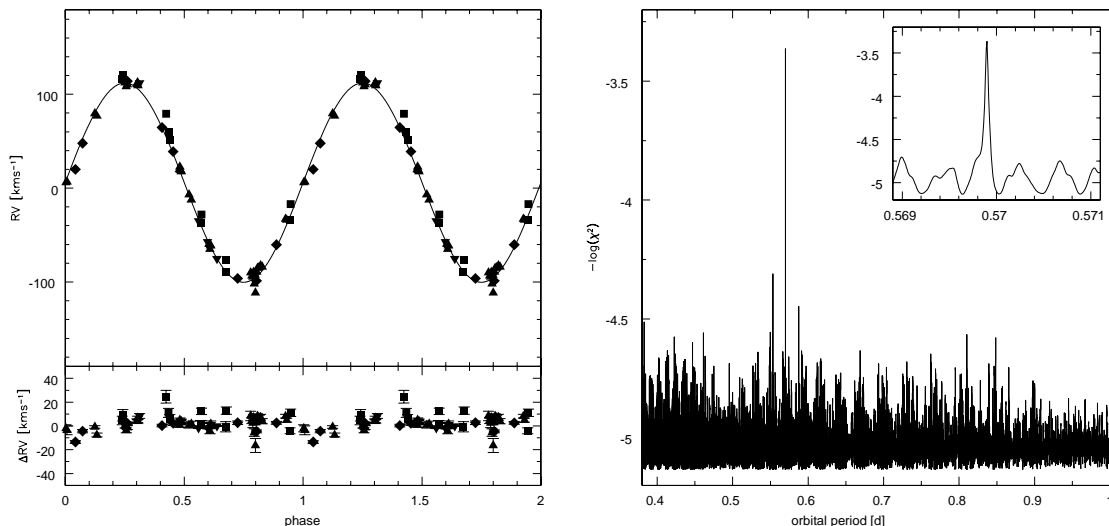
Figure 4.2: Radial velocity curve and power spectrum of PG 0101+039 (see Fig. 2.5).
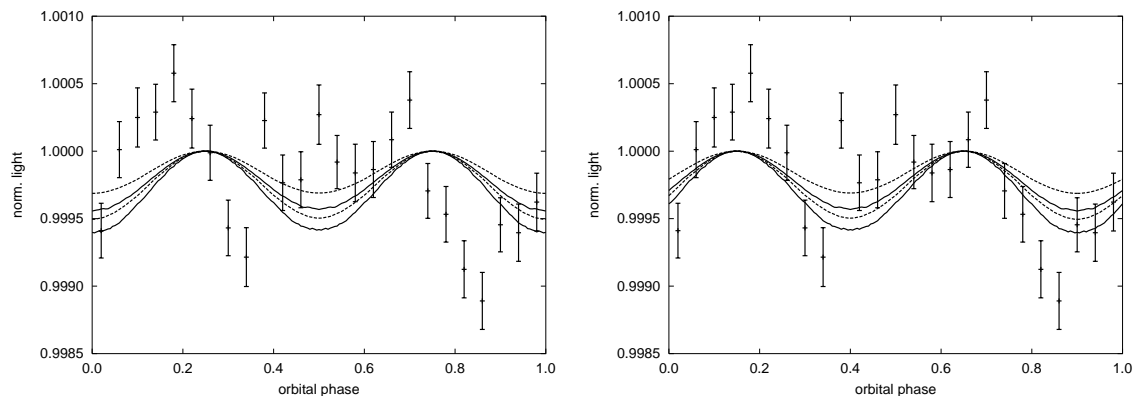
Figure 4.3: Lightcurve data with superimposed models. The two solid curves confine the best fit models with parameters and associated uncertainties derived from spectroscopy under the assumption of orbital synchronisation and $M_{\rm sdB} = 0.3\,M_\odot$. The two dotted curves confine models for $M_{\rm sdB} = 0.7\,M_\odot$. *Left panel* Phasing the data to the orbital solution results in a significant phase shift. *Right panel* The model light curve is shifted by -0.1 in phase.

4.4.2 Gravity, projected rotational velocity and analysis

Low resolution spectra obtained by Randall et al. (2005) and Maxted et al. (2001) were used to derive the atmospheric parameters. Synthetic line profiles calculated from metal line-blanketed LTE model atmospheres with solar metal content (Heber et al. 2000) were matched to the observed Balmer and helium line profiles as described in Sect. 3.7.

The resulting parameters are $T_{\rm eff} = 27\,700\,{\rm K}$, $\log g = 5.55$, $\log N({\rm He})/N({\rm H}) = -2.62$ from the spectra of Randall et al. (2005) and $T_{\rm eff} = 27\,300\,{\rm K}$, $\log g = 5.50$, $\log N({\rm He})/N({\rm H}) = -2.71$ from the spectra of Maxted et al. (2001) with formal statistical fitting errors of less than $100\,{\rm K}$, $0.02\,{\rm dex}$ and $0.02\,{\rm dex}$, respectively, which are unrealistically low. The true uncertainties are dominated by systematic inaccuracies in both the observations and model atmospheres, and can be estimated from repeated observations and the use of different model grids. Taking into account the discussion of typical systematic errors obtained when applying this method in Sect. 3.7, we adopt $T_{\rm eff} = 27\,500 \pm 500\,{\rm K}$, $\log g = 5.53 \pm 0.07$, $\log N({\rm He})/N({\rm H}) = -2.66 \pm 0.1$.

The projected rotational velocity was measured simultaneously with the elemental abundances to $v_{\rm rot}\sin i = 10.9 \pm 1.1\,{\rm kms}^{-1}$ as described in Sect. 3.3 from the coadded FOCES high-res spectrum using 17 suitable metal lines.

The system has been analysed in the way described in Sect. 3.1. For the most likely sdB mass of $0.47\,M_\odot$ the binary parameters are: $R_{\rm sdB} = 0.19 \pm 0.02\,R_\odot$, $M_{\rm WD} = 0.72 \pm 0.10\,M_\odot$, inclination $i = 40 \pm 6\,^\circ$ and separation $a = 3.1 \pm 0.4\,R_\odot$.

4.4.3 Light curve and ellipsoidal variation

The MOST photometric data were folded on the orbital period and re-binned to get a better signal to noise ratio (see Fig. 4.3). As PG 0101+039 is a pulsating sdB star of V1093 Her type, the light curve had to be pre-whitened for the pulsational frequencies beforehand.

Each bin contains more than 400 original measurements. Light curve variations at half the orbital period with a semi-amplitude of 0.025% were detected. Therefore PG 0101+039 shows the smallest ellipsoidal variation ever measured. In order to compare with synthetic light

curves, we had to phase the photometry properly, taking the zero point from the orbital solution. Because the amplitude of the variation is very low, Doppler boosting arising from the orbital motion affects the light curve significantly. A resulting factor of $(1 - v(t)/c)$ was applied to the total flux to correct for this effect.

The light curve was modelled with the light curve synthesis and solution code MORO, based on the model by Wilson & Devinney (1971). The details of the Bamberg implementation are given by Drechsel et al. (1995). The software uses a modified Roche model for light curve synthesis. It is capable of simulating the distortions of the stars induced by a companion. Light curves for different component masses and orbital inclinations were synthesised. For typical values of M_{sdB} appropriate ranges of $\sin i$ and R_{sdB} values were computed, covering the full parameter space (including error limits) allowed by the spectroscopic analysis.

We used sdB masses from $0.3 - 0.7 M_\odot$ to calculate the model light curves and compared the models to the observations in Fig. 4.3. The synthetic light curve matches the semi-amplitude of the observed light curve quite well. Taking into account the extremely low amplitude of the variation, the consistency with the model is remarkable. However, there is a significant phase shift between the observed and the predicted light curve. The best fit to the data is phase shifted by -0.1 with respect to the model calculated with proper orbital phase (see Fig. 4.3 right panel). Despite our efforts to derive a high precision orbital period, we can not rule out completely the possibility that this shift is caused by systematic effects when RV measurements from different instruments are combined. To match the observed light curve would require the period to differ by $0.00008\,\mathrm{d}$ from our results. Given the overall consistency of our orbital parameter determination, such a large deviation ($80\times$ period error) seems to be rather unlikely.

Alternative explanations, like super-synchronous rotation of the sdB that may cause the observed phase shift, seem to be unlikely because a deviation of $10\,\%$ from equilibrium would require fast rotation of the sdB. In this case the inclination would be very low and the companion mass would rise dramatically. A simultaneous measurement of the radial velocity curve and a high precision light curve would be necessary to solve this problem.

4.4.4 Implications for orbital synchronisation in sdB binaries

In conclusion, we found a strong indication that the surface rotation of the sdB star PG 0101+039 is tidally locked to its orbit. Hence, other sdB stars in close binaries should also be synchronised if their orbital period is less than that of PG 0101+039 (P $= 0.567\,\mathrm{d}$). We conclude that tidally locked surface rotation is at least established in sdB binaries with orbital periods of less than half a day.

4.5 Empirical evidence: Asteroseismology

An independent method to proof orbital synchronisation is provided by asteroseismology. Van Grootel et al. (2008) were able to reproduce the main pulsation modes of the short period pulsating sdB Feige 48 ($P \approx 0.38\,\mathrm{d}$), derived the surface rotation from the splitting of the modes and concluded that the subdwarf rotates synchronously.

Charpinet et al. (2008) reach a similar conclusion for the short period eclipsing binary PG 1336$-$018 ($P \approx 0.10\,\mathrm{d}$). Furthermore they probed the internal rotation of the star below the surface layers by applying a differential rotation law and showed that the sdB rotates as a rigid body at least down to $0.55\,R_{sdB}$. The remarkable consistency of the binary parameters derived

by asteroseismology (Charpinet et al. 2008), binary light curve synthesis (Vučković et al. 2007) and the analysis presented here has to be pointed out again (see Sect. 3.8.1). Asteroseismic analyses revealed that sdB binaries up to orbital periods of about 0.4 d are synchronised. We therefore conclude that all sdB in close binaries with shorter periods should be synchronised as well.

4.6 Post-RGB binaries and synchronisation

4.6.1 Analysis of post-RGB binaries

Our sample contains at least three stars, which most likely don't burn helium in their cores and evolve directly from the RGB to the WD cooling tracks crossing the EHB (see Sect. 1.2). Little is known about this class of objects. Therefore we present an analysis of these candidate post-RGB binaries. **HD 188112** has been identified as post-RGB object by Heber et al. (2003). This bright subdwarf shows strong Balmer, but almost no helium or metal lines. According to its atmospheric parameters it is situated well below the EHB (Tab. 4.1, Fig. 4.5). By interpolation of evolutionary tracks from Driebe et al. (1998) a mass of $0.23\,M_\odot$ could be derived. This theoretically predicted mass could be verified directly, because an accurate parallax of this object was obtained by the HIPPARCOS satellite. Combined with a quantitative spectral analysis the mass of the star was measured to $0.24\,M_\odot$ in perfect agreement with post-RGB evolution theory. HD 188112 is a single-lined close binary system. The minimum mass of the invisible companion exceeds $0.73\,M_\odot$. For inclination angles lower than $< 48°$ the companion mass would exceed the Chandrasekhar limit.

Because of the very interesting properties of this object, we included it in our sample. Due to the excellent quality of the spectrum the $v_{\rm rot}\sin i$ could be measured with sufficient accuracy, although only two lines (He I 5867 and Mg II 4481) could be used (Tab. 4.2). Despite the short orbital period of 0.6 d the primary turned out to rotate faster than synchronised (Tab. 4.3).

Although the orbital parameters of **PG 1247+554** were derived by Maxted et al. (2000b), no atmospheric parameters for this star could be found in literature. A low resolution spectrum (Østensen priv. comm.) was therefore used to obtain these parameters by fitting LTE model spectra (the method is described in Sect. 3.7). The surface gravity turned out to be very high ($\log g = 6.35$), placing this object below the helium main sequence (He-MS Tab. 4.1, Fig. 4.5). By interpolation of evolutionary tracks from Driebe et al. (1998) a mass of $0.29\,M_\odot$ is derived. Assuming a synchronised orbit the minimum primary mass is $0.55\,M_\odot$ and therefore too high. Despite its short orbital period of 0.6 d PG 1247+554 spins faster than synchronised (Tab. 4.3).

PG 2345+318 is a short period (0.24 d) sdB binary. Green et al. (2004) showed a light curve of this star, where the eclipse of a WD companion is clearly visible. Besides KPD 0422+5421 (Orosz & Wade 1999) and PG 0941+280 (Green et al. 2004) this is just the third such system known. The atmospheric parameters of this star (see Tab. 4.1) place it right at the bottom of the EHB (Fig. 4.5). From the atmospheric parameters alone there is no reason to classify this star as post-RGB object, because the EHB is of course mainly populated by EHB stars. Assuming a normal helium core burning star with a mass of $0.47\,M_\odot$ and tidal synchronisation the companion mass would be $1.9 \pm 0.3\,M_\odot$ at an inclination angle of about $23°$. Without the additional information from the light curve this object would therefore become another candidate for sdB+NS/BH binary. The detection of eclipses immediately rules out this scenario. The inclination angle has to be near $90°$ and the companion a WD with a mass of $0.38\,M_\odot$ according

to the constraint set by the binary mass function. This means that the sdB star in this binary rotates more slowly than synchronised (Tab. 4.3).

This discovery seems to prove that sdBs spinning slower than synchronised exist in binaries with short orbital periods. Although this would be hard to explain from the theoretical point of view, it would solve the problem of the numerous sdBs with heavy compact companions. If exactly these binaries for whatever reason should rotate slower than synchronised, the real companion masses would be lower. But this is not the whole story. The light curve presented by Green et al. (2004) reveals more information. The depth of the eclipse equals about 1.5% of the total flux. Assuming $0.47\,M_\odot$ and taking the surface gravity from Tab. 4.1 the radius of the sdB can be calculated with the mass radius relation to $R_{\mathrm{sdB}} = 0.16\,R_\odot$. The radius of the WD $R_{\mathrm{WD}} = 0.014\,R_\odot$ was calculated with the mass-radius-relation $R \approx 0.01 M^{-1/3}$ in solar units taken from Hansen & Kawaler (1994). The expected eclipse depth was calculated for this configuration $R_{\mathrm{WD}}^2/R_{\mathrm{sdB}}^2 \approx 0.008$. This fraction of 0.8% is just half of the depth observed. We conclude that PG 2345+318 cannot be an EHB star with canonical mass.

Under the assumption that PG 2345+318 is a post-RGB star the tracks of Driebe et al. (1998) suggest a mass of about $0.26\,M_\odot$. A companion mass of $0.27\,M_\odot$ is then constrained by the mass function. Performing the same calculations as in the last paragraph we get $R_{\mathrm{sdB}} = 0.12\,R_\odot$ and $R_{\mathrm{WD}} = 0.015\,R_\odot$ and with this an eclipse depth of about 1.6%. This result is in good agreement with observation. We conclude that PG 2345+318 is most likely a close binary consisting of a post-RGB object and a low mass WD. A detailed photometric analysis of this star's light curve is necessary to constrain the binary parameters more accurately. Most recently Østensen et al. (2008) proposed a similar scenario for the eclipsing binary HS 2231+2441. In this case a post-RGB star is orbited by a brown dwarf companion. A high resolution spectrum of this star is necessary to see whether it is synchronised or not.

From our analysis of three post-RGB binaries we find that tidal synchronisation of the primary is not established in these systems. Rauch & Werner (2003) report a similar result for the putative post-RGB binary **AA Dor** (LB 3459). From a photometric and spectroscopic analysis (Rauch 2000) of this eclipsing binary they conclude that AA Dor is most likely a post-RGB star with a mass of $0.33\,M_\odot$ orbited by a brown dwarf companion (Fig. 4.5). After measuring the projected rotational velocity of AA Dor Rauch & Werner (2003) found that the primary rotates faster than synchronised if the subdwarf radius derived from the light curve solution is adopted.

Obtaining the parameters of AA Dor (Tabs. 4.1, 4.2) from Rauch (2000) and Rauch & Werner (2003) we calculate a minimum mass of $0.35\,M_\odot$ for the subdwarf and $0.065\,M_\odot$ for the companion, reproducing their result for the spectoscopically derived sdB radius. In this case AA Dor rotates a little faster than synchronised. Vučković et al. (2008) were able to detect emission lines of reflected light from the surface of the cool companion and measure a lower limit for its RV semiamplitude. With this additional information they put lower limits on the masses in the AA Dor system. The subdwarf primary has to be heavier than $0.45\,M_\odot$ and the companion more massive than $0.076\,M_\odot$. These limits are not consistent with the post-RGB scenario and suggest that AA Dor is rather a post-EHB star. In this case the binary should be synchronised. And indeed, adopting the minimum sdB mass of $0.45\,M_\odot$ the binary can be solved consistently under the assumption of synchronisation. For subdwarf masses exceeding $0.49\,M_\odot$ the range of possible inclinations is not consistent with eclipses any more. This gives an upper limit for the subdwarf mass. The companion mass range is constrained to $0.087 - 0.098\,M_\odot$ compatible with a late M dwarf. It has to be noted that due to the uncertainties of the key parameters $v_{\mathrm{rot}} \sin i$

Table 4.1: Stellar parameters of candidate post-RGB objects (similar to Tab. 3.5): Effective temperatures, surface gravities, orbital periods and radial velocity semi-amplitudes of the visible components. The parameters are taken from [1]Edelmann 2005a, [2]Heber et al. 2003, [3]Maxted et al. 2000b, [4]Moran et al. 1999, [5]Rauch 2000, [6]Rauch & Werner 2003, [7]Saffer et al. 1998 and this work[8].

System	T_{eff} [K]	$\log g$	P [d]	K [km s^{-1}]
PG 2345+318[4,7]	27500	5.70	0.2409458 ± 0.000008	141.2 ± 1.1
AA Dor[5,6]	42000	5.21	0.26158 ± 0.000001	39.19 ± 0.05
PG 1247+554[3,8]	30500	6.36	0.602740 ± 0.000006	32.2 ± 1.0
HD 188112[1,2]	21500	5.66	$0.60658125 \pm 0.00000005$	188.4 ± 0.2

Table 4.2: Projected rotational velocities of candidate post-RGB binaries (similar to Tabs. 3.2, 3.1). For binaries with high $v_{\mathrm{rot}} \sin i$ helium lines and Balmer lines cores (H/He) are used instead of metal lines. [1]Results taken from Rauch & Werner 2003.

	m_B [mag]	S/N	N_{lines}	$v_{\mathrm{rot}} \sin i$ [kms^{-1}]	Instrument
PG 2345+318	14.4	92	21	12.9 ± 0.8	HRS
AA Dor[1]	10.8	200	H/He	47 ± 5	UVES
PG 1247+554	12.4	87	14	6.8 ± 1.0	HRS
HD 188112	10.0	187	1/He	20 ± 2	FEROS

and $\log g$ the propagated error in i is quite high. We conclude that AA Dor is a post-EHB star with a mass near the canonical value in synchronised rotation.

Most recently Fleig et al. (2008) analysed UV-spectra of AA Dor obtained with FUSE. From five blended metal lines they derive a rotational velocity of $35 \pm 5\,\mathrm{kms}^{-1}$ consistent with synchronised rotation, if the primary should be a post-RGB star. It has to be pointed out that the resolution of the FUSE spectra (about 1 Å) is one order of magnitude lower than the resolution of the UVES spectra used by Rauch & Werner (2003) to determine $v_{\mathrm{rot}} \sin i$. This makes FUSE spectra much less suitable for $v_{\mathrm{rot}} \sin i$ measurements of relatively slow rotators. We therefore still consider the result obtained by Rauch & Werner (2003) and with this the post-EHB scenario as more reliable.

If the observed division between synchronously rotating (post-)EHB stars and non-synchronously rotating post-RGB stars is correct (especially the sample size of known post-RGB binaries has to be enhanced to check this) the super-synchronously rotating systems KPD 1946+4340 and UVO 1735+22 could be explained as post-RGB binaries. In this case the masses of the subdwarfs should be $\approx 0.3\,M_{\odot}$ (Fig. 4.5). Especially for the bright star UVO 1735+22 this prediction could be verified by obtaining a trigonometric parallax.

Table 4.3: Derived ranges of inclination angles, companion masses and possible nature of the companions (similar to Tab. 3.6). Additional constraints to clarify the nature of the unseen companion: [r]The detection of a reflection effect from a cool MS/BD. The presence of eclipses[ec] in the light curves. These informations are taken from [1]Green et al. 2004 and [2]Rauch 2000

System	i [deg]	M_{sdB} $[M_\odot]$	M_{comp} $[M_\odot]$	Companion
PG 2345+318[1]	–	–	–	WD[ec] not synchronised
AA Dor[2]	$48 - 90$	$0.45 - 0.49$	$0.088 - 0.098$	MS[r,ec]
PG 1247+554	–	0.29	–	not sychronised
HD 188112	–	0.24	>0.72	WD/NS/BH[f] not synchronised

4.6.2 Non-synchronous rotation in post-RGB binaries and the implications

The obvious deviation from synchronism in all post-RGB subdwarf close binaries analysed so far is remarkable and requires an explanation. In the case of the more massive post-RGB stars ($> 0.30 \, M_\odot$) this explanation may be given by their typical evolutionary timescales (Driebe et al. 1998). These stars are expected to evolve towards the WD cooling sequence within a few million years or less. In the low mass post-RGB regime the evolutionary timescales get similar to the lifetime on the EHB. In Fig. 4.4 synchronisation timescales for the five proposed post-RGB stars from our sample are calculated and divided by the lifetimes on the post-RGB tracks corresponding to the primary masses (Driebe et al. 1998). It has been assumed that the post-RGB stars have the same internal structure as the EHB stars and the minimum mass of the secondaries derived from the mass functions have been adopted. Due to the lower masses of the primaries, both their radii and the companion masses are much smaller than in the case of helium core burning stars. This leads to much longer synchronisation times near or exceeding the corresponding post-RGB lifetimes compared to the EHB stars (see Fig. 4.1) and explains why post-RGB are not synchronised.

What has not been taken into account so far was the different internal structure of (post-)EHB and post-RGB stars. While the first ones burn helium in their cores (or in a shell) the latter ones are just cooling down and develop a more and more degenerate core. It is known that WDs in close binaries are in general not synchronised unless they are in extremely close AM CVn systems with mass transfer or they are spun down by strong magnetic fields like in polars. Campbell (1984) calculated theoretical timescales for the synchronisation of double degenerate binaries. According to his calculations an AM CVn system with an orbital period of 0.03 d takes about 10^9 yr to get synchronised. Since the mechanism Zahn (1977) suggested to be responsible for the synchronisation of hot stars requires the excitation of dynamical tides at the border region between convective core and radiative envelope, it has to be investigated how this should work in the partly degenerate cores of post-RGB stars. Due to the different internal structure it can therefore be concluded that tidal synchronisation in post-RGB stars should be much less efficient than in (post-)EHB stars. Hence the numbers given in Fig. 4.4 are most likely lower limits, which makes it even less likely that these binaries are synchronised.

Our analysis revealed that most sdB binaries with periods shorter than 1.3 d can be solved
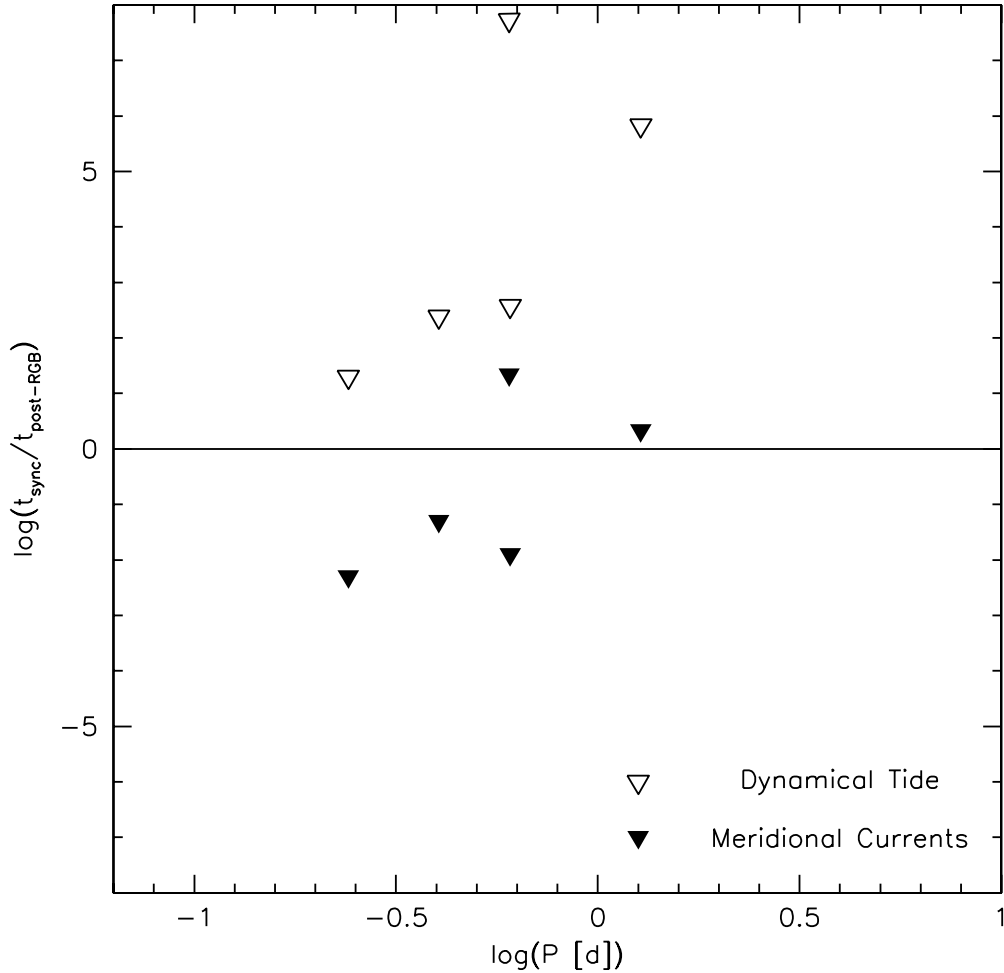
Figure 4.4: The logarithm of the orbital period is plotted against the synchronisation times of Zahn (1977, open symbols) and Tassoul & Tassoul (1992, filled symbols) both divided by the lifetime on the post-RGB track corresponding to the primary mass (Driebe et al. 1998) and in logarithmic scale. The solid horizontal line marks border between synchronisation within the lifetime and synchronisation times longer than the lifetime. None of the systems can be solved with the assumption of synchronisation.

consistently under the assumption of synchronisation. Binaries with periods up to $0.6\,\mathrm{d}$ were shown to be synchronised with independent methods (light curve modelling and asteroseismology). All subdwarf binaries with orbital periods longer than $1.7\,\mathrm{d}$ rotate faster than synchronised. This means that at this limiting period the synchronisation time most likely exceeds the EHB lifetime. Important constraints have been put on theoretical models dealing with orbital synchronisation in hot subdwarf binaries.

What are the implications for our candidate sample of 9 sdB binaries with massive compact companions? Looking at Fig. 4.6 the red circles mark these stars, which are more or less
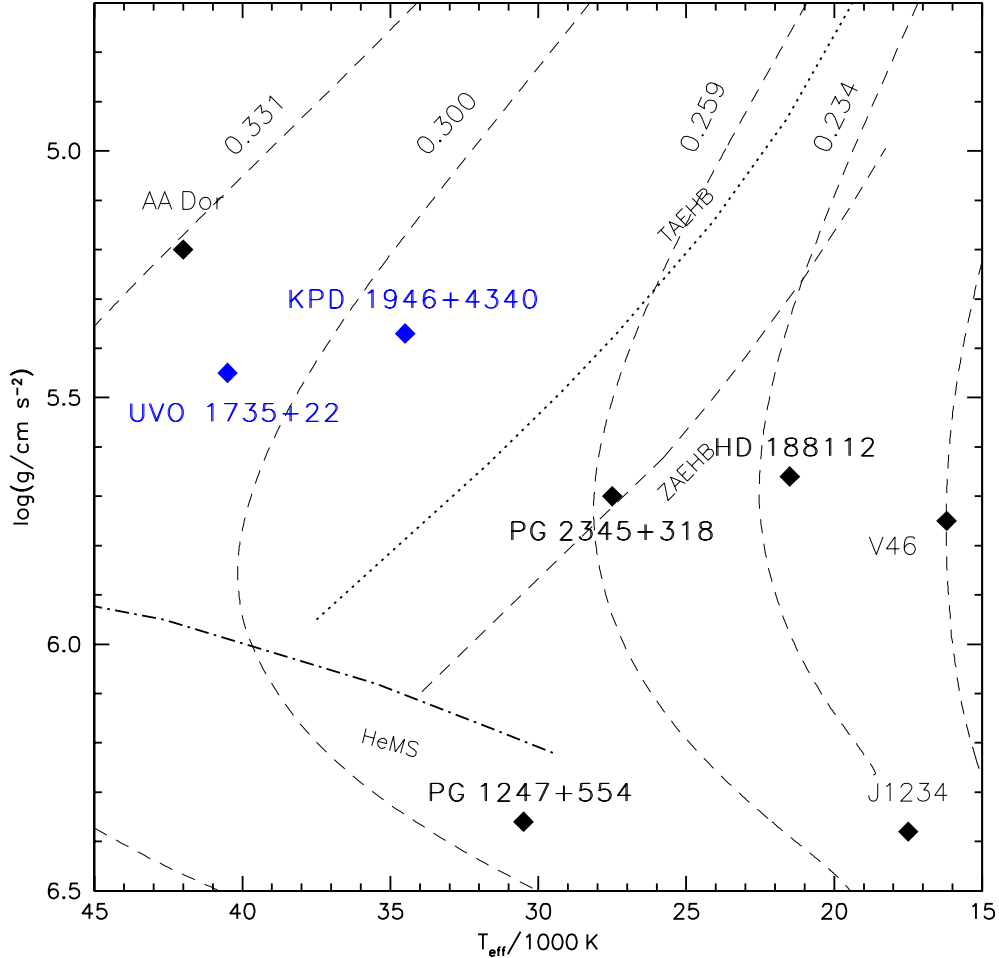
Figure 4.5: $T_{\text{eff}} - log\,g$-diagram. Helium main sequence and EHB are superimposed with post-RGB evolutionary tracks from Driebe et al. (1998) for different masses. The black filled diamonds mark known post-RGB binaries and candidates. AA Dor turned out to be more likely a post-EHB star (see text).

randomly distributed all over the EHB. One could argue that at least three of them are situated very near the Zero Age EHB (ZAEHB) and may therefore not be sychronised. But the exact location of the EHB in the T_{eff}-$log\,g$-diagram depends on several parameters, some of them quite uncertain (like the thickness of the hydrogen layer, see Han et al. 2002), and is therefore not carved in stone. The orbital periods of these binaries range from 0.26 d to 0.83 d were synchronisation should be established according to the results presented here. Six of them have periods even shorter than 0.6 d at which period synchronisation could be proved for PG 0101−039 (Geier et al. 2008). And four of these binaries have periods shorter than 0.38 d, the period of the binary Feige 48, which could be shown to be synchronised by asteroseismology (van Grootel et al. 2008). Given these short orbital periods, the binaries in question are very likely synchronised.
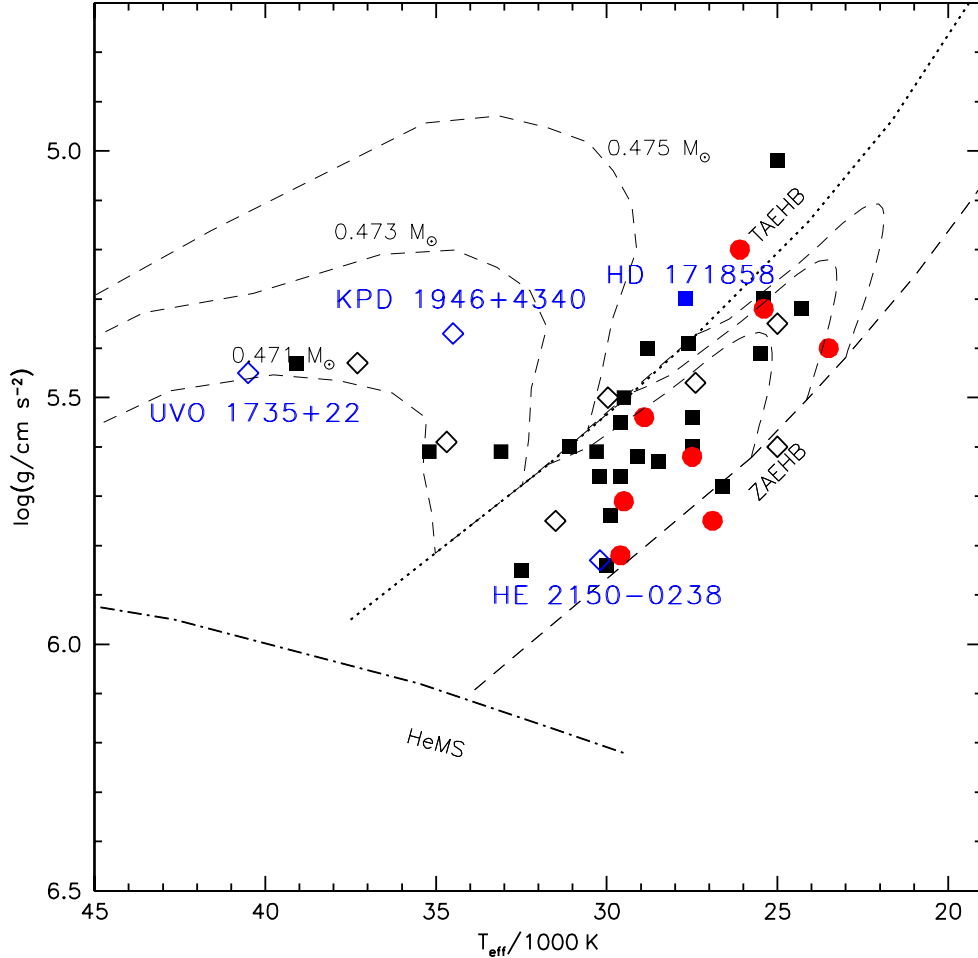
Figure 4.6: $T_{\text{eff}} - \log g$-diagram. Helium main sequence and EHB are superimposed with EHB evolutionary tracks from Dorman et al. (1993) for different masses. The black filled rectangles mark binaries, which could be solved consistently under the assumption of synchronisation. The red filled circles mark the subdwarfs with heavy compact companions. All binaries with inconsistent solutions are marked with blank diamonds. Objects of special interest for synchronisation timescales (see text) are labeled and colored in blue.

The discovery of non-synchronously rotating post-RGB stars on the other hand seems to provide a convenient explanation for the putative high fraction of sdB binaries with massive compact companions. If these binaries should have post-RGB primaries, which cannot be ruled out with the data at hand, they shouldn't be synchronised and hence the derived companion masses would be wrong. This scenario is unlikely for two reasons. First of all, it seems that most putative post-RGB stars in binaries (including KPD 1946+4340 and UVO 1735+22) rotate faster than synchronised. The only exception is PG 2345+318. But for the putative sdB+NS/BH systems low projected rotational velocities are measured. If the sdBs should rotate even faster

than synchronised, the inclination angle would get even lower and the derived companion masses would go up.

Then the number fraction of post-RGB stars is too low to account for up to 20 % of the sdB binaries in our sample. There may be some post-RGB stars like PG 2345+318 "contaminating" the EHB, but it cannot be that many. Since the evolution of post-RGB stars to the WD cooling tracks is supposed to be uniform in time (Driebe et al. 1998), the number density of post-RGB stars above and below the EHB should be the same as on the EHB (especially at the low temperature end, where the evolutionary times are the longest), where they are hidden between the helium core burning stars. This is not the case. In the interesting region most stars are clumped along the EHB (see e.g. Lisker et al. 2005 and Fig. 8.1). We therefore conclude that post-RGB stars are too rare to account for the observed high fraction of sdB binaries with heavy compact companions.

Chapter 5

The formation of sdB+NS/BH binaries

The exciting discovery of sdB+NS/BH binaries seems to challenge our understanding of stellar evolution. Not many neutron stars or stellar mass black holes could be found up to now. On the other hand non-interacting binaries containing such objects should exist, since X-ray binaries only represent a relatively short phase of stellar evolution. The existence of sdB+NS/BH systems requires an appropriate formation channel. Fortunately, Podsiadlowski (priv. comm.) was able to explain the formation of such systems performing binary evolution calculations.

Neutron stars and stellar-mass black holes are the remnants of massive stars ending their lifes in supernova explosions. Detecting these exotic objects is possible when they are in a close orbit with another star. If matter is transferred from the companion star to the compact object, X-rays are emitted.

Without ongoing mass transfer the companion remains invisible, but can be detected indirectly from the reflex motion of the visible star, which causes periodic variations of its radial velocity (RV). These variations are measureable via the Doppler effect from spectral line shifts. Stellar evolution models predict the existence of a hidden population of such compact objects.

Because neutron stars and black holes are rare, it is surprising to find such a large fraction in our sample. How do such systems form? The evolution that leads to such systems requires an initial binary, consisting of a primary star that is sufficiently massive to produce a neutron star or black hole, and a companion, the progenitor of the hot subdwarf, of typically several solar masses. The initial orbital period has to be quite large (a few to 20 years), so that mass transfer only starts late in the evolution of the star, and these systems generally experience two mass-transfer phases and one supernova explosion (see Fig. 5.1). The short orbital periods observed for our systems imply that the second mass-transfer phase from the red giant progenitor of the subdwarf to the compact companion had to be unstable, leading to a common-envelope and spiral-in phase of the compact object. The condition for unstable mass transfer constrains the mass of the progenitor to be larger than the mass of the compact object (otherwise, mass transfer would be stable and lead to a much wider system, Podsiadlowski et al. 2002). Fig. 5.1 illustrates the evolution that leads to systems of this type for two typical examples. While this scenario can explain most of our systems with high-mass compact components, the inferred masses of the putative black holes in PG 1232−136 and PG 1743+477 are somewhat larger than we would estimate ($\leq 3\,M_\odot$) for a $0.5\,M_\odot$ sdB star. This may suggest that these systems have experienced another mass-transfer phase after the two common-envelope phases in which mass

was transferred from the sdB star to the compact object. It should also be noted that, while we assume here that the mass of the subdwarf is $\sim 0.5\,M_\odot$, consistent with the properties of the observed systems, the sdB mass range allowed by this scenario is $0.3 - 1.1\,M_\odot$ for the neutron-star systems and $0.5 - 1.1\,M_\odot$ for the black-hole systems. Compared with the mass range of $0.3 - 0.7\,M_\odot$ for the standard evolutionary channel (Han et al. 2002, 2003), the subdwarf may therefore be more massive. An independent determination of the sdB mass by (e.g. by obtaining parallaxes) could therefore help to verify this scenario.

At the beginning of the second mass-transfer phase, these systems are expected to pass through a short X-ray binary phase, lasting $\sim 10^5\,\mathrm{yr}$, in which a neutron star may accrete up to $\sim 10^{-3}\,M_\odot$ and become a moderately recycled millisecond pulsar (Podsiadlowski et al. 2002). This links these system to the X-ray binary population (in a sense, they are failed low-mass X-ray binaries). Population synthesis estimates (Pfahl et al. 2003) suggest that up to one in 10^4 stars in the Galaxy experience this evolution, implying that of order $1\,\%$ of all hot subdwarfs should have neutron-star or black-hole companions. This means that tens of thousands of these systems could exist in the Galaxy compared to just about 300 known X-ray binaries.

According to this theoretical calculations about $2\,\%$ of all sdBs in close binary systems should have massive compact companions like neutron stars or black holes. This number fraction is ten times less than we observe. We have to point out that close sdB+NS/BH binaries are predicted by binary evolution theory. The question is therefore not, whether such systems exist, but how many of them are present in our Galaxy.

Formation of subdwarfs with neutron stars
Initial binary: $M_1 = 15\,M_\odot$, $M_2 = 3\,M_\odot$, $P_{orb} \sim 4\,\mathrm{yr}$.

First unstable mass transfer (when the primary is a red supergiant; case C transfer) leading to a common-envelope and spiral-in phase.

Helium-star binary with $M_{He} = 5\,M_\odot$ and $M_2 = 3\,M_\odot$, $P_{orb} = 10\,\mathrm{d}$.

Supernova (Type Ib/c) of the primary, producing a neutron star with $M_{NS} \simeq 1.4\,M_\odot$ and $M_2 = 3\,M_\odot$ in a highly eccentric orbit with $P_{orb} \sim 0.5\,\mathrm{yr}$.

Second unstable mass transfer (when the secondary is a red giant; case B mass transfer) after a brief X-ray binary phase.

Helium-core burning hot subdwarf with $M_{sdb} \simeq 0.5\,M_\odot$ and a neutron star in an ultracompact orbit with $P_{orb} \simeq 10\,\mathrm{hr}$.
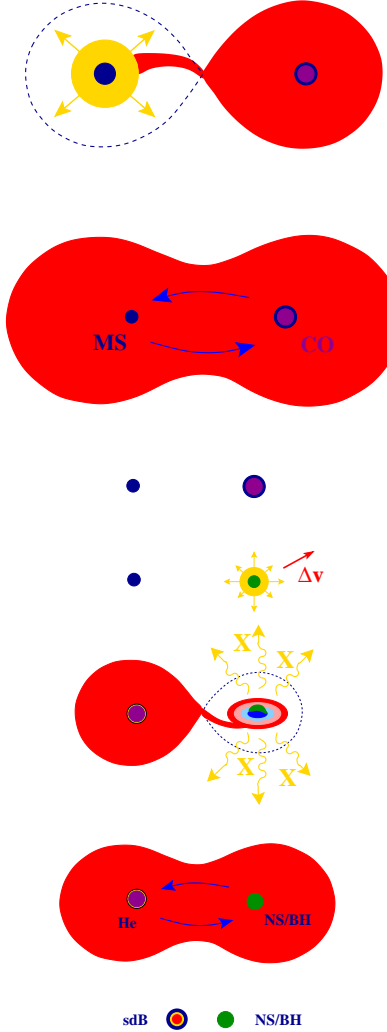
Formation of subdwarfs with black holes
Initial binary: $M_1 = 30\,M_\odot$, $M_2 = 5\,M_\odot$, $P_{orb} \sim 10\,\mathrm{yr}$.

First unstable mass transfer (when the primary is a red supergiant; case C transfer) leading to a common-envelope and spiral-in phase.

Helium-star binary with $M_{He} = 10\,M_\odot$ and $M_2 = 5\,M_\odot$, $P_{orb} = 20\,\mathrm{d}$.

Supernova (Type Ib/c) of the primary, producing a black hole with $M_{BH} \sim 4\,M_\odot$ and $M_2 = 5\,M_\odot$ in a highly eccentric orbit with $P_{orb} \sim 1\,\mathrm{yr}$.

Second unstable mass transfer (when the secondary is a red giant; case B mass transfer) after a brief X-ray binary phase.

Helium-core burning hot subdwarf with $M_{sdb} \simeq 0.5 - 1\,M_\odot$ and a black hole in an ultracompact orbit with $P_{orb} \simeq 10\,\mathrm{hr}$.

Figure 5.1: Schematic diagram of formation scenarios leading to hot subdwarf binaries with neutron-star (right hand panel) or black-hole (left hand panel) companions.

Chapter 6

The fraction of sdB+NS/BH systems and selection effects

It turned out that the observed fraction of sdB+NS/BH binaries is one order of magnitude higher than the theoretical predicted one. In order to compare the observed fraction of putative sdB+NS/BH binaries with the theoretical predictions, it is necessary to correct these numbers for selection effects. It has to be pointed out that our sample size of 32 binaries only allows to do small number statistics. The purpose of this chapter is to investigate some important selection effects in a qualitative way and try to show that these selection effects are most likely responsible for some putative inconsistencies in our results.

6.1   Projected rotational velocity and quality of the data

The most important test for the overall consistency of our results is the comparison of the derived binary inclinations (under the assumption of canonical sdB mass $0.47\,M_\odot$) with the expected random distribution. For geometrical reasons it is much more probable to observe high inclination systems than binaries with low inclination (see Gray 1992 for a very clear explanation of this effect and Fig. 6.1). In Fig. 6.2 an overabundance of binaries with low inclination can be seen, while there is an apparent lack of binaries with high inclination. Even stranger appears the fact that all of our putative sdB+NS/BH binaries have low inclinations ranging from $13°$ to $41°$.

To explain this apparent discrepancy one has to remember the process of measuring projected rotational velocities described in Sect. 3.3–3.5. Metal lines can be used to measure $v_{\rm rot}\sin i$ up to about $25\,{\rm kms}^{-1}$ unless the data has excellent quality. Helium lines and Balmer line cores start to get sensitive at typical $v_{\rm rot}\sin i$ of about $50\,{\rm kms}^{-1}$ in medium quality data (S/N=$20-30$). This leads to a blind spot of our analysis method for projected rotational velocities between $\approx 25\,{\rm kms}^{-1}$ and $\approx 50\,{\rm kms}^{-1}$, which could only be avoided with excellent high S/N spectra (How difficult it is to determine $v_{\rm rot}\sin i$-values in this range can be seen in the case of AA Dor, where three attempts have been made by Rauch 2000, Rauch & Werner 2003 and Fleig et al. 2008 up to now). Using the data at hand binaries with such projected rotational velocities could not be analysed.

Under the assumption of synchronisation, the equitorial rotational velocities of all binaries in our sample can be calculated, if the orbital parameters and the surface gravities are known (see Sect. 3.1). Binaries with orbital periods between $0.2\,{\rm d}$ and $0.4\,{\rm d}$ turn out to have equatorial
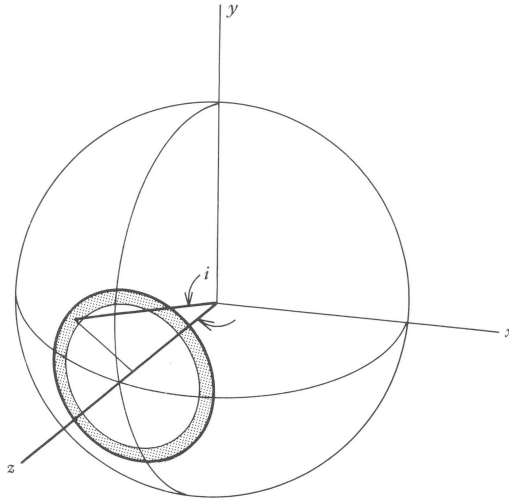
Figure 6.1: For randomly oriented axes, the probability to look at any inclination angle i is proportional to the area of the shaded ring between i and $i + \mathrm{d}i$. High inclinations are therefore most probable, while the probability of looking at a binary with $i = 0°$ goes to zero. The picture is taken from Gray (1992).

.

rotational velocities falling right into the blind spot. This means that high inclination systems ($\sin i \approx 1$) with such orbital periods could not be analysed, because in this case $v_{\mathrm{rot}} \approx v_{\mathrm{rot}} \sin i$. And that leads to a selection of low inclination binaries in this range of orbital periods. Fig. 6.3 again shows the distribution of inclinations. This time all eight binaries with periods in the suspicious range are plotted in red and excluded from the sample. The distribution of the remaining stars is fully consistent with the random distribution expected.

6.2   Radial velocity variability

Another very important selection effect is caused by the way, RV surveys are usually conducted. A sample of known subdwarf stars is observed two times or more at different epochs. The shifts in RV are measured for all stars and the ones with significant shifts are classified as RV variable. Most surveys for close binary sdBs have been conducted with medium resolution spectrographs ($1 - 2\,\text{Å}$) resulting in a detection limit of about $10\,\mathrm{km s^{-1}}$. Follow-up observations usually focus on the stars with the highest RV shifts. This implies that even if significant, but low RV shifts were detected these stars may never be reobserved, mainly because of the way observing time is distributed among astronomers and the pressure to present interesting results within a short time.

Depending on the yet uncertain properties of the sdB binary population, especially the distribution of orbital periods and subdwarf as well as companion masses, this has a huge influence on the selection of the sample, which therefore gets highly biased. We know that most of the analysed close sdB binaries have late M or WD companions with masses ranging from $0.1 - 0.7\,M_\odot$ and periods between $0.1 - 1.0\,\mathrm{d}$. Short period systems with more massive
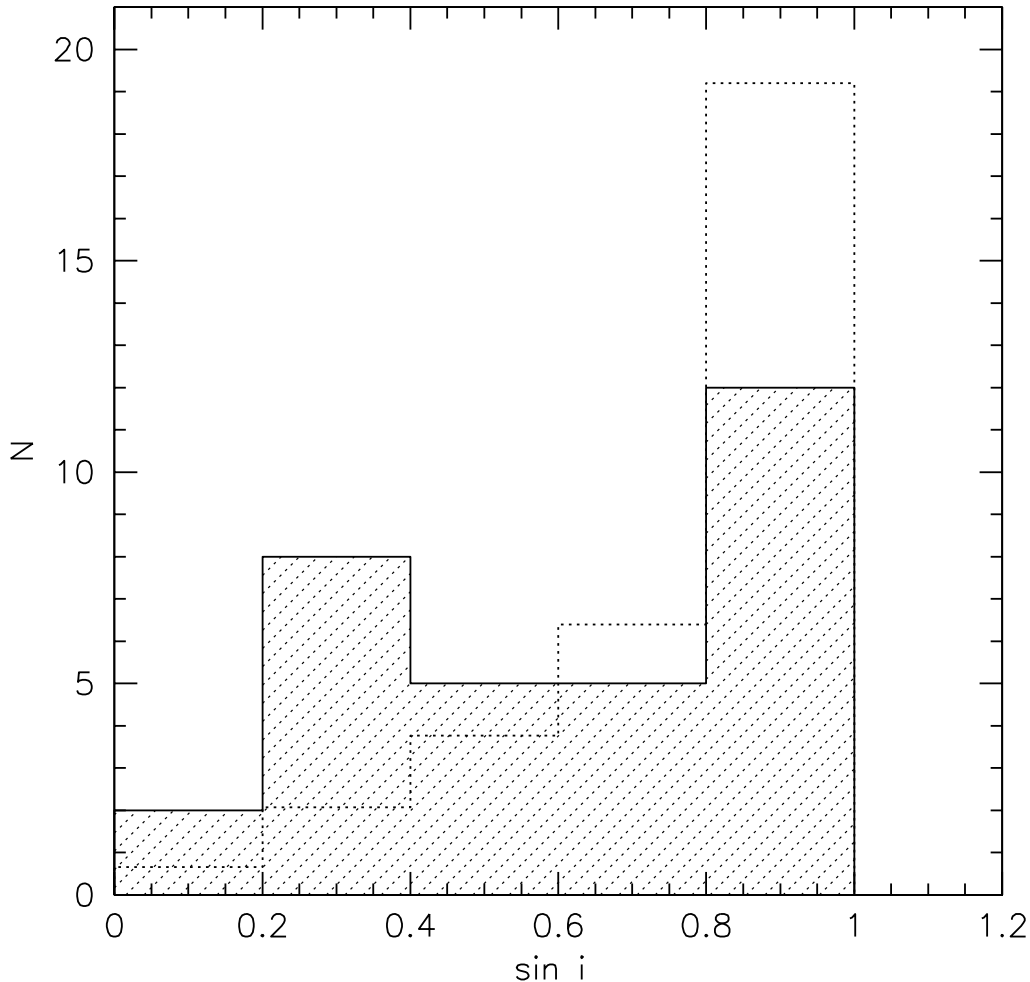
Figure 6.2: $\sin i$ plotted against number of binaries under the assumption of canonical sdB mass $0.47\,M_\odot$. The expected random distribution for the 32 programme binaries calculated as described in Gray (1992) is plotted as dotted histogram.

companions have high radial velocity amplitudes, whereas binaries with longer orbital periods and/or less massive companions show much less RV variation. Roughly $50\,\%$ of all close binaries present are seen at low inclination. This means that the projected radial velocity amplitude is lower than in high inclination systems. It is therefore less likely (or even not possible) to measure a high RV shift at two different epochs. Conducting an RV survey we therefore select against low mass companions (and/or long orbital periods) at low inclination. If on the other hand a binary with low inclination shows a high RV shift, it must have a massive compact (and/or short orbital period).

From Tab. 3.6 it can be verified whether our sample is biased by this effect. Under the assumption of canonical sdB masses 10 binaries have companion masses lower than $0.3\,M_\odot$. From these binaries seven are seen at high inclinations ($i > 50°$). Since much more single-lined,
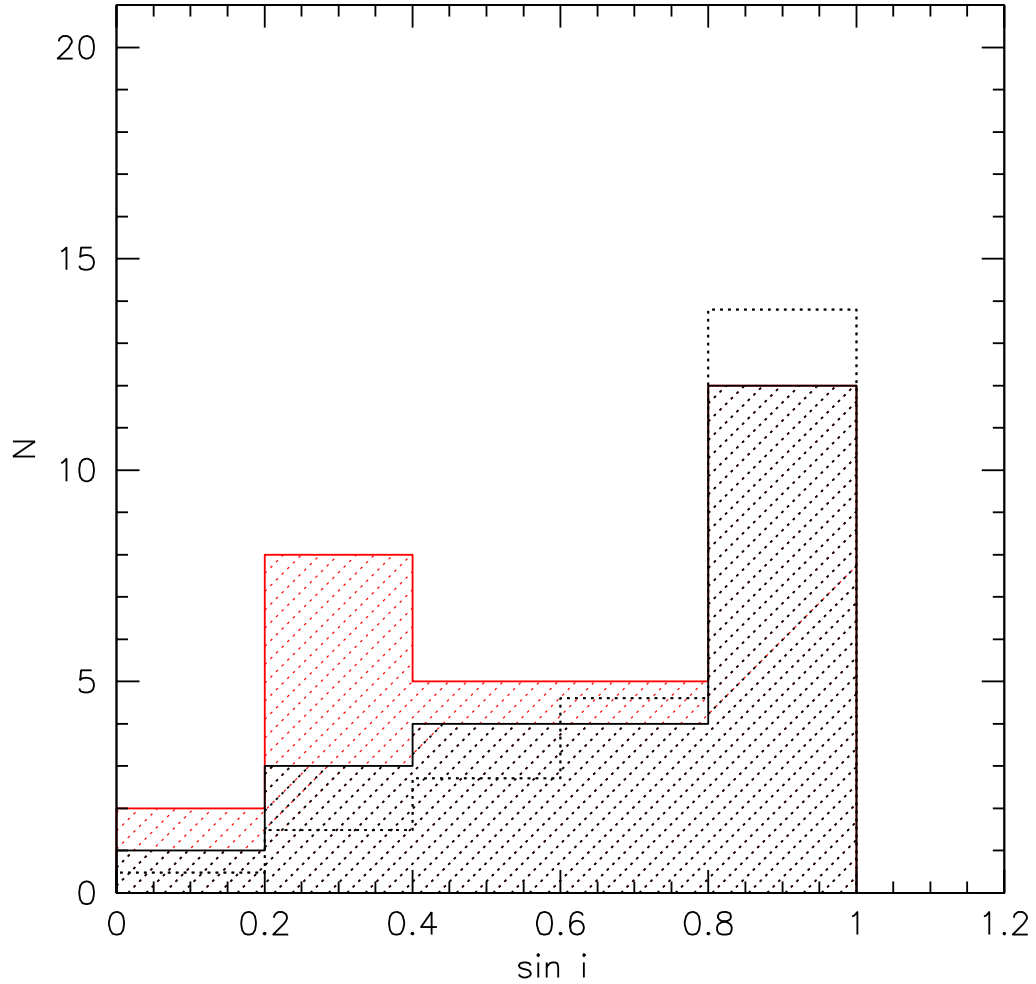
Figure 6.3: $\sin i$ plotted against number of binaries under the assumption of canonical sdB mass $0.47 \, M_\odot$. Binaries with orbital periods between $0.2 \, d$ and $0.4 \, d$ are plotted as red histogram. The expected random distribution for the remaining programme binaries calculated as described in Gray (1992) is plotted as dotted histogram.

close binary sdB have low mass companions than companions exceeding $1.0 \, d$, one can state that high inclination binaries observed so far have most likely low mass companions. From a total of 10 binaries with companion masses higher than $0.9 \, M_\odot$ we found 8 to be seen at low inclination. This selection effect explains qualitatively the high fraction of massive companions at low inclinations.

6.3 Photometric selection

A huge fraction of subdwarf binaries with short periods and high inclinations have initially been found due to indicative features in their light curves as a by-product of photometric surveys searching for pulsating sdBs (see Sect. 2.1). Five of the binaries in our sample have been discovered in this way. The photometric selection effect biases our sample mainly towards short period systems with M dwarf companions, where the reflection is detectable (e.g. the prototype HW Vir, Menzies 1986). If the precision of the time resolved photometry is sufficiently high, also short period systems with heavy compact companions are singled out, as soon as light variations caused by the ellipsoidal deformation of the tidally distorted subdwarf become detectable. This led to the discovery of KPD 1930+2752 (Billerés et al. 2000), the sdB binary with the highest companion mass independently confirmed by photometry (Geier et al. 2007).

6.4 The high fraction of sdB+NS/BH binaries and selection effects

Due to the highly biased sample it is not possible to derive quantitative information like true number fractions out of it. The selection effects presented so far are only the most important ones. Other biases like e.g. the selection of targets with high mass functions for the high-resolution follow-up or the lack of metal lines at the hot end of the EHB also play a role and it is impossible to disentangle all these superimposed effects. A really unbiased sample is the only way to get reliable numbers. But this would be a gigantic life time effort for one single astronomer.

We conclude that selection biases are in part responsible for the apparent high fraction of sdB+NS/BH binaries in our sample and the effect that most of these binaries are seen at low inclination. But this alone cannot account for a fraction of up to 20 % of our sample. If these systems exist, about 50 % of them should be seen at high inclination. These binaries would have radial velocity semiamplitudes of up to $500 \, \mathrm{kms^{-1}}$ and would therefore show high RV shifts. The minimum companion masses of such systems derived directly from the mass function without any other assumptions should already exceed the Chandrasekhar limit. Up to now no such binary has been found.

Theory predicts a fraction of about 2 % of all close binary sdBs to have NS/BH companions (see Chap. 5). That means about 1 % have NS/BH companions and are seen at high inclination. The catalog of Ritter & Kolb (1998) counts 81 close binary sdBs published until December 2007. For 66 of them a companion mass or minimum mass is given. This sample should contain only one sdB+NS/BH binary at high inclination (or maybe two if selection effects are taken into account). A non-detection is therefore roughly consistent with theoretical predictions. Allowing for minimum companion masses of less than $1.4 \, M_\odot$, but still more massive than the average WD mass of $0.6 \, M_\odot$, two binaries are found in the catalog ($M_{\mathrm{comp}} > 0.90 \, M_\odot$ KPD 1930+2752, $M_{\mathrm{comp}} > 0.72 \, M_\odot$ HD 188112). On the other hand a non-detection of sdB+NS/BH binaries in previous RV surveys gets very unlikely, if the fraction of these binaries should be 20 % or even 10 % (arbitrarily corrected for selection effects).

We therefore conclude that selection effects alone are not able to explain the high fraction of sdB+NS/BH binaries and although the non-detection of such systems in previously conducted RV surveys is still compatible with binary evolution theory, it is not consistent with the fraction of such binaries found in our sample.
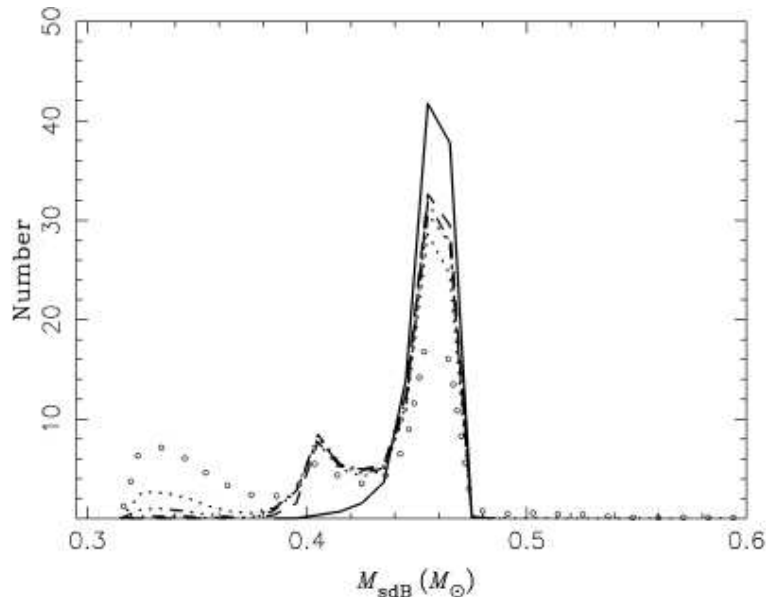
Figure 6.4: Simulated distribution of sdB masses for binaries formed via CE ejection. The different curves correspond to simulations with different combinations of CE ejection parameters. The fraction of low mass sdBs is very sensitive to these parameters. The figure is taken from Han et al. (2002).

6.5 Low mass EHB stars and the fraction of sdB+NS/BH binaries

It was argued that our analysis method works and yields consistent results for low mass companions, which could be verified for some special objects by independent means. The assumption of tidal synchronisation in these binary systems has been shown to be justified. The high fraction of sdB+NS/BH systems is not compatible with theoretical predictions as well as the non-detection of such systems in prior surveys. It is not possible to explain this discrepancy by selection effects (although they obviously play a role) or a contamination of the EHB with non-synchronously rotating post-RGB objects.

We therefore conclude that the companion masses of most binaries in question have to be lower than taken into account up to now despite the fact that our assumptions and analysis method turned out to be correct. This can only be achieved, if the masses of the sdB primaries are much lower than the canonical mass of $0.47\,M_\odot$. As can be seen in Tab. 3.6 there is indeed a possibility for a subdwarf star which underwent the CE channel to ignite core helium burning at masses down to $0.3\,M_\odot$ (Han et al. 2002, 2003; Hu et al. 2008), although this sdB masses are much less probable (see Fig. 6.4). In Fig. 6.5 the companion mass distribution is plotted under the extreme assumption that all sdBs have this minimum mass for core helium burning (or the minimum mass allowed by other constraints). Looking at the low mass regime and comparing the distribution with Fig. 3.13 one can immediately see that this assumption leads to unphysical results. The distribution of low mass companions peaks at masses lower than $0.2\,M_\odot$, which is very unlikely especially for WD companions.

Under this extreme assumption only the companions of PG 1232−136 and PG 1743+477 remain significantly more massive than the Chandrasekhar limit. The companion of HE 0532−4503 falls slightly below the limit. The fraction of sdB+NS/BH systems drops from 20% to 5%. This number is much closer to the theoretical prediction and more consistent with the results of prior RV studies. Nevertheless it has to be pointed out that even under the most conservative assumptions we end up with at least two sdB+NS/BH binaries.

To explain our results it is necessary that most sdBs should have masses near the canonical value, especially the ones with low mass companions. A certain fraction of sdBs with low inclinations and high companion masses are required to have masses lower than the canonical value. Detailed binary population synthesis calculations will be necessary to verify this scenario. The predicted low masses of the sdBs should be checked by observations (e.g. trigonometric parallaxes for the brighter ones).
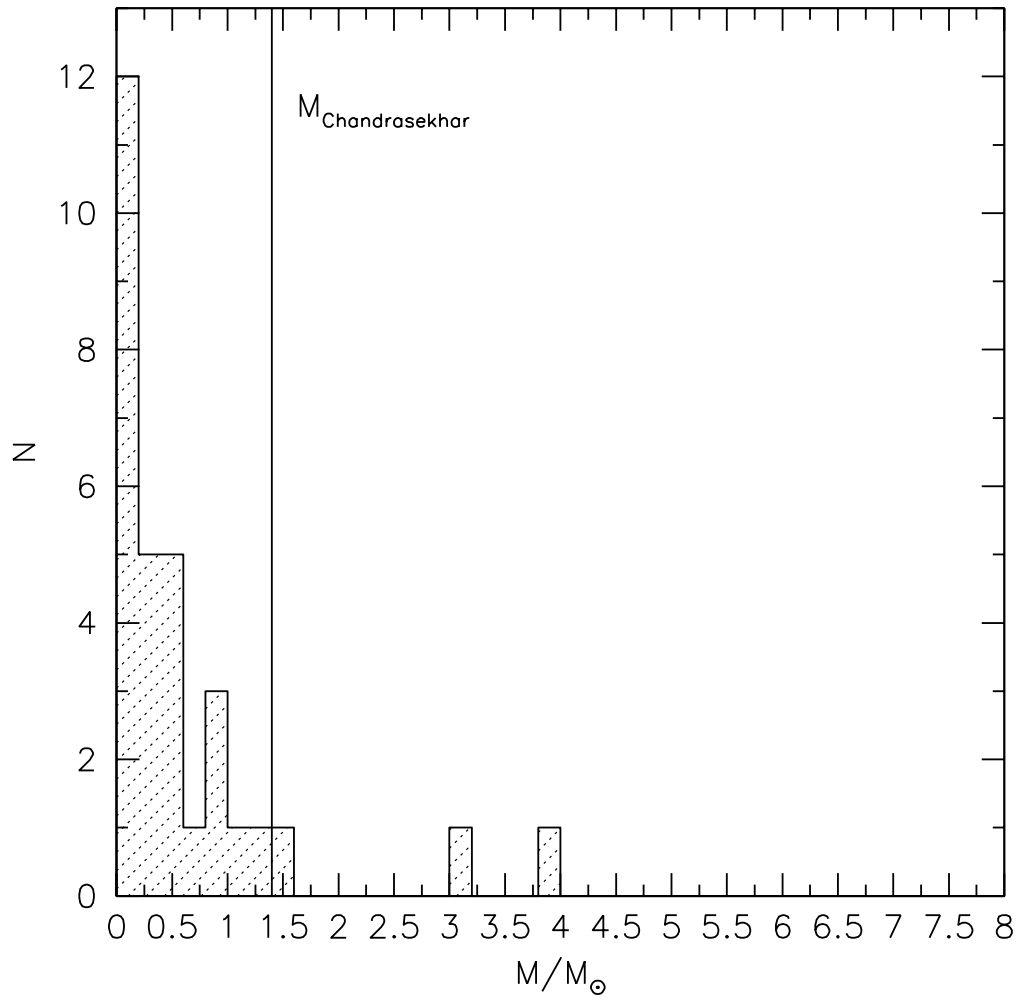
Figure 6.5: Mass distribution of the unseen companion stars (see Fig. 3.12). The companion mass is plotted against the total number of binaries under the assumption of the lowest possible sdB mass $0.30\,M_\odot$. The solid vertical line marks the Chandrasekhar limit. The last bin at $4.0\,M_\odot$ is a lower limit.

Chapter 7

Rotational properties of single sdBs

7.1 Previous work

Our sample also contains single and wide binary sdBs. This allows us for the first time to study the intrinsic rotational properties of sdBs. While the rotational properties of Blue Horizontal Branch (BHB) stars both in globular clusters and in the field are thoroughly examined (see Behr et al. 2003b and references therein), there is no systematic study for EHB stars. From $v_{\mathrm{rot}} \sin i$ measurements of single sdBs, which are considered to populate the EHB, it is known that most of these stars are slow rotators with $v_{\mathrm{rot}} \sin i < 10\,\mathrm{km s}^{-1}$ (Heber et al. 2000; Napiwotzki et al. 2001; Edelmann 2005a). This means that the projected rotational velocity of most sdBs can only be measured from weak metal lines in high resolution spectra.

Two single sdBs are known to have broadened lines, which can only be fitted with $v_{\mathrm{rot}} \sin i > 25\,\mathrm{km s}^{-1}$. These two stars (PG 1605+074 Heber et al. 1999; Balloon 090100001 Telting et al. 2008) turned out to be pulsating sdBs with very strong main pulsation modes. Recently Telting et al. (2008) showed that the line broadening of Balloon 090100001 is in part caused by unresolved short period pulsations. The same effect very likely causes most of the line broadening of PG 1605+074.

Subdwarfs in close binaries with short periods of about 0.1 d have high projected rotational velocities ($v_{\mathrm{rot}} \sin i \approx 40 - 150\,\mathrm{km s}^{-1}$) due to the tidal interaction with their companions. These stars are spun up until orbital synchronisation is reached. Since all of these objects have very short orbital periods around 0.1 d it is not surprising, that they are spun up by their close companions (see Chap. 4).

On the other hand tidal interaction with the companion in the much more numerous close sdB binaries with typical periods between 0.3 d and 1.0 d was not investigated so far. To prove whether a close companion influences the rotation of an sdB star, it is at first necessary to get an idea of the intrinsic rotational velocity of these objects. Since only the projected rotational velocity can be measured, a huge sample of sdBs not showing RV variability must be analysed to see whether their $v_{\mathrm{rot}} \sin i$-distribution is uniform or shows more than one peak. A sample of known close binary sdBs has to be analysed in the same way. If the $v_{\mathrm{rot}} \sin i$-distribution looks different, the tidal interaction with the companions is most likely responsible. Here we report the first systematic determination of projected rotational velocities for a huge sample of single sdBs. A comparison with the $v_{\mathrm{rot}} \sin i$-distribution of the close binary sample was done in Sect. 3.6.
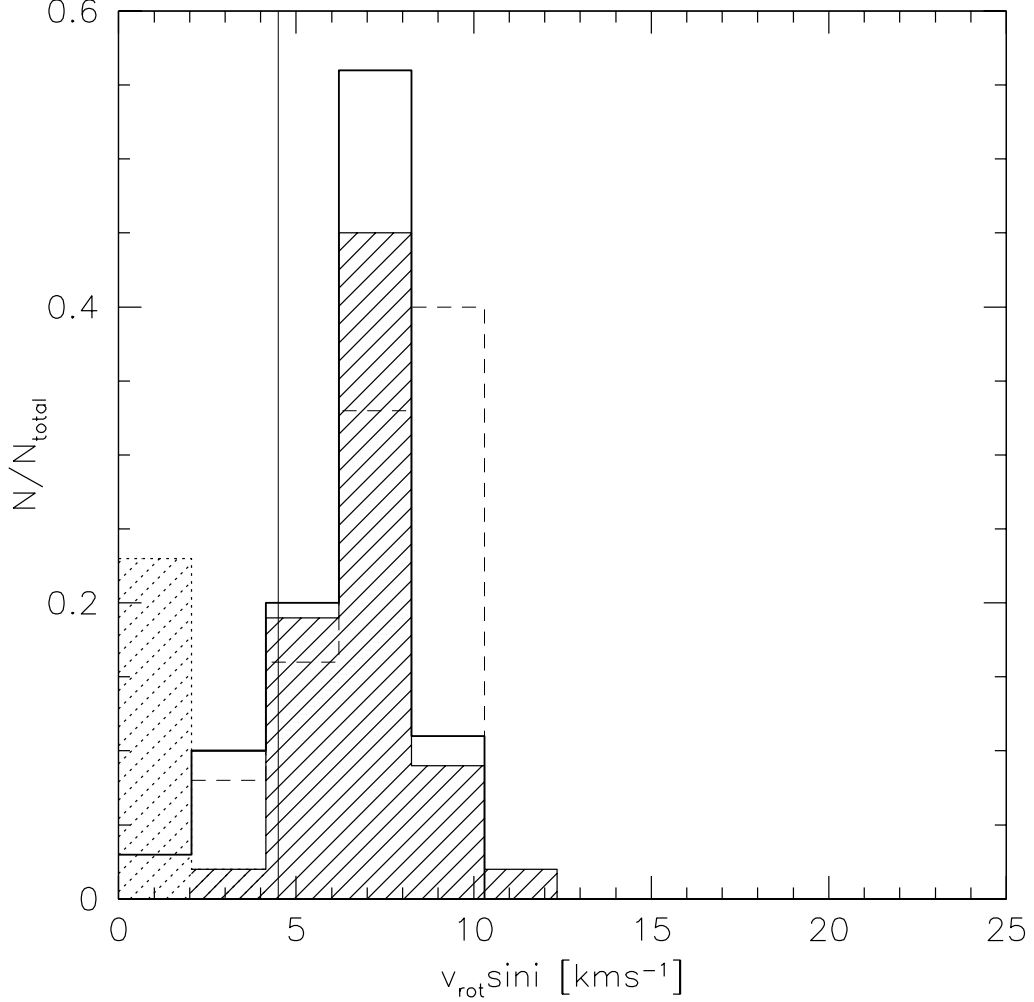
Figure 7.1: The measured $v_{\rm rot} \sin i$ of the 49 single sdBs is plotted against relative fraction of stars as shaded histogram. The size fo the bins is given by the average error of the measurements. The blank histogram marks the expected uniform distribution of $v_{\rm rot} \sin i$ under the assumption of randomly oriented polar axes and the same rotational velocity $v_{\rm rot} = 8.3 \, {\rm kms}^{-1}$ for all stars. The dashed histogram shows this distribution for $v_{\rm rot} = 9.0 \, {\rm kms}^{-1}$. The solid vertical line at $v_{\rm rot} \sin i \approx 4.5 \, {\rm kms}^{-1}$ marks the detection limit. All sdBs with lower $v_{\rm rot} \sin i$ are stacked into the first bin (dotted histogram).

7.2   Uniform rotation of single sdBs

The measured values of $v_{\rm rot} \sin i$ for single sdBs from the SPY sample are shown in Tab. 7.1. Apparent magnitude $m_{\rm B}$, S/N, average seeing and the number of fitted lines are plotted to give an impression of the spectral quality. Only four spectra could not been analysed because of low S/N or poor seeing.

All projected rotational velocities are low, ranging from below $5.0 \, {\rm kms}^{-1}$ to $10.0 \, {\rm kms}^{-1}$. To

get an idea of the intrinsic projected rotational velocities of sdBs the close binaries have to be excluded, because their rotational behaviour is likely to be influenced by their companions. The remaining 49 objects (single sdBs or wide binaries without tidal interaction) show a very interesting behaviour. Plotting the $v_{rot} \sin i$ distribution of these stars a peak at about $8 \, \mathrm{kms}^{-1}$ can be seen (see Fig. 7.1). Only one star rotates significantly faster. Assuming random orientation of the inclination angles and the same constant rotational velocity v_{rot} for all stars, it is possible to calculate the expected distribution for $v_{rot} \sin i$ (see Gray 1992). This was done for different values of v_{rot} and a χ^2 fit was performed with respect to the observed distribution. Most observed sdBs appear to have the same rotational velocity of $v_{rot} \approx 8.3 \, \mathrm{kms}^{-1}$. The theoretical distribution is very sensitive to v_{rot} as can be seen from the dashed histogram which is calculated for $v_{rot} = 9.0 \, \mathrm{kms}^{-1}$. Two populations of sdBs with different v_{rot} would be visible as bimodal distribution. One possibility could be, that there exists a population of extremly slow rotators with $v_{rot} \leq 4.5 \, \mathrm{kms}^{-1}$ which cannot be seen due to the limited quality of our data. To get statistically more significant results, more measurements at higher resolution are needed.

7.3 Implications for sdB formation scenarios

There are no theoretical predictions about the expected rotational velocities of single sdBs, which underwent the different formation channels. But the uniform distribution of low projected rotational velocities can be discussed at least qualitatively. All scenarios requiring a huge mass loss during the helium flash (see Sect. 1.3) will also lead to a loss of angular momentum. A low rotational velocity of the remnant sdBs is expected in this scenarios.

The WD merger scenario on the other hand is hardly compatible with the observed $v_{rot} \sin i$-distribution. Although Gourgouliatos and Jeffery (2006) showed, that He-WDs have to lose a lot of angular momentum during the merger process because otherwise the merged objects rotation would exceed the breakup velocity, it is very unlikely that the result of a merger has low rotational velocity. If a fraction of the observed single sdBs is formed in this way, one would expect a second peak in the distribution at higher $v_{rot} \sin i$ as seen in the case of the cooler BHB stars. Given a larger sample upper limits could be put on the contribution of the WD merger channel to the total number of single sdBs.

7.4 Rotation along the Horizontal Branch

Field Blue Horizontal Branch (BHB) stars hotter than $11\,500 \, \mathrm{K}$, the cooler neighbours of sdBs on the Horizontal Branch, behave in the same way with measured $v_{rot} \sin i \leq 8.0 \, \mathrm{kms}^{-1}$. BHB stars with lower temperatures show a bimodal distribution. Roughly one third is spinning with $v_{rot} = 30 - 35 \, \mathrm{kms}^{-1}$ and a slow population with $v_{rot} = 10 - 15 \, \mathrm{kms}^{-1}$ is also present (see Behr 2003b and references therein). The uniform behaviour at the hot end of the HB may be explained by similar formation channels, at least with respect to the angular momentum evolution.

Table 7.1: Projected rotational velocities of 49 sdBs from SPY. ^{c}Companion visible in the spectrum †Preliminary result

	m_B [mag]	S/N	seeing [arcsec]	N_{lines}	$v_{\rm rot} \sin i$ [kms^{-1}]
HE 0007−2212	14.9	29	0.6	25	7.4 ± 1.0
HE 0016+0044	14.6	29	0.7	14	6.5 ± 1.3
HE 0019−5545	15.8	22	0.8	6	5.9 ± 2.3
HE 0101−2707	15.0	33	0.8	11	8.1 ± 1.5
HE 0123−3330	15.4	29	0.7	7	6.9 ± 1.8
HE 0135−6150	16.3	15	0.7	12	5.5 ± 1.7
HE 0151−3919	14.1	44	1.1	29	< 5.0
HE 0207+0030	14.6	20	1.3	6	5.1 ± 2.3
HE 0321−0918	15.2	32	1.2	6	5.6 ± 2.3
HE 0415−2417	16.2	18	0.8	11	< 5.0
HE 0513−2354	15.8	13	1.0	18	< 5.0
HE 0539−4246	14.6	23	0.9	23	< 5.0
HE 1021−0255	15.3	31	1.6	−	−
HE 1038−2326^c	15.8	22	1.3	27	< 5.0
HE 1050−0630	13.7	48	1.2	11	7.3 ± 1.4
HE 1200−0931^c	16.2	13	0.9	12	< 5.0
HE 1221−2618 ^{c}	14.8	30	1.1	14	6.8 ± 1.6
HE 1254−1540^c	15.4	27	0.8	21	7.2 ± 1.3
HE 1352−1827	16.2	13	0.8	4	8.2 ± 2.7
HE 1407+0033	15.5	22	0.7	9	< 5.0
HE 1415−0309	16.3	12	1.5	8	< 5.0
HE 1419−1205^c	16.2	13	0.7	16	< 5.0
HE 1422−1851^c	16.3	6	0.6	10	< 5.0
HE 1441−0558^c	14.4	24	0.7	9	6.9 ± 2.0
HE 1450−0957	15.1	20	0.7	6	9.0 ± 2.4
HE 1519−0708	15.6	15	0.8	8	7.6 ± 2.1
HE 2151−1001	15.6	22	0.7	6	6.7 ± 2.4
HE 2156−3927^c	14.8	32	0.6	16	7.0 ± 1.2
HE 2201−0001	16.0	19	1.1	26	< 5.0

	m_B [mag]	S/N	seeing [arcsec]	N_{lines}	$v_{\rm rot} \sin i$ [kms^{-1}]
HE 2222−3738	14.7	33	0.8	30	8.7 ± 0.9
HE 2237+0150	15.8	18	0.8	11	8.5 ± 1.8
HE 2238−1455	16.0	23	0.8	14	< 5.0
HE 2307−0340	15.8	29	0.9	6	4.6 ± 2.3
HE 2322−0617^c	15.7	27	0.7	15	6.8 ± 1.3
HE 2349−3135	15.6	33	1.1	12	10.0 ± 1.7
HS 1710+1614	15.7	24	1.3	14	< 5.0
HS 2033+0821	14.4	26	1.1	8	7.4 ± 2.1
HS 2125+1105^c	16.4	14	0.8	8	6.0 ± 2.1
HS 2216+1833^c	13.9	32	0.9	9	5.3 ± 1.6
HS 2357+2201^r	13.3	29	0.7	26	6.1 ± 1.1
WD 0021−234^c	15.9	19	0.8	14	< 5.0
WD 0031−274	13.8	43	0.8	9	6.1 ± 1.5
WD 0109−264	13.0	62	0.7	24	7.2 ± 0.8
WD 0154−071^c	15.5	28	0.9	8	7.2 ± 2.1
WD 0258+184^c	15.2	27	1.0	12	7.2 ± 1.7
WD 1207−032	13.1	34	0.6	9	6.6 ± 1.6
WD 1433−270	15.0	37	1.2	21	5.6 ± 1.1
WD 1549−000	15.2	25	1.1	11	7.7 ± 1.8
WD 2122+157^c	14.5	30	0.8	13	7.9 ± 1.4
WD 2329−291	13.5	41	0.9	15	6.9 ± 1.2

Chapter 8

Metal Abundances of Hot Subdwarf Stars from the SPY Survey

From the observational point of view there is a need for abundance analyses of sdB stars covering the entire parameter range to search for global abundance patterns and trends. The ESO Supernovae Ia Progenitor Survey (SPY, Napiwotzki et al. 2003) provided a large set of suitable high-resolution spectra of sdBs. The atmospheric parameters have already been derived by Lisker et al. (2005). Here we present abundance analyses of 71 sdB stars covering the entire parameter range (see Fig. 8.1). This sample more than doubles the number of sdBs for which surface abundances are available.

8.1 Semi-automatic abundance analysis

71 subluminous B stars were observed in the course of the SPY project with the high resolution spectrograph UVES at the ESO VLT (Dekker et al. 2000). The spectra were reduced as described in Sect. 2.3.1. In order to derive the metal abundances we compared the observed spectra with synthetic line profiles. Metal line-blanketed LTE model atmospheres were computed for the stellar parameters given in Lisker et al. (2005) in the way described in Sect. 3.3.

A standard set of lines was chosen taking into account several criteria. First of all the lines had to be strong enough to be detectable in noisy spectra. Blends with lines of different ions were not used. Only line blends of the same ion could be handled because only one abundance was fitted to individual lines or multiplets. Some ions could not be detected in the spectra at all. In this case spectral lines of these ions were only put on the list if the derived upper limits constrained the abundance in a reasonable way. We selected a set of 69 metal lines from 24 different ions (see Tab. 8.1) and used atomic data from the lists of Kurucz (1992), Wiese et al. (1996), Ekberg (1993), and Hirata & Horaguchi (1995). For carbon, nitrogen, oxygen and silicon, the NIST database was used to obtain state of the art atomic data.

In 17 of our programme stars, Mg I lines are visible in the spectra, which indicate the presence of a cool main sequence companion contributing significantly to the flux (Lisker et al. 2005). Since this contribution gets stronger towards the red end of our spectral range, we only analysed metal lines with wavelengths shorter than 4500 Å. As can be seen in Tab. 8.1, the line list was shortened to 52 metal lines and no abundances of N III, Ar II and Ti IV could be measured in these cases. The derived abundances agree well with the ones of single stars in the same parameter range.
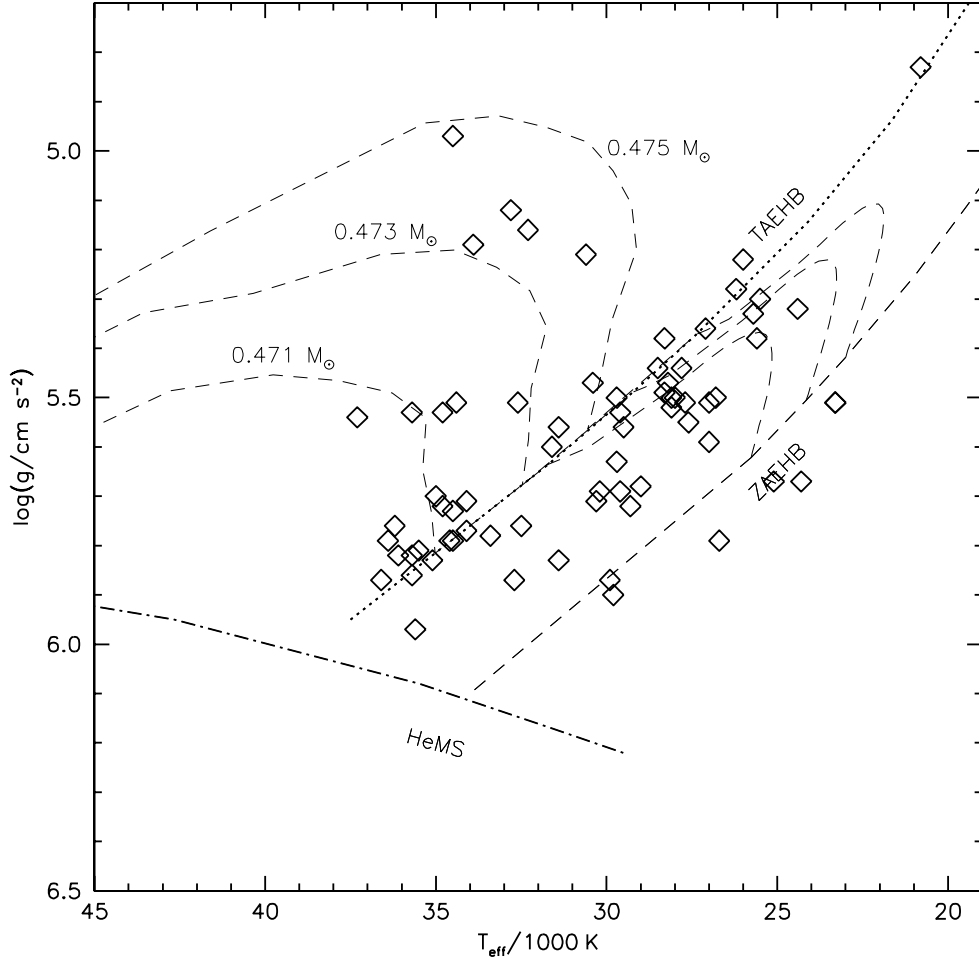
Figure 8.1: Surface gravity is plotted against effective temperature. The open diamonds mark the programme stars from the SPY survey. Zero Age Horizontal Branch (ZAEHB) and Terminal Horizontal Branch (TAEHB) are plotted as well as the Helium Main Sequence (HeMS). Tracks for canonical EHB stars are taken from Dorman et al. (1993). The sample covers the whole parameter range on the EHB and also subdwarfs that already evolved away from the EHB.

A simultaneous fit of elemental abundance, projected rotational velocity and radial velocity was then performed for every identified line. Inappropiate lines were automatically rejected (see Sect. 3.3 for the rejection criteria). Mean value and standard deviation were calculated from all abundance measurements of each ion. Upper limits were calculated by comparing the depth of the rotationally broadened synthetic spectral lines with the noise level. If only one line was found suitable for determining the abundance, the upper limits derived for the other lines of the same element were compared to this abundance. Only consistent results (within the error margins) were taken as measurements, lowering the probability of misidentifications. All outputs of the pipeline have been checked by visual inspection.

Table 8.1: Standard line list for the semi–automatic pipeline.

C ɪɪ	4267.001	N ɪɪ	3994.997	O ɪɪ	4069.642
C ɪɪ	4267.261	N ɪɪ	4035.081	O ɪɪ	4069.892
C ɪɪɪ	4162.877	N ɪɪ	4041.310	O ɪɪ	4072.155
C ɪɪɪ	4647.418	N ɪɪ	4447.030	O ɪɪ	4119.215
C ɪɪɪ	4650.246	N ɪɪ	4630.539	O ɪɪ	4414.884
		N ɪɪ	5001.134	O ɪɪ	4416.970
		N ɪɪ	5001.474	O ɪɪ	4641.825
		N ɪɪ	5005.150		
		N ɪɪɪ	4634.126		
		N ɪɪɪ	4640.644		
Ne ɪɪ	3694.212	Mg ɪɪ	4481.126	Al ɪɪɪ	3601.630
Ne ɪɪ	3713.080	Mg ɪɪ	4481.325	Al ɪɪɪ	3612.355
Si ɪɪɪ	3796.124	P ɪɪɪ	4059.312	S ɪɪ	4815.552
Si ɪɪɪ	4716.654	P ɪɪɪ	4080.089	S ɪɪɪ	4253.589
Si ɪɪɪ	4828.951			S ɪɪɪ	4284.979
Si ɪᴠ	4088.862				
Si ɪᴠ	4116.104				
Si ɪᴠ	4654.312				
Ar ɪɪ	4735.906	K ɪɪ	4134.723	Ca ɪɪɪ	4233.713
Ar ɪɪ	4806.021	K ɪɪ	4186.162	Ca ɪɪɪ	4233.736
Ar ɪɪ	4879.863	K ɪɪ	4263.447	Ca ɪɪɪ	4240.742
Sc ɪɪɪ	4061.210	Ti ɪɪɪ	4200.067	V ɪɪɪ	4268.183
Sc ɪɪɪ	5032.072	Ti ɪɪɪ	4207.491	V ɪɪɪ	4274.417
		Ti ɪɪɪ	4215.525	V ɪɪɪ	4294.919
		Ti ɪɪɪ	4281.555	V ɪɪɪ	4383.391
		Ti ɪᴠ	5398.930		
		Ti ɪᴠ	5492.512		
Cr ɪɪɪ	3649.777	Fe ɪɪɪ	4137.764	Co ɪɪɪ	3677.033
Cr ɪɪɪ	3700.768	Fe ɪɪɪ	4139.350	Co ɪɪɪ	3680.580
		Fe ɪɪɪ	4164.731		
		Fe ɪɪɪ	4164.916		
Zn ɪɪɪ	3683.387				

The accuracy of our results is limited by the quality of the spectra which ranges from $S/N \approx 7 - 80$ per resolution element. Fig. 8.2 shows two examples of spectra with highly different quality. The errors plotted in Tab. C.1 are the standard deviations of the individual line measurements. Numerical simulations were carried out to quantify the impact of noise on the result (see Sect. 3.4). We therefore regard $0.2 - 0.3$ dex as typical error of our abundance
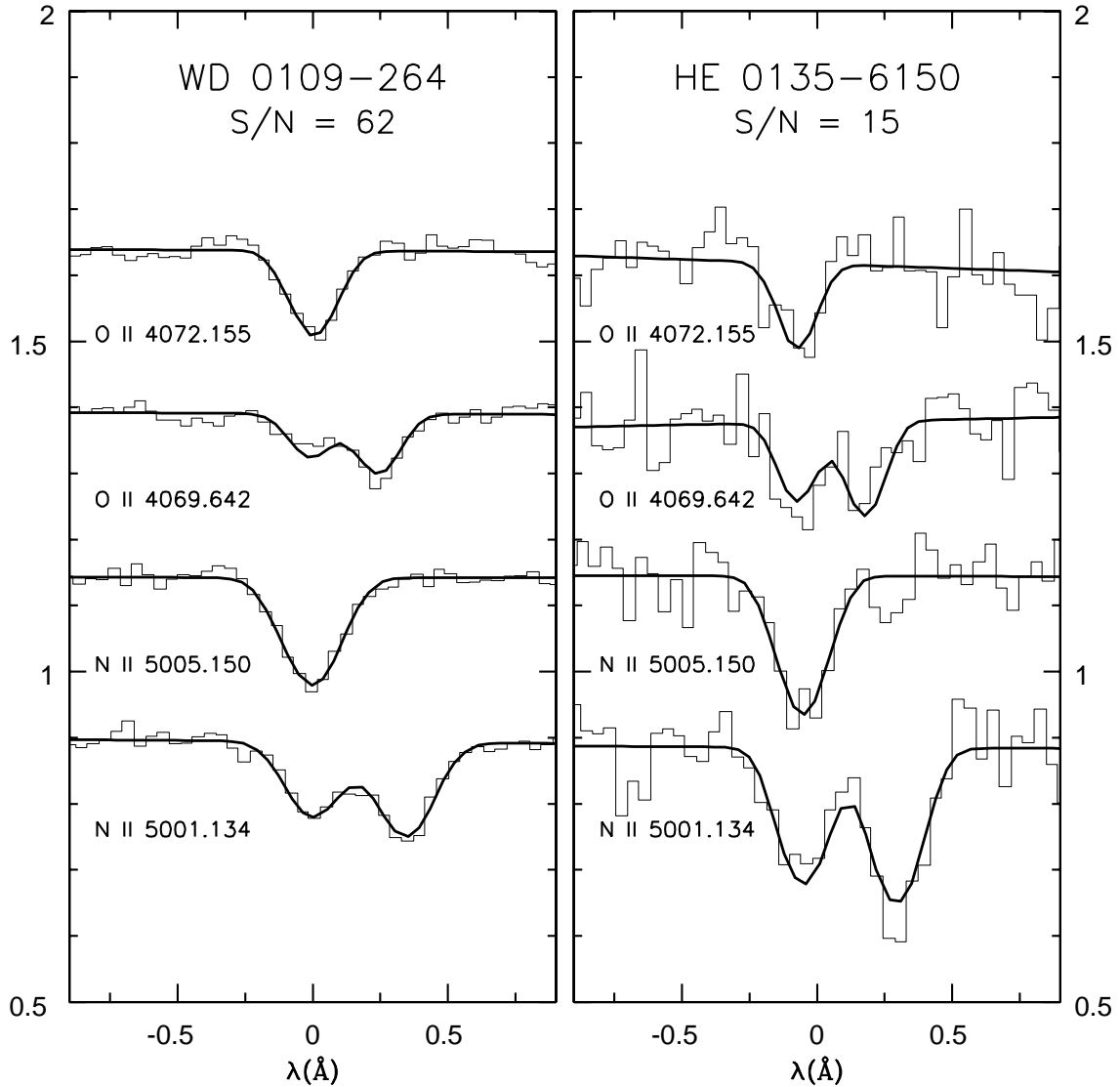
Figure 8.2: Example fits of common oxygen and nitrogen lines for two spectra with different quality. Although the fit quality deteriorates it is still possible to fit models with reasonable equivalent widths.

analysis for spectra with $S/N > 15$. In cases of lower quality spectra the error can be as high as $0.5\,$dex. The quality of the individual spectra is given in Tab. 7.1. To check the accuracy of our analysis pipeline, we compared it with another well established analysis method (see following Section).

One of our programme stars, the close binary sdB HE 1047−0436 was observed with UVES during the follow-up campaign and the high quality coadded spectrum was used to perform an abundance analysis with an alternative method by Napiwotzki et al. (2001). The equivalent
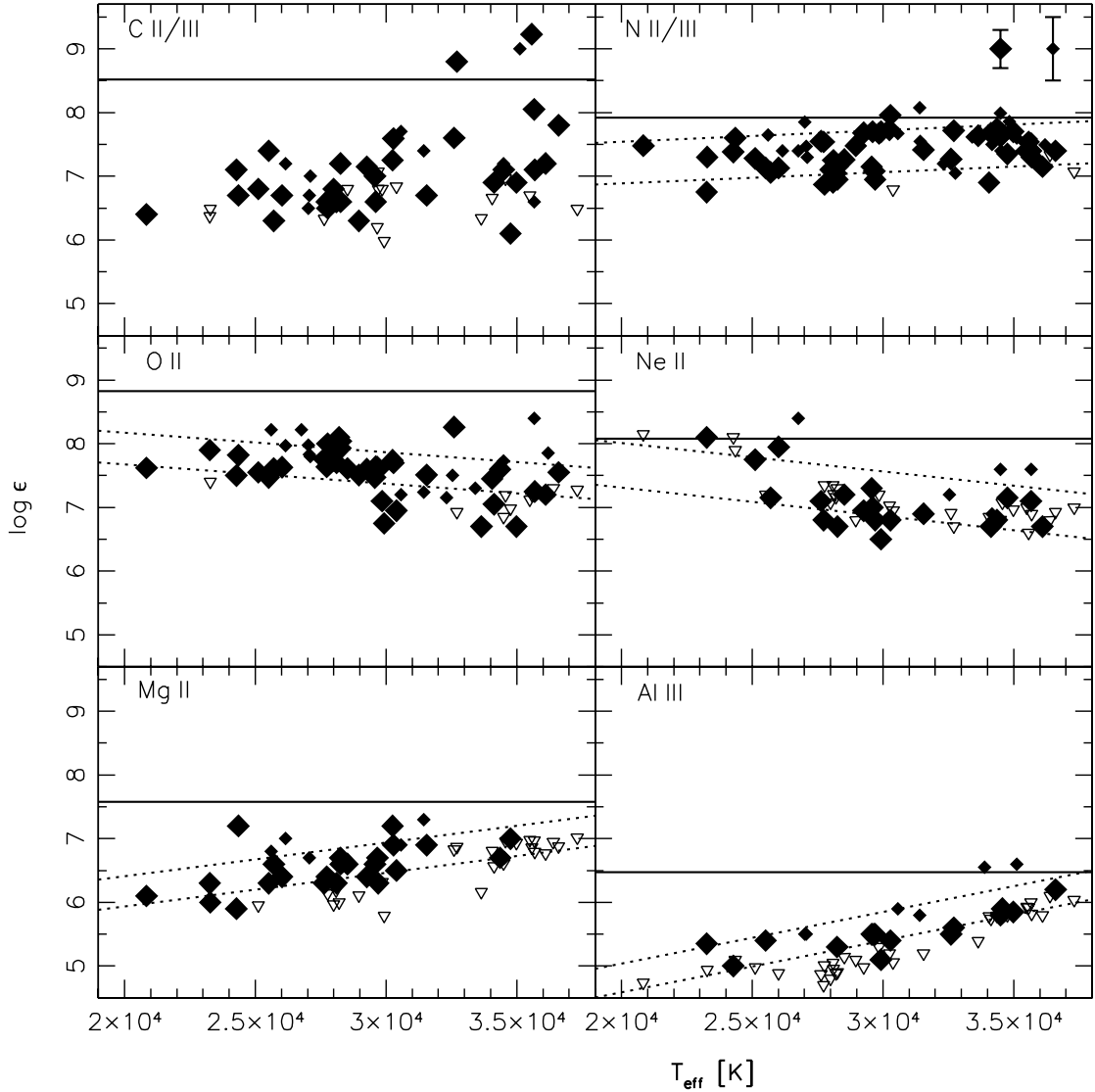
Figure 8.3: Elemental abundances from carbon to aluminium plotted against effective temperature. If two ionization stages are present, the average abundance is given. The small filled diamonds mark spectra with $S/N < 15$, the bigger ones spectra with $S/N > 15$. Typical error bars for both cases are given in the upper right corner. The solid horizontal lines mark solar abundances (Grevesse & Sauval 1998). The dotted lines mark the best fitting linear trends to the data points.

widths of all lines of C II, C III, N II, N III, O II, Mg II, Al III, Si III, Si IV, S II, S III, Ar II, and Fe III visible in the spectra were measured. Model atmospheres were calculated in the same way and with the same atomic data as described here. These models were used to calculate curve-of-growth for the observed metal lines. Blends were omitted from the analysis. Finally,
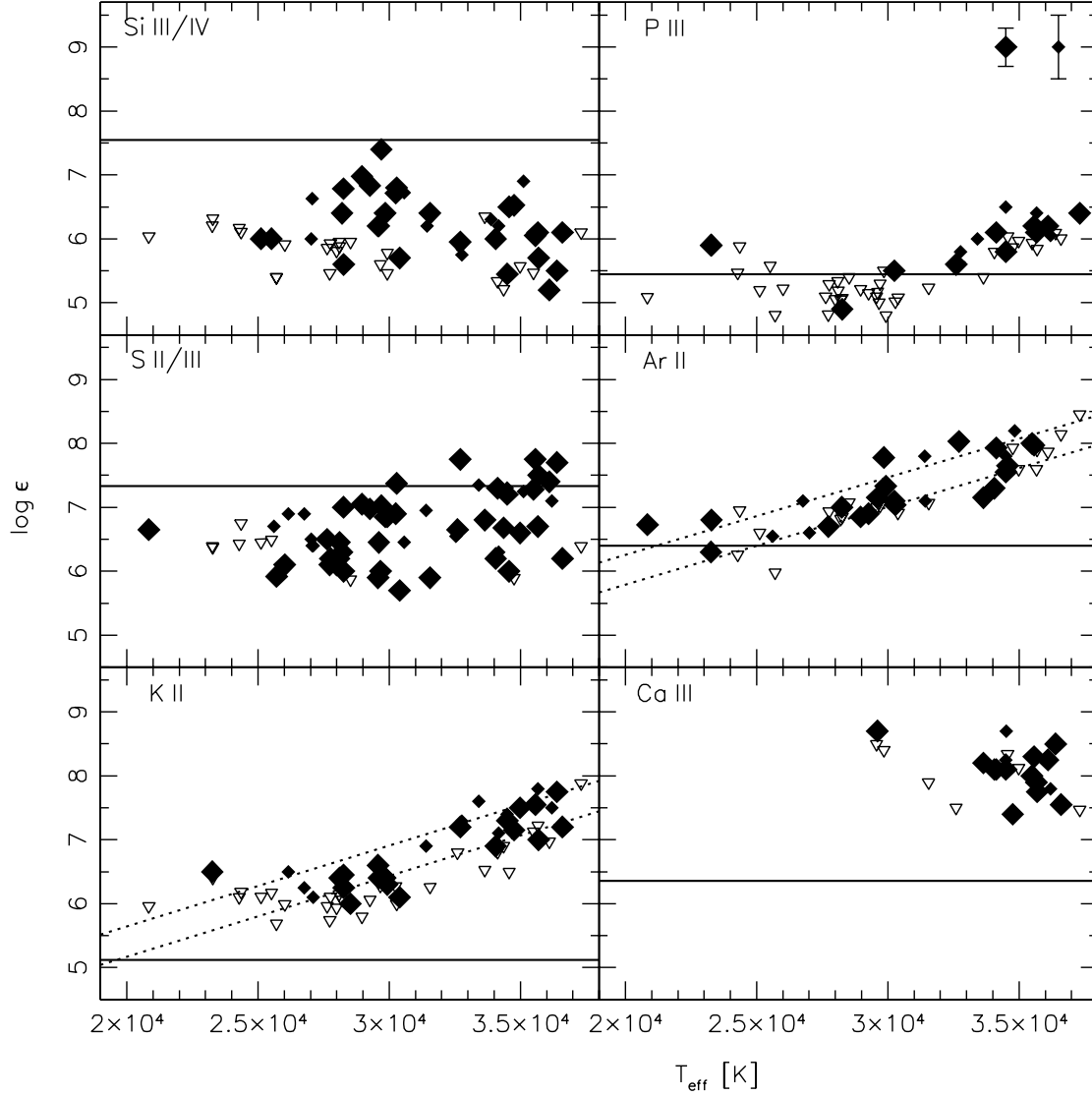
Figure 8.4: Elemental abundances from silicon to calcium plotted against effective temperature (see Fig. 8.3).

the abundances were determined from a detailed spectrum synthesis by means of LINFOR using all visible metal lines. The results of both methods are compared in Tab. C.3 and agree very well. The only exception is the carbon abundance, which was derived only from the notorious C II lines at 4267 Å, which are known to be affected by NLTE-effects (Nieva et al. 2008). We therefore conclude that this lines give a systematically lower abundance than other carbon lines.
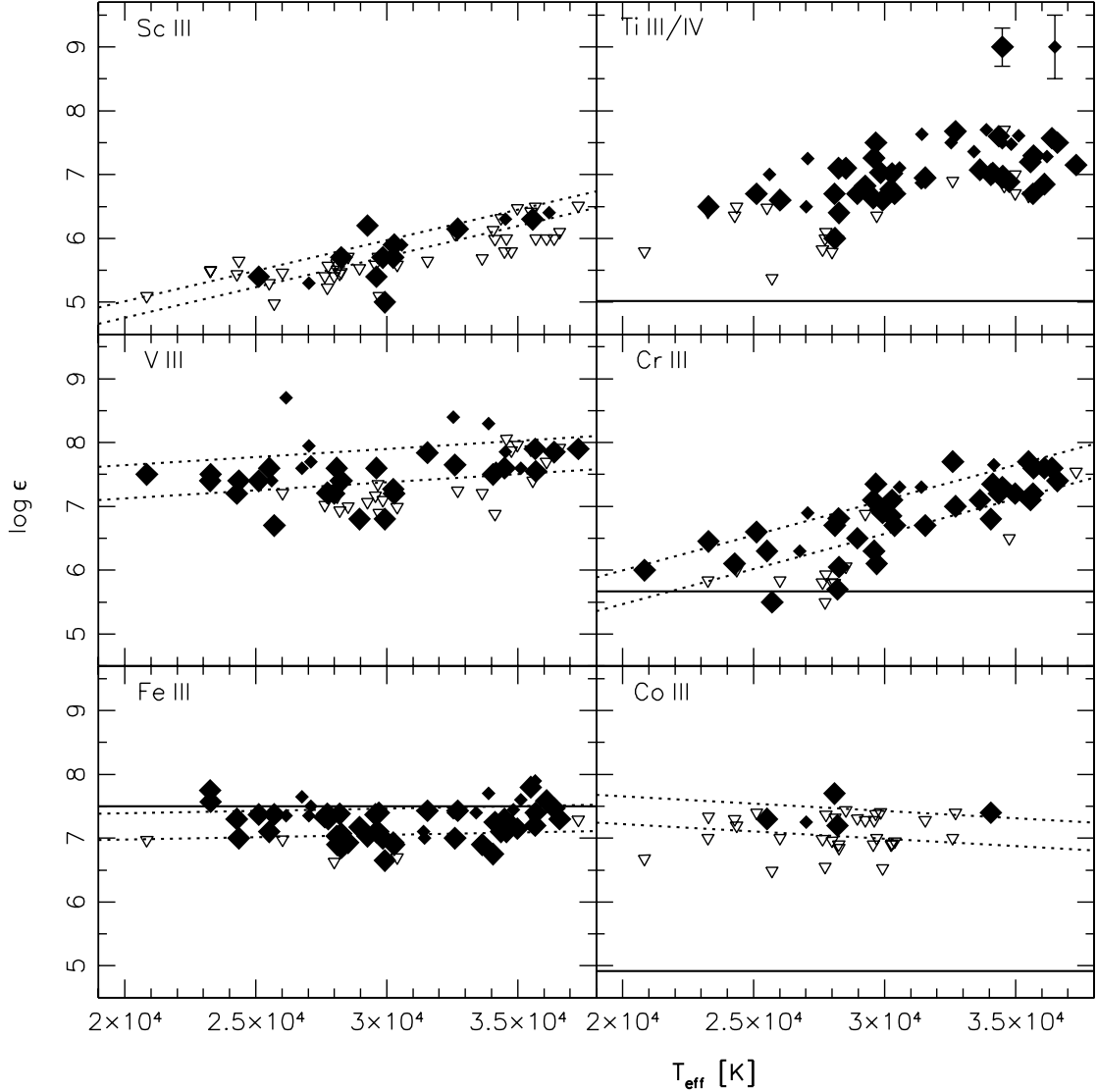
Figure 8.5: Elemental abundances from scandium to cobalt plotted against effective temperature (see Fig. 8.3). In the case of scandium and vanadium the solar abundances are lower than 4.5 dex (see text)

8.2 Metal abundances

The results of the semi-automatic pipeline for all stars are given in Tabs. C.1 and C.2 in the Appendix. Atmospheric parameters and helium abundances are published in Lisker et al. (2005), projected rotational velocities in Sect. 3.6 and 7.2. A comparison between the results of the equivalent width method and the automatic pipeline for the already published sdB+WD binary HE 1047−0436 (Napiwotzki et al. 2001) is given in Tab. C.3. The results agree very well. The

semi-automatic analysis pipeline turned out to be a reliable alternative to the equivalent width method.

8.2.1 General trends

The dominating trend which was found in the abundance data is an enrichment of most heavier metals with effective temperature. Less pronounced trends were found with respect to surface gravity, helium abundance and luminosity. All these quantities were found to increase with temperature (Lisker et al. 2005). The ages of the subdwarfs where interpolated using the horizontal branch evolutionary tracks of Dorman et al. (1993). No age dependent trends could clearly be found. Because the faintest stars have distances of up to $6\,\mathrm{kpc}$ (Lisker et al. 2005) and the SPY survey was directed perpendicular to the Galactic disc, subdwarfs of different populations should be present in the sample. The subwarf progenitors in the thin disc should have been formed from gas with nearly solar metal abundance, while the thick disc and halo sdBs should have had progenitors with sub-solar metallicity. The distance from the Galatic plane is one indicator of galatic population. No metallicity gradient was found, which is consistent with the assumption that the observed abundances in sdBs are caused by processes in the stellar atmosphere and are not representing the composition of the primordial gas. A detailed galactic kinematical study of stars from the SPY survey will be undertaken in Richter et al. (in prep.). Close binary subdwarfs as well as double lined wide binaries show the same abundance patterns as single stars. Two of our programme subdwarfs are central stars of planetary nebula (EGB 5 = PN G 211.9+22.6, PHL 932 = PN G 125.9−47.0). The abundance patterns of these objects do not differ from the rest of the sample. The following results are presented relative to solar values (Grevesse & Sauval 1998). Linear trends have been fitted to some of the observed abundances. The mean deviation of the measurements from these trends are then given as uncertainties.

8.2.2 Carbon, nitrogen, oxygen

The observed C II abundances scatter from -2.0 to -1.0 subsolar (solar abundance $8.52\,\mathrm{dex}$). C III becomes visible at $T_\mathrm{eff} > 27\,000\,\mathrm{K}$. The abundances of most stars are $-0.9 \pm 0.5\,\mathrm{dex}$. Four exceptional sdBs with $T_\mathrm{eff} > 32\,000\,\mathrm{K}$ show nearly solar to supersolar abundances up to $+1.0\,\mathrm{dex}$. All of these sdBs are enriched in helium compared to the rest of the sample. The abundances of C II and C III differ by more than $0.7\,\mathrm{dex}$ in some stars while the abundances of other elements in different ionization stages are consistent within the error margins. This may be caused by NLTE effects since the C II lines at $4267\,\text{Å}$ are known to be very sensitive in this respect (Przybilla priv. comm.). We therefore consider the abundances derived from the C III lines as more reliable in these cases. The N II abundances (solar abundance $7.92\,\mathrm{dex}$) are constant at $-0.5 \pm 0.3\,\mathrm{dex}$. N III lines become visible at $T_\mathrm{eff} > 30\,000\,\mathrm{K}$. The abundances decrease with temperature from $+0.3 \pm 0.2\,\mathrm{dex}$ to $-0.7 \pm 0.2\,\mathrm{dex}$. The abundances of N II and N III are consistent in most sdBs. The oxygen abundance (solar abundance $8.83\,\mathrm{dex}$) is constant at $-1.1 \pm 0.3\,\mathrm{dex}$.

8.2.3 Neon and magnesium

At low temperatures $T_\mathrm{eff} < 27\,000\,\mathrm{K}$ the Ne II abundance scatters from $-1.0\,\mathrm{dex}$ to $+0.3\,\mathrm{dex}$ (solar abundance $8.08\,\mathrm{dex}$). Then it drops to a constant value at $-1.1 \pm 0.4\,\mathrm{dex}$. A slight trend can be seen with temperature in the magnesium abundance (solar abundance $7.58\,\mathrm{dex}$). Mg II

increases from -1.3 ± 0.2 dex to -0.5 ± 0.2 dex until the temperature reaches $T_{\text{eff}} \approx 31\,000$ K. Here the trend stops and only a few stars show magnesium lines any more.

8.2.4   Aluminium and silicon

A trend with temperature is present in the Al III abundance (solar abundance 6.47 dex). Aluminium increases from -1.4 ± 0.2 dex to -0.2 ± 0.2 dex. The Si III as well as the Si IV abundance (solar abundance 7.55 dex) show a large scatter between -2.0 dex and 0.0 dex. No trend with temperature is visible. Subdwarfs with strong silicon lines are present in the same temperature range as sdBs where only low upper limits can be given. Si IV lines get visible at $T_{\text{eff}} > 28\,000$ K. The abundances of Si III and Si IV agree within the given error margins for all stars where both ionisation stages are present.

8.2.5   Phosphorus and sulfur

A trend with temperature is present in the P III abundance (solar abundance 5.45 dex). Phosphorus increases starting at a temperature of $T_{\text{eff}} > 28\,000$ K from $+0.0 \pm 0.3$ dex to $+0.6 \pm 0.3$ dex. Two stars with temperatures of about $23\,000$ K show lines at a wavelength of P III 4080.089 Å. Although no possible blends were found in line lists, these lines may be misidentifications since the derived abundances seem to be too high to fit in the overall trend. The S II and especially S III abundances (solar abundance 7.33 dex) scatter between -2.0 dex and $+0.7$ dex. Similar to the silicon abundances no trend with temperature is visible. At about $T_{\text{eff}} = 30\,000$ K most sulfur is in the higher ionization stage. The abundances of S II and S III are consistent in almost all sdBs within the error margins (see Fig. 8.4).

8.2.6   Argon, potassium, calcium

Ar II is clearly enriched and increases with temperature from solar abundance to $+1.8 \pm 0.2$ dex (solar abundance 6.40 dex). This trend has not been reported in prior analyses. Potassium has not been discovered in sdB atmospheres so far (solar abundance 5.12 dex). K II is enriched and strongly increases with temperature similar to Ar II from $+0.7 \pm 0.2$ dex to $+2.6 \pm 0.2$ dex. Ca III (solar abundance 6.36 dex) is present at temperatures higher than $T_{\text{eff}} > 29\,000$ K. The abundances are constant at $+1.7 \pm 0.3$ dex. Ca II was not included in our analysis because the most prominent lines are usually blended with interstellar lines. Care has to be taken in the case of visible main sequence companions in the spectra. In this case lines of neutral iron from the companion can be misidentified as calcium lines. For this reason no calcium abundances were measured for stars with visible companions (see Fig. 8.4).

8.2.7   Scandium, titanium, vanadium, chromium

Scandium (solar abundance 3.17 dex) strongly increases with temperature from $+2.0 \pm 0.1$ dex to $+3.4 \pm 0.1$ dex. Ti III (solar abundance 5.02 dex) is enriched and scatters from $+1.4$ dex to $+2.5$ dex. Ti IV lines get visible at $T_{\text{eff}} > 27\,000$ K. The abundances drop from $+3.2$ dex to $+1.6$ dex with increasing temperature. The abundances of Ti III and Ti IV agree within the given error margins in some stars while in others the difference can be as high as 1.0 dex. V III (solar abundance 4.00 dex) is highly enriched independent of the temperature at $+3.7 \pm 0.3$ dex. Cr III (solar abundance 5.67 dex) increases with temperature from $+0.3 \pm 0.3$ dex to $+2.0 \pm 0.3$ dex (see Fig. 8.5).

8.2.8   Iron, cobalt, zinc

Iron (solar abundance 7.50 dex) is constant at -0.2 ± 0.2 dex. For cobalt (solar abundance 4.92 dex) and zinc (solar abundance 4.60 dex) more or less only upper limits could be given. The limits are consistent with high enrichments of these elements up to $+2.0$ dex. This is consistent with results from O'Toole & Heber (2006), Chayer et al. (2006) and Blanchette et al. (2008) who measured abundances of heavy metals from UV spectra (see Fig. 8.5 zinc is not shown because upper limits could only be derived from one line).

8.3   Diffusion in sdB atmospheres

The metal abundances of the sdBs discovered during the SPY survey show a clear pattern, which could not been seen before. While the light elements carbon, nitrogen, oxygen and neon are not affected by higher temperatures, most heavier elements from magnesium to chromium are getting enriched in hotter atmospheres. The scatters in silicon and sulfur abundance are important exceptions and might be caused by shortcomings in the LTE-analysis. A trend in calcium could not be seen because single ionized calcium was not included in the analysis. Iron, on the other hand, seems to be not affected by temperature. A higher temperature leads to a higher radiation pressure. The radiative acceleration on a component of the stellar atmosphere depends on the mass of the considered ions and the absorption cross section. Here the contribution of the lines is generally much larger than the contribution of the continuum. Heavier elements in general have much more absorption lines than lighter ones. The radiative acceleration on these elements should therefore be higher. At timescales much shorter than the lifetime on the EHB an equilibrium between this radiative levitation, the gravitational settling and a weak stellar wind should be reached. At higher temperatures, where radiative levitation plays a more important role, this equilibrium should be shifted to higher enrichment of heavy elements. Especially heavy elements with low primordial abundances like scandium or vanadium are expected to be highly enriched, because the radiation pressure also increases with lower abundance (Unglaub priv. comm.).

This is exactly what can be seen in the data. While the equilibrium is not shifted in case of the light elements (except helium, see Lisker et al. 2005) within the sdB temperature range, all elements heavier than magnesium are enriched. The only exception is iron, which remains solar all over the temperature range. An explanation for this behaviour is given in the next section. The lack of any age effects confirms the assumption, that diffusion processes with much shorter timescales are responsible for the peculiar abundance patterns of sdBs. The similarity of sdBs in different galactic populations points into the same direction. Close binary sdBs, which are in some cases considerably spun up by the tidal forces of their companions, don't show any differences in their abundance patterns compared to single ones.

It has been noted by several authors (e.g. Lamontagne et al. 1985, 1987; O'Toole & Heber 2006) that the silicon abundance in sdB stars appears to drop sharply at $T_{\mathrm{eff}} > 32\,000$ K. Fractionated winds have been invoked to explain this strange observation (Unglaub 2006). This seemed to be also the case for aluminium. As can be clearly seen in Figs. 8.3 and 8.4 this assumption has to be dropped. Silicon as well as aluminium are present all over the temperature range of sdBs. O'Toole & Heber (2006) also reported a possible anti-correlation between iron and the other heavy elements. The SPY sdBs do not show any clear trend like that. Edelmann et al. (2006) discovered three hot sdBs with peculiar abundances and named them super metal

rich sdBs because their metal abundances seemed to be particularly high. With the results presented here it is possible to show that this enrichment is quite normal for sdBs at the high temperature range. Nevertheless these three subdwarfs remain peculiar objects, which will be shown in Sect. 8.5.

Although the general pattern may be qualitatively explained in this way, some questions remain open. All observed trends are superimposed by a scatter, which is most prominent in the carbon, silicon and sulfur abundances. Furthermore the fitted abundance trends of Si III and Si IV and especially Ti III and Ti IV diverge significantly. Before trying to explain this scatter with effects like stellar winds, one has to be sure, that it is not caused by errors in the abundance determination. Other important error sources are discussed in Przybilla et al. (2006) and references therein. Enhanced metal abundances can have an effect on atmospheric parameter determination. These parameters are used to construct the model spectra for measuring the metal abundances. Some lines are much more sensitive to a change in the atmospheric parameters than others. Fine tuning may be necessary to fit all ionization equilibria simultaneously. Improper line data can cause significant errors. Especially for the heavier elements there is a severe lack of adequate data. NLTE effects which are neglected in this analysis become important especially at higher temperatures. The resulting trends with temperature can be very similar to the trends found in this analysis. Not all lines are equally affected by NLTE effects. Some were found to behave well in LTE, while others can deviate in abundance by orders of magnitude when NLTE effects are taken into account (Nieva, Przybilla priv. comm.). The relatively low number of lines per ion that could be used in this analysis could therefore lead to inaccurate results, if accidentally the "wrong" lines were chosen. To handle all these systematics a consistent analysis of a large sample of high quality sdB spectra is necessary. Metal line blanketing as well as NLTE effects should be taken into account.

8.4 Beyond the EHB - diffusion on the Horizontal Branch

The Blue Horizontal Branch (BHB) stars are the cooler neighbours of the EHB stars (for a more detailed review see Behr 2003a). Their chemical composition is of interest especially in globular cluster research (see Sect. 1.8). Since the morphology of the HB in globular clusters still remains unclear, different explanations for the shape of and the apparent gaps along the HB have been proposed.

In globular clusters all stars belong to the same population and should therefore have similar chemical composition (at least to first order, see Sect. 1.8). Glaspey et al. (1989) were the first to discover a significant change of chemical abundances as function of the position on the HB. While a BHB star with $T_{\rm eff} \approx 10\,000\,{\rm K}$ in NGC 6752 showed helium and iron abundances similar to the cluster composition (which is normally derived from abundance studies of Red Giants), a hotter one ($T_{\rm eff} \approx 16\,000\,{\rm K}$) turned out to show depletion of helium and strong enrichment of iron. Further abundance studies of BHB stars in several GCs revealed a general pattern (Moehler et al. 1999; Behr et al. 2003a; Fabbian et al. 2005; Pace et al. 2006), which can also be observed in field BHB stars (Behr et al. 2003b). Stars cooler than about $11\,500\,{\rm K}$ show the typical abundances of their parent population, while stars hotter than that are in general depleted in helium and strongly enriched in iron and other heavy elements like titanium or chromium. Lighter elements like magnesium and silicon on the other hand have normal abundances.

Diffusion processes in the stellar atmosphere are responsible for this effect. Michaud et al.
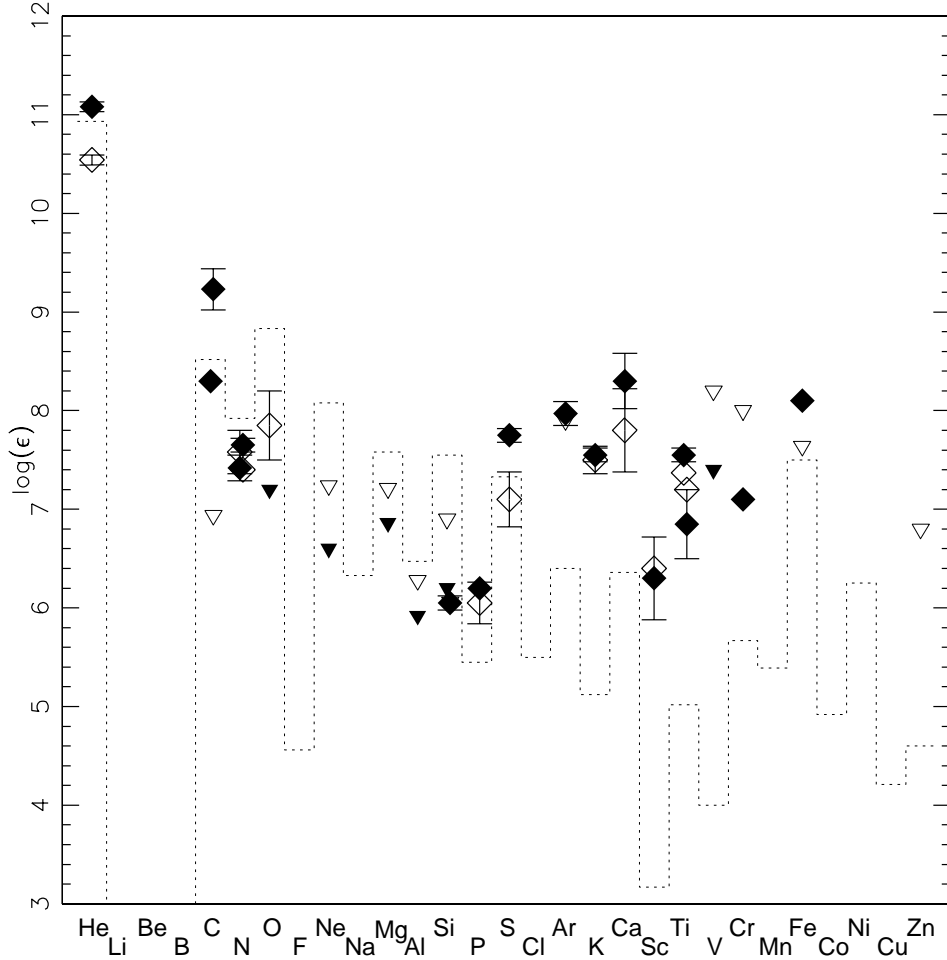
Figure 8.6: Superposition of the abundance patterns of the carbon rich sdB HE 0101−2707 ($T_{\mathrm{eff}} = 35\,568\,\mathrm{K}$, $\log g = 5.97$, filled symbols) and the carbon poor HE 1033−2353 ($T_{\mathrm{eff}} = 36\,207\,\mathrm{K}$, $\log g = 5.76$, open symbols). While the abundance pattern of the heavier elements looks similar, carbon and helium show a discrepancy. The histogram marks solar abundances (Grevesse & Sauval 1998). Some elements show two ionization stages (the lower stage symbol is slightly shifted to the left).

(1989) predicted such abundance patterns before the anomalies were observed. Caloi (1999) explained the sharp transition between the two abundance patterns as disappearance of subsurface convection layers at a critical temperature. Sweigart (1997b) indeed found by modelling BHB stars that thin convective layers below the surface driven by hydrogen ionization should exist and move closer to the surface, if the temperature increases. At about 12 000 K the convection zone reaches the surface and the outer layer of the star gets fully radiative. Since convection is very efficient in mixing the envelope, diffusion processes cannot set in below this limit. In hotter stars with radiative atmospheres helium is expected to diffuse downward, since its mean
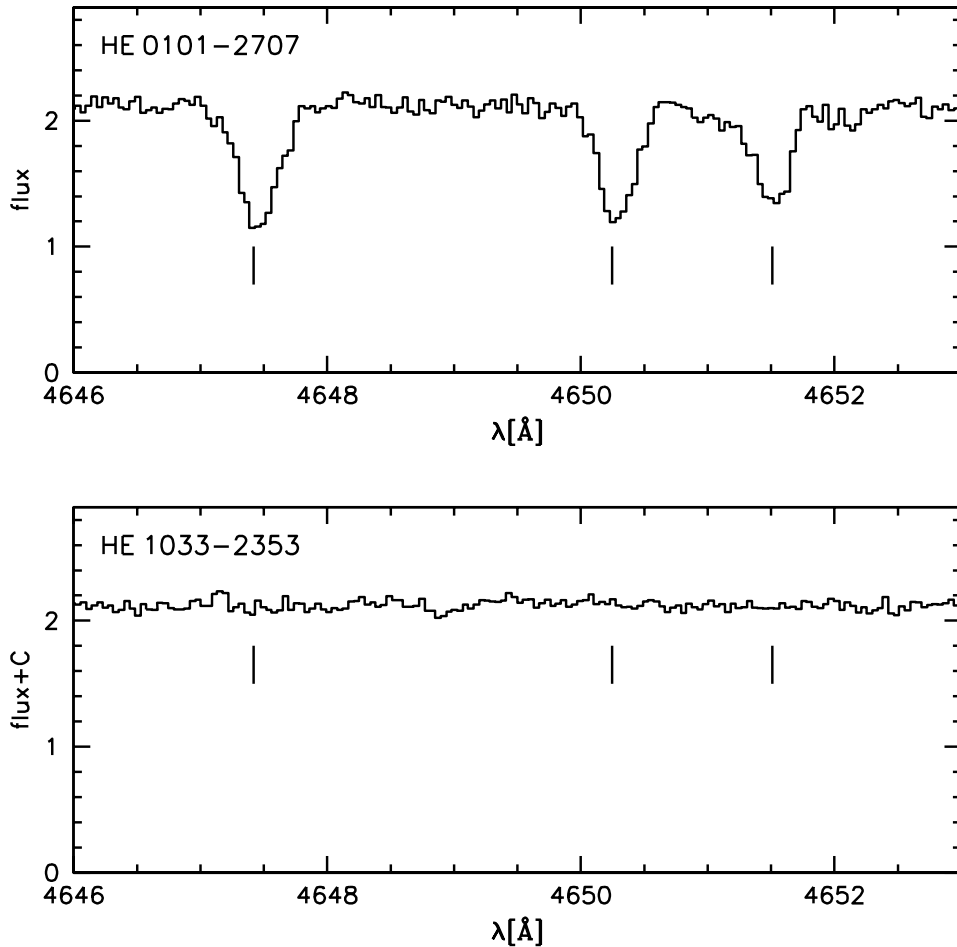
Figure 8.7: UVES spectra details of the carbon rich sdB HE 0101−2707 (upper panel) and the carbon poor sdB HE 1033−2353. While HE 0101−2707 shows strong C III lines at 4647 Å, 4650 Å and 4651 Å, no lines can be detected in HE 1033−235.

molecular weight is higher than the one of hydrogen. Heavier elements on the other hand present sufficiently large cross sections to the outgoing radiation field and experience radiative accelerations greater than gravity. Hence these elements get enriched in the atmosphere. If the radiative acceleration almost equals gravity, the diffusion timescales get very long and the element is not significantly affected by diffusion. Most recently Michaud et al. (2008) modelled these effects and reproduced for the first time the observed abundance patterns of BHB stars very well.

The observed trends in metal abundances of BHB stars dependent on effective temperature published by Behr et al. (2003b, 2003a), Fabbian et al. (2005) and Pace et al. (2006) and our results on EHB stars complement on each other. That's why it is worth looking at the bigger picture. In Fig. 8.8 the abundances of iron and titanium are plotted against effective temperature. Abundances of all BHB stars are plotted together, although they are derived

from stars coming from very different populations. Eight different GCs as well as field stars are put together here. At first glance this makes absolutely no sense, because stars from different chemical environments should have different abundances. This would result in a scattered plot from which no relevant information could be derived.

But Fig. 8.8 proves that this is not the case. Although there is a huge scatter in the iron abundance at low temperatures, all stars hotter than about 11 500 K end up at almost solar abundance with a significantly lower scatter. As soon as diffusion sets in, the primordial abundances are not important any more and the atmospheres of stars from different populations get similar. The distribution of sdBs now shows that the iron abundance remains indeed saturated at this value up to temperatures of 40 000 K. This plot clearly illustrates that the abundance of iron in EHB and the hottest BHB stars is not "solar" for reasons of star formation and stellar evolution. This just by chance "solar" abundance reflects the surface concentration of iron caused by an interplay of gravitational settling and radiative levitation, which gets saturated in stars hotter than 11 500 K and was precisely modelled by Michaud et al. (2008) for BHB stars. A similar behaviour is predicted by Michaud et al. (2008) for the titanium abundance. In BHB stars only a rise of the titanium abundance can be observed, which is more continuous than in the case of iron. Adding the sdBs one can see that the abundance gets saturated at an effective temperature of about 30 000 K and an abundance roughly 100 times solar. This behaviour proves in a most convincing way, that heavy elements in EHB and hot BHB stars are enriched by radiative levitation. Extending the analysis of Michaud et al. (2008) to higher temperatures would be the next logical step to learn more about these effects.

Figure 8.8: *Left panel* Iron abundance is plotted against effective temperature. The filled diamonds mark the results from the sdBs. The filled rectangles mark the combined results for BHB stars from seven globular clusters and the field (Behr et al. 2003b, 2003a; Fabbian et al. 2005). *Right panel* Titanium abundance is plotted against effective temperature. The filled diamonds mark the results from the sdBs. The filled rectangles mark the combined results for BHB stars from eight globular clusters and the field (Behr et al. 2003b, 2003a; Fabbian et al. 2005; Pace et al. 2006).

Fig. 8.9 shows the magnesium abundances plotted against effective temperature. It was reported by Behr et al. (2003a), Fabbian et al. (2005) and Pace et al. (2006) that the magnesium abundances derived from globular clusters are in general not affected by diffusion and consistent with the chemical composition of the cluster derived from Red Giants. In Fig. 8.9 the magnesium abundances of the two globular clusters M3 and M68 (Behr et al. 2003a) are marked in blue and red colour. One can see that they are concentrated around distinct values. The magnesium abundances of the field BHB stars (Behr et al. 2003b) on the other hand show a large scatter due to the fact that they come from different populations. The scatter in the sdB magnesium abundances is lower and no enrichment can be seen along the whole temperature range. The explanation for the different scatter may be just a selection effect. BHBs are bigger and in general intrinsically more luminous than sdBs. This means that the sample of Behr et al. (2003b) reaches further out into the halo and may contain more halo stars with lower primordial metallicity compared to the disk populations. This may account for the few BHB stars with the lowest magnesium abundance. In this case the scatter in the field BHB and sdB abundances becomes comparable. Given these results can be backed up by diffusion models, it would mean that the magnesium abundances in sdB atmospheres are not affected by diffusion and could therefore be used as a tracer for population membership or different formation channels. This can be checked by kinematical studies. In Sect. 8.3 the large scatter in the abundances of carbon, silicon and sulfur derived for our programme stars was discussed. In Fig. 8.9 our results for silicon are combined with the ones from Fabbian et al. (2005) for the globular cluster NGC 1904. Again no trend with temperature can be seen over the whole range indicating that radiative levitation plays a minor role. On the other hand it is quite surprising that the scatter observed in BHB silicon abundances looks very similar to the one in sdBs (and is significantly larger than the corresponding error bars). Especially if one takes into account that all the BHBs studied are members of just one globular cluster with a silicon abundance of about -1.3 dex relative to solar. Compared to the magnesium abundances of BHBs in globular clusters, the scatter in silicon is significantly higher. Whatever happens to silicon in the atmospheres of sdBs seems to happen in quite a similar way at lower temperatures. It remains to be seen, whether this has something to do with diffusion or other yet unknown effects.

8.5 Two populations of hot sdBs

Looking at high resolution spectra of a sample of sdBs the most obvious observation is, that most of them show a lot of metal lines, but some of them don't show any metal lines at all. At first instance one could argue, that there exist two different populations of sdBs with different metallicities. This would be contrary to the assumption, that the elemental composition of sdBs is caused by diffusion processes in the stellar atmosphere alone. Our results provide a natural explanations for this effect. All stars without metal lines are lying at the hot end of the EHB with temperatures higher than $T_{\mathrm{eff}} > 33\,000\,\mathrm{K}$. At these temperatures the optical lines are getting so weak that they are only observable in high S/N spectra. This is caused by shifts in ionisation stages with increasing temperature. The corresponding lines of these higher ionized elements are only visible in the UV and not in the optical.

Four sdBs show a strong enrichment in carbon from almost solar to ten times supersolar (HE 0019−5545, HE 0101−2707, HS 1536+0944, HS 2033+0821). Their temperatures range from 32 000 K to 36 000 K, the surface gravities from 5.83 to 5.97 and the helium abundances are the highest of the sample (-0.49 to $+0.25$). While HE 0019−5545, HE 0101−2707 and HS 2033+0821
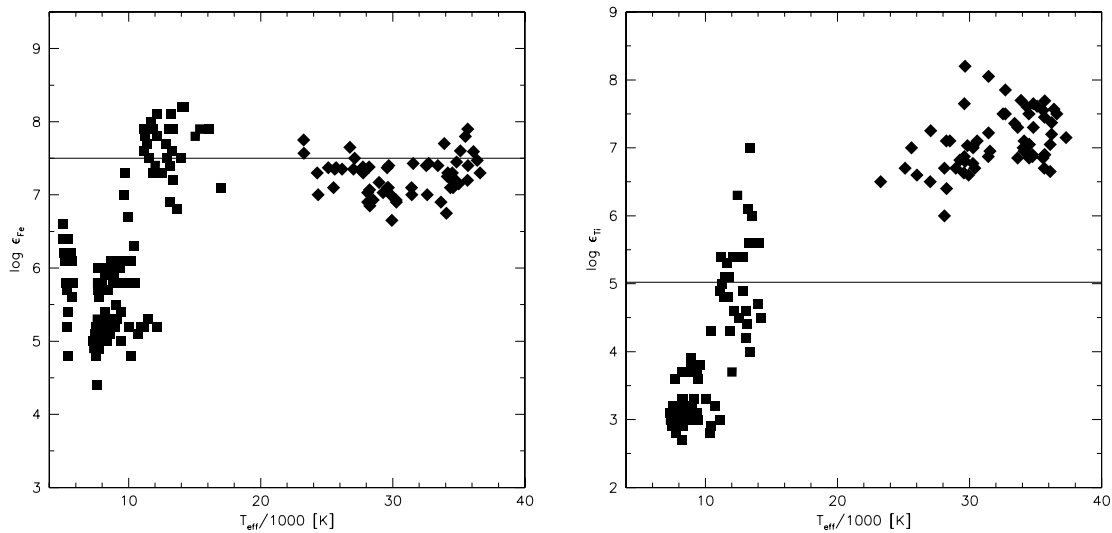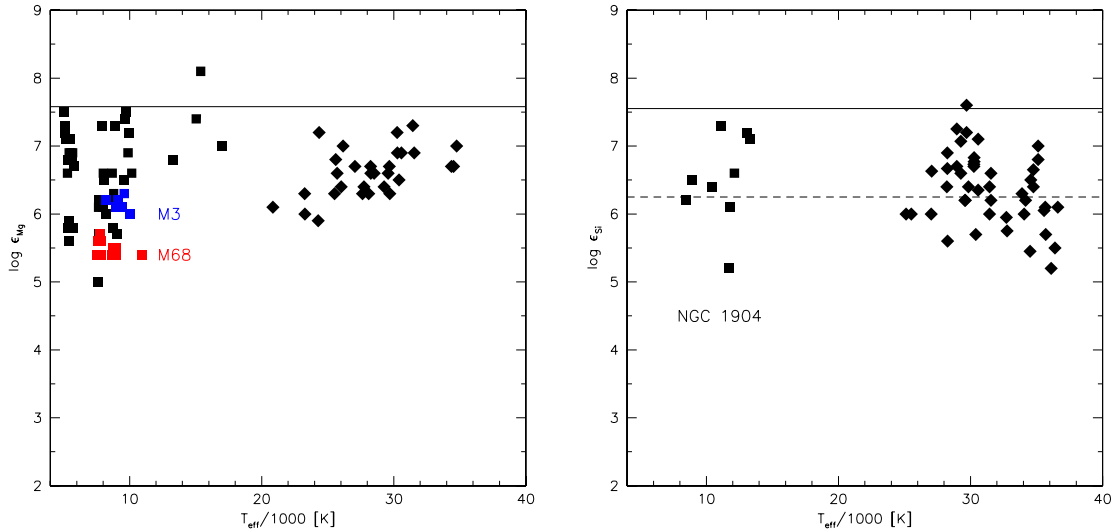
Figure 8.9: *Left panel* Magnesium abundance is plotted against effective temperature. The filled diamonds mark the results from the sdBs. The filled rectangles mark the combined results for BHB stars from two globular clusters and the field (Behr et al. 2003b, 2003a). *Right panel* Silicon abundance is plotted against effective temperature. The filled diamonds mark the results from the sdBs. The filled rectangles mark the results for BHB stars from the globular cluster NGC 1904. The cluster silicon abundance is indicated by the dashed horizontal line (Fabbian et al. 2005).

are single sdBs, HS 1536+0944 has a main sequence companion (Lisker et al. 2005). They are situated at the hot end of the EHB, but this region is not exclusively occupied by these carbon rich sdBs (see Fig. 8.7). Subdwarfs with very similar atmospheric parameters don't show any carbon enrichment up to supersolar. Edelmann et al. (2006) found three similar objects in their sample of bright sdBs. From 117 analysed stars of both samples 7 or about 6% happen to be carbon sdBs. All of these stars do not show any oxygen lines in the optical and none or just weak iron lines. This effect can be explained by the high temperature and surface gravity of these stars, which make the lines too weak to be detected in the optical. The high carbon enrichment is accompanied by helium enrichment compared to normal sdBs with similar atmospheric parameters.

8.6 Carbon rich sdBs – a missing link in sdB formation?

The presence of two populations of hot sdBs may provide new insights considering the open question of hot subdwarf formation. While the normal sdB stars populate the EHB homogeneously, carbon rich sdBs are located at its hot edge only. In this temperature range a very small fraction ($\leq 5\%$) of the subdwarf population shows strong neutral helium lines (Green et al. 1986). A study of Ahmad & Jeffery (2003) showed that these so called He-sdBs exhibit a wide range in helium abundance and temperature partially overlapping with both sdB and sdO stars. Only a few He-sdBs have been studied in detail so far (Lanz et al. 2004, Ahmad & Jeffery
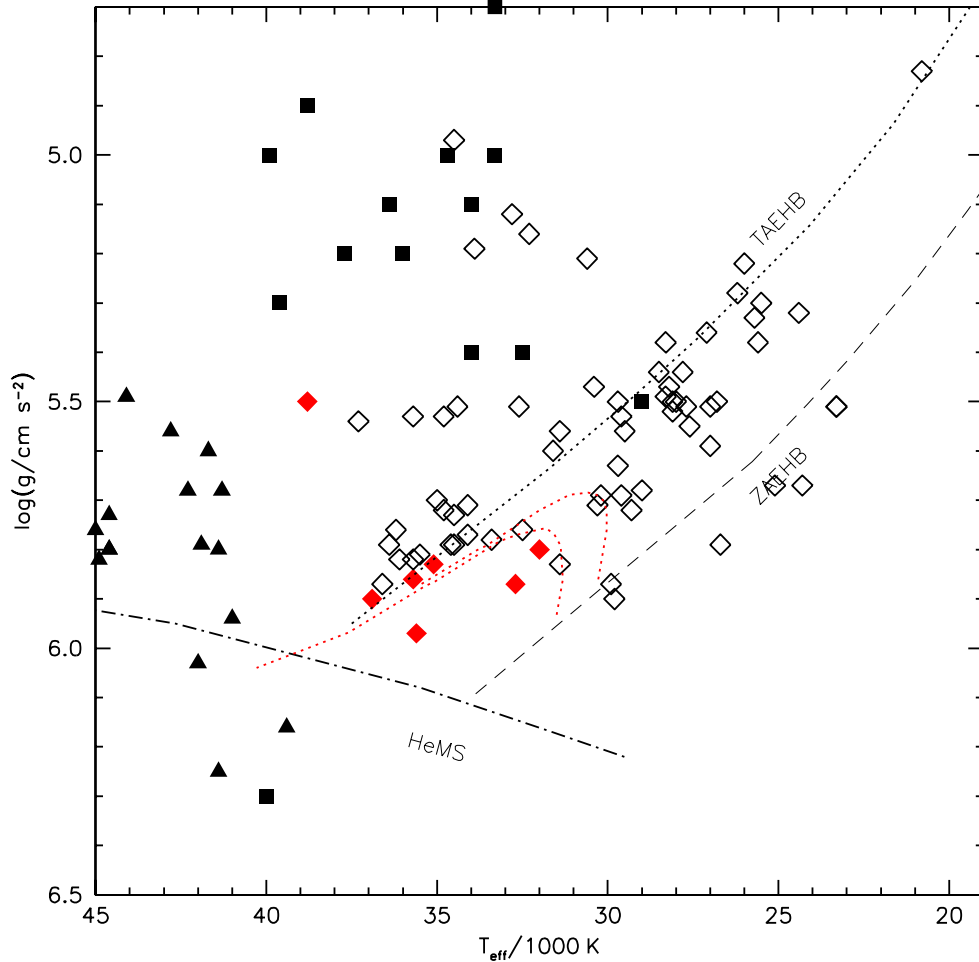
Figure 8.10: Surface gravity is plotted against effective temperature. The open diamonds mark the normal sdBs from the SPY survey. Carbon rich sdBs discovered here and by Edelmann et al. (2006) are plotted as filled diamonds. The filled rectangles mark He-sdBs (Ahmad & Jeffery 2003; Lanz et al. 2004), the triangles He-sdOs from the SPY survey (Ströer et al. 2007). Zero Age Horizontal Branch (ZAEHB) and Terminal Age Horizontal Branch (TAEHB) are plotted as well as the Helium Main Sequence (HeMS). The two evolutionary tracks are late hot flasher tracks with shallow mixing (Lanz et al. 2004).

2006). All of them show an enrichment in carbon up to $+2.0$ dex supersolar and somewhat less in nitrogen. The carbon rich sdBs have the appropriate temperature and surface gravity and show an enrichment in helium and carbon compared to normal sdBs. Both types of sdBs are equally numerous ($\approx 5-6\%$ of the sdB population). Carbon and nitrogen enrichment is also characteristic for He-sdOs (see Fig. 8.10). These stars show He I and He II lines, but no hydrogen at all. They are situated on the $T_{\mathrm{eff}} - \log g$ diagram right next to the He-sdBs at higher temperatures of about $40\,000 - 50\,000$ K (Ströer et al. 2007, a detailed abundance analysis of

the SPY objects is in preparation by Hirsch et al.).

Canonical EHB evolution (e.g. Dorman et al. 1993) fails to explain the enrichment of helium, carbon and nitrogen in He-sdBs as well as He-sdOs. The situation is very similar in the case of the carbon rich sdBs. Alternative scenarios have been invoked to explain the formation of He-sdBs and He-sdOs, which may also be applicable to carbon rich sdBs.

While the merger of two He-WDs is invoked as a possible formation channel for carbon poor sdBs (see Han et al. 2002, 2003), a low mass CO+He WD merger might produce a carbon rich He-sdB/O (Saio & Jeffery 2000). This formation channel is unlikely in the case of carbon rich sdBs for two reasons. First, although the stars are enriched in helium compared to other sdBs, hydrogen is still by far the most abundant element in their atmospheres. During the merger event almost all hydrogen should have been burnt. Second, the projected rotational velocities of all carbon rich sdBs are low (see Tab. 7.1; Edelmann 2003). Only in the case of HS 1536+0944 it exceeds $10\,\mathrm{km s^{-1}}$. This star is suspected to be a close binary and it should therefore have been spun up by its companion (see Tabs. 2.4,3.1). Although it was shown by Gourgouliatos & Jeffery (2006) that a lot of angular momentum has to be lost during the merger event, it is very unlikely that the outcome would be a slowly rotating star. So the WD merger channel fails to explain the formation of carbon rich sdBs and at least one exceptional He-sdB, which shows hydrogen lines and is a slow rotator (JL 87 see Ahmad & Jeffery 2006).

Close binary formation channels are discussed to explain the formation of normal sdBs (see Sect. 1.3). In these scenarios most of the hydrogen envelope is lost because of binary interaction. Either it is slowly transfered to the companion or ejected after a common envelope phase. Only one of the seven known carbon rich sdBs is a binary with a main sequence companion. The remaining six stars don't show any signs of binarity. Close binary scenarios are not well suited to explain the formation of carbon rich sdBs.

The late hot flasher scenario proposed by Sweigart (1997a) and further elaborated by Lanz et al. (2004) is based on the assumption that stars evolving with high mass-loss on the red giant branch are directly moving towards the white dwarf cooling track. A late core helium flash happens on the cooling track and the reborn star settles near the helium main sequence. During this late flash, core material is mixed to the surface, which leads to an enrichment of helium, carbon and nitrogen. Depending on the size of the convection zone, Lanz et al. (2004) distinguish between deep and shallow mixing. In the latter case, a significant amount of hydrogen may remain in the atmosphere. Shallow mixing was invoked to explain the formation of objects like JL 87 and may explain the carbon rich sdBs as well. With only one exception all carbon rich sdBs lie on the shallow mixing tracks of Lanz et al. (2004) as can be seen in Fig. 8.10. Although this scenario provides enough helium and carbon to explain an enrichment in the atmosphere right after the flash, diffusion processes should at short timescales lead to similar equilibrium abundances as observed in normal sdBs. But if diffusion in the stellar atmosphere is the only reason for the observed abundance patterns, why do we see two different carbon abundances at the same atmospheric parameters (see Fig. 8.7)?

A mechanism is needed which constantly transports helium and carbon in the atmosphere and therefore counteracts diffusion at least to some extend, because the observed helium and carbon abundances of carbon rich sdBs are still much lower than in He-sdBs. Photospheric convection may be this mechanism (Bues priv. comm.). Greenstein & Sargent (1974) suggested for the first time, that a He^+/He^{2+} convection zone could transport helium from deeper layers into the photosphere of subdwarfs hotter than $30\,000\,\mathrm{K}$. Groth et al. (1985) rejected this possibility for sdBs with subsolar helium abundances. In the case of helium enrichment prior to

the subdwarf stage (as provided by the late hot flasher scenario), they predict a broad convection zone, which is able to mix nuclear processed material in the atmosphere and should therefore destroy diffusive patterns as observed in sdBs. This is consistent with analyses of He-sdBs, which show patterns different from hydrogen rich sdBs (Lanz et al. 2004; Ahmad & Jeffery 2006). If hydrogen is present, the convection zone just reaches down to the bottom of the atmosphere and is not deep enough to reach helium rich layers. But a deep convection zone is not necessary, if helium, carbon and nitrogen were already mixed into the photosphere during the formation of the subdwarf. This would have been the case in both the late hot flasher and in the white dwarf merger scenario. Efficient convection would destroy diffusion patterns within a short time. So maybe the thin convection zone in hydrogen rich sdBs derived by Groth et al. (1985) can provide some enrichment of helium, carbon and nitrogen while preserving the normal diffusion pattern of the heavier elements. Theoretical calculations are necessary to show, whether this mechanism could work or not. The much shorter timescales of convection compared to diffusion may be problematic. If the shallow convection zone right beneath the photosphere is changing with time, a periodic enrichment with helium and carbon by convective overshooting could be possible as well. Episodes of convective enrichment would then be followed by phases of undisturbed diffusion.

Carbon rich sdBs would then constitute the very edge of the photospheric convective domain (see Fig. 8.10). At higher temperatures and helium enrichments, the diffusion patterns should vanish and nuclear processed material should be mixed up to the surface. This is consistent with analyses of He-sdBs (Ahmad & Jeffery 2006) as well as preliminary results for He-sdOs (Ströer et al. 2007; Hirsch et al. 2008), which both indicate high enrichment in helium, carbon and nitrogen, but no peculiar enriched heavy metals. Hydrogen rich sdBs and sdOs on the other hand should show a diffusive pattern with temperature trends. The study of Edelmann et al. (2006) and this work clearly show that this is valid for normal sdBs. The very detailed analysis of the eclipsing binary system AA Dor by Rauch (2000), who derived a temperature of $42\,000\,$K for the sdOB primary, reveals a diffusion pattern and no enrichment of helium and carbon. Combining all these results, it may be possible to improve on the studies of Groth et al. (1985) and set observational constraints on the convective zone in subdwarf photospheres. Groth et al. (1985) used mixing length theory. Three dimensional hydrodynamical calculations are required for more realistic treatment of convection.

Most recent results by Miller-Bertolami et al. (2008) considering the formation of He-rich sdO/Bs may provide a very promising alternative explanation. They performed numerical simulations and studied the hot flasher scenario for different metallicities and other physical assumptions. Furthermore they provided timescales for the change of the surface abundances due to diffusion. They also propose a completely new formation scenario for hot hydrogen rich sdBs. According to this scenario He-sdOs are formed after a late hot flash as described by Sweigart (1997a) and Lanz et al. (2004). Due to deep mixing of the outer layers their atmospheres should be enriched in helium, carbon and nitrogen. Most recent results by Unglaub (2008) predict that in the typical parameter range of He-sdOs stellar wind mass loss cannot be chemically homogeneous and is therefore too weak to influence the surface abundance patterns. Without wind mass loss the originally mixed abundance pattern will be altered by diffusion processes, which lead to an enrichment of hydrogen accompanied by depletion of helium, carbon and nitrogen after about $10^7\,$yr (see Fig. 8.11). The He-sdOs eventually turn into sdBs and settle at the ZAEHB. After the helium core burning phase they evolve in a more or less canonical way towards the white dwarf cooling tracks (see Fig. 8.12).
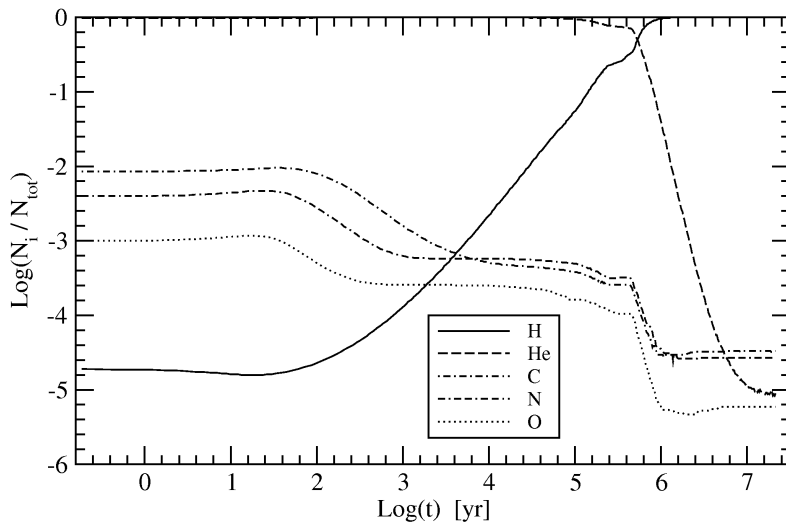
Figure 8.11: Time evolution of the chemical surface abundances as a consequence of diffusion taken from Miller Bertolami et al. (2008).

Could the carbon rich sdBs be in the proposed transition phase between He-sdOs and sdBs? Comparing their atmospheric parameters with the theoretical tracks given by Miller Bertolami et al. (2008) on can immediately see that they populate exactly the right region in the $T_{\text{eff}} - \log g$-diagram (see Figs. 8.10, 8.12 lower panel). Even more remarkable is the predicted number fraction for such transition stars. According to diffusion calculations from Miller Bertolami et al. (2008) the typical abundance pattern of carbon rich sdBs is reached after about 10^6 yr. Assuming an average EHB lifetime of 10^8 yr one would roughly expect $1\,\%$ of the stars to be in this transition stage. The carbon rich sdB fraction of $6\,\%$ comes close to this number taking into account selection effects and shortcomings in the diffusion model. It may also be possible that the sdBs formed through this channel may keep a small convection zone as described above and that helium and carbon will not get more depleted during EHB evolution, since Fig. 8.10 suggests a rather sharp transition between normal sdBs and carbon enriched ones. We conclude that the existence and properties of carbon rich sdBs backs the formation scenario proposed by Miller Bertolami et al. (2008).

8.7 Metal line blanketing and improved model atmospheres

To determine the basic atmospheric parameters of sdB stars ($T_{\text{eff}}, \log g, \log \frac{n_{\text{He}}}{n_{\text{H}}}$) synthetic spectra calculated from LTE or NLTE model atmospheres are matched to the observations. In most cases the models are either metal-free or solar abundances are assumed. These simplifactions can lead to systematic shifts of the atmospheric parameters. The so-called helium ionization problem occurred during analyses of hot subdwarf B stars, where a simultaneous fit of hydrogen and some helium lines (mostly He II) was not possible (Heber et al. 2000; Edelmann 2003; Geier et al. 2007). The analysis of HST-UV spectra of hot sdB stars revealed supersolar abundances of the iron group elements (O'Toole & Heber 2006). Those stars also displayed the optical
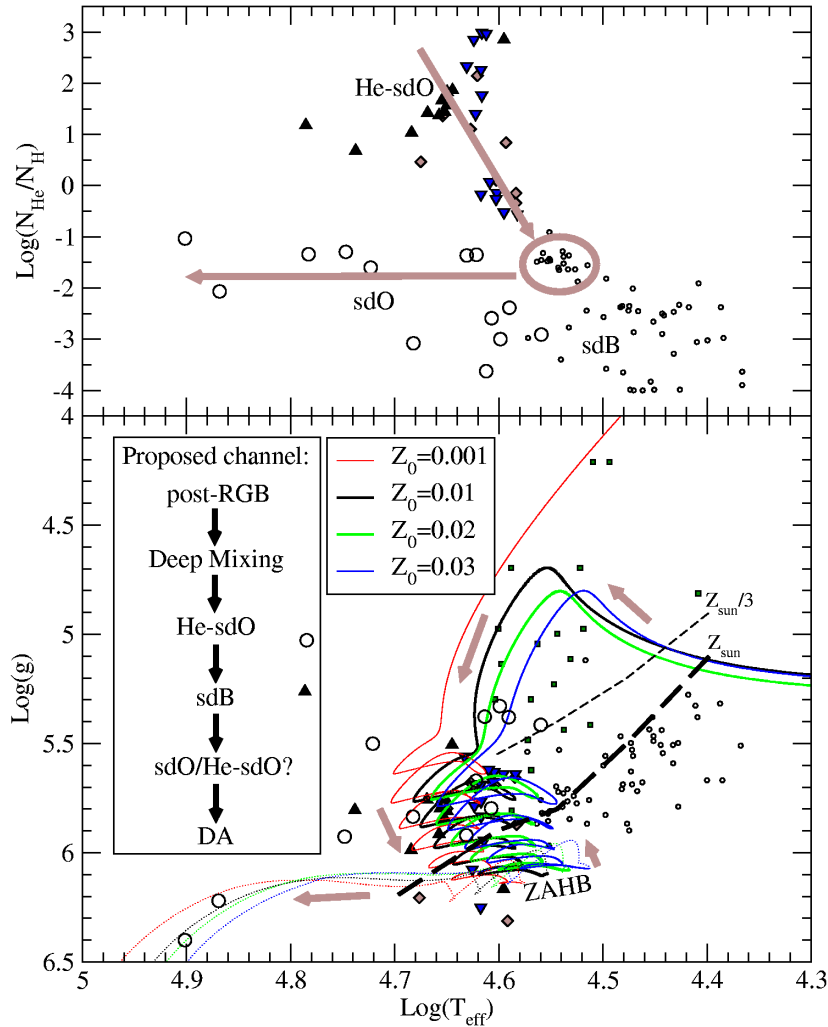
Figure 8.12: Sketch of the proposed channel for the evolution after a Deep Mixing event taken from Miller Bertolami et al. (2008).

He ionization problem. With more appropriate metal-rich models (10 times solar metallicity), the problem could be remedied because of a modified atmospheric temperature structure due to significantly increased line blanketing (see also Heber et al. 1999). The observed metal enrichment in hot sdBs from our sample explains the helium ionization problem. Metal line blanketing with supersolar total metallicity has to be adopted to fit all hydrogen and helium lines simultaneously and derive proper atmospheric parameters of hot sdBs. With the detailed abundance patterns shown here it should be possible to account for all the individual elemental abundances using opacity sampling and calculate the metal line blanketing more accurately.

Figure 9.1: Schematic view of the (HYPER-)MUCHFUSS project.
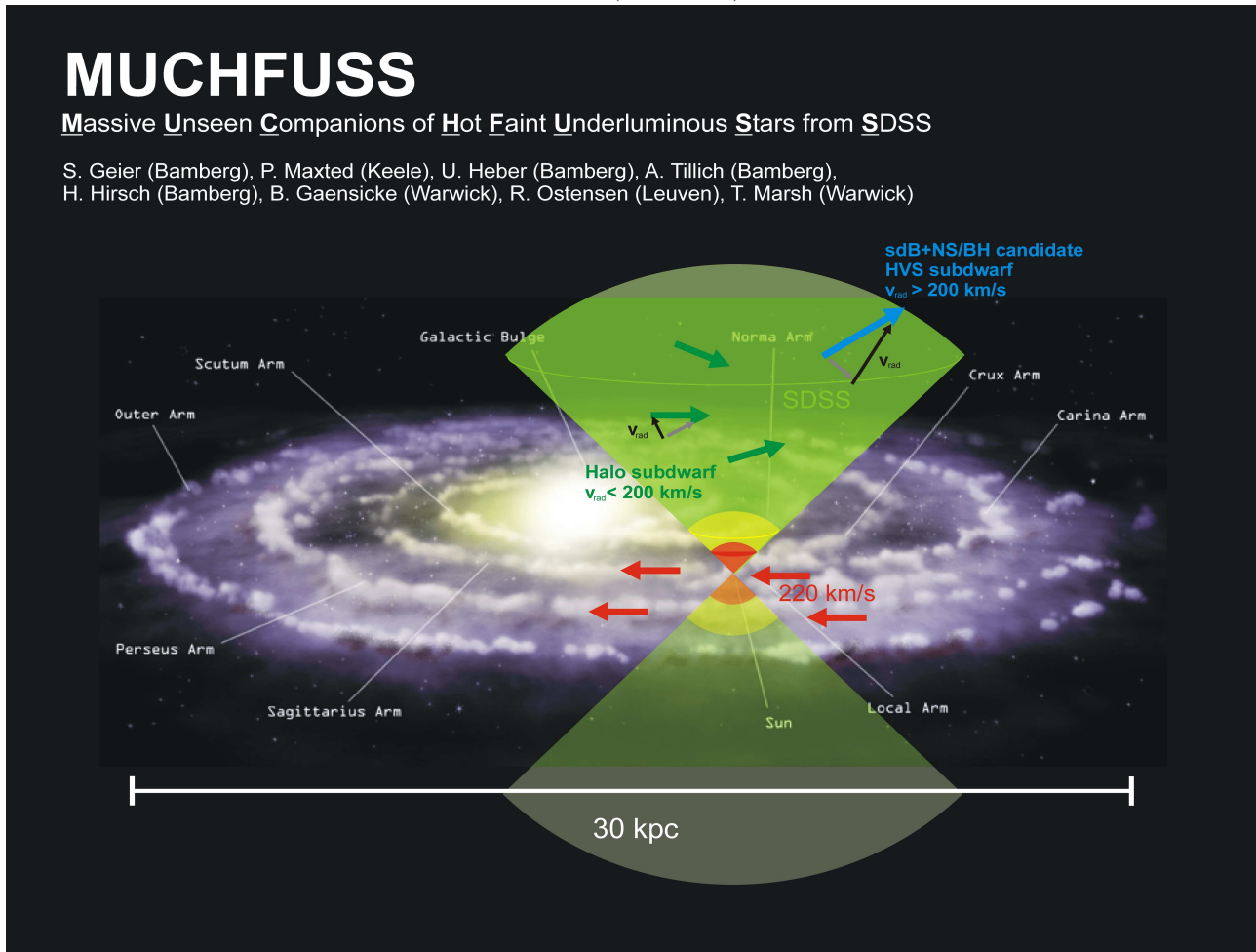
Chapter 9

Outlook: The (HYPER-)MUCHFUSS survey

The surprising discovery of candidate sdB+NS/BH systems triggered a new project devoted to search for such objects. The survey was originally named Massive Unseen Companions to Hot Faint Underluminous Stars from SDSS (MUCHFUSS, PI: S. Geier). If sdB+NS/BH binaries are present in our Galaxy, more than half of them should be seen at high inclination (see Sect. 7). In this case the lower mass limit derived from the mass function should already exceed the Chandrasekhar limit (see Sect. 4.1). Assuming $M_{\rm sdB} = 0.47\,M_\odot$, $M_{\rm comp} > 1.40\,M_\odot$ and $\sin i = 1$ one can derive the minimum RV semi-amplitude K necessary to fulfill these conditions for every given orbital period P. Orbital periods shorter than $0.05\,{\rm d}$ are not possible because in this case the sdB would fill its Roche lobe and mass would be transferred to the secondary. The spectral signature of this process could not be overlooked. Tab. 9.1 gives examples for orbital parameters of putative sdB+NS/BH stars seen at high inclination. Our survey is dedicated to find such sdB binaries with large RV variability.

Table 9.1: Orbital parameters of hypothetical sdB+NS/BH binaries seen at high inclination. The mass function of these binaries exceeds the Chandrasekhar limit. For typical orbital periods P the minimum RV semi-amplitude K is given.

| P | $K_{\rm min}$ |
[d]	[kms^{-1}]
0.05	530
0.10	420
0.20	330
0.50	240
1.00	190
1.30	180

The Sloan Digital Sky Survey (SDSS) and the Sloan Extension for Galactic Understanding and Exploration (SEGUE) provide a unique source of spectral data for different kinds of stars. To identify the hot subdwarfs blue stars were selected by colour. This reduced the sample size

from about 300 000 to about 40 000. All of these spectra were classified by visual inspection (H. Hirsch) and about 1 300 hot subdwarfs of different types could be identified. First epoch RVs have been measured by fitting suitable Balmer lines.

We selected targets from the SDSS DR6 and SEGUE catalogues with heliocentric velocity $> 100\,\mathrm{kms}^{-1}$. First priority is given to systems with $|v_{\mathrm{rad}}| > 200\,\mathrm{kms}^{-1}$. Most single stars in the Galactic disk have heliocentric RVs less than $\pm 100\,\mathrm{kms}^{-1}$, because they are orbiting around the Galactic center just as the sun does. The RV cut therefore enables us to filter out the single (i.e. non RV-variable) stars from the disk population.

Equally important, the selection criterium also filters out the more normal sdB binary systems which have RV amplitudes well below $100\,\mathrm{kms}^{-1}$. Evidently, we will miss some high velocity-amplitude systems because from the SDSS spectra the radial velocity has been measured at random time and hence at random phase. For a $400\,\mathrm{kms}^{-1}$ amplitude system the loss is of order $10\,\%$.

We tested our selection criteria with the sample given in Tab. 3.5, which is dominated by stars with amplitudes of less than $100\,\mathrm{kms}^{-1}$. Taking into account the system velocities and randomised phases only about $15\,\%$ of this sample would have been detected if our MUCHFUSS target pre-selection strategy were applied to our pilot sample (only $2\,\%$ if we restrict it to $200\,\mathrm{kms}^{-1}$). Hence the MUCHFUSS sample of sdB binaries will be quite different from that of all other RV selected sdB samples analysed so far (e.g. Maxted et al. 2001; Napiwotzki et al. 2004a). Close binary sdBs with low mass companions are effectively filtered out. Due to our careful selection method we are able to focus on promising well classified candidate subdwarfs with high RVs. This brings the initial sample of more than thousand subdwarfs down to less than three hundred.

We also select sdB stars with high, but constant RV. These stars are candidates for hyper-velocity stars (see Sect. 2.7). Due to the similarity of the target selection we merged the MUCHFUSS-survey with an ongoing project looking for hyper-velocity subdwarfs (PI: A. Tillich). The HYPERMUCHFUSS-survey was born. For our preselected sample additional RV measurement are necessary to distinguish between HVS candidates (RV constant) and close binaries (RV variable). The binary stars will be followed up to derive their orbital parameters. The most promising targets will be observed with high-resolution spectrographs to allow for a full analysis. Photometric follow-up is planned to detect indicative features in the light curves like eclipses, ellipsoidal deformations, reflection effects or pulsations.

Observing time was granted with ESO-NTT/EFOSC2 and ESO-VLT/FORS1 to cover the southern sky. The northern sky will be observed with CAHA 3.5m/TWIN as well as WHT/ISIS. The project is undertaken in collaboration with U. Heber, A. Tillich, H. Hirsch (Bamberg), P. Maxted (Keele), R. Napiwotzki (Hatfield), B. Gänsicke, T. Marsh (Warwick) and R. Østensen (Leuwen).

Appendix A

Radial velocities of programme stars

Table A.1: Radial velocities of programme stars.

Run	mid HJD [$-2\,450\,000$]	RV_{primary} [kms^{-1}]
Albus 1		
NTT	4476.67364	-31.8 ± 4.9
	4476.72033	-32.0 ± 4.8
	4477.66701	16.3 ± 2.2
	4477.83549	27.2 ± 7.7
	4478.61086	15.9 ± 6.7
	4478.66696	-4.3 ± 5.5
	4478.75702	-15.9 ± 5.0
	4479.64573	-39.8 ± 5.6
	4479.65126	-26.7 ± 7.2
	4479.70277	-21.2 ± 5.0
	4479.70722	-44.8 ± 5.1
	4479.71159	-31.9 ± 4.9
	4479.76992	-37.1 ± 5.8
	4479.73092	-26.5 ± 6.2
	4479.78020	-34.4 ± 6.3

Run	mid HJD [$-2\,450\,000$]	RV_{primary} [kms^{-1}]
ASAS 102322		
NTT	4476.71105	83.5±2.7
	4476.72520	56.8±5.1
	4476.79240	−40.0±4.8
	4477.71457	30.2±5.1
	4477.73271	−43.2±4.9
	4477.75678	−60.8±1.9
	4477.83961	75.5±4.9
	4477.87069	−32.7±4.6
	4477.87494	−46.9±5.2
	4478.65824	93.1±5.5
	4478.68417	46.8±5.5
	4478.76238	−12.1±5.0
	4478.87023	−75.1±4.8
	4479.73634	−0.6±4.9
	4479.73634	−49.9±5.3
BPS CS 22879−82		
NTT	4253.32226	−83.2±8.0
	4254.30933	−34.2±32.3
BPS CS 22879−149		
NTT	4252.43610	−22.3±8.0
	4253.31517	−72.1±8.0
	4253.40017	−12.1±8.0
	4254.24924	−71.7±8.0
	4254.30224	−47.5±8.0
	4254.36425	19.7±8.0
BPS CS 22937−84		
NTT	4253.33081	118.7±7.9
	4254.31788	143.0±9.5
BPS CS 22947−99		
NTT	4253.27545	−80.1±8.0
	4253.40846	−76.4±8.0
	4254.15049	−92.2±8.0
	4254.24250	−85.3±8.0
	4254.29450	−82.1±8.0
	4254.35850	−93.2±8.0
	4254.40051	−113.6±8.0

Run	mid HJD $[-2\,450\,000]$	RV_{primary} $[\text{kms}^{-1}]$
BPS CS 22947−299		
NTT	4253.28322	96.5±8.6
HE 1033−2353		
SPY	1656.54086	25.9±2.1
	1681.52399	25.2±3.6
NTT	4254.60675	−23.5±6.0
	4476.78129	12.3±8.4
	4479.83664	37.0±8.1
HE 1130−0620		
SPY	1739.47790	49.2±8.0
	1683.54483	−8.9±8.0
NTT	4252.97257	-25.6±8.0
	4253.09756	-39.4±8.0
	4254.08047	-32.6±8.0
	4477.80495	11.0±11.5
	4478.78734	19.0±7.5
	4479.80438	0.5±10.8
WHT	4588.37330	6.0±16.3
	4588.37494	12.8±18.6
HE 1140−0500		
SPY	2657.74031	−46.5±5.0
	2387.48739	−46.5±5.0
	2393.68163	−39.5±5.0
NTT	4253.61774	−93.3±8.0
	4254.59966	−108.0±8.0
	4476.80115	−35.5±7.5
	4477.81998	−34.4±10.1
	4477.80234	−61.8±3.4
	4479.78855	−73.4±12.7
WHT	4587.40173	−31.8±3.0
HE 1415−0510		
SPY	1740.63899	258.2±8.0
	1755.48571	203.1±8.0
NTT	4253.49757	149.0±7.9
	4253.63156	−86.9±8.0
	4254.52251	185.0±10.0
	4254.68650	162.6±12.8
	4476.85174	27.0±8.6
	4479.86504	253.0±15.0
WHT	4587.64673	−11.2±13.5

Run	mid HJD $[-2\,450\,000]$	RV_{primary} $[\text{kms}^{-1}]$
HE 1423−0119		
SPY	1740.64912	−26.9±5.9
	1755.57119	−11.1±5.6
NTT	4253.52060	−48.9±6.7
	4253.66060	−103.8±29.8
	4253.72759	−34.3±9.5
	4254.70854	−37.8±4.7
HE 1518−0948		
SPY	2387.86322	-106.5±5.0
McDonald	3934.64046	-6.3±15.0
NTT	4253.09344	−190.1±10.0
	4254.23740	−147.7±10.0
WHT	4587.56440	−54.2±15.8
	4587.57274	−84.6±10.3
	4587.58117	−82.5±20.9
	4587.63476	−101.8±13.9
HE 2322−4559		
SPY	2162.59563	17.6±5.0
	2466.91085	40.8±5.0
NTT	4252.90176	−98.4±14.3
	4253.79583	−132.1±22.2
	4253.85684	−92.1±13.2
	4254.77290	−92.2±11.4
	4254.84291	−82.2±10.3
	4476.53261	−73.5±7.4
	4477.57356	−103.3±10.5
	4478.56151	−65.6±14.3
HS 1536+0944		
SPY	2387.84766	−98.3±5.0
NTT	4253.55282	−221.6±11.9
	4253.68881	−128.4±20.8
	4254.63378	−76.3±20.5
WHT	4588.71758	−94.0±14.2
	4588.73133	−120.0±10.0

Run	mid HJD [$-2\,450\,000$]	RV_{primary} [kms^{-1}]
HS 2043+0615		
SPY	2387.90703	27.2 ± 5.0
	2521.66074	-108.9 ± 5.0
NTT	4252.88665	-93.9 ± 8.0
	4253.75520	-42.5 ± 8.0
	4253.84117	-170.2 ± 8.0
	4253.91546	-152.8 ± 8.0
	4254.75730	-143.3 ± 8.0
	4254.82763	-137.5 ± 8.0
	4254.88140	-132.1 ± 8.0
WHT	4586.73051	-19.2 ± 11.0
	4586.73799	-31.0 ± 10.9
KPD 0629−0016		
NTT	4476.69426	37.1 ± 8.6
	4477.61197	-1.3 ± 8.0
	4477.68846	-13.4 ± 3.4
	4478.62101	-34.4 ± 7.1
	4478.67763	-58.2 ± 3.7
	4478.77402	-73.3 ± 4.3
	4479.62414	-75.1 ± 8.9
	4479.63799	-46.8 ± 10.1
	4479.66199	-53.9 ± 8.3
	4479.67306	-63.6 ± 8.1
	4479.68573	-74.7 ± 8.2
	4479.69438	-47.8 ± 7.7
PG 0941+280		
MMT	3715.01112	212.6 ± 1.0
	3716.99883	-60.4 ± 2.0
	3717.02115	-60.3 ± 2.0
	3766.89779	109.3 ± 3.0
	3768.86376	212.3 ± 2.0
NTT	4476.76052	-3.3 ± 9.2
	4476.84388	184.8 ± 13.5
	4477.78158	190.7 ± 6.5
	4477.83014	159.0 ± 11.8
	4478.75103	190.3 ± 6.8
	4478.82365	58.8 ± 11.1
	4478.86683	-40.0 ± 4.2
	4479.71960	174.8 ± 13.8

Run	mid HJD [−2 450 000]	RV_{primary} [kms^{-1}]
V 1405 Ori		
NTT	4476.68258	17.3±10.3
	4477.59921	−68.1±18.4
	4477.64791	−129.6±13.4
	4477.69907	−108.1±31.6
	4478.58382	9.3±17.0
	4478.64047	63.7±8.6
	4478.70892	26.3±14.5
	4479.61084	−117.8±7.9
	4479.75802	−40.1±9.3
WD 0107−342		
SPY	1737.8352	162.9±4.0
	1740.7656	63.1±4.0
NTT	3337.6738	−40.5±5.3
	3338.5941	17.4±4.1
	3339.6139	−87.6±4.0
	3339.6723	−64.7±4.1
	3340.5405	130.1±4.7
	4252.8724	−13.5±11.0
	4252.9224	82.4±9.8
	4253.8735	−103.3±8.0
	4253.9285	−120.4±8.0
	4254.8676	136.3±11.1
	4476.5455	162.1±6.3
	4477.5624	−18.6±5.8
	4477.6524	136.1±8.6

Appendix B

Radial velocity curves and power spectra
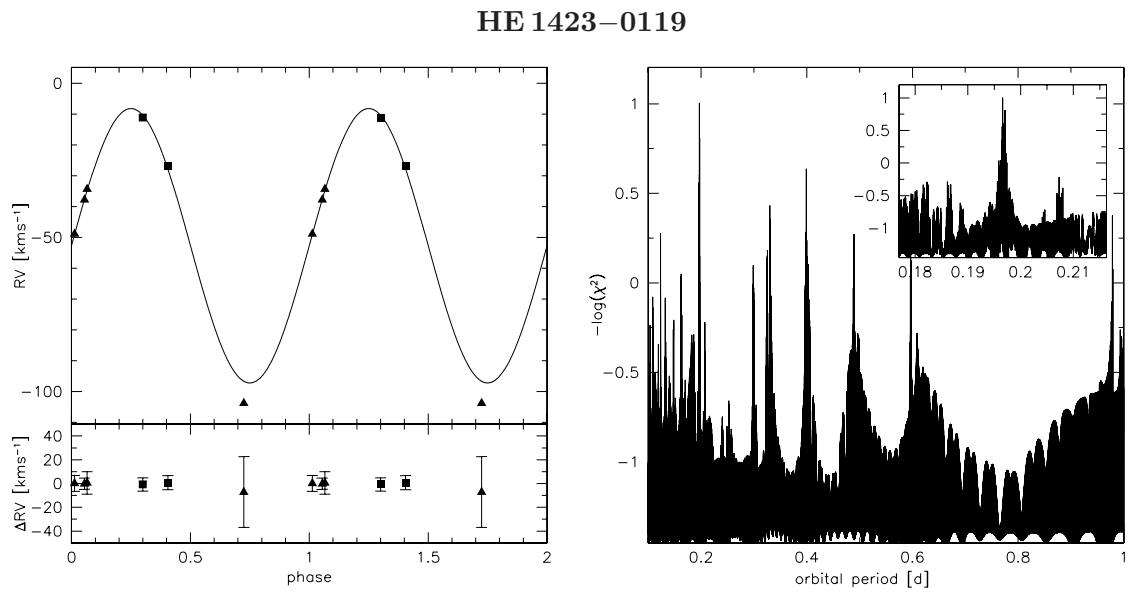
HE 1423−0119

Figure B.1: Radial velocity curve and power spectrum of HE 1423−0119 (see Fig. 2.5).

PG 0941+280
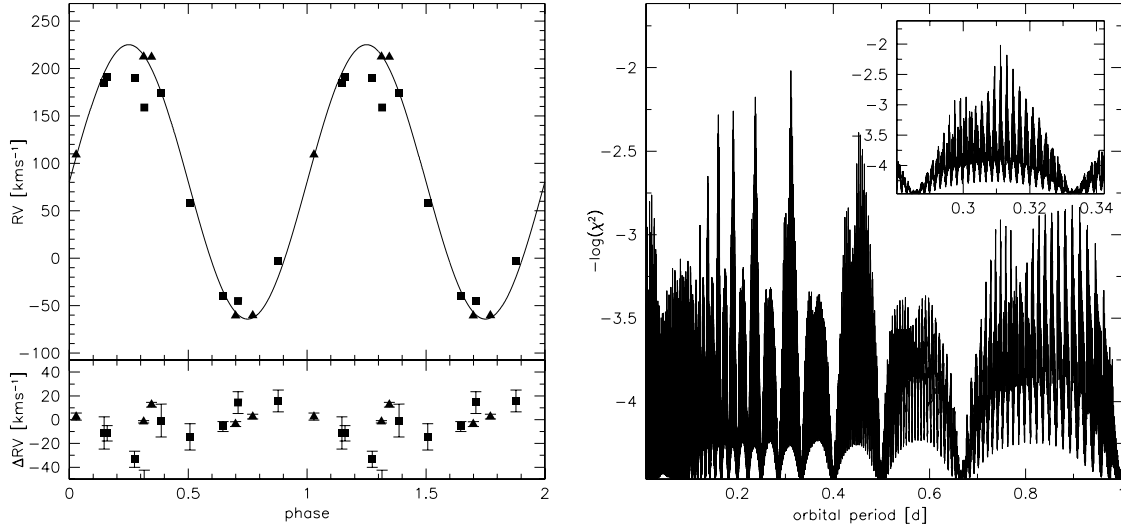
Figure B.2: Radial velocity curve and power spectrum of PG 0941+280 (see Fig. 2.5).

WD 0107−342
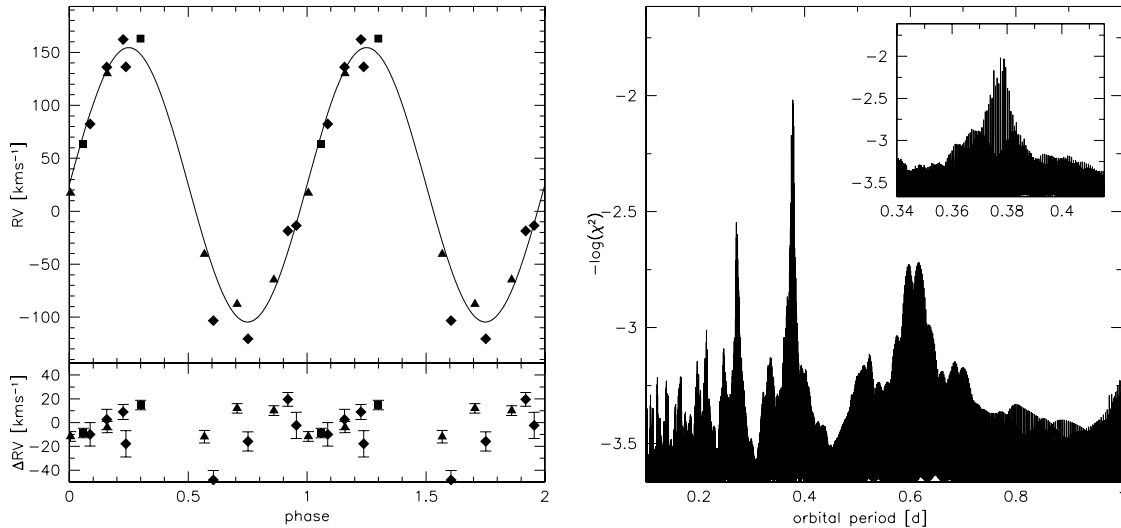
Figure B.3: Radial velocity curve and power spectrum of WD 0107−342 (see Fig. 2.5).

V 1405 Ori
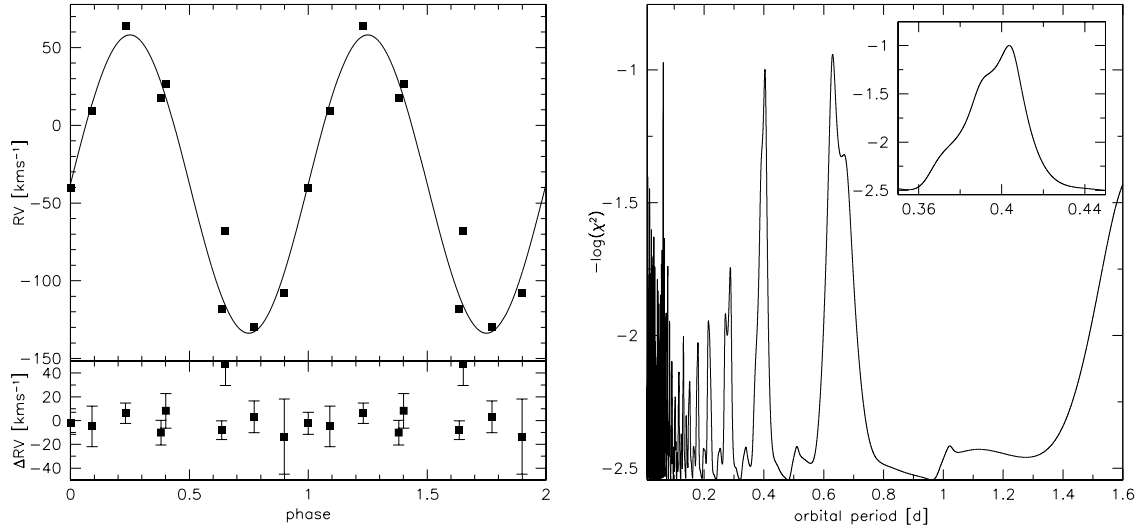
Figure B.4: Radial velocity curve and power spectrum of V 1405 Ori (see Fig. 2.5).

Albus 1
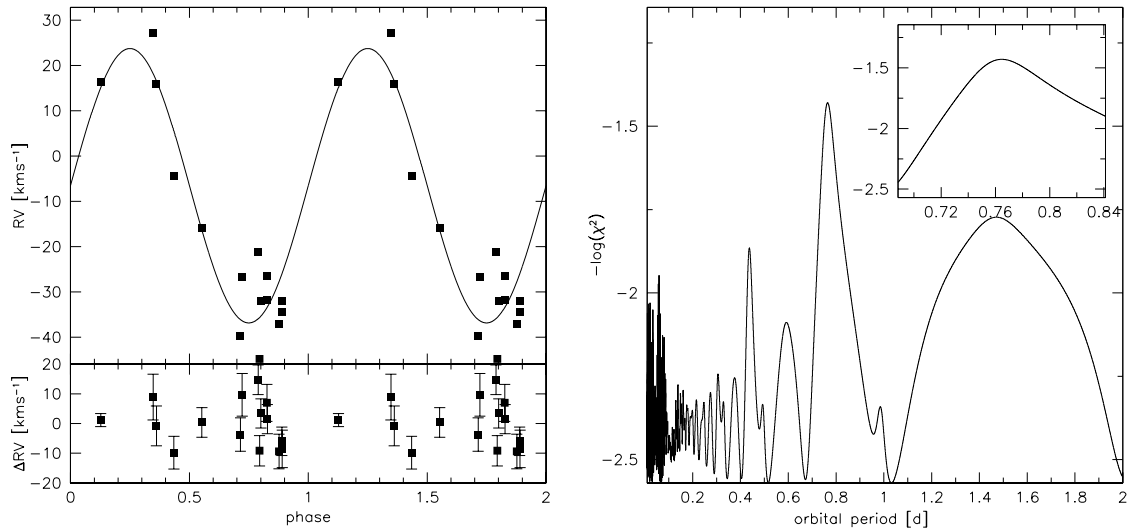
Figure B.5: Radial velocity curve and power spectrum of Albus 1 (see Fig. 2.5).

HE 1130−0620
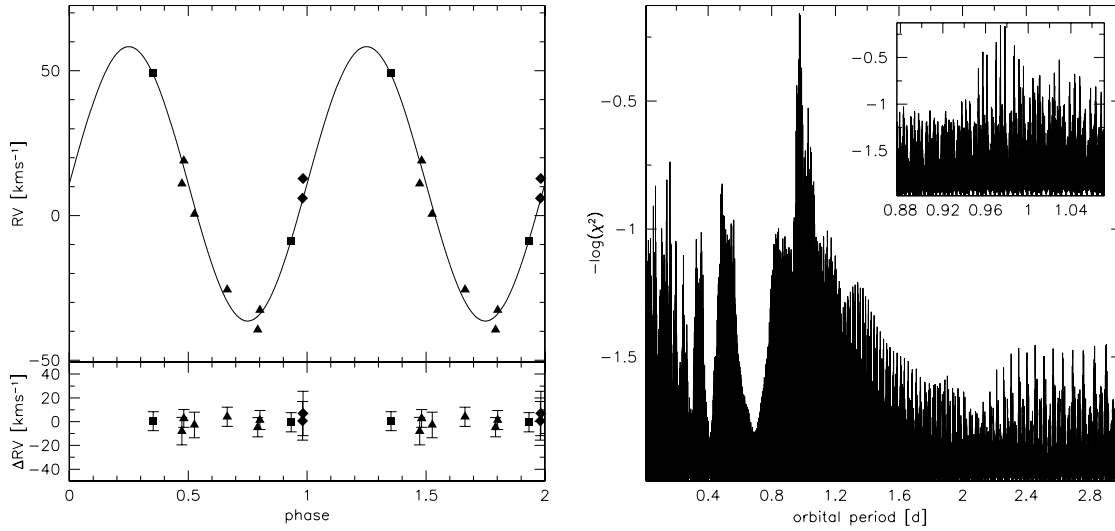
Figure B.6: Radial velocity curve and power spectrum of HE 1130−0620 (see Fig. 2.5).

HE 1415+0309
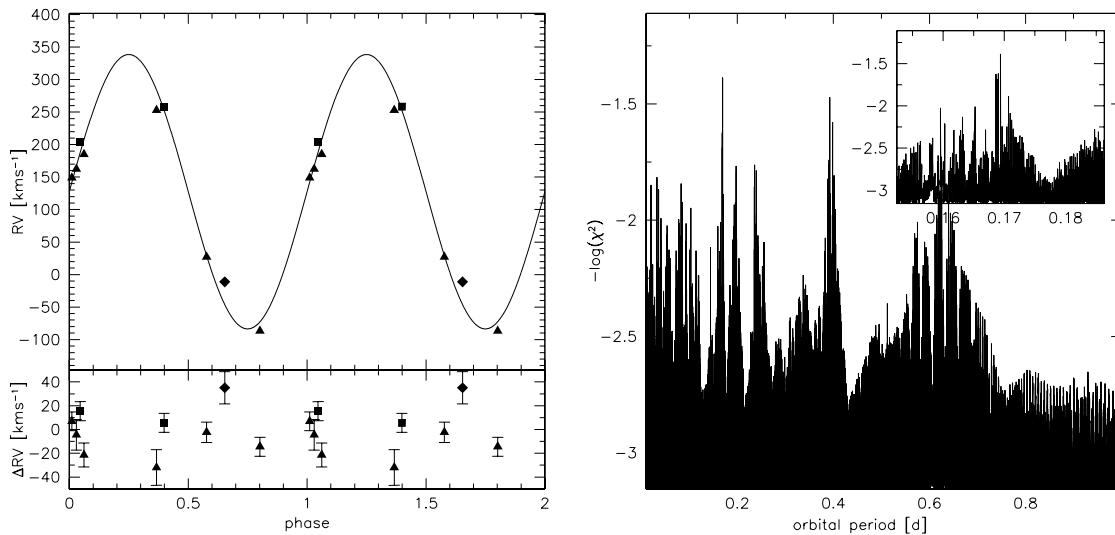
Figure B.7: Preliminary radial velocity curve and power spectrum of HE 1415+0309 (see Fig. 2.5).

HE 1140+0500
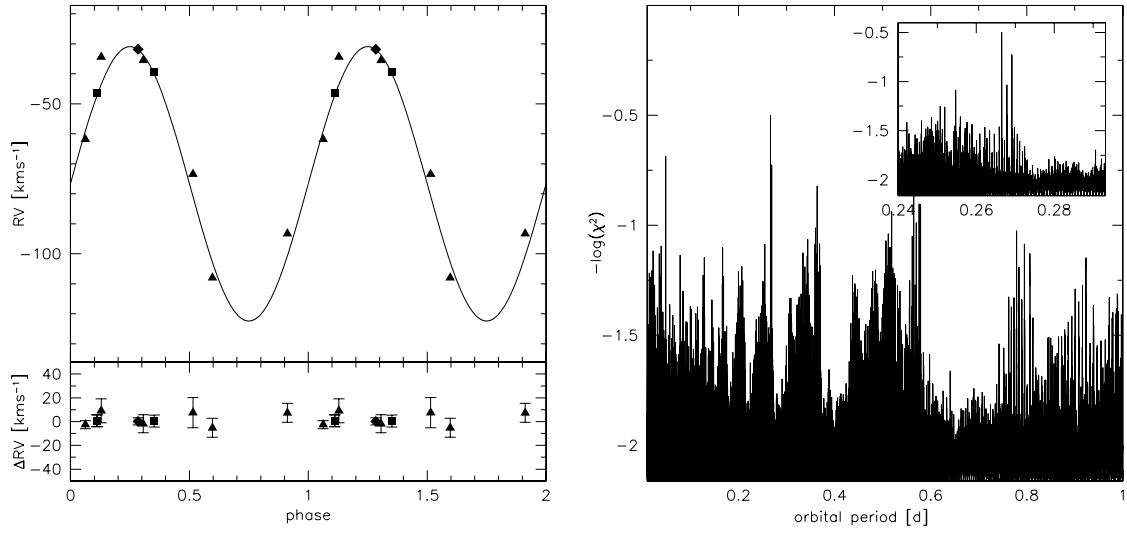
Figure B.8: Preliminary radial velocity curve and power spectrum of HE 1140+0500 (see Fig. 2.5).

HS 2043+0615
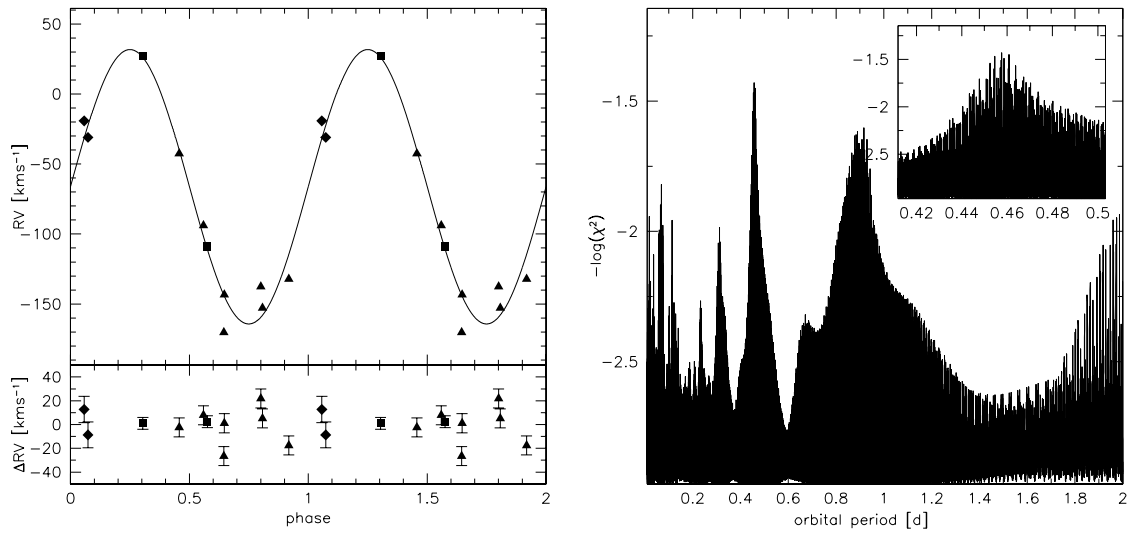
Figure B.9: Preliminary radial velocity curve and power spectrum of HS 2043+0615 (see Fig. 2.5).

KPD 0629−0016
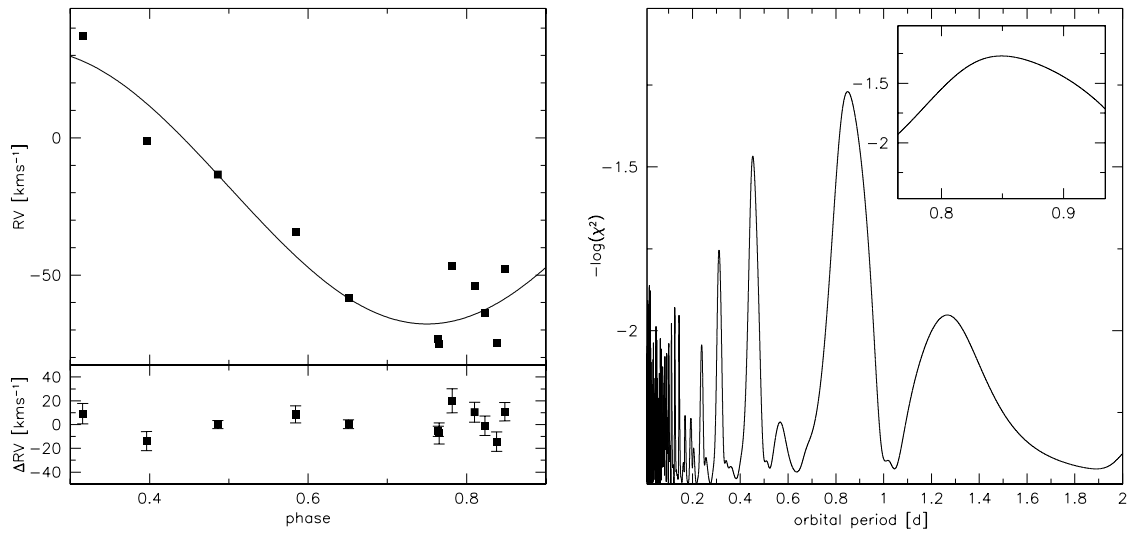
Figure B.10: Preliminary radial velocity curve and power spectrum of KPD 0629−0016 (see Fig. 2.5). A detail of the RV curve is plotted to show a yet unexplained modulation.

Appendix C

Metal abundances

Table C.1: Elemental abundances of sdBs from SPY. The stars are sorted with increasing effective temperature. Average abundances with standard deviations are given, if more than one line was fitted. Single line measurements are given without errors. To estimate realistic errors it is necessary to take the spectral quality into account (see Sect. 4.4.2). Upper limits are only given, if they constrain the abundances in a reasonable way. *The atmospheric parameters as well as the helium abundances are taken from Lisker et al. 2005. †Spectra with $S/N < 15$ and therefore higher error limits. ^{c}Spectra with significant flux contribution from a main sequence companion (see Lisker et al. 2005). Only metal lines with wavelengths shorter than $4\,500\,\text{Å}$ have been analysed.

| | HE 0151−3919 | HE 2307−0340 | HE 0539−4246 | HE 2208+0126 | GD 687 | HE 0321−0918 |
	20841 K 4.83 *	23260 K 5.51 *	23279 K 5.51 *	24277 K 5.67 *	24350 K 5.32 *	25114 K 5.67 *
He I/II*	9.93	8.35	8.09	9.02	9.62	8.98
C II	6.40	<6.37	<6.49	7.10	6.70	6.80
C III	−	−	−	−	−	−
N II	7.48 ± 0.13	6.75 ± 0.07	7.30 ± 0.22	7.38 ± 0.26	7.60 ± 0.28	7.28 ± 0.13
N III	−	−	−	<7.08	<7.14	−
O II	7.62 ± 0.26	7.90	<7.40	7.50 ± 0.26	7.82 ± 0.41	7.55 ± 0.07
Ne II	<8.15	8.10 ± 0.28	<8.05	<8.10	<7.90	7.75 ± 0.07
Mg II	6.10	6.30	6.00	5.90	7.20	<5.95
Al III	<4.74	5.35 ± 0.07	<4.94	5.00	<5.10	<4.98
Si III	<6.04	<6.21	<6.32	<6.17	<6.11	6.00
Si IV	−	−	−	−	−	−
P III	<5.09	5.90	5.90	<5.47	<5.88	<5.20
S II	6.40	<6.39	<6.38	<6.43	<6.75	<6.45
S III	6.90	−	−	−	<6.20	−
Ar II	6.73 ± 0.21	6.30	6.80	<6.26	<6.95	<6.60
K II	<5.96	6.50	<6.40	<6.10	<6.19	<6.11
Ca III	−	−	−	−	−	−
Sc III	<5.10	<5.49	<5.50	<5.44	<5.65	5.40
Ti III	<5.80	<6.42	6.50	<6.36	<6.50	6.70
Ti IV	−	−	−	−	−	−
V III	7.50	7.40	7.50	7.20	7.40	7.40
Cr III	6.00	<5.84	6.45 ± 0.49	6.10 ± 0.42	<6.00	6.60 ± 0.42
Fe III	<6.97	7.75 ± 0.17	7.57 ± 0.25	7.30 ± 0.28	7.00	7.37 ± 0.06
Co III	<6.68	<7.00	<7.34	<7.30	<7.20	<7.40
Zn III	<7.44	<7.57	<7.62	<7.10	<7.50	<7.40

| | HE 2322−4559^c | HE 2237+0150† | HE0532−4503 | PG 2122+157^c | HS 2043+0615 † | HE 0513−2354† |
	25512 K 5.30 *	25606 K 5.38 *	25710 K 5.33 *	26015 K 5.22 *	26157 K 5.28 *	26758 K 5.50 *
He I/II*	9.53	10.08	8.93	9.31	9.62	9.67
C II	7.40	<6.90	6.30	6.70	7.20	<7.10
C III	−	−	<7.30	−	−	−
N II	7.13 ± 0.35	7.65 ± 0.15	7.06 ± 0.18	7.13 ± 0.23	7.40 ± 0.17	7.40 ± 0.01
N III	−	−	<6.74	−	<7.36	−
O II	7.47 ± 0.44	8.22 ± 0.39	7.61 ± 0.17	7.63 ± 0.35	7.97 ± 0.29	8.22 ± 0.22
Ne II	<7.20	<8.31	7.15 ± 0.07	7.95 ± 0.07	<8.37	8.40
Mg II	6.30	6.80	6.60	6.40	7.00	<6.60
Al III	5.40	<5.19	<4.17	<4.89	<5.35	<5.24
Si III	6.00	<6.25	<5.40	<5.91	<6.31	<6.41
Si IV	−	−	−	−	−	−
P III	<5.58	<5.97	<4.81	<5.22	<6.06	<6.08
S II	<6.49	7.00	<6.27	<5.88	<7.56	<7.57
S III	−	6.40	5.92 ± 0.07	6.10	6.90	6.90 ± 0.28
Ar II	−	6.55 ± 0.07	<5.98	−	<7.27	7.10
K II	<6.17	<6.20	<5.69	<5.99	6.50	6.25 ± 0.35
Ca III	−	−	−	−	−	−
Sc III	<5.30	<5.79	<4.98	<5.46	<5.99	<5.85
Ti III	<6.48	7.00	<5.38	6.60	<6.72	<6.64
Ti IV	−	−	−	−	−	−
V III	7.60	7.40	6.70	<7.21	8.70	7.60
Cr III	6.30 ± 0.42	<6.11	5.50	<5.84	<6.26	6.30
Fe III	7.10	7.35 ± 0.21	7.37 ± 0.17	<6.98	7.35 ± 0.49	7.65 ± 0.21
Co III	7.30	<7.62	<6.49	<7.00	<7.20	<7.55
Zn III	−	<7.63	−	−	<7.69	<7.75

141

| | HE 0135−6150 † | HE 2201−0001 † | HE 1309−1102ᶜ† | HS 2357+2201ᶜ | SB 485 | KUV 01542−0710 |
	27020 K 5.59 *	27062 K 5.51 *	27109 K 5.36 *	27629 K 5.55 *	27738 K 5.51 *	27760 K 5.44 *
He I/II*	9.53	8.71	9.54	9.46	9.50	9.09
C II	6.50	6.70	7.00	<6.33	6.60	6.50
C III	−	−	−	−	−	<7.92
N II	7.85 ± 0.16	7.47 ± 0.19	7.30 ± 0.28	7.55 ± 0.13	7.54 ± 0.05	6.87 ± 0.25
N III	−	−	−	−	<8.11	−
O II	7.98 ± 0.28	7.83 ± 0.33	7.83 ± 0.06	7.76 ± 0.17	7.64 ± 0.17	8.00 ± 0.24
Ne II	<8.21	<7.60	<8.20	7.10	6.80	<7.35
Mg II	<6.37	6.70	<6.40	6.30	6.40	<6.14
Al III	5.50	5.50	<5.41	<4.87	<4.70	<5.01
Si III	6.00	6.63 ± 0.31	<6.55	<5.86	<5.46	<5.93
Si IV	−	<7.48	−	−	−	−
P III	<5.94	<5.38	<6.23	<5.10	<4.82	<5.29
S II	<7.44	<6.98	−	<6.11	<6.48	−
S III	6.50	6.40 ± 0.14	6.40 ± 0.14	6.50	6.10 ± 0.28	6.20
Ar II	6.60	<6.94	−	−	6.70	<6.94
K II	<6.36	<6.26	6.10	<5.96	<5.74	<6.11
Ca III	−	−	−	−	−	−
Sc III	5.30	<5.62	<6.08	<5.41	<5.23	<5.57
Ti III	6.50	7.25 ± 0.07	<6.79	<5.83	<6.00	<6.10
Ti IV	−	−	−	−	−	−
V III	7.95 ± 0.64	<7.19	7.70	<7.02	7.21	7.20
Cr III	<6.08	6.90	<6.22	<5.81	<5.50	<5.93
Fe III	7.35 ± 0.07	<7.10	7.50	7.33 ± 0.28	7.38 ± 0.15	7.30
Co III	7.25 ± 0.21	<7.39	<7.40	<6.99	<6.55	<7.37
Zn III	<6.70	<7.00	<7.93	−	<6.40	<6.72

	HE 2156−3927[c]	PG 0258+184	HE 2322−0617[c]	HE 0136−2758	PG 1549−001	HE 0016+0044
	27995 K 5.50 *	28092 K 5.52 *	28106 K 5.50 *	28202 K 5.47 *	28252 K 5.49 *	28264 K 5.38 *
He I/II*	9.65	9.97	10.07	8.00	9.34	9.34
C II	6.80	6.60	6.60	−	7.20	6.60
C III	−	−	−	−	<7.60	<7.20
N II	7.10 ± 0.23	6.90 ± 0.20	7.25 ± 0.21	7.05 ± 0.26	7.15 ± 0.13	6.95 ± 0.13
N III	−	−	−	−	<6.91	−
O II	7.74 ± 0.21	7.90 ± 0.28	7.70 ± 0.21	8.10 ± 0.14	7.93 ± 0.16	8.04 ± 0.22
Ne II	<7.08	<7.35	<7.21	<7.16	<7.30	6.70
Mg II	<5.97	<6.19	6.30	<6.00	6.70	6.60
Al III	<4.80	<5.05	<4.96	<4.89	5.30 ± 0.14	<4.90
Si III	<5.81	<5.95	<5.88	6.40 ± 0.14	6.67 ± 0.49	5.60
Si IV	−	−	−	<6.42	6.90 ± 0.14	<6.25
P III	<5.06	<5.34	<5.19	<5.05	<5.07	4.90
S II	<6.91	−	<7.29	<6.90	7.10	−
S III	6.10 ± 0.14	6.20	6.45 ± 0.07	6.30 ± 0.14	6.90 ± 0.14	6.00
Ar II	−	−	−	<6.82	7.00 ± 0.14	<6.85
K II	<5.94	<6.15	6.40	<6.06	6.45 ± 0.21	6.25 ± 0.07
Ca III	−	−	−	−	−	−
Sc III	<5.41	<5.61	<5.51	<5.45	<5.47	5.70
Ti III	<5.79	6.70 ± 0.57	6.00 ± 0.28	<5.98	7.10 ± 0.30	6.40
Ti IV	−	−	−	<5.98	−	−
V III	7.20	7.60	<7.15	<6.94	7.40	7.40
Cr III	<5.81	<5.80	6.70	5.70	6.81	6.05 ± 0.49
Fe III	<6.63	7.03 ± 0.15	6.90 ± 0.28	7.38 ± 0.17	7.07 ± 0.15	6.85 ± 0.07
Co III	<6.96	7.70	<7.32	7.20 ± 0.28	<6.90	<6.85
Zn III	<6.60	<6.70	<6.61	<6.51	<6.50	<6.49

143

| | HE 2349−3135 | HE 0007−2212 | WD 1433−270 | HE 1415−0309† | HE 1421−1206 | HE 0929−0424 |
	28520 K 5.44 *	28964 K 5.68 *	29262 K 5.72 *	29520 K 5.56 *	29570 K 5.53 *	29602 K 5.69 *
He I/II*	8.16	8.00	9.54	9.13	8.00	9.99
C II	<6.80	6.30	7.00	<7.42	6.80	6.60
C III	−	−	7.30	−	7.20	<7.53
N II	7.26 ± 0.11	7.48 ± 0.16	7.68 ± 0.08	<7.80	7.15 ± 0.24	7.70 ± 0.16
N III	<7.07	<8.00	<8.37	−	−	<8.31
O II	7.61 ± 0.17	7.51 ± 0.19	7.60 ± 0.14	<7.80	7.47 ± 0.16	7.64 ± 0.14
Ne II	7.20	<6.80	6.95 ± 0.21	<7.70	7.30 ± 0.42	7.00
Mg II	6.60	<6.11	6.40	<7.35	6.60	−
Al III	<5.14	<5.10	<4.98	<5.90	5.50	5.50
Si III	<5.95	6.70 ± 0.28	7.07 ± 0.23	<6.61	6.20	<6.30
Si IV	−	7.25 ± 0.21	6.60	−	<6.75	6.20 ± 0.28
P III	<5.40	<5.21	<5.15	<6.24	<5.10	<5.17
S II	−	<7.29	7.30	−	−	<7.30
S III	<5.87	7.05 ± 0.07	6.65 ± 0.07	<6.91	5.90	6.45 ± 0.07
Ar II	<7.08	6.85 ± 0.07	6.90	<7.56	<7.00	7.15 ± 0.21
K II	6.00	<5.80	<6.06	<7.15	6.60	6.40
Ca III	−	−	−	−	<8.50	8.70
Sc III	<5.71	<5.53	6.20	<6.20	<5.59	5.40
Ti III	7.10 ± 0.14	6.70 ± 0.54	6.82 ± 0.45	<6.40	6.63 ± 0.47	6.87 ± 0.15
Ti IV	<6.43	<7.70	<7.98	−	<6.59	7.65 ± 0.21
V III	<7.00	6.80 ± 0.14	<7.07	−	<7.17	7.60 ± 0.28
Cr III	<6.06	6.50 ± 0.28	<6.88	<6.61	7.10 ± 0.14	6.30
Fe III	6.93 ± 0.21	7.17 ± 0.15	7.03 ± 0.10	<7.44	7.37 ± 0.15	7.10
Co III	<7.44	<7.31	<7.28	−	<6.90	<7.28
Zn III	<6.72	<6.20	<6.30	<7.90	−	6.20

| | PHL 861 | HE 1254−1540 | HE 2150−0238 | HE 2135−3749 | HE 2222−3738 | HE 1047−0436 |
	29668 K 5.50 *	29700 K 5.63 *	29846 K 5.90 *	29924 K 5.87 *	30248 K 5.69 *	30280 K 5.71 *
He I/II*	8.00	8.00	9.64	9.55	8.35	9.65
C II	<6.20	<6.80	<6.80	<5.98	7.10	7.30
C III	−	<7.07	−	−	7.40	7.88
N II	7.08 ± 0.16	6.95 ± 0.21	7.67 ± 0.18	7.50 ± 0.09	7.73 ± 0.08	7.92 ± 0.12
N III	−	<7.55	<8.00	7.90	<8.18	8.00 ± 0.01
O II	7.63 ± 0.20	7.60 ± 0.21	7.10 ± 0.17	6.75 ± 0.07	7.74 ± 0.26	7.70 ± 0.13
Ne II	<6.80	6.80 ± 0.14	<7.20	6.50	<7.03	6.80
Mg II	6.70	6.30	<6.32	<5.79	7.20	6.90
Al III	5.50	5.50	<5.30	5.10	<5.20	5.40
Si III	<5.60	7.20 ± 0.20	6.40 ± 0.28	<5.46	6.73 ± 0.15	6.83 ± 0.25
Si IV	<6.21	7.60 ± 0.10	<6.40	<5.78	6.70 ± 0.42	6.77 ± 0.38
P III	<5.00	<5.30	<5.50	<4.80	5.50	<5.02
S II	−	7.00	<7.40	7.00	7.00	7.60
S III	6.00	7.05 ± 0.07	6.85 ± 0.21	6.70	6.80 ± 0.14	7.15 ± 0.07
Ar II	<7.08	<7.02	7.78 ± 0.02	7.33 ± 0.29	7.10 ± 0.17	7.04 ± 0.16
K II	<6.28	<6.40	6.40	6.30 ± 0.10	<6.27	<6.00
Ca III	−	−	<8.40	−	−	−
Sc III	<5.71	<5.10	5.70	5.00	5.70	5.90
Ti III	6.80 ± 0.14	<6.36	7.03 ± 0.46	6.60 ± 0.27	6.77 ± 0.47	7.03 ± 0.41
Ti IV	8.20 ± 0.14	−	−	<7.37	<7.49	7.00
V III	<7.35	<6.90	<7.10	6.80	7.27	7.20
Cr III	7.35 ± 0.35	6.10	6.95 ± 0.07	6.90 ± 0.14	6.85 ± 0.07	7.10 ± 0.42
Fe III	7.10 ± 0.28	7.40 ± 0.36	7.00	6.65 ± 0.35	6.93 ± 0.40	6.90 ± 0.36
Co III	<7.38	<7.00	<7.41	<6.53	<6.90	<6.92
Zn III	<6.70	−	<6.69	−	<6.54	−

| | HE 2238−1455 | HE 1038−2326^c† | HE 0207+0030† | HS 2359+1942† | HE 0230−4323 | TON S 155^c† |
	30393 K 5.47 *	30573 K 5.21 *	31414 K 5.83 *	31434 K 5.56 *	31552 K 5.60 *	32318 K 5.16 *
He I/II*	9.63	10.27	10.17	8.42	9.42	8.96
C II	<6.84	7.70	<7.06	<7.05	6.70	<7.05
C III	−	−	−	7.40	<6.71	−
N II	<6.79	7.67 ± 0.30	7.60 ± 0.13	7.10 ± 0.26	7.28 ± 0.13	7.20 ± 0.01
N III	−	−	8.55 ± 0.07	8.00 ± 0.14	7.55 ± 0.07	−
O II	6.95 ± 0.13	7.20	<7.40	7.24 ± 0.15	7.51 ± 0.18	7.15 ± 0.21
Ne II	<6.95	<7.06	<7.26	<7.19	6.90 ± 0.14	<6.94
Mg II	6.50	6.90	<6.97	7.30	6.90	<6.94
Al III	<5.06	5.90 ± 0.14	5.80	<5.58	<5.20	<5.50
Si III	<5.89	7.10 ± 0.14	<6.23	6.00	6.20 ± 0.20	−
Si IV	5.70	6.35 ± 0.07	−	6.40	6.60 ± 0.44	<5.50
P III	<5.08	<5.27	<5.90	<5.30	<5.24	<5.57
S II	−	−	<7.80	−	−	−
S III	5.70	6.45 ± 0.21	6.95 ± 0.07	<5.70	5.90 ± 0.14	<5.58
Ar II	<6.91	−	7.80	7.10	<7.07	<7.41
K II	6.10	<6.88	6.90	<6.92	<6.26	<6.70
Ca III	−	−	−	<8.10	<7.90	<8.31
Sc III	<5.59	5.90	<5.80	<6.05	<5.65	<6.10
Ti III	6.70	7.10	6.87 ± 0.25	7.22	6.95 ± 0.07	<6.49
Ti IV	<6.31	−	<7.73	8.05 ± 0.21	<7.46	−
V III	<6.99	<7.30	<7.98	<7.33	7.84	<7.30
Cr III	6.70 ± 0.28	7.30 ± 0.14	7.30	<6.52	6.70	<6.81
Fe III	<6.70	<6.92	7.10 ± 0.14	7.00	7.43 ± 0.17	<6.94
Co III	<6.95	<7.32	<7.53	<7.38	<7.28	<7.36
Zn III	−	<6.60	7.30	<6.58	<5.90	−

| | HS 2125+1105^{c}† | HE 1221−2618^{c} | HS 2033+0821 | HE 0415−2417† | HE 1200−0931† | HE 1422−1851^{c}† |
	32542 K 5.76 *	32606 K 5.51 *	32706 K 5.87 *	32768 K 5.12 *	33419 K 5.78 *	33896 K 5.19 *
He I/II*	10.14	10.16	10.44	9.56	10.12	8.93
C II	<7.26	7.60	7.60	—	<7.34	—
C III	—	—	8.80 ± 0.26	<6.83	—	—
N II	7.30 ± 0.26	7.27 ± 0.31	7.63 ± 0.20	7.05 ± 0.35	7.33 ± 0.25	<7.80
N III	—	—	7.80 ± 0.14	<7.55	7.90	—
O II	7.50 ± 0.14	8.26 ± 0.27	<6.93	<7.04	7.30	<8.13
Ne II	7.20	<6.91	<6.70	<6.70	<7.19	<7.58
Mg II	<7.11	<6.83	<6.87	<6.98	<7.14	<7.69
Al III	<6.00	5.50	5.60	<5.86	<6.00	6.55 ± 0.21
Si III	—	—	<6.10	—	—	<7.35
Si IV	<6.35	<5.92	5.95 ± 0.35	5.75 ± 0.03	<6.21	6.30
P III	<6.04	5.60	<5.59	5.80	6.00	<6.47
S II	—	—	7.90	—	—	—
S III	6.55 ± 0.35	6.65 ± 0.05	7.60 ± 0.01	<5.67	7.35 ± 0.07	<6.93
Ar II	—	—	8.03 ± 0.21	<7.93	<8.07	—
K II	<6.90	<6.80	7.20	7.29 ± 0.30	7.60	—
Ca III	—	<7.50	—	<8.31	<8.68	—
Sc III	<6.63	<6.08	6.15 ± 0.07	<6.42	<6.56	<7.04
Ti III	7.50 ± 0.40	<6.90	7.50 ± 0.46	<6.56	7.36 ± 0.50	7.70
Ti IV	—	—	7.85 ± 0.21	<7.02	<7.90	—
V III	8.40	7.65 ± 0.07	<7.25	<7.47	<8.06	8.30
Cr III	<7.08	7.70 ± 0.42	7.00	<6.87	<7.01	<7.58
Fe III	7.40 ± 0.28	7.00	7.43 ± 0.23	<6.90	7.40	7.70
Co III	<7.75	<7.00	<7.40	—	—	—
Zn III	—	<6.20	—	<6.50	<6.60	—

	PHL 555	HE 1419−1205^c†	HS 2216+1833^c	HE 1519−0708†	HE 1050−0630	HE 1140−050^c†
	34126 K 5.77 *	34171 K 5.71 *	34361 K 5.51 *	34498 K 5.73 *	34501 K 5.79 *	34522 K 4.97 *
He I/II*	10.64	10.35	10.30	10.48	10.60	9.38
C II	<6.50	<7.34	<6.98	<7.60	<6.88	−
C III	6.90	−	−	7.20	7.10	−
N II	7.70 ± 0.06	7.50 ± 0.28	7.75 ± 0.21	7.78 ± 0.42	7.56 ± 0.18	7.40 ± 0.28
N III	7.65 ± 0.07	−	−	8.20	7.70 ± 0.14	−
O II	7.05 ± 0.07	7.10	7.60	7.73 ± 0.32	<6.85	<7.17
Ne II	6.70	6.90 ± 0.28	6.80	7.60	<6.80	<7.05
Mg II	<6.57	<7.09	6.70	<7.23	<6.61	6.70
Al III	<5.74	<5.98	<5.79	<6.25	5.80	<5.95
Si III	−	6.20	−	−	<6.09	−
Si IV	<5.34	<6.08	<5.21	<6.24	5.45 ± 0.07	<5.21
P III	6.10	<5.99	<5.80	6.50	5.80	<5.96
S II	−	−	−	−	−	−
S III	7.30 ± 0.14	6.30	6.68 ± 0.25	7.30 ± 0.28	7.20 ± 0.01	<5.99
Ar II	7.93 ± 0.21	−	−	7.80	7.55 ± 0.07	−
K II	<6.81	7.10	<6.90	7.40	7.30	<7.20
Ca III	8.10 ± 0.42	<7.90	−	8.25 ± 0.35	8.10	8.72
Sc III	<5.99	<6.00	<6.32	<6.30	<5.80	6.30
Ti III	7.10 ± 0.57	<6.74	7.60	7.50	6.85 ± 0.35	7.05 ± 0.64
Ti IV	6.95 ± 0.21	−	−	<8.03	7.05 ± 0.07	−
V III	<6.88	7.60	<7.60	<8.32	7.60	7.85 ± 0.21
Cr III	7.35 ± 0.49	7.65 ± 0.49	7.20	<7.00	7.30	<7.00
Fe III	7.25 ± 0.35	7.30	7.10	7.20	7.30 ± 0.28	<7.14
Co III	−	−	−	−	−	−
Zn III	<6.47	−	−	7.00	<6.50	<6.64

	HE 1450−0957 34563 K 5.79 *	HE 1448−0510 34760 K 5.53 *	HS 1710+1614 † 34826 K 5.72 *	HE 2151−1001 34984 K 5.70 *	HS 1536+0944^c† 35114 K 5.83 *	HE 1021−0255 35494 K 5.81 *
He I/II*	10.71	8.59	10.36	10.40	11.18	10.54
C II	−	<7.04	−	6.90	9.10	−
C III	<6.96	6.10	<6.79	<6.68	9.00	<6.70
N II	7.62 ± 0.10	7.50 ± 0.28	7.53 ± 0.21	7.40 ± 0.14	7.60 ± 0.14	<7.20
N III	7.70 ± 0.42	7.20	8.19 ± 0.20	8.00 ± 0.14	−	7.40
O II	<7.19	<6.98	<7.12	6.70	<7.60	<7.12
Ne II	<7.08	7.15 ± 0.35	<6.97	<6.97	<6.90	<7.00
Mg II	<6.96	7.00	<6.99	<6.93	<7.10	<6.98
Al III	5.90 ± 0.14	<5.80	<5.92	5.85 ± 0.21	6.60	<5.93
Si III	<6.85	6.65 ± 0.07	−	−	6.80	−
Si IV	6.50 ± 0.28	6.40 ± 0.10	<5.55	<5.57	7.00 ± 0.28	<5.47
P III	<6.04	<5.87	<5.93	<5.97	<6.05	<5.94
S II	−	−	−	−	−	−
S III	6.00	<5.89	<5.97	6.60	7.25 ± 0.21	7.28
Ar II	7.65 ± 0.07	<7.93	8.20	<7.60	−	8.00
K II	<6.50	7.15 ± 0.07	<7.08	7.50	<7.24	<7.13
Ca III	<8.34	7.40	<8.16	<8.12	<8.28	8.00
Sc III	<6.00	<5.80	<6.43	<6.47	6.35 ± 0.07	<6.42
Ti III	<6.82	6.87 ± 0.50	7.65 ± 0.21	<6.71	7.61	−
Ti IV	<7.70	6.90	7.30	<7.00	−	<6.67
V III	<8.06	<7.88	<7.92	<7.96	7.60	<7.89
Cr III	<7.24	<6.50	<7.02	7.20	<7.10	7.70
Fe III	7.10 ± 0.28	7.20	7.45 ± 0.21	7.15 ± 0.21	7.60	7.80 ± 0.01
Co III	−	−	−	−	−	−
Zn III	−	−	<6.90	−	<7.00	<6.71

	HE 0101−2707	HE 0019−5545	HE 1352−1827†	PG 1207−032	GD 619	HE 1033−2353†
	35568 K 5.97 *	35662 K 5.86 *	35674 K 5.53 *	35693 K 5.82 *	36097 K 5.82 *	36204 K 5.76 *
He I/II*	11.08	10.56	10.23	10.52	10.67	10.54
C II	8.30	−	<8.10	<7.01	<7.00	−
C III	9.23 ± 0.21	8.05 ± 0.07	6.60	7.10	7.20	<6.94
N II	7.42 ± 0.13	7.40	7.77 ± 0.21	7.25 ± 0.13	7.15 ± 0.21	7.58 ± 0.22
N III	7.65 ± 0.07	7.40	7.40	7.35 ± 0.07	7.15 ± 0.07	7.40
O II	<7.20	<7.19	8.40	7.25 ± 0.35	7.20	7.85 ± 0.35
Ne II	<6.60	7.10	7.60	<6.90	6.70	<7.24
Mg II	<6.86	<6.97	<7.34	<6.79	<6.77	<7.21
Al III	<5.92	<6.00	<6.48	<5.82	<5.80	<6.28
Si III	<6.20	<6.85	−	<6.35	<5.55	<6.90
Si IV	6.05 ± 0.07	6.10 ± 0.14	<6.21	5.70	5.20	<6.06
P III	6.20	6.10	6.40	<5.84	6.20	6.05 ± 0.21
S II	−	−	−	−	−	−
S III	7.75 ± 0.07	6.70	<6.72	7.50 ± 0.01	7.40 ± 0.01	7.10 ± 0.28
Ar II	7.97 ± 0.12	<7.60	−	<7.90	<7.87	<7.90
K II	7.55 ± 0.07	<7.22	7.80	7.00 ± 0.28	<6.97	7.50 ± 0.14
Ca III	8.30 ± 0.28	7.90 ± 0.28	<8.20	7.75 ± 0.35	8.25 ± 0.07	7.80 ± 0.42
Sc III	6.30 ± 0.42	<6.50	<6.99	<6.00	<6.00	6.40
Ti III	7.55 ± 0.07	<6.79	7.45 ± 0.21	7.69	7.05 ± 0.07	7.37
Ti IV	6.85 ± 0.35	6.70 ± 0.42	6.90	6.90 ± 0.14	6.65 ± 0.21	7.20
V III	<7.40	7.90	−	7.55 ± 0.07	<7.70	<8.20
Cr III	7.10	7.20	−	7.60	7.60	<8.00
Fe III	<7.34	7.20	7.90	7.40	7.59 ± 0.10	<7.64
Co III	−	−	−	−	−	−
Zn III	−	−	−	<6.70	−	<6.80

| | HE 1441−0558^c | HE 0123−3330 | HE 1407+0033 |
	36396 K 5.79 *	36602 K 5.87 *	37309 K 5.54 *
He I/II*	10.37	10.51	9.01
C II	−	−	−
C III	−	7.80	<6.49
N II	<7.34	7.50	<7.07
N III	−	7.30 ± 0.28	−
O II	<7.30	7.55 ± 0.35	<7.28
Ne II	<6.80	<6.93	<7.00
Mg II	<6.95	<6.88	<7.02
Al III	<6.10	6.20	<6.04
Si III	<5.91	<6.80	−
Si IV	5.50	6.10 ± 0.30	<6.10
P III	<6.09	<6.01	6.40
S II	−	−	−
S III	7.70 ± 0.28	6.20	<6.39
Ar II	−	<8.14	<8.45
K II	7.75 ± 0.21	7.20 ± 0.57	<7.88
Ca III	8.50 ± 0.30	7.55 ± 0.07	<7.47
Sc III	<6.00	<6.10	<6.51
Ti III	7.57 ± 0.25	7.50 ± 0.28	7.15 ± 0.35
Ti IV	−	−	<6.63
V III	7.85 ± 0.49	<7.92	7.90
Cr III	7.60	7.40	<7.54
Fe III	7.47 ± 0.56	7.30 ± 0.14	<7.29
Co III	−	−	−
Zn III	<6.90	−	<6.70

Table C.2: Elemental abundances of two central stars of planetary nebula from SPY (EGB 5 = PN G 211.9+22.6, PHL 932 = PN G 125.9−47.0). Average values with standard deviations are given, if more than one line was fitted. Single line measurements are given without errors. To estimate realistic errors it is necessary to take the spectral quality into account (see Sect. 4.4.2). Upper limits are only given, if they constrain the abundances in a reasonable way. *The atmospheric parameters as well as the helium abundances are taken from Lisker et al. 2005.

| | EGB 5 | PHL 932 |
	34060 K 5.85 *	33644 K 5.74 *
He I/II*	10.30	11.43
C II	−	−
C III	<6.66	<6.34
N II	6.90 ± 0.28	7.37 ± 0.10
N III	7.70 ± 0.01	7.90
O II	7.45 ± 0.21	<6.70
Ne II	<6.85	<6.74
Mg II	<6.81	<6.16
Al III	<5.78	<5.39
Si III	<6.00	−
Si IV	<5.52	<5.13
P II	−	−
P III	<5.80	<5.40
S II	−	−
S III	6.20 ± 0.21	6.80 ± 0.01
Ar II	7.30	7.15 ± 0.07
K II	<6.90	<6.53
Ca III	8.10 ± 0.14	8.20 ± 0.14
Sc III	<6.13	<5.69
Ti III	7.00	7.30 ± 0.14
Ti IV	7.00 ± 0.28	6.85 ± 0.21
V III	<7.63	<7.21
Cr III	6.80	7.10
Fe III	6.75 ± 0.07	6.90 ± 0.28
Co III	7.40	−
Zn III	<6.54	<6.00

Table C.3: Elemental abundances of HE 1047−0436 derived with the automatic pipeline and the equivalent width method published by Napiwotzki et al. (2001). Average values with standard deviations are given, if more than one line was fitted. Single line measurements are given without errors. Upper limits are only given, if they constrain the abundances in a reasonable way.

	HE 1047−0436	
	automatic	equivalent width method
C II	7.30	8.03 ± 0.12
C III	7.88	7.94 ± 0.11
N II	7.92 ± 0.12	8.01 ± 0.19
N III	8.00 ± 0.01	8.40
O II	7.70 ± 0.13	7.80 ± 0.11
Ne II	6.80	−
Mg II	6.90	6.78
Al III	5.40	5.60 ± 0.03
Si III	6.83 ± 0.25	6.82 ± 0.23
Si IV	6.77 ± 0.38	6.60
P III	<5.02	−
S II	7.60	7.57 ± 0.23
S III	7.15 ± 0.07	7.48 ± 0.33
Ar II	6.80	7.17 ± 0.22
K II	<6.00	−
Ca III	−	−
Sc III	5.90	−
Ti III	7.03 ± 0.41	−
Ti IV	7.00	−
V III	7.20	−
Cr III	7.10 ± 0.42	−
Fe III	6.90 ± 0.36	< 6.80
Co III	<6.92	−
Zn III	−	−

References

Ahmad, A., & Jeffery, C. S. 2003, A&A, 402, 335

Ahmad, A., & Jeffery, C. S. 2005, A&A, 437, L51

Ahmad, A., & Jeffery, C. S. 2006, Baltic Astronomy, 15, 139

Ahmad, A., Jeffery, C. S., & Fullerton, A. W. 2004, A&A, 418, 275

Alexander, D. M., Bauer, F. E., Brandt, W. N., et al. 2003, AJ, 126, 539

Allard, F., Wesemael, F., Fontaine, G., Bergeron, P., & Lamontagne, R. 1994, AJ, 107, 1565

Aznar Cuadrado, R., & Jeffery, C. S. 2001, A&A, 368, 994

Bailyn, C. D., Sarajedini, A., Cohn, H., Lugger, P. M., & Grindlay, J. E. 1992, AJ, 103, 1564

Baran, A., Pigulski, A., Kozieł, D., et al. 2005, MNRAS, 360, 737

Barcons, X., Carrera, F. J., Ceballos, M. T., et al. 2003, AN, 324, 44

Baschek, B., Sargent, W. L. W., & Searle, L. 1972, AJ, 173, 611

Baschek, B., Hoeflich, P., & Scholz, M. 1982a, A&A, 112, 76

Baschek, B., Scholz, M., Kudritzki, R.-P., & Simon, K. P. 1982b, A&A, 108, 387

Bedin, L. R., Piotto, G., Anderson, J., et al. 2004, ApJ, 605, L125

Bedin, L. R., Piotto, G., Zoccali, M., et al. 2000, A&A, 363, 159

Beers, T. C., Preston, G. W., Shectman, S. A., Doinidis, S. P., & Griffin, K. E. 1992, AJ, 103, 267

Behr, B. 2003, ApJS, 149, 67

Behr, B. 2003, ApJS, 149, 101

Berger, L., Koester, D., Napiwotzki, R., Reid, I. N., & Zuckerman, B. 2005, 444, 565

Bergeron, P., Wesemael, F., Michaud, G., & Fontaine, G. 1988, ApJ, 332, 964

Bertola, F., Capacciolo, M., & Oke, J. B. 1982, ApJ, 254, 494

Billères, M., Fontaine, G., Brassard, P., et al. 2000, ApJ, 530, 441

Blanchette, J.-P., Chayer, P., Wesemael, F., et al. 2008, ApJ, 678, 1329

Brassard, P., Fontaine, G., Billères, M., et al. 2001, ApJ, 563, 1013

Bressan, A., Chiosi, C., & Fagotto, F. 1994, ApJS, 94, 63

Bromley, B. C., Kenyon, S. J., Geller, M. J., et al. 2006, ApJ, 653, 1194

Brown, T. M., Bowers, C. W., Kimble, R. A., & Sweigart, A. V. 2000, ApJ, 532, 308

Brown, T. M., Ferguson, H. C., & Davidsen, A. F. 1995, ApJ, 454, L15

Brown, T. M., Ferguson, H. C., Davidsen, A. F., & Dorman, B, 1997, ApJ, 482, 685

Brown, W. R., Geller, M. J., & Kenyon, S. J. 2008, ApJ, accepted (arXiv:0808.2469B)

Brown, W. R., Geller, M. J., Kenyon, S. J., & Kurtz, M. J. 2005, ApJ, 622, L33

Brown, W. R., Geller, M. J., Kenyon, S. J., & Kurtz, M. J. 2006a, ApJ, 640, L35

Brown, W. R., Geller, M. J., Kenyon, S. J., & Kurtz, M. J. 2006b, ApJ, 647, 303

Brown, W. R., Geller, M. J., Kenyon, S. J., & Kurtz, M. J. 2007a, ApJ, 660, 311

Brown, W. R., Geller, M. J., Kenyon, S. J., Kurtz, M. J., & Bromley, B. C. 2007b, ApJ, 671, 1708

Buonanno, R., Corsi, C., Bellazzini, M., Ferraro, F. R., & Fusi Pecci, F. 1997, AJ, 113, 706

Busso, G. & Moehler, S. 2008, ASPCS, 392, 39

Butler, K., & Giddings, J. R. 1985, in Newsletter on Analysis of Astronomical Spectra, No. 9 (London: Univ. London)

Cackett, E. M., & Miller, J. M. 2006, ATel, 937, 1

Caloi, V. 1972, A&A, 20, 357

Caloi, V. 1999, A&A, 343, 904

Campbell, G. C. 1984, MNRAS, 207, 433

Charles, P. A., & Coe, M. J. 2006, in Compact Stellar X-ray Sources, Cambridge Astrophysics Series, Vol. 39, ed. W. H. G. Lewin, & M. van der Klis (Cambridge: University Press), 215

Charpinet, S., Fontaine, G., Brassard, P., et al. 1997, ApJ, 483, 123

Charpinet, S., Fontaine, G., Brassard, P., et al. 2005, A&A, 437, 575

Charpinet, S., Fontaine, G., Brassard, P., et al. 2005, A&A, 443, 251

Charpinet, S., Silvotti, R., Bonanno, A., et al. 2006, A&A, 459, 565

Charpinet, S., van Grootel, V., Reese, D., et al. 2008, A&A, 489, 377

155

Chayer, P., Fontaine, M., Fontaine, G., Wesemael, F., & Dupius, J. 2006, Baltic Astronomy, 15, 131

Claret, A., & Cunha, N. C. S. 1997, A&A, 318, 187

Claret, A., Giménez, & Cunha, N. C. S. 1995, A&A, 299, 724

Code, A. D. 1969, PASP, 81, 475

Crocker, D. A., Rood, R. T., & O'Connell, R. W. 1988, ApJ, 332, 236

D'Antona, F., Bellazzini, M., Caloi, V., et al. 2005, ApJ, 631, 868

D'Cruz, N. L., Dorman, B., Rood, R. T., & OĆonnell, R. W. 1996, ApJ, 466, 359

de Boer, K. S. 1982, A&AS, 50, 247

Dekker, H., D'Odorico, S., Kaufer, A., et al., Proc. SPIE, 4008, 534

de Marchi. G., & Paresce, F. 1996, ApJ, 467, 658

Demers, S., Wesemael, F., Irwin, M. J., et al. 1990, ApJ, 351, 271

Dorman, B., O'Connell, R. W., & Rood, R. T. 1995, ApJ, 442, 105

Dorman, B., Rood, R. T., & O'Connell, R. W. 1993, ApJ, 419, 596

Downes, R. A. 1986, ApJS, 61, 569

Drechsel, H., Haas, S., Lorenz, R., & Gayler, S. 1995, A&A, 294, 723

Drechsel, H., Heber, U., Napiwotzki, R., et al. 2001, A&A, 379, 893

Driebe, T., Schönberner, D., Böcker, T., & Herwig, F. 1998, A&A, 339, 123

Edelmann, H. 2003, Ph. D thesis, Univ. Erlangen-Nürnberg

Edelmann, H. 2008, ASPCS, 392, 187

Edelmann, H., Heber, U., Altmann, M., Karl, C., & Lisker, T. 2005a, A&A 442, 1023

Edelmann, H., Heber, U., & Napiwotzki, R., 2006, Baltic Astronomy, 15, 103

Edelmann, H., Napiwotzki, R., Heber, U., Christlieb, N., & Reimers, D. 2005b, ApJ, 634, L181

Ekberg, J. O. 1993, A&AS, 101, 1

Ergma, E., Fedorova, A. V., & Yungelson, L. R. 2001, A&A, 376, L9

Fabbian, D., Recio-Blanco, A., Gratton, R. G., & Piotto, G. 2005, A&A, 434, 235

Farihi, J., Becklin, E. E., & Zuckerman, B. 2005, ApJS, 161, 394

Feige, J. 1958, ApJ, 128, 267

Ferguson, H. C., Davidsen, A. F., Kriss, G. A., et al. 1991, ApJ, 382, L69

Ferguson, D. H., Green, R. F., & Liebert, J. 1984, ApJ, 287, 320

Ferraro, F. R., Paltrinieri, B., Fusi Pecci, F., et al. 1997, ApJ, 484, L145

Fleig, J., Rauch, T., Werner, K., & Kruk, J. W. 2008, A&A, submitted (arXiv:0809.2746)

Fontaine, G. Brassard, P., Charpinet, S., et al. 2003, ApJ, 597, 518

Fontaine, G. Brassard, P., Charpinet, S., et al. 2008, ASPCS, 392, 231

Fontaine, G., Brassard, P., Green, E. M., et al. 2008, A&A, 486, 39

Fontaine, G., Chayer, P. 1997, in Proc. of Conference on Faint Blue Stars, ed. A. G. D. Philip, J. Liebert, R. A. Saffer, & D. S. Hayes (Schenectady: L. Davis Press), 169

Fontaine, M., Chayer, P., Wesemael, F., et al. 2006, ASPC, 348, 224

For, B.-Q., Edelmann, H., Green, E. M., et al. 2008, ASPCS, 392, 203

Frank, J., King, A., & Raine, D. J. 2002, Accretion power in astrophysics (Cambridge: University Press)

Fusi Pecci, F., Ferraro, F. R., Bellazzini, M., et al. 1993, AJ, 105, 1145

Geier, S., Nesslinger, S., Heber, U., et al. 2007, A&A, 464, 299

Geier, S., Nesslinger, S., Heber, U., et al. 2008, A&A, 477, L13

Giddings J. R. 1981, Ph. D thesis, Univ. London

Giuricin, G., Mardirossian, F., & Mezzetti, M. 1984, A&A, 135, 393

Glaspey, J. W., Michaud, G., Moffat, A. F., & Demers, S. 1989, ApJ, 339, 926

Gnedin, O. Y., Gould, A., Miralda-Escude, J., & Zentner, A. R. 2005, ApJ, 634, 344

Goldreich, P., & Nicolson, P. D. 1989, ApJ, 342, 1079

Gourgouliatos, K. N., & Jeffery, C. S. 2006, MNRAS, 371, 1381

Gray, D. F. 1992, The observation and analysis of stellar photospheres, 2nd edn. (Cambridge: University Press)

Green, E. M., Fontaine, G., Hyde, E. A., For, B.-Q., & Chayer, P. 2008, ASPCS, 392, 75

Green, E. M., Fontaine, G., Reed, M. D., et al. 2003, ApJ, 583, L31

Green, E. M., For, B., Hyde, E. A., et al. 2004, ApSS, 291, 267

Green, E. M., Liebert, J. W., & Saffer, R. A. 1997, in Third Conference on Faint Blue Stars, ed. A. G. D. Philip, J. Liebert, R. Saffer, & D. S. Hayes, (Schenectady: L. Davis Press), 417

Green, R. F., Schmidt, M., & Liebert, J. 1986, ApJS, 61, 304

Greenstein, J. L. 1954, AJ 59, 322

Greenstein, J. L. 1971, in IAU Symp. 42, White Dwarfs, ed. W. J. Luyten (Dordrecht: Reidel), 46

Greenstein, J. L., Truran, J. W., & Cameron, A. G. W. 1967, Nature 213, 871

Greenstein, J. L., & Sargent, A. I. 1974, ApJS, 28, 157

Grevesse, N., & Sauval, A. J. 1998, SSRv, 85, 161

Groth, H. G., Kudritzki, R.-P., & Heber, U. 1985, A&A, 152, 107

Hagen, H.-J., Groote, D., Engels, D., & Reimers, D. 1995, A&AS, 134, 483

Hamada, T., & Salpeter, E. E., 1961, ApJ, 134, 638

Han, Z. 2008, A&A, 484, L31

Han, Z., Podsiadlowski, P., & Lynas-Gray, A. E. 2007, MNRAS, 380, 1098

Han, Z., Podsiadlowski, P., Maxted, P. F. L., Marsh, T. R., & Ivanova, N. 2002, MNRAS, 336, 449

Han, Z., Podsiadlowski, P., Maxted, P. F. L., & Marsh, T. R. 2003, MNRAS, 341, 669

Hansen, C. J., Kawaler, S. D. 1994, Stellar interiors: Physical principles, structure, and evolution (Heidelberg: Springer), 125

Heber, U. 1986, A&A, 155, 33

Heber, U., Drechsel, H., Østensen, R., et al. 2004, A&A, 420, 251

Heber, U., & Edelmann, H., 2004, Ap&SS, 291, 341

Heber, U., Edelmann, H., Lisker, T., & Napiwotzki, R. 2003, A&A, 411, 477

Heber, U., Hirsch, H., Edelmann, H., Napiwotzki, R., & O'Toole, S. J. 2008, ASPCS, 392, 167

Heber, U., Hunger, K., Jonas, G., & Kudritzki, R. P. 1984, A&A, 130, 119

Heber, U., Reid, I. N., & Werner, K. 1999, A&A, 348, L25

Heber, U., Reid, I. N., & Werner, K. 2000, A&A, 363, 198

Heggie, D. C. 1975, MNRAS, 173, 729

Hills, J. G. 1971, A&A, 12, 1

Hills, J. G. 1988, Nature, 331, 687

Hirata, R., & Horaguchi, T. 1995, Atomic spectral line list, Department of Astronomy (Kyoto: University and National Science Museum)

Hirsch, H. A., Heber, U., & O'Toole, S. J. ASPCS, 392, 131

Hirsch, H. A., Heber, U., O'Toole, S. J., & Bresolin, F. 2005, A&A, 444, L61

Hu, H., Dupret, M.-A., Aerts, C., et al. 2008, A&A, 490, 243

Humason, M. L., & Zwicky, F. 1947, ApJ, 105, 85

Hurley, J. R., Tout, C. A., & Pols, O. R. 2002, MNRAS, 329, 897

Iben, I. 1990, ApJ, 353, 215

Iben, I., & Tutukov, A. V. 1984, ApJ, 284, 719

Israel, G. L., Stella, L., Angelini, L., et al. 1997, ApJ, 474, L53

Jeffery, C. S. 2008, ASPCS, 391, 3

Jeffery, C. S., Drilling, J. S., Harrison, P. M., Heber, U., & Moehler, S. 1997, A&AS, 125, 501

Jeffery, C. S., & Pollacco, D. L. 1998, MNRAS, 298, 179

Karl, C., Heber, U., Napiwotzki, R., & Geier, S. 2006, Baltic Astronomy, 15, 151

Karl, C., Napiwotzki, R., Nelemans, G., et al. 2003, A&A, 410, 663

Karl, C. 2004, Ph. D thesis, Univ. Erlangen-Nürnberg

Kilic, M., Prieto, C. A., Brown, W. D., & Koester, D. 2007, ApJ, 660, 1451

Kilkenny, D., Hilditch, R. W., & Penfold, J. E. 1978, MNRAS, 183, 523

Kilkenny, D., Koen, C., O'Donoghue, D., & Stobie, R. S. 1997, MNRAS, 285, 640

Kilkenny, D., O'Donoghue, D., Koen, C., Lynas-Gray, A. E., & van Wyk, F. 1998, MNRAS, 296, 329

Kilkenny, D., O'Donoghue, D., & Stobie, R. S. 1990, MNRAS, 248, 664

Koen, C. 2007, MNRAS, 377, 1275

Koen, C., & Green, E. M. 2007, MNRAS, 377, 1605

Koen, C., Orosz, J., & Wade, R. A. 1998, MNRAS, 300, 695

Kudritzki, R. P., & Simon, K. P. 1978, A&A, 70, 653

Kurucz, R. L 1992, in Proc. of the 149th Symposium of the IAU, ed. B. Barbuy, & A. Renzini (Dordrecht: Kluwer Academic Publishers), 225

Kurucz, R. L. 1993, Kurucz CD-ROM No. 13 (Cambridge, Mass.: Smithsonian Astrophysical Observatory)

Kurucz, R. L. 1996, in Model Atmospheres and Spectrum Synthesis, ed. S. J. Adelman, F. Kupka & W. W. Weiss (San Francisco: ASP), 160

Lamers, H. J. G. L. M., & Cassinelli, J. P. 1999, Introduction to stellar winds (Cambridge: University Press)

Lamontagne, R., Wesemael, F., Fontaine, G., & Sion, E. M. 1985, ApJ, 299, 496

Lamontagne, R., Wesemael, F., & Fontaine, G. 1987, ApJ, 318, 844

Lanz, T., Brown, T. M., Sweigart, A. V., Hubeny, I., & Landsman, W. B. 2004, ApJ, 602, 342

Lee, Y. W. 1994, ApJ, 430, L113

Leibundgut, B. 2001, ARA&A, 39, 67

Lemke, M. 1997, A&AS, 122, 285

Liebert, J., Bergeron, P., Eisenstein, D., et al. 2004, ApJ, 606, L147

Lisker, T., Heber, U., Napiwotzki, R., et al. 2005, A&A, 430, 223

Livio, M. 2000, in Type Ia Supernovae: Theory and Cosmology, ed. J. C. Niemeyer, J. C., & J. W. Truran (Cambridge: University Press), 33

Lorenz, R., Mayer, P., & Drechsel, H. 1998, A&A, 332, 909

Lutz, R., Schuh, S., Silvotti, R., et al. 2008, ASPCS, 392, 339

Marietta, E., Burrows, A., & Fryxell, B. 2000, ApJS, 128, 615

Marsh, T. R., Dhillon, V. S., & Duck, S. R. 1995, MNRAS, 275, 828

Maxted, P. F. L., Heber, U., Marsh, T. R., & North, R. C. 2001, MNRAS, 326, 1391

Maxted, P. F. L., Marsh, T. R., & North, R. C. 2000, MNRAS, 317, L41

Maxted, P. F. L., Marsh, T. R., Heber, U., et al. 2002, MNRAS, 333, 231

Maxted, P. F. L., Morales-Rueda, L., & Marsh, T. 2004, Ap&SS, 291, 307

Maxted, P. F. L., Moran, C. K. J., Marsh, T. R., & Gatti, A. A. 2000, MNRAS, 311, 877

Menou, K., Narayan, R., & Lasota, J.-P. 1999, ApJ, 513, 811

Menzies, J. W. 1986, Ann. Rep. S. Afr. Astron. Obs. 1985, 20

Michaud, G., Vauclair, G., & Vauclair, S. 1983, ApJ, 267, 256

Michaud, G., Bergeron, P., Heber, U., & Wesemael, F. 1989, ApJ, 338, 417

Michaud, G., Richer, J., & Richard, O. 2008, ApJ, 675, 1223

Miller Bertolami, M. M., Althaus, L. G., Unglaub, K., & Weiss, A. 2008, A&A, accepted (arXiv:0808.3580)

Moehler, S., Richtler, T., de Boer, K. S., Dettmar, R. J., & Heber, U. 1990, A&AS, 86, 53

Moehler, S., Sweigart, A. V., Landsmann, W. B., Heber, U., & Catelan, M. 1999, A&A, 346, 1

Moni Bidin, C., Catelan, M., Villanova, S., et al. 2008, ASPCS, 392, 27

Morales-Rueda, L., Maxted, P. F. L., Marsh, T. R., North, R. C., & Heber, U. 2003, MNRAS, 338, 752

Morales-Rueda, L., Maxted, P. F. L., Marsh, T. R., Kilkenny, D., & O'Donoghue, D. 2004, ASPCS, 334, 333

Moran, C. 1999, Ph.D. thesis, Univ. Southampton

Moran, C., Maxted, P. F. L., Marsh, T. R., Saffer, R. A., & Livio, M. 1999, MNRAS, 304, 535

Napiwotzki, R. 2008, ASPCS, 392, 139

Napiwotzki, R. 1999, A&A, 350, 101

Napiwotzki, R., Christlieb, N., Drechsel, H., et al. 2003, ESO Msngr, 112, 25

Napiwotzki, R., Edelmann, H., Heber, U., et al. 2001, A&A, 378, L17

Napiwotzki, R., Karl, C. A., Lisker, T., et al. 2004, Ap&SS, 291, 321

Napiwotzki, R., Koester, D., Nelemans, G., et al. 2002, A&A, 386, 957

Napiwotzki, R., Yungelson, L., Nelemans, G. et al. 2004, ASPCS, 318, 402

Nieva, M. F., & Przybilla, N. 2008, A&A, 481, 199

Nobili, S., Amanullah, R., Garavini, G., Goobar, A., & Lidman, C. 2005, A&A, 437, 789

O'Connell, R. W. 1999, ARAA, 37, 603

Ohl, R. G., Chayer, P., & Moos, H. W. 2000, ApJ, 538, L95

Oreiro, R., Perez Hernandez, F., Ulla, A., et al. 2005, A&A, 438, 257

Orosz, J. A., & Wade, R. A. 1999, MNRAS, 310, 773

Østensen, R. 2006, Baltic Astronomy, 15, 85

Østensen, R., Oreiro, R., Drechsel, H., et al. 2007, ASPCS, 372, 483

Østensen, R., Oreiro, R., Hu, H., Drechsel, H., & Heber, U. 2008, ASPCS, 392, 221

O'Toole, S. J., & Heber, U. 2006, A&A, 452, 579

O'Toole, S. J., Heber, U., & Benjamin, R. A. 2004, A&A, 422, 1053

O'Toole, S. J., Napiwotzki, R., Heber, U., et al. 2006, Baltic Astronomy, 15, 61

Pace, G., Recio-Blanco, A., Piotto, G., & Momany, Y. 2006, A&A, 452, 493

Paczyński, B. 1976, in Structure and Evolution of Close Binaries, ed. P. P. Eggleton, S. Mitton, & J. Whelan (Dordrecht: Kluwer), 75

Padmanabhan, T. 2001, Theoretical Astrophysics, Vol. II: Stars and Stellar Systems (Cambridge: University Press), 354

Park, J. H., & Lee, Y. W. 1997, ApJ, 476, 28

Pauli, E.-M., Napiwotzki, R., Altmann, M., et al. 2003, A&A, 400, 877

Pauli, E.-M., Napiwotzki, R., Heber, U., Altmann, M., & Odenkirchen, M. 2006, A&A, 447, 173

Perlmutter, S., Aldering, G., Goldhaber, G., et al., 1999, ApJ, 517, 565

Pfahl, E., Rappaport, S., & Podsiadlowski, Ph. 2003, ApJ, 597, 1036

Piotto, G., Bedin, L. R., Anderson, J., et al. 2007, ApJ, 661, L53

Piotto, G., Villanova, S., Bedin, L. R., et al. 2005, ApJ, 621, 777

Podsiadlowski, Ph. 2008, ASPCS, 391, 323

Podsiadlowski, Ph., Rappaport, S., & Pfahl, E. D. 2002, ApJ, 565, 1107

Pojmanski, G. 2002, Acta Astronomica, 52, 397

Politano, M., Taam, R. E., van der Sluys, M., & Willems, B. 2008, ApJ, accepted (arXiv:0808.1367)

Połubek, G., Pigulski, A., Baran, A., & Udalski, A. 2007, ASPCS, 372, 487

Przybilla, N. 2005, A&A, 443, 293

Przybilla, N., & Butler, K. 2004, ApJ, 609, 1181

Przybilla, N., Nieva, M. F., & Edelmann, H. 2006, Baltic Astronomy, 15, 107

Randall, S. K., Matthews, J. M., Fontaine, G., et al. 2005, ApJ, 633, 460

Randall, S. K., Fontaine, G., Charpinet, S., et al. 2006, ApJ, 648, 637

Rauch, T. 2000, A&A, 356, 665

Rauch, T., & Werner, K. 2003, A&A, 400, 271

Reed, M. D., & Stiening, R. 2004, PASP, 116, 506

Rich, R. M., Sosin, C., Djorgovski, S. G., et al. 1997, ApJ, 484, L25

Riess, A. G., Fillipenko, A. V., Challis, P., et al. 1998, AJ, 116, 1009

Rieutord, M. 1992, A&A, 259, 581

Ritter, H., & Kolb, U. 1998, A&AS, 129, 83

Saffer, R. A., Bergeron, P., Koester, D., & Liebert, J. 1994, ApJ, 432, 351

Saffer, R. A., Livio, M., & Yungelson, L. R. 1998, ApJ, 502, 394

Saio, H., & Jeffery, C. S. 2000, MNRAS, 313, 671

Sandage, A., & Wallerstein, G. 1960, ApJ, 131, 598

Sandage, A., & Wildey, R. 1967, ApJ, 150, 469

Sarazin, M., & Roddier, F. 1990, A&A, 227, 294

Sargent, W. L. W., & Searle, L. 1966, ApJ, 145, 652

Sargent, W. L. W., & Searle, L. 1968, ApJ, 152, 443

Schuh, S., Huber, J., Dreizler, S., et al. 2006, A&A, 445, 31

Silvotti, R., Schuh, S., Janulis, R., et al. 2007, ASPCS, 372, 369

Silvotti, R., Schuh, S., Janulis, R., et al. 2007, Nature, 449, 189

Slettebak, A., & Brundage, R. K. 1971, AJ, 76, 338

Soker, N. 1998, AJ, 116, 1308

Sosin, C., Dorman, B., Djorgovski, S. G., et al. 1997, ApJ, 480, L35

Stark, M. A., & Wade, R. A. 2003, AJ, 126, 1455

Stehlé, C., & Hutcheon, R. 1999, A&AS, 140, 93

Ströer, A., Heber, U., Lisker, T., et al. 2007, A&A, 462, 269

Sweigart, A. V. 1997a, in Third Conference on Faint Blue Stars, ed. A. G. D. Philip, J. Liebert,
    R. Saffer, & D. S. Hayes, (Schenectady: L. Davis Press), 3

Sweigart, A. V. 1997b, ApJ, 474, L23

Tassoul, J.-L., & Tassoul, M. 1992, ApJ, 395, 259

Tassoul, M., & Tassoul, J.-L. 1997, ApJ, 481, 363

Telting, J. H., Geier, S., Østensen, R . H., et al. 2008, A&A, accepted

Terman, J. L., Taam, R. E., & Hernquist, L. 1994, ApJ, 422, 729

Thackeray, A. D. 1970, MNRAS, 150, 215

Thejll, P., Ulla, A., & McDonald, J. 1995, A&A, 303, 773

Ulla, A., & Thejll, P. 1998, A&AS, 132, 1

Unglaub, K., & Bues I. 2001, A&A, 374, 570

Unglaub, K. 2006, Baltic Astronomy, 15, 147

Unglaub, K. 2008, A&A, 486, 923

van Grootel, V., Charpinet, S., Fontaine, G., & Brassard, P. 2008, A&A, 483, 875

van den Bergh, S. 1967, AJ, 72, 70

Vauclair, S., & Vauclair, G. 1982, ARAA, 20, 37

Vennes, S., Kawka, A., & Smith, J. A. 2007, ApJ, 668, L59

Vink, J. S., & Cassisi, S. 2002, A&A, 392, 553

Voges, W., Aschenbach, B., Boller, T., et al. 1999, A&A, 349, 389

von Rudloff, I. R., Vandenberg, D. A., & Hartwick, F. D. A. 1988, ApJ, 324, 840

Vidal, C. R., Cooper, J., & Smith, E. W. 1973, ApJS, 25, 37

Vučković, M., Aerts, C., Østensen, R., et al. 2007, A&A, 471, 605

Vučković, M., Østensen, R., Bloemen, S., Decoster, I., & Aerts, C. 2008, ASPCS, 392, 199

Wallerstein, G., & Spinrad, H. 1960, PASP, 72, 486

Webbink, R. F. 1984, ApJ, 277, 355

Whelan, J., & Iben, I. Jr. 1973, ApJ, 186, 1007

Wiese, W. L., Fuhr, J. L., Deters, T. M. 1996, Atomic transition probabilities of carbon, nitrogen and oxygen: a critical data compilation (Washingtion DC: American Chemical Society for the National Institute of Standards and Technology)

Wils, P., di Scalia, G., & Otero, S. A. 2007, IBVS, 5800, 1

Wilson, R. E., & Devinney, E. J. 1971, ApJ, 166, 605

Wisotzki, L., Reimers, D., & Wamsteker, W. 1991, A&A, 247, L17

Wood, J. H., Zhang, E.-H.& Robinson, E. L. 1993, MNRAS, 261, 103

Woudt, P. A., Kilkenny, D., Zietsman, E., et al. 2006, MNRAS, 371, 1497

Wu, C. C., Faber, S. M., Gallagher, J. S., Peck, M., & Tinsley, B. M. 1980, ApJ, 237, 290

Yi, S. K., Demarque, P., & Oemler A. Jr. 1997, ApJ, 486, 201

Yu, Q., & Tremaine, S. 2003, ApJ, 599, 112

Zahn, J.-P. 1977, A&A, 57, 383

Zahn, J.-P. 2005, ASPCS, 333, 4

Acknowledgements

Lebenslauf

Name: Stephan Alfred Geier
Geburtsdatum: 12. Oktober 1977, Stadtsteinach
Staatsangehörigkeit: Deutsch

Grundschule:	09/1984−07/1988	Volksschule Stadtsteinach
Gymnasium:	09/1988−07/1997	Markgraf–Georg–Friedrich–Gymnasium Kulmbach
Zivildienst:	11/1997−09/1998	Fachklinik Stadtsteinach, technischer Dienst

Studium:	10/1998−10/2005	Friedrich–Alexander–Universität Erlangen–Nürnberg
		Studienfächer: Physik (Diplom)
		Neuere und Neueste Geschichte, Alte Geschichte,
		Klassische Archäologie (M. A.)
		(Doppelstudium mit Sondergenehmigung)
		Hochbegabtenstipendium nach Art. 10 des Bayerischen
		Begabtenförderungsgesetzes (BayBFG)
	08/2002−12/2002	Auslandssemester an der University of Hawai'i at Manoa
		Honolulu, USA
	04/2004−08/2004	Magisterarbeit in Neuester Geschichte
		Thema: Die Nuklearstrategie der USA
		Betreuer: Prof. Dr. Gregor Schöllgen
		Universität Erlangen–Nürnberg
	09/2004−09/2005	Diplomarbeit an der Dr. Remeis–Sternwarte Bamberg,
		Astronomisches Insitut der Universität Erlangen–Nürnberg
		Thema: Zeitaufgelöste Spektroskopie von KPD 1930+2752
		Betreuer: Prof. Dr. Uli Heber
	10/2005	Abschluss des Studiums:
		Dipl. Phys. Univ. (Note 1.17), M. A. (Note 1.15)
	10/2005−04/2009	Doktorand an der Dr. Remeis–Sternwarte Bamberg,
		Finanziert durch die Deutsche Forschungsgemeinschaft
		Thema: Hot Subdwarf Stars in Close–up View
		Betreuer: Prof. Dr. Uli Heber